Synergizing Experimental and Computational Methods for Gas Separation Membrane Characterization

By

Zheng Cao

Thesis submitted to the University of Ottawa
In partial Fulfillment of the requirements for the
Doctorate in Philosophy in Chemical Engineering

Department of Chemical and Biological Engineering
Faculty of Engineering
University of Ottawa

Abstract

The field of membrane science has experienced remarkable advancements in gas separation technologies recently. A key challenge in enhancing membrane performance is exceeding the "upper bound" limit, which requires simultaneously high permeability and selectivity. To meet this goal, reliable and swift membrane characterization techniques are critical in the process of developing new materials for gas separation membranes. The time-lag method is the most widely used technique for determining the gas transport coefficients in gas separation membranes, which allows evaluating membrane permeability (P), diffusivity (D), and solubility (S) coefficients in a single permeation experiment. However, the conventional time-lag method is limited by the accuracy of the monitoring system, and when applied to more complex cases or more advanced materials. The objective of this thesis is to explore more efficient and reliable membrane characterization techniques to overcome these challenges.

In this project, we developed and employed a novel constant-volume (CV) system that enables simultaneous monitoring of dynamic upstream pressure decay and the downstream pressure rise. This innovative CV system allowed us to leverage both upstream pressure decay and downstream pressure rise to propose new membrane characterization methods for a more robust determination of P, D, and S. The resolution and the accuracy of the system were significantly improved by splitting the upstream into the working volume and the reference volume. A new experiment protocol was also presented to minimize the impact of the adiabatic expansion during the initiation of the test. Thanks to the advantage of the system, we proposed and validated a series of new methods using a rubbery membrane, namely polydimethylsiloxane (PDMS). The transport properties obtained through these new methods yielded transport coefficients that were very close to those determined using the conventional time-lag method.

To better calibrate the system, this work also studied some potential artifacts in the system. The effect of using a porous support disc on estimating the membrane's effective transport parameters was explored by numerical simulations. The results show that

relative diffusivity and relative permeability are strictly a function of the porosity of the porous disc and the ratio of the pore diameter to the membrane thickness, which can be used to correct the impact of the porous plate and recover the intrinsic membrane properties.

Based on the improved experimental system and analytical protocol, we investigated the influence of the applied pressure on membrane transport properties due to the phenomenon known as the membrane compaction effect. To systematically evaluate this effect, we first measured the thickness of the compressed membranes under different loads in a high-precision testing machine. Next, we utilized our novel CV system to characterize the membrane transport properties under different pressure conditions. The experimental results revealed an apparent reduction in the transport properties of the PDMS membrane as it underwent compression due to gas pressure differentials.

To determine the most probable values of the transport, a data reconciliation technique was employed, considering both methods and measurement deviation. This approach minimizes an objective function that integrates all sources of variation. A gradient descent optimization algorithm was then applied to converge on the best estimates of P, D, and S. The reconciled results improve the consistency and precision in estimating transport properties compared to the original results.

In parallel with our experimental work, we conducted numerical simulations, including the finite difference (FD) method, electrical analogy networks, and the Monte Carlo (MC) technique, to complement and enhance our findings. These simulations generated upstream and downstream pressure-time profiles corresponding to membrane behavior, providing valuable insight into the actual experimental data. To examine the effect of a porous support disc on the membrane's effective transport parameters under ideal conditions, we solved Fick's second law of diffusion using the finite difference method. The results clearly showed that the membrane thickness, the pore size, and the disc porosity can significantly influence the estimation of the diffusivity and permeability of the membrane when using the time-lag method. These findings not only help calibrate our new CV system more accurately but also offer theoretical support for characterizing more complex materials, such as glassy polymers and mixed-matrix membranes.

Résumé

Le domaine de la science des membranes a connu des avancées remarquables dans les technologies de séparation des gaz ces dernières années. Un défi majeur pour améliorer les performances des membranes consiste à dépasser la limite supérieure, ce qui exige à la fois une perméabilité et une sélectivité élevées. Pour atteindre cet objectif, des techniques de caractérisation des membranes fiables et rapides sont essentielles dans le développement de nouveaux matériaux pour les membranes de séparation gazeuse. La méthode du temps de décalage (time-lag) est la technique la plus largement utilisée pour déterminer les coefficients de transport des gaz dans les membranes, permettant d'évaluer les coefficients de perméabilité (*P*), de diffusivité (*D*) et de solubilité (*S*) en une seule expérience de perméation. Cependant, la méthode conventionnelle du temps de décalage est limitée par la précision du système de surveillance, notamment lorsqu'elle est appliquée à des cas plus complexes ou à des matériaux plus avancés. L'objectif de cette thèse est d'explorer des techniques de caractérisation des membranes plus efficaces et fiables pour surmonter ces défis.

Dans ce projet, nous avons développé et employé un nouveau système à volume constant (VC) permettant un suivi simultané de la décroissance dynamique de la pression en amont et de l'augmentation de la pression en aval. Ce système innovant nous a permis d'exploiter à la fois la décroissance de la pression en amont et l'augmentation de la pression en aval pour proposer de nouvelles méthodes de caractérisation des membranes, afin de déterminer de manière plus robuste *P*, *D* et *S*. Grâce à cet avantage, nous avons proposé et validé une série de nouvelles méthodes en utilisant une membrane caoutchouteuse, le polydiméthylsiloxane (PDMS). Les propriétés de transport obtenues par ces nouvelles méthodes ont donné des coefficients très proches de ceux déterminés par la méthode conventionnelle du temps de décalage.

Sur la base du système expérimental amélioré et du protocole analytique, nous avons étudié l'influence de la pression appliquée sur les propriétés de transport de la membrane en raison d'un phénomène connu sous le nom d'effet de compaction. Pour évaluer

systématiquement cet effet, nous avons d'abord mesuré l'épaisseur des membranes comprimées sous différentes charges à l'aide d'une machine de test ayant une précision élevée. Ensuite, nous avons utilisé notre nouveau système VC pour caractériser les propriétés de transport de la membrane sous différentes conditions de pression. Les résultats expérimentaux ont révélé une réduction apparente des propriétés de transport de la membrane PDMS lorsqu'elle est soumise à une compression due aux différences de pression gazeuse.

En parallèle de nos travaux expérimentaux, nous avons réalisé des simulations numériques, incluant la méthode des différences finies (FD), les réseaux d'analogie électrique et la technique de Monte Carlo (MC), pour compléter et enrichir nos résultats. Ces simulations ont généré des profils pression-temps en amont et en aval correspondant au comportement de la membrane, fournissant des informations précieuses pour interpréter les données expérimentales. Pour examiner l'effet d'un disque poreux, servant à supporter la membrane en aval, sur les paramètres de transport effectifs de la membrane dans des conditions idéales, nous avons résolu la seconde loi de diffusion de Fick à l'aide de la méthode des différences finies. Les résultats ont clairement montré que l'épaisseur de la membrane, la taille des pores et la porosité du disque peuvent influencer significativement l'estimation de la diffusivité et de la perméabilité de la membrane lors de l'utilisation de la méthode du temps de décalage. Ces résultats permettent non seulement de calibrer plus précisément notre nouveau système VC, mais offrent également un soutien théorique pour la caractérisation de matériaux plus complexes, tels que les polymères vitreux et les membranes mixtes.

Acknowledgements

As the saying goes, good things take time. This project spanned over five and a half years, encompassing two semesters of the MASc program project and thirteen semesters of my Ph.D. project. It began at a particularly challenging time, when COVID-19 pandemic significantly hindered research progress throughout 2020 and 2021. The project gradually regained momentum as I committed myself fully to membrane characterization experiments and simulations of mixed matrix membranes (MMMs). The completion of this thesis is the result of countless contributions from many individuals. I would like to take this opportunity to express my deepest gratitude to everyone who supported me along the way.

I would first like to express my heartfelt gratitude to my esteemed supervisors, Dr. Jules Thibault and Dr. Boguslaw Kruczek. They introduced me to the field of membrane characterization, recognized my potential, and generously supported my transition from the MASc program to Ph.D., enabling me to continue exploring this fantastic topic. Their unwavering support extended beyond research and technical guidance; they also offered invaluable advice on my academic career. Without their professional guidance and constant encouragement, this thesis would not have been possible. Working with them has taught me the true meaning of professionalism and revealed the depth of passion they hold for their areas of interest. I will always remember the things and merits I learnt from them for the rest of my life.

I would like to thank Drs. George Psofogiannakis, Jan Haelssig, and Handan Tezel for participating as committee members for my comprehensive exam and reviewing my final thesis. Their comments, questions, and suggestions made this thesis more precise and understandable to a broader audience.

Special thanks to the department technicians, namely Gérard, Franco, and Patrick, for their invaluable technical support and advice. I am especially grateful to thank Franco

for his assistance in enhancing the CV system and for his contributions to the mechanical work.

I also wish to thank the previous Ph.D. student, Dr. Haoyu Wu, who helped me to start my research program and provided support in the MMM simulations. Sincere appreciation is also given to Mr. Peter Leszczynski, who guided me on operating the membrane characterization system and the spin coating of PPO membranes.

I would like to thank the National Science and Engineering Research Council (NSERC) for the financial support for this project, the University of Ottawa for the International Doctoral Scholarship, and the Department of Chemical and Biological Engineering for the Wilfrid Brisson Graduate Scholarship. These financial supports made my life easier and enabled me to be more focused on my graduate studies.

Last but not least, I am grateful for the unconditional love from my family, especially the selfless support from my wife, Emily Pan. They made my pursuit of knowledge more meaningful.

This thesis work is not the end of my exploration but only a humble beginning for my academic career.

Statement of contributions of collaborators

I hereby declare that I, Zheng Cao, am the sole author and the principal researcher of this thesis and that no parts of this work have been submitted or accepted for any other degree.

Drs. Boguslaw Kruczek and Jules Thibault supervised this thesis. Both provided continued guidance during the work carried out and editorial comments to the publications and the final version of this thesis. Mr. Peter Leszczynski and Dr. Haoyu Wu have co-authored the paper in **Chapter 2**. Mr. Peter Leszczynski helped with the development of the final membrane characterization system. Dr. Haoyu Wu helped with modifying and improving the system and generating the original model. The tensile stretch test on the PDMS membrane in **Chapter 5** was performed by the PhD student Hongchen Wang from the University of Toronto. The original computer code in this thesis was written by Dr. Jules Thibault in **Chapters 4, 7, and 8.**

The responsibilities of the author, Zheng Cao, to fulfill the requirements of this thesis were as follows:

1. Modify the constant-volume system and analytical protocols to accurately evaluate the upstream time lag.
2. Develop and implement a novel analysis technique to characterize membrane properties based on the time-dependent gas accumulation within the membrane.
3. Evaluate the discrepancies between experimental and simulation results for the PDMS membrane under varying feed pressures.
4. Investigate the compaction effects of the PDMS membrane under the various applied pressures.
5. Simulate and analyze the impact of the presence of a downstream porous support plate on the estimation of the transport properties of the membrane.

6. Apply the data reconciliation technique to the experimental data to minimize the uncertainties in measurement and evaluation methods.
7. Prepare a thesis in partial fulfillment of the requirements for a Ph.D. degree in Chemical Engineering.

Table of contents

List of Figures

List of Tables

Chapter 1

Introduction

1.1 Introduction

Since asymmetric polymeric membranes were invented for water desalination, they have experienced continuous growth in applications due to their numerous advantages, including a small space footprint, low energy consumption, operational simplicity, and environmental friendliness [1,2]. These compelling benefits have led to their widespread use in diverse industries, including biotechnology, water treatment, pharmaceutical manufacturing, food processing, petroleum refining, and gas separation [3,4]. For the selective separation of industrial mixtures, membranes are typically engineered with a selective layer that exploits differential permeability among components [5]. Despite the significant progress in synthetic membranes, polymeric membranes, such as polysulfones, cellulose acetates, polyphenylene oxide, aramids, polycarbonates, and polyimides, are the most extensively used in commercial applications [6-8]. Mixed-matrix membranes (MMMs), which incorporate fillers into polymeric matrices, have also attracted significant research interest due to their expanding potential applications [8]. To achieve high performance in gas separation industries, such as carbon dioxide capture, hydrogen recovery, and biogas purification, it is essential to develop advanced materials for gas separation membranes [9,10]. Membrane research primarily focuses on creating novel materials to enhance permeation rates and selectivity, with the ultimate goal of surpassing the "upper bound" limit [11] by simultaneously achieving high permeability and selectivity.

The transport of a gas across a membrane is described by the solution-diffusion model, which comprises three steps. Gas molecules first dissolve at the upstream interface, then diffuse through the membrane, and eventually desorb at the permeate side. According

to the solution-diffusion model, gas permeability (P) in the membrane is a product of its diffusivity (D) and solubility (S):

$$P = SD \tag{1.1}$$

The separation potential of the membrane material for gases i and j, often referred to as the ideal selectivity ($\alpha_{i/j}$) or permselectivity, is simply the ratio of the respective permeability coefficients:

$$\alpha_{i/j} = \frac{P_i}{P_j} \tag{1.2}$$

Moreover, the ideal selectivity is a product of diffusivity selectivity (α_D) and solubility selectivity (α_S):

$$\alpha_{i/j} = \alpha_D \alpha_S \tag{1.3}$$

In turn, α_D and α_S are ratios of the respective diffusivity and solubility coefficients. Therefore, the critical step for the characterization of a new membrane material is the determination of P, D, and S of different gases in that material. These three transport coefficients are conventionally determined in a single dynamic experiment, often referred to as a time lag method, which is attributed to Daynes [12].

The time-lag experiments are generally performed in constant volume (CV) systems. A degassed, homogeneous membrane from the tested material is exposed to a stepwise pressure increase at one side (the feed side). The resulting pressure rise at the other (permeate) side of the membrane is monitored in real-time. The tangent of the linear portion of the pressure rise, associated with a constant permeation rate, is directly proportional to P. The extrapolation of that linear portion to the time axis yields a time lag (θ_d), which is related to the diffusivity by:

$$\theta_d = \frac{L^2}{6D} \tag{1.4}$$

where L is the membrane thickness. Knowing P and D, according to Eq. (1.1), S is the ratio of P and D. These three transport coefficients are considered intrinsic properties of

the membrane material, i.e., they are independent of the feed pressure at which they are determined. However, this is the case only for rubbery polymeric materials and ideal gases for which gas sorption obeys Henry's law. Most of the commercial gas separation membranes are made from glassy polymers, for which Henry's law does not apply. Moreover, the same is true for most new high-performance membrane materials, including mixed matrix membranes (MMMs), for which the complete characterization of gas transport requires evaluation of additional parameters. These may include the capacity of the Langmuir sites, the affinity of the permeating molecules toward the Langmuir sites, the ratio of the diffusivity of penetrants in the Langmuir and Henry's sites, etc. Although the time-lag experiment can be performed regardless of the membrane material, the resulting P, D, and S values are effective rather than intrinsic. Therefore, the complete characterization of gas transport in the membrane material requires time-lag experiments at different feed pressures.

The validity of Eq. (1.4), and by extension the time-lag method, assumes that the permeant concentration remains constant at both the feed and permeate interfaces of the membrane, and specifically with zero concentration on the permeate side. In practice, however, as the gas enters the membrane, the feed pressure and the corresponding concentration gradually decrease. The opposite is true at the permeate interface, where the concentration increases with time. However, in properly designed time-lag experiments, the error associated with the variation of concentrations at the feed and permeate interfaces of the membrane is generally negligible [13,14].

The time-lag method also assumes that the membrane is the only resistance to gas transport during the permeation experiment. The implications of this unwritten assumption are a step change in pressure to initiate the time-lag experiment, and that pressure downstream from the membrane is only a function of time, not position. Indeed, unless the time-lag experiment is performed using a vapour rather than a gas, the pressure increase to initiate the experiments should occur in a step-wise manner [15]. On the other hand, because the gas accumulates at a high vacuum on the permeate side, the transport downstream from the membrane, i.e., gas accumulation, is governed by Knudsen diffusion, with the corresponding diffusivity directly proportional to the internal tube diameter [16]. In principle, resistance to gas accumulation is inversely proportional to the

Knudsen diffusion coefficient. However, a combination of an accumulation tank, which because of a relatively large internal diameter can be considered resistance-free, with a tube(s) connecting the membrane cell with the accumulation tank may lead to significant underestimation of the measured time lag and thus an overestimation of the measured diffusivity of the gas in the tested membrane [17–19]. Still, the effects of the resistance to gas on the estimated time lag of the membrane can be minimized in properly designed downstream receivers of the CV system [20].

Additionally, downstream from the membrane, a porous plate supports the membrane to withstand the pressure gradient during gas permeation tests. The resistance to gas transport through the porous support is negligible. However, the presence of the porous support reduces the effective area for gas transport at the membrane-porous support interface, leading to an underestimation of the experimentally measured P [21,22]. At the same time, the effect of the porous plate on the diffusivity and solubility coefficients, as determined in the time-lag experiments, has not been previously explored.

As previously noted, the complete characterization of membrane materials in which sorption does not follow Henry's law requires time-lag experiments at multiple feed pressures, which assumes that the membrane structure is not affected by the applied feed pressure. On the other hand, a decrease in the thickness of asymmetric cellulose acetate membranes was demonstrated in real time during the actual gas separation tests, using an ultrasonic time-domain reflectometry (TDR) technique [23]. The resulting membrane compaction was attributed to the compaction of the porous support layer of the membrane under high pressures. The TDR technique does not allow distinguishing between the compaction in the selective (dense) layer and the porous sublayer of the membrane. It is essential to emphasize that membrane compaction and the resulting decline in flux during operation are significant problems in the practical application of polymeric gas separation membranes [24]. Using the argument of decreased free volume due to the pressure gradient across the membrane, one could expect a corresponding decrease in diffusivity and solubility. However, to our knowledge, there is no study on the effect of feed pressure on D and S in dense rubbery membranes.

When performing the time-lag experiment in a CV system, in addition to the pressure rise downstream from the membrane, the upstream pressure, i.e., the feed

pressure, decreases. The benefits of applying the pressure decay method in membrane characterization were first discussed 30 years ago [25]. Monitoring the upstream pressure decay can offer some unique advantages, particularly when characterizing barrier materials for which reaching the steady-state permeation (necessary to determine the time lag) could take not seconds or minutes, but hours or even days. Combining the upstream pressure decay with the downstream pressure rise allowed Al-Ismaily et al. to determine *P* from transient permeation data before reaching a steady state [26]. Immediately after initiating the gas permeation experiment, the membrane behaves as a semi-infinite solid, and the pressure decay at the membrane upstream is a linear function of the square root of time, with the slope directly proportional to $S\sqrt{D}$ and zero intercept. In other words, *S* and *D* are coupled to the initial pressure decay. However, it was shown that laminating the tested membrane with a film of known properties (e.g. silicone rubber) results in an intercept that depends on the tested membrane's *S* and *D* [27]. Therefore, the mathematical expression for the intercept yields the second independent equation, thus allowing the determination of *D*, *S*, and *P* from the upstream pressure decay before the gas leaves the tested barrier material. It was shown that if the tested membrane is not laminated and the gas emerges from the membrane, the deviation from the initial linear response in the square root of the time domain depends on *D* but not *S* [28]. Therefore, *D* can be evaluated from the observed deviation at the specific time, and knowing *D*, *S* can be determined from the initial slope of pressure decay vs the square root of time.

Another advantage of monitoring the pressure decay in time-lag experiments, in particular for the membrane materials for which Henry's law is not applicable, was demonstrated by Al-Qasas et al. [29]. Using the example of polyphenylene oxide (PPO), which is a glassy polymer, and assuming complete immobilization of permeating molecules in Langmuir sites as well as an instantaneous equilibrium between the penetrants in the Henry's and Langmuir sites, they showed that the complete characterization of PPO can be accomplished in two rather than four time-lag experiments at different feed pressures. Despite the potential advantages of monitoring the pressure decay in membrane characterization, this approach did not gain much attention in the membrane community. There are two main reasons for that. First, the resolution of the absolute pressure transducers depends on the maximum pressure they can measure.

Because the pressure at the upstream side of the membrane is orders of magnitude greater than that at the permeate side, the pressure rise in the conventional time-lag method can be monitored with an excellent resolution, but not the pressure decay at the upstream side of the membrane. Another challenge when monitoring pressure decay is the temperature drift [30]. To address the limitation of absolute pressure transducers' resolution to measure pressure decay accurately, Al-Ismaily et al. [26] adopted the concept of a two-tank volume, initially developed by Arkilic et al. [31] for microfluidic measurements. However, the time-lag experiments could not be performed at pressures greater than 175 Torr. Moreover, the upstream and downstream time lag ratio did not yield a reasonable value, attributed to a "compression effect." [26]. Our research group has recently addressed the problems faced by Al-Ismaily et al. by developing a new generation of the CV system [32], which increased the range of the feed pressure to 2000 Torr and eliminated the compression effect. However, despite the possibility of monitoring the pressure decay immediately after the experiment's initiation, an inevitable expansion occurs, associated with the experiment's initiation, which leads to the Joule-Thomson effect, rendering the pressure decay in the first few seconds of the experiment unreliable [32].

1.2 Objectives

This doctoral research program focuses on enhancing the efficiency and accuracy of extracting comprehensive transport properties of gas separation membranes in time-lag experiments utilizing the new generation of CV systems developed by our research group. Inaccuracies in estimating these transport properties often arise from multiple sources: deviations from idealized analytical models, measurement errors within the experimental setup, and overlooked system effects.

This thesis focuses on calibrating the new CV system using commercial PDMS membranes and nitrogen, which can be considered an ideal gas. PDMS is a rubbery polymer, and as such, P, D, and S determined in the conventional time-lag experiments represent the intrinsic properties of this material. Therefore, any deviations between the experiments performed at different pressures might be an indication of experimental

artifacts. The specific effects targeted in this thesis are the potential compaction of the membranes by the applied pressure gradient and the impact of the porous support. Although these parameters have already been investigated, previous studies have focused primarily on the permeability coefficients. To our knowledge, no studies have been conducted on the effect of pressure and porous plate support on the diffusivity and solubility coefficients. The primary tools employed in this work are our novel CV system, which enables the simultaneous monitoring of conventional pressure rise and pressure decay during time-lag experiments, and numerical methods. The latter are particularly important when no experimental results exist and the transport problem cannot be solved analytically. The results of numerical simulations, for which we primarily apply the finite difference (FD) method, are to provide the framework for future experiments. Additionally, numerical simulations can help distinguish between artifacts and genuine, fundamental trends observed in experimental results. Another numerical tool used in this thesis is the Monte Carlo (MC) simulation, which may provide reliable variation ranges of experimentally determined parameters, given the realistic confidence ranges of different factors contributing to the experimentally measured transport coefficients. Additionally, given the possibility of multiple methods for determining transport coefficients, as offered by the simultaneous monitoring of the pressure rise and pressure decay in our CV system, MC provides data reconciliation to uncover the actual transport coefficients.

To more effectively evaluate the gas separation membrane performance, a comprehensive experimental and analytical protocol is critical for reliably predicting and interpreting the experimental results.

The following are the specific objectives of this thesis.

1. Improving the experimental system and protocol. This includes demonstrating the capabilities of the newly developed CV system to accurately monitor pressure decay during dynamic gas permeation tests, in addition to simultaneously monitoring the conventional downstream pressure rise.
2. Extracting from the experimental results, alternative ways for the determination of the basic transport coefficients. In particular, it is desired to develop a method for the direct determination of the solubility coefficient.

3. Analyzing the impact of porous support plates. Using finite difference simulations, the effects of the porous support plate on the effective *P*, *D*, and *S* of the membrane system are examined.
4. Investigating pressure compaction and effective thickness effects. The externally applied pressure on membrane compaction and its impact on the effective thickness are studied within the context of time-lag experiments.
5. Application of data reconciliation to extract the most probable values for *P*, *D*, and *S* from among alternative characterization methods, enabled by simultaneous monitoring of pressure rise and pressure decay in our CV system.
6. Application of Monte Carlo simulations for the estimation of the effective permeability of mixed-matrix membranes.
7. To explore using Electrical Network Models for solving Fick's second law of diffusion in homogeneous and mixed matrix membranes as an alternative to the Finite Difference method.

Figure 1.1 provides the flow chart encompassing all current aspects of the thesis.

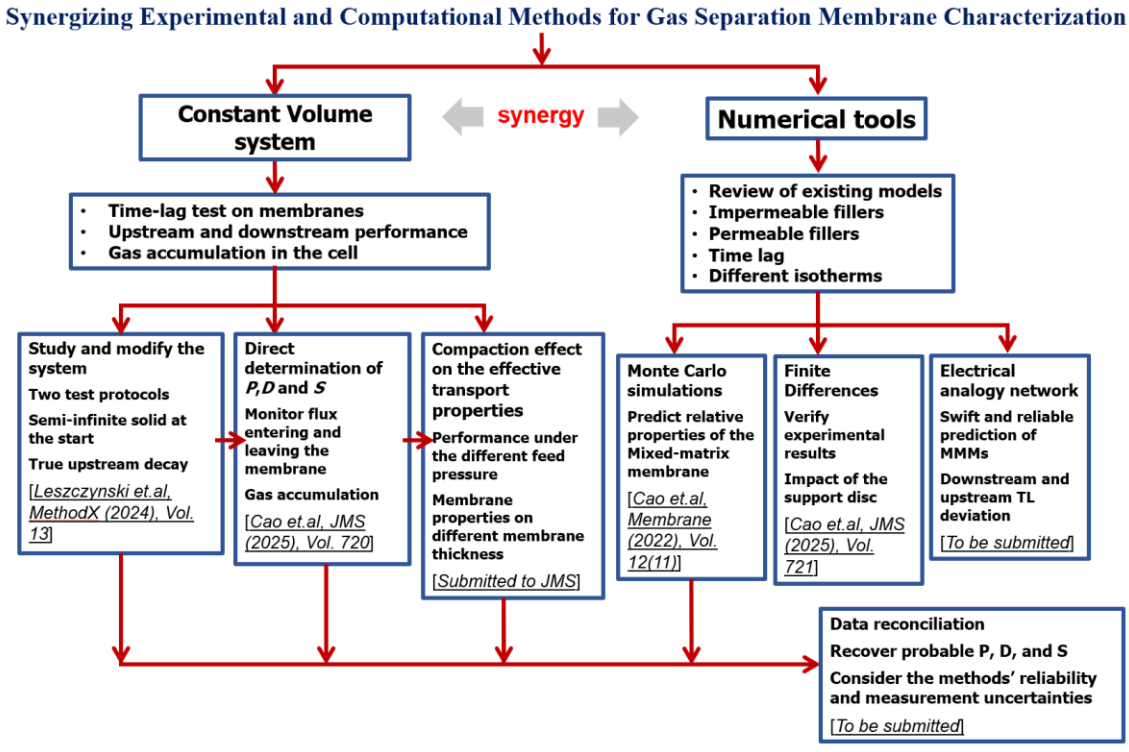

Figure 1.1 Flow chart summarizing the main aspects of the thesis.

1.3 Thesis structure

This thesis comprises nine chapters, including Chapter 1 for the introduction and Chapter 9 for the conclusions and recommendations. Chapters 2-8 comprise the main chapters of the thesis, which cover seven specific aspects of the thesis. Chapters 2, 3, 4, and 7 are scientific articles already published in peer-reviewed journals. Chapters 5, 6 and 8 are articles that were submitted or are to be submitted to reviewed journals.

Chapter 2, titled "*Determination of time lag by accurate monitoring of pressure decay in a new generation constant volume system*," presents the experimental protocols and analytical methods used in permeation studies conducted with the modified CV system, incorporating both upstream and downstream pressure data. The chapter also addresses key challenges, including pressure transducer resolution and the Joule-Thompson effect. It establishes the operational and analytical standards for time-lag experiments that serve as the foundation for the subsequent experimental chapters.

Chapter 3, titled "*Direct determination of permeability, diffusivity and solubility of gases in membrane based on simultaneous monitoring of pressure rise and decay in a single time-lag experiment*," introduces the procedures and the mathematical fundamentals of a newly developed method for directly measuring the membrane's permeability, diffusivity, and solubility.

Chapter 4, titled "*Impact of the porous support disc of a gas permeation cell on the estimation of the membrane transport properties*," explores how the presence of a porous support disc influences the accuracy of membrane permeation parameter estimates. The impact of a porous disc supporting an ideal membrane was assessed by solving Fick's second law of diffusion using the finite difference method.

Chapter 5, titled "*Effect of feed pressure on the membrane thickness and membrane transport properties via the time-lag method*," examines how the pressure-induced compressibility affects the thickness, permeability, diffusivity, and solubility of PDMS membrane during time-lag experiments. This chapter builds upon previously established protocols and analytical methods to assess these effects.

Chapter 6, titled "*Membrane characterization in the time-lag experiment applying data reconciliation techniques*," focuses on recovering the most probable transport properties (P, D, and S) from all the estimation methods applied on the simultaneous time-lag experiment, when both the reliability of data measurements and the accuracy of each estimation method are taken into consideration.

Chapter 7, titled "*Monte Carlo simulations for the estimation of the effective permeability of Mixed-Matrix Membranes*," proposes a Monte Carlo (MC) algorithm designed to rapidly and accurately estimate the relative permeability of ideal MMMs over a wide range of conditions. The simulation results closely align with established models, and the effect of filler geometries is thoroughly examined.

Chapter 8, titled "*Leveraging Electrical Network Models for Solving Fick's Second Law of Diffusion in Membrane Gas Permeation*," presents an innovative approach that applies electrical network analogies to solve transient gas permeation governed by Fick's second law of diffusion in non-porous membranes. The method is systematically validated through permeability predictions for various filler geometries in MMMs.

References

[1] A. Fauzi Ismail, T. Djoko Kusworo, H. Hasbullah, Understanding the solution-diffusion mechanism in gas separation membrane for engineering students, Regional Conference on Engineering Education, Johor, 2005. https://www.researchgate.net/publication/279647120.

[2] K.C. Chong, S.O. Lai, H.S. Thiam, H.C. Teoh, S.L. Heng, Recent progress of Oxygen/Nitrogen separation using membrane technology, Journal of Engineering Science and Technology 11 (2016) 1016–1030.

[3] A. Asad, D. Sameoto, M. Sadrzadeh, Overview of membrane technology, in: Nanocomposite Membranes for Water and Gas Separation, Elsevier, 2019: pp. 1–28. https://doi.org/10.1016/B978-0-12-816710-6.00001-8.

[4] C. Charcosset, Membrane processes in biotechnology: An overview, Biotechnol Adv 24 (2006) 482–492. https://doi.org/10.1016/j.biotechadv.2006.03.002.

[5] Z.W. Abdullah, Y. Dong, I.J. Davies, S. Barbhuiya, PVA, PVA Blends, and Their Nanocomposites for Biodegradable Packaging Application, Polymer - Plastics Technology and Engineering 56 (2017) 1307–1344. https://doi.org/10.1080/03602559.2016.1275684.

[6] W.J. Koros, G.K. Fleming, Membrane-based gas separation, J Memb Sci 83 (1993) 1–80. https://doi.org/10.1016/0376-7388(93)80013-N.

[7] B. Kruczek, T. Matsuura, Development and characterization of homogeneous membranes from high molecular weight sulfonated polyphenylene oxide, n.d.

[8] I. Salahshoori, A. Seyfaee, A. Babapoor, Recent advances in synthesis and applications of mixed matrix membranes, Synthesis and Sintering 1 (2021) 1–27. https://doi.org/10.53063/synsint.2021.116.

[9] F. Vagk, Z. Broi, A method for determination of gas diffusion and solubility coefficients in poly (vinyltrimethylsilane) using a personal computer, J Memb Sci 82 (1993) 265–276. https://doi.org/10.1016/0376-7388(93)85191-X.

[10] K. Ghosal, B.D. Freeman, Gas separation using polymer membranes: an overview, Polym Adv Technol 5 (1994) 673–697. https://doi.org/10.1002/pat.1994.220051102.

[11] L.M. Robeson, Correlation of Separation Factor versus Permeability for Polymeric Membranes, J Memb Sci 62 (1991) 165–185. https://doi.org/10.1016/0376-7388(91)80060-J.

[12] H.A. Daynes, The process of diffusion through a rubber membrane, Royal Society of London 97 (1920) 286–307. https://doi.org/10.1098/rspa.1920.0034.

[13] P. Taveira, A. Mendes, C. Costa, On the determination of diffusivity and sorption coefficients using different time-lag models, J. Memb. Sci. 221 (2003) 123–133. https://doi.org/10.1016/S0376-7388(03)00252-7.

[14] N. Al-Qasas, J. Thibault, B. Kruczek, The effect of the downstream pressure accumulation on the time-lag accuracy for membranes with non-linear isotherms, J. Memb. Sci. 511 (2016). https://doi.org/10.1016/j.memsci.2016.03.047.

[15] E. Favre, N. Morliere, D. Roizard, Experimental evidence and implications of an imperfect upstream pressure step for the time-lag technique, J Memb Sci 207 (2002) 59–72. https://doi.org/10.1016/S0376-7388(02)00039-X.

[16] B. Kruczek, H.L. Frisch, R. Chapanian, Analytical solution for the effective time lag of a membrane in a permeate tube collector in which Knudsen flow regime exists, J Memb Sci 256 (2005) 57–63. https://doi.org/10.1016/j.memsci.2005.02.006.

[17] B. Kruczek, F. Shemshaki, S. Lashkari, R. Chapanian, H.L. Frisch, Effect of a resistance-free tank on the resistance to gas transport in high vacuum tube, J Memb Sci 280 (2006) 29–36. https://doi.org/10.1016/j.memsci.2006.01.001.

[18] S. Lashkari, B. Kruczek, Effect of resistance to gas accumulation in multi-tank receivers on membrane characterization by the time lag method. Analytical approach for optimization of the receiver, J Memb Sci 360 (2010) 442–453. https://doi.org/10.1016/j.memsci.2010.05.043.

[19] S. Lashkari, B. Kruczek, H.L. Frisch, General solution for the time lag of a single-tank receiver in the Knudsen flow regime and its implications for the receiver's configuration, J Memb Sci 283 (2006) 88–101. https://doi.org/10.1016/j.memsci.2006.06.015.

[20] P.J. Leszczynski, S. Lashkari, B. Kruczek, Revisiting the Effect of the Resistance to Gas Accumulation in Constant Volume Systems on the Membrane Time Lag, Membranes (Basel) 14 (2024). https://doi.org/10.3390/membranes14080167.

[21] G.Z. Ramon, M.C.Y. Wong, E.M.V. Hoek, Transport through composite membrane, Part 1: Is there an optimal support membrane?, J Memb Sci 415–416 (2012) 298–305. https://doi.org/10.1016/j.memsci.2012.05.013.

[22] L. Zhu, W. Jia, M. Kattula, K. Ponnuru, E.P. Furlani, H. Lin, Effect of porous supports on the permeance of thin film composite membranes: Part I. Track-etched polycarbonate supports, J Memb Sci 514 (2016) 684–695. https://doi.org/10.1016/j.memsci.2015.11.043.

[23] V.E. Reinsch, A.R. Greenberg, S.S. Kelley, R. Peterson, L.J. Bond, A new technique for the simultaneous, real-time measurement of membrane compaction and performance during exposure to high-pressure gas, J Memb Sci 171 (2000). https://doi.org/10.1016/S0376-7388(00)00307-0.

[24] R.R. Zolandz, G.K. Fleming, Design of gas permeation systems, Springer US, New York, 1992. https://doi.org/10.1007/978-1-4615-3548-5.

[25] X.Q. Nguyen, Z. Brož, F. Vašák, Q.T. Nguyen, Manometric techniques for determination of gas transport parameters in membranes. Application to the study of dense and asymmetric poly(vinyltrimethylsilane) membranes, J. Memb. Sci. 91 (1994) 65–76. https://doi.org/10.1016/0376-7388(94)00019-0.

[26] M. Al-Ismaily, J.G. Wijmans, B. Kruczek, A shortcut method for faster determination of permeability coefficient from time lag experiments, J. Memb. Sci. 423–424 (2012). https://doi.org/10.1016/j.memsci.2012.08.009.

[27] N. Al-Qasas, J. Thibault, B. Kruczek, Analysis of gas transport in laminated semi-infinite solid: Novel method for complete membrane characterization during highly transient state, J. Memb. Sci. 460 (2014). https://doi.org/10.1016/j.memsci.2014.02.024.

[28] N. Al-Qasas, J. Thibault, B. Kruczek, Membrane Characterization Based on the Upstream Pressure Decay in a Dynamic Gas Permeation Test, J. Fluid Flow, Heat Mass Transf. 1 (2014) 57–64. https://doi.org/10.11159/jffhmt.2014.009.

[29] Al-Qasas, Neveen, Jules Thibault, and Boguslaw Kruczek. "A New Characterization Method of Membranes with Nonlinear Sorption Isotherm Systems Based on Continuous Upstream and Downstream Time-Lag Measurements."

Journal of Membrane Science 542 (2017): 91–101. https://doi.org/10.1016/j.memsci.2017.07.039.

[30] B. Kruczek, S. Lashkari, Challenges in Microflow Measurements in Flow Measurement, Eds. G. U. Beltrán and L. L. Castro Gómez, (2012) 1–34.

[31] E.B. Arkilic, M.A. Schmidt, K.S. Breuer, Gaseous slip flow in long microchannels, J. Microelectromechanical Syst. 6 (1997) 167–178. https://doi.org/10.1109/84.585795.

[32] P.J. Leszczynski, A Novel Constant Volume System for Determining Transport Properties in Polymeric Membranes, University of Ottawa, 2023.

Chapter 2

Determination of time lag by accurate monitoring of pressure decay in a new generation constant volume system

Peter Leszczynski, Zheng Cao, Haoyu Wu, Jules Thibault, Boguslaw Kruczek*

Abstract

The time-lag method is the standard approach for evaluating membrane permeability, diffusion, and solubility in a single gas permeation experiment. The conventional time-lag method relies on accurately monitoring the pressure rise in a constant volume downstream from the membrane following a change in pressure upstream from the membrane. The same information could be extracted from the upstream pressure decay in the same time-lag experiment. However, accurately monitoring the pressure decay presents a challenge due to the resolution limitations of absolute pressure transducers. If the membrane was characterized based on pressure decay, a mass spectrometer could be used to simultaneously monitor the composition of the gas permeating from the membrane. It would open the time-lag method to gas mixtures. Also, the simultaneous monitoring of pressure rise and decay could provide additional information about gas transport in the membrane, which is critical for more complex membrane materials.

- We have overcome the resolution challenge by splitting the upstream volume into the working and reference volumes and monitoring pressure decay using a differential pressure transducer between the two volumes.
- The validity of the measured pressure decay was confirmed by the unique relation between the upstream and downstream time lags for a commercial PDMS membrane.

Keywords: Membrane characterization; Constant volume systems; Time-lag method; Pressure decay; Differential pressure transducer

Graphical abstract

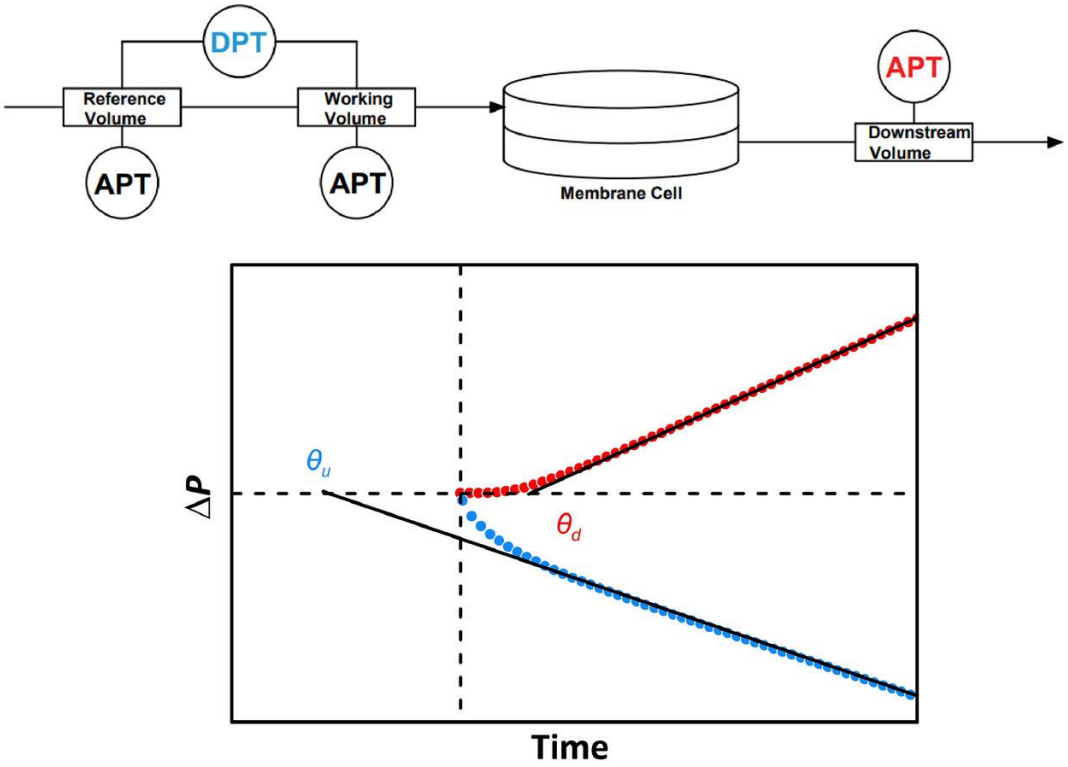

Publication status: MethodsX 13(2024) 102858

***Corresponding author**

Specification table

Subject area	Chemical Engineering
More specific subject area	Gas transport properties in polymer membranes
Name of your method	Determination of membrane time lag based on pressure decay in a constant volume system.
Name and reference of original method	M. Al-Ismaily, J.G. Wijmans, B. Kruczek, A shortcut method for faster determination of permeability coefficient from time lag experiments, J. Memb. Sci. 423–424 (2012). https://doi.org/10.1016/j.memsci.2012.08.009
Resource availability	Custom-made constant volume (CV) system, major components include: • One capacitance-based differential pressure transducer (CCR Process Products, MKS698A) • Two absolute pressure transducers 0 to 10 Torr (CCR Process Products MKS627F11TBC1B) • Two absolute pressure transducers 0-2000 Torr (CCR Process Products, MKS627F13TBC1B) • Rotary vacuum pump (Edwards RV3, A65201906) • Turbomolecular pump (Edwards TS85D1002) • Remotely operated valves: valve body + actuator (Swagelok SS-4BK-VCR-1D & SS-4BK-1C-K10)

2.1 Introduction and background

Permeability (P), diffusivity (D), and solubility (S) coefficients are the critical properties of membrane materials. They are determined in a single time-lag experiment performed in a constant volume (CV) system. A degassed membrane from the tested material is exposed to a step pressure increase while the resulting pressure rise at the

permeate side of the membrane is monitored. The tangent of the linear portion of the pressure rise is directly proportional to *P*. The extrapolation of that linear portion to the time axis yields a time lag (θ_d), which is related to the diffusivity:

$$\theta_d = \frac{L^2}{6D} \tag{2.1}$$

where L is the membrane thickness. According to the solution-diffusion model, the ratio of P and D represents S.

Following the change in feed pressure, the time-lag method could also rely on monitoring the pressure decay in a constant volume upstream from the membrane. The corresponding expression for the upstream time lag (θ_u) is given by [1]:

$$\theta_u = -\frac{L^2}{3D} \tag{2.2}$$

The measurements in the CV system require accurate monitoring of the pressure change with time. Typically, the resolution of a high-quality absolute pressure transducer is 1/10,000 of its maximum reading. When monitoring the pressure rise at a high vacuum, it is sufficient to use the pressure transducer with a maximum reading of 1 Torr with the corresponding resolution of 0.0001 Torr. On the other hand, a pressure transducer with a maximum reading of at least 1000 Torr would be required to monitor the pressure decay in a time-lag experiment. The corresponding resolution of 0.1 Torr is insufficient when characterizing low-permeability materials.

Al-Ismaily et al. [2] addressed the resolution problem of absolute pressure transducers by adopting the concept of a two-tank volume developed by Arkilic et al. [3]. In a two-tank volume system, one tank is a reference volume, and the other is a working volume. The microflow in or out of the working volume is measured by comparing the resulting pressure change relative to the constant reference volume pressure using a differential pressure transducer (DPT). For microflows, the maximum range of DPT can be small (e.g. 1 Torr), and its resolution is very high. Because a step change in feed pressure is needed to initiate time-lag experiments, the working volume must be split to maintain the membrane at a high vacuum before the experiment. This creates a dead volume that includes the upstream part of the membrane cell. The initiation of the

experiment results in an expansion in the working volume greater than the maximum reading of DPT, regardless of how small the dead volume is. As a result, Al-Ismaily et al. started experiments when the reference and working volumes were connected, and the progress of the experiments could only be monitored after separating the two volumes. In addition, closing the valve between the two volumes was associated with a "compression effect" which caused an extra pressure drop in upstream volume and led to $|\theta_u/\theta_d|$ much greater than the theoretical value of 2. Moreover, the feed pressure in time-lag experiments was limited to 175 Torr [2]. To overcome these challenges, we designed the next-generation CV system.

Simultaneous monitoring of pressure decay and rise opens enormous possibilities for characterizing complex membrane materials with strongly nonlinear sorption behaviour. For example, it can completely characterize dual-mode sorption membranes based on instantaneous upstream and downstream time lags and their ratio without additional sorption experiments [4]. To demonstrate the capability of monitoring genuine pressure decay in the new CV system requires selecting the membrane material for which $|\theta_u / \theta_d|$ has a unique value, and polydimethylsiloxane (PDMS), a rubbery polymer, is a material for which this ratio should equal 2 [4].

2.2 Method details

2.2.1 Equipment and materials

Figure 2.1 presents a scaled schematic of the CV system, which comprises three distinct sections: (1) the upstream section, which is bounded by valves FV-3, FV-5, and FCV-7; (2) the membrane cell; and (3) the downstream receiver, which is bounded by the membrane cell, FV-8, and FV-13. The upstream portion of the CV system includes two sections: the working volume (V-101, V_w = 89 cm^3) and the reference volume (V-100, V_r = 96 cm^3). The valve FCV-1 separates volumes V-100 and V-101. During experiments, when FCV-7 is open, the working volume includes a dead volume (V_{ud}) that is enclosed between FCV-7 and the upstream portion of the membrane cell. The dead volume is 11 cm3 but can be reduced to 4 cm^3 by inserting a metal disk into the upstream portion of the membrane cell. This reduction in V_{ud} helps decrease gas expansion when the experiment

begins. The downstream section featured three additional volumes (V-300, V-301, and V-302) that can easily be added or removed from the downstream receiver depending on the anticipated permeability of the tested membrane [5]. When testing barrier materials, FV-9 can be closed to minimize the volume of the downstream receiver.

The membranes are characterized by monitoring the pressure rise and decay responses to a step change in feed pressure. The pressure rise is measured with 10-Torr absolute pressure transducers APT2 and APT3 (CCR Process Products Kanata, Ontario, Canada, MKS627F11TBC1B, 10-5 full-scale resolution, accuracy: 0.12% of reading, range: 0 to 10 Torr). The pressure decay is measured using a pressure differential between V-100 and V-101 with a capacitance-based differential pressure transducer DPT1 (CCR Process Products Kanata, Ontario, Canada, MKS698A ±1 Torr, 10^{-6} full-scale resolution, accuracy: 0.05% of reading). There are also two identical absolute pressure transducers, APT1 and APT4 (CCR Process Products Kanata, Ontario, Canada, MKS627F13TBC1B, 10-5 full-scale resolution, accuracy: 0.12% of reading, range: 0 to 2000 Torr) to monitor the pressures in the working and reference volumes in the upstream section of the system, respectively. In principle, APT1 and APT4 (when FCV-1 is open) or APT1 (when FCV-1 is closed) can also be used to monitor the pressure decay in the upstream portion of the CV system during time-lag experiments, albeit at a much lower resolution than DPT1.

All valves in Figure 2.1 were procured from Weston Valve & Fitting LTD, Mississauga, ON (Canada). The FV valves are manually operated stainless steel bellows-sealed valves (Swagelok SC-4BK-VCR). The remotely-operated FCV valves comprise a valve body and an actuator (Swagelok SS-4BK-VCR-1D & SS-4BK-1C-K10). The valve connections are either brazed or sealed tightly with metal gasket face seals to reduce possible sources of leaks. All components of the system, except for a rotary vacuum pump, P-400 (CANVACTECH, Ottawa, Ontario, Canada, Edwards RV3, A65201906, ultimate pressure: 1.5×10^{-3} Torr), a turbomolecular pump P-401 (Edwards Vacuum LLC Sanborn, New York, USA, Edwards TS85D1002, ultimate pressure: $< 3.75 \times 10^{-10}$ Torr) and a gas cylinder TK-400, are enclosed in a temperature-controlled chamber. The operational temperature range of the chamber is between 273 K and 313 K. The chamber could be heated to higher temperatures, but the APTs and DPT would lose accuracy at temperatures greater than 313 K. The details of the heating and cooling components of the system are

described elsewhere [5]. The picture of the system components inside the chamber is shown in Figure 2.2.

The operation of the system was demonstrated using commercially available polydimethylsiloxane (PDMS) membranes (SSPM823-010-12"-SSP-M823-Platinum Cured Silicone), purchased from Interstate Specialty Products (Sutton, MA). These membranes were supplied with a white virgin Teflon backing. As per the supplier's information, the thickness of the PDMS membranes was 0.010" ± 0.002" (0.254 mm ± 0.051 mm) thickness. All experiments were performed using a 99.99% pure N_2 from the compressed gas cylinder, TK-400.

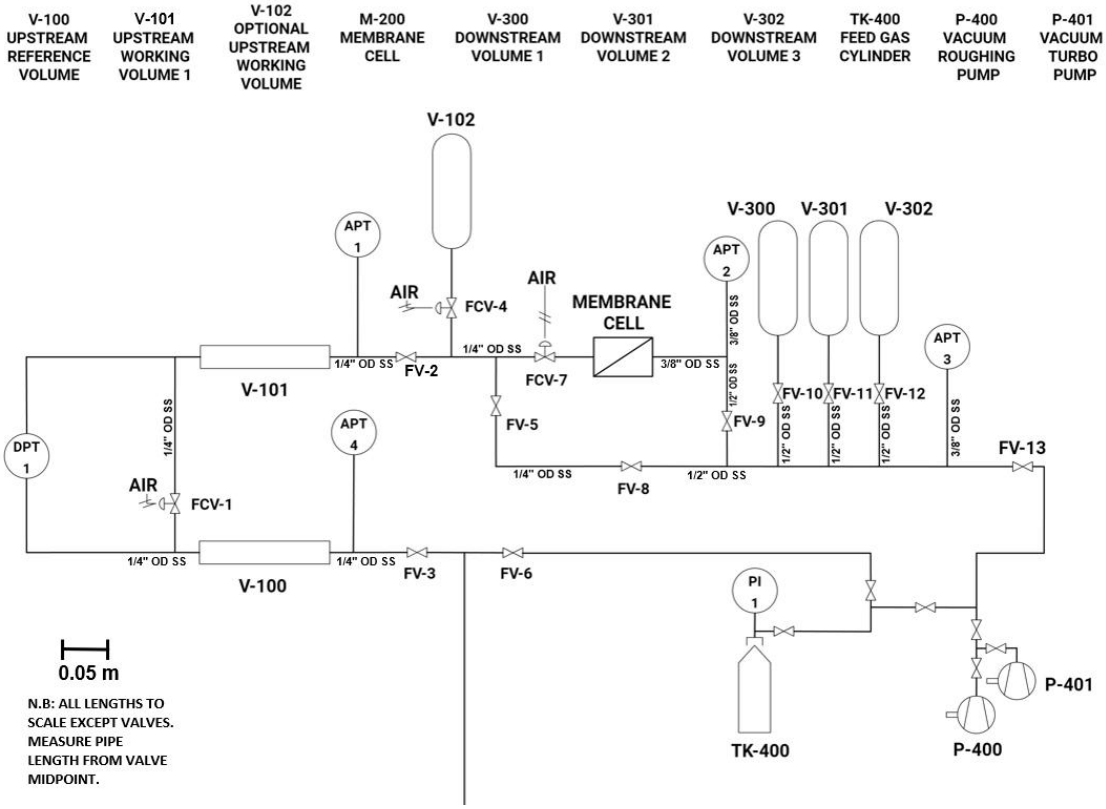

Figure 2.1 A scaled schematic of the constant volume (CV) system.

Figure 2.2 The picture of the inside of the controlled temperature chamber. Referring to Figure 2.1, the components on the picture's left and right are DPT1 and APT3, respectively.

2.2.2 Experimental protocols

Once the membrane was installed within the cell, the system underwent extensive evacuation to degas the membrane using two vacuum pumps, P-400 and P-401. The available valves allowed for the compartmentalization of the system. For example, when FV-13 was open and both FV-8 and FV-9 were closed, the evacuation was confined to the downstream section of the system. The downstream part of the membrane cell was included in the evacuation process by opening FV-9. The entire membrane cell could be evacuated by opening the bypass line (with FV-8, FV5, and FCV 7 open) while keeping FV-2 and FCV-4 closed. The upstream part of the system, which includes the working and reference volumes, could be evacuated via the bypass line and by opening FV-2 (while keeping FV-3 closed). However, the working and reference volumes were evacuated directly via open FV-6 and FV-3, while keeping FV-13 and FCV-1 closed. Before each gas permeation test, the leak rates in different parts of the system were evaluated by monitoring the pressure rise using the appropriate absolute pressure transducers after the system had been fully evacuated (more than 24 hours). Table 2.1 presents typical leak rates in different parts of the system.

Table 2.1 Typical leak rates within the CV

system.Section	Bounds	Volume (cm^3)	Leak rate (Torr/s)
Reference volume	FCV-1, FV-6	96	6.0×10^{-7}
Total working volume	FCV-1, FCV-4, FV-5, membrane	93 (100*)	9.0×10^{-7}
Downstream volume (tubing)	Membrane, FV-8, FV-10, FV-11, FV-12, FV-13	81	8.1×10^{-7}

*without a metal disk in the upstream part of the membrane cell

The leak rates in Table 2.1 are negligible as they were 4 to 5 orders of magnitude lower than the measured pressure decay and rise typically encountered within the upstream and downstream sections of the CV system during membrane characterization trials.

Following the completion of leak tests in different sections, the system underwent another round of evacuation. Then, the valves were closed in the following sequence: FCV-7, FV-5, FV-8, and FV-13. For the pressure rise, the downstream receiver was configured to include only the tubing. This was achieved by closing FV-10, FV-11, and FV-12, while opening FV-9. The gas from TK-400 was then introduced into V-101 and V-100 at a pressure exceeding the level desired for the time-lag experiment. FV-6 was closed and FV-2 opened, allowing the gas to flow through FV-5 and FCV-7. FCV-1 was closed to isolate the working and reference volumes, and the gas was allowed to equilibrate thermally with the air in the chamber.

Due to the presence of a dead volume, initiating the experiment by opening FCV-7 was associated with a gas expansion much larger than 1 Torr, which is the upper limit of DPT-1. Therefore, before initiating the experiment, the pressure within V-100 had to be reduced by an amount equivalent to the expected pressure drop in V-101. This drop was

directly proportional to the feed pressure. The relationship between the feed pressure and the expansion in V-101 was evaluated in parallel experiments using an impermeable film in the membrane cell. These experiments utilized the pressures recorded by APT-1 and APT-4. The pressure reduction within V-100 was achieved using P-400, and the rate of evacuation was regulated by partially opening valve FV-6. Once the desired pressure in V-100 was reached, FV-6 was closed, and P-400 was disengaged to minimize vibrations in the system. The time-lag experiment was then initiated by opening FCV-7, with the pressure rise and decay being simultaneously monitored and recorded in real time.

The experimental protocol described above is referred to as Method 1. This method was not feasible with the first generation of the CV system, as described in Ref. [2]. For comparison, the membranes were also tested using the following protocol, referred to as Method 2. In Method 2, the working and reference volumes remained interconnected even after establishing the desired feed pressure in V-100 and V-101. Similar to Method 1, the experiment was initiated by opening FCV-7. However, because FCV-1 was open, DPT-1 was unable to measure the pressure decay resulting from gas permeation into the membrane. This measurement was only possible after closing FCV-1. Both FCV-1 and FCV-7 are pressure-actuated valves that can be remotely controlled, eliminating the need for manual operations within the temperature-controlled chamber during the initiation of the experiment in both methods. Moreover, in Method 2, the time interval between the opening of FCV-7 and the closing of FCV-1 could be precisely controlled, improving the repeatability of the experiments. This feature was not available in the first generation of the system [2].

2.2.3 Processing of pressure decay data

Figure 2.3 presents the pressure decay observed in an experiment performed with N_2 at a pressure of 1524.2 Torr and a temperature of 303 K using Method 1. The top panel of Figure 2.3 shows the pressure decay recorded by DPT-1, while the bottom panel displays the corresponding absolute pressures measured by APT-1 in the working volume and APT-4 in the reference volume. The pressures were recorded for a duration of 50 s before the initiation of the experiment, as indicated by the constant pressures in the

working and reference volumes when time t is less than 0. Before the experiment, the pressure in the working volume was 1712.8 Torr, which was 187.2 Torr higher than the pressure in the reference volume. This pressure difference was in line with the anticipated pressure drop in the working volume upon the initiation of the experiment, i.e., the pressurization of the membrane that was initially in a vacuum when V_{ud} was 11 cm^3.

It is observed that a of 187.2 Torr in the working volume corresponds to a 1.8 Torr pressure drop in the reference volume. The differential pressure transducer operates by measuring the change in capacitance resulting from the deflection of a metal diaphragm. This diaphragm serves to compare pressures within the working and reference volumes. Because of the large diameter of this diaphragm, even a minor displacement can lead to a non-negligible change in both volumes. As the gas expands into the dead volume and the pressure within the working volume decreases, the diaphragm shifts towards the working volume, reducing its volume, thereby increasing the reference volume. The volume change (V_c) was estimated from Eq. (2.3).

$$p_1 V_r = p_2 \left(V_r + V_C \right) \tag{2.3}$$

where p_1 and p_2, according to Figure 2.3, were 1525.6 Torr and 1523.8 Torr, respectively, and V_r = 96 cm^3. Accordingly, V_c = 0.11 cm^3. The CCR Process Products in Kanata, Ontario, the supplier of the differential pressure transducer, confirmed this phenomenon associated with the operation of DPT-1. The volume displacements due to the sudden pressure changes can be in the order of 0.5 cm^3. The calculated V_c of 0.11 cm^3 was less than 0.5 cm^3. The diaphragm displacement resulting from the step change in pressure to initiate the gas permeation experiments was considered when adjusting the pressure in the reference volume using Method 1.

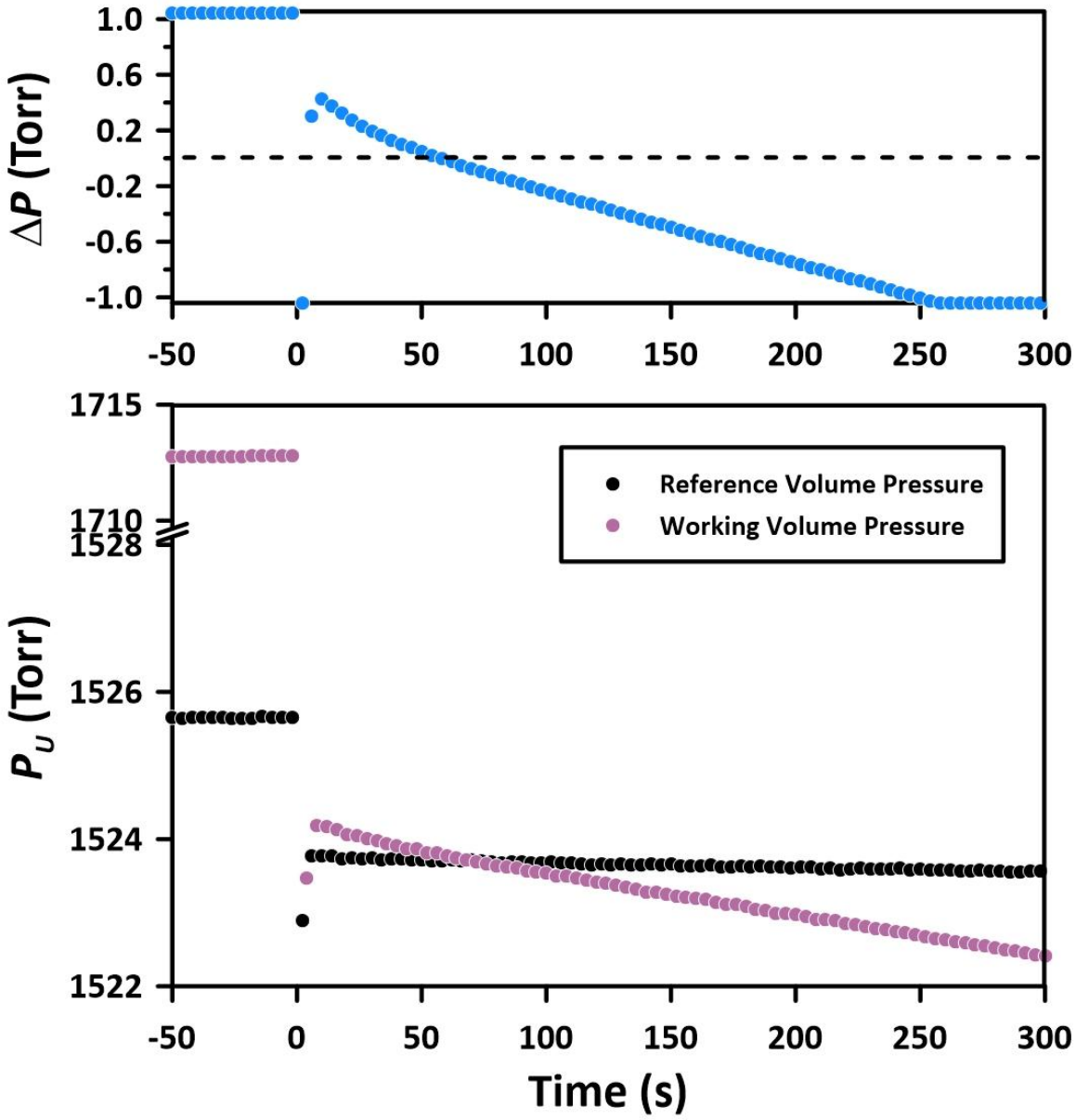

Figure 2.3 Progress of the experiment with N_2 at 1524.2 Torr and 303 K performed using Method 1 with the dead volume of 11 cm^3. The top panel shows the recorded pressure decay by DPT-1; the bottom part shows the corresponding absolute pressures by APT-1 in the working volume and APT-4 in the reference volume.

Immediately after initiating the gas permeation experiment, the membrane is expected to act as a semi-infinite solid. It has been shown that during this period, the pressure decay (denoted as Δp_u) should be a linear function of the square root of time [2]:

$$\Delta p_u = -\frac{2 p_u SRTA\sqrt{D}}{V_u \sqrt{\pi}} \sqrt{t} \tag{2.4}$$

where p_u is the upstream (feed) pressure, V_u is the total working (upstream) volume, A is the membrane area, T is the absolute temperature, and R is the universal gas constant. Eq. (2.4) implies that $\Delta p_u << p_u$. The slope of Δp_u vs $\sqrt{t}$ is directly proportional to $S\sqrt{D}$, but the intercept derived from Eq. (4) is zero. Consequently, the plot Δp_u versus $\sqrt{t}$, at early times, should lead to a straight line with a nil intercept. This observation forms the foundation for correcting the pressure decay as measured by DPT-1.

Figure 2.4 presents the pressure decay results, as shown in the top panel of Figure 2.3, but transformed into the square root of the time domain. Except for the first few readings, the pressure decay shows the expected linear relationship. At the $\sqrt{t} \sim 9$, i.e., at $t > 80$ s, the rate of pressure decay increases, deviating from the linear trend. This deviation indicates that the gas molecules are exiting the membrane at the permeate side, indicating that the membrane can no longer be treated as a semi-infinite solid. The original pressure decay data leads to an intercept of approximately 0.6 Torr. Therefore, all pressure decay data was corrected by this factor so that the intercept would be zero. We will refer to this data manipulation as the 1st correction. The first three points in Figure 2.4 fall below the expected straight line. Although Method 1 allows recording the pressure decay right after the initiation of the experiment, the pressure decay becomes a linear function of time only after 5 to 6 s ($\sqrt{t} \sim 2.4$). The *Limitations* section will further discuss why the early pressure decay data is unreliable.

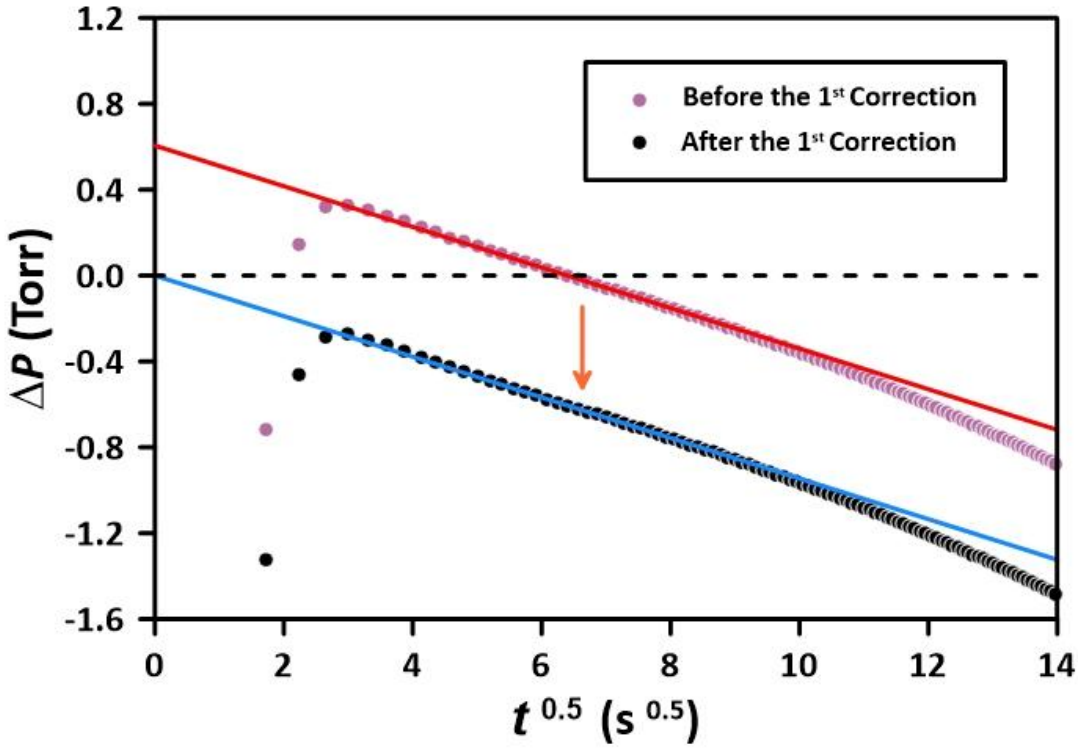

Figure 2.4 Application of the 1st correction to pressure decay data based on the expected zero intercept in the square root of the time domain. The experiment with N_2 at 1524.2 Torr and 303 K was performed using Method 1.

The displacement of the diaphragm at the initiation of the experiment, which was responsible for a 1.8 Torr pressure drop in the reference volume, was not exclusive to scenarios involving a sudden change in pressure. A micro-displacement of the diaphragm inside the differential pressure transducer towards the working volume occurred continuously as long as the pressure in the working volume decreased because of gas permeation into the membrane. Figure 2.5 presents a magnified view of the lower panel of Figure 2.3. The inset in Figure 2.5 reproduces the original p_r versus t from Figure 2.3. When the pressure scale is reduced, it becomes apparent that p_r decreases with t. Despite the low resolution (p_r was monitored using APT-4), it is evident that this decrease generally follows a linear function of time. The linear regression of the pressure data in Figure 2.5 gives dp_r/dt = 0.0006321 Torr/s. Knowing dp_r/dt, the corresponding pressure increase in the working volume due to the diaphragm displacement (dp_{wd}/dt) can be approximated by:

$$\frac{dp_{wd}}{dt} = \left|\frac{dp_r}{dt}\right| \frac{V_r}{V_w} \tag{2.5}$$

Assuming that for a given feed pressure, the pressure changes, dp_r/dt and dp_{wd}/dt, were constant, the actual upstream pressure can be calculated using:

$$p_u = p_m + \left(\left|\frac{dp_r}{dt}\right| + \frac{dp_{wd}}{dt} \right) t \tag{2.6}$$

where p_m is the measured pressure in the working volume. As a result of the 2nd correction, the pressure decay rate increases.

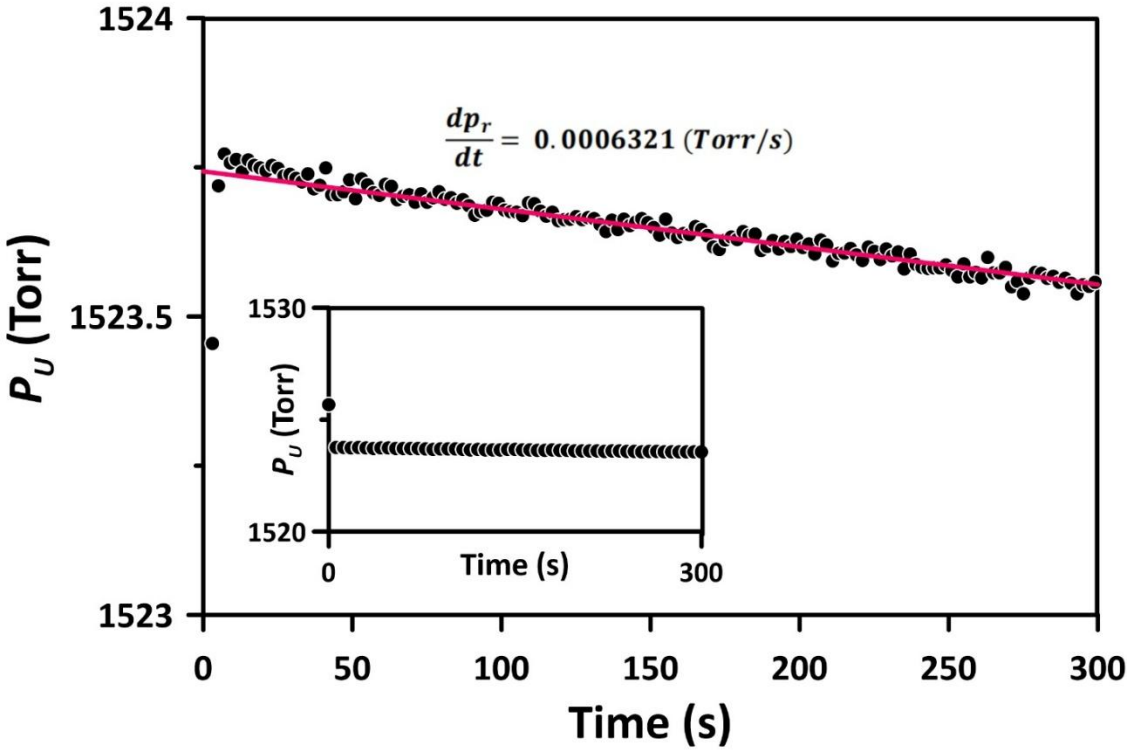

Figure 2.5 Pressure in the reference volume as a function of time in the experiment with N_2 at 1524.2 Torr and 303 K using Method 1. The inset shows the exact relation between the reference pressure and time in the scale used in Figure 2.3.

Figure 2.6, akin to Figure 2.3, presents the pressure decay in an experiment performed using Method 2 with N_2 at a pressure of 1504 Torr and a temperature of 303 K. FCV-1 was opened 5 s after initiating the experiment (i.e., upon opening FCV-7). The top

panel of Figure 2.6 shows the pressure decay recorded by DPT-1, while the bottom panel presents the corresponding absolute pressures measured by APT-1 in V-101 and APT-4 in V-100. Before starting the experiment, the pressure was 1535 Torr. The significantly smaller pressure drop observed at the start of the experiment in Figure 2.6 (21 Torr) compared to that in Figure 2.3 (187.2 Torr) can be attributed to two factors. Firstly, V-100 and V-101 were connected, resulting in a combined volume of 185 cm^3, compared to 89 cm^3 when V-100 and V-101 were separated in Method 1. Secondly, the dead volume in Figure 2.6 was 4 cm^3, which is smaller than the 11 cm^3 in Figure 2.3. Despite the considerably smaller pressure drop, the original pressure decay data still required the application of the 1^{st} correction. The application of the 1^{st} correction is shown in Figure 2.7.

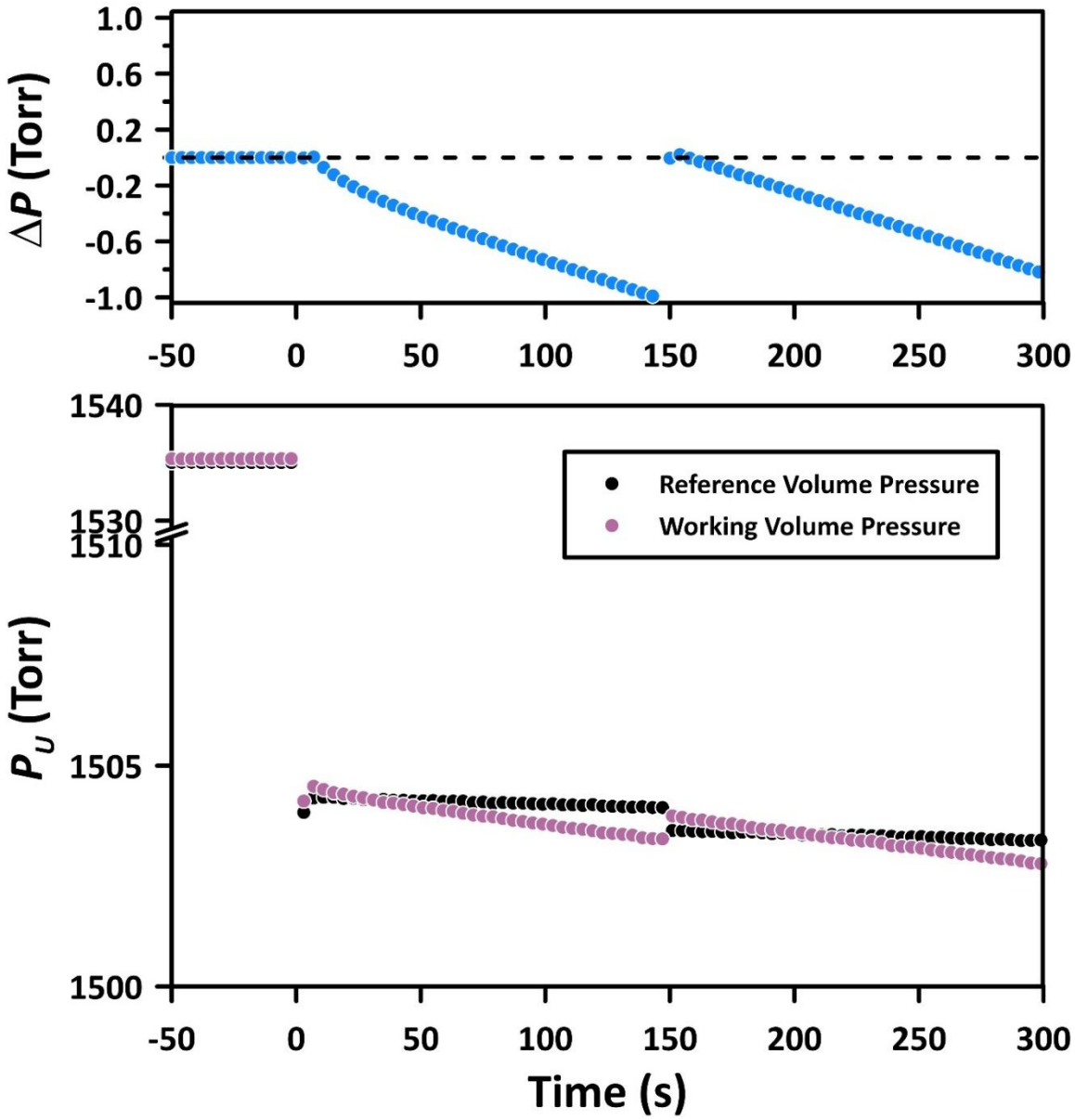

Figure 2.6 Progress of the experiment with N_2 at 1504 Torr and 303 K performed using Method 2 with the dead volume of 4 cm^3. The top panel shows the recorded pressure decay by DPT-1; the bottom panel shows the corresponding absolute pressures by APT-1 in the working volume and APT-4 in the reference volume.

When compared to Figure 2.4, the intercept in Figure 2.6, which represents the 1st correction, is significantly smaller, being 0.14 Torr as opposed to 0.6 Torr in Figure 2.6. Also, after closing FCV-1, the deviation from the semi-infinite model is much less pronounced than in Method 1. Interestingly, the initial deviation from the semi-infinite is

slightly positive, unlike the negative deviation in Figure 2.4. Similarly to Method 1 (Fig. 5), after closing FCV-1, the pressure in the reference volume decreased linearly with time due to the gas permeation into the membrane. Therefore, the 2nd correction of the pressure decay data, as described by Eqs. (2.5) and (2.6), is also required in Method 2.

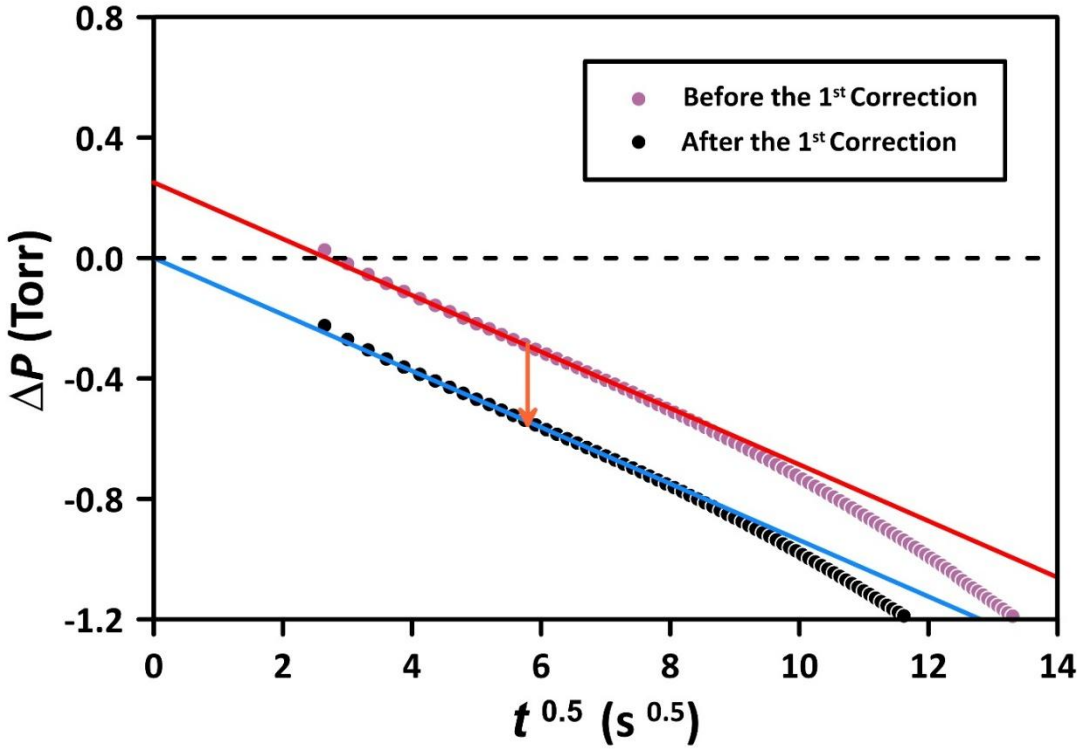

Figure 2.7 Application of the 1st correction to pressure decay data based on the expected zero intercept in the square root of the time domain. The experiment with N_2 at 1504 Torr and 303 K was performed using Method 2.

2.3 Limitations

The rationale of Method 1 was to record the pressure decay right after the initiation of the experiment. Although the current CV system allows for the reduction of pressure in the reference volume to match the anticipated pressure drop upon initiation of the experiment, the results from the first 5-6 s had to be discarded (as shown in Figure 2.4). The initiation of the time-lag experiment is associated with an adiabatic gas expansion in the working volume, which leads to a sudden decrease in gas temperature from T_i to T_f, where:

$$T_f = T_i \left(\frac{V_i}{V_f} \right)^{\gamma - 1} \tag{2.7}$$

where $V_i = V_w$ is the working volume before starting the experiment, $V_f = V_u$ is the total working volume after starting the experiment, which includes the dead volume, and γ is the ratio of the specific heats (C_p/C_v), which for most common gases, including N_2 is equal to 1.4. As previously discussed, because of the deflection of a metal diaphragm in the differential pressure transducer, the expansion of the working volume was also associated with a slight expansion in the reference volume (by 0.11 cm^3). Because gas molecules constantly collide with the tube walls, the gas temperature after the initiation of the experiment quickly returns to the initial value (T_i) because the thermal capacity of the gas is negligible compared to the capacity of the tubes containing the gas. This effect is evident in the bottom panel of Figure 2.3 (0-5s). Because of the instantaneous cooling and the quick return to T_i, the pressures in the working and reference volumes right after the initiation of the experiment were below the expected values, resulting in unreliable readings by the DPT-1 in the first 5-6 s (Figure 2.4). The phenomenon described above is also evident in Method 2 (Figure 2.4). The pressures recorded by APT-1 and APT-4 in the working and reference volumes dropped momentarily below the expected values after the initiation of the experiment. However, because the valve connecting the working and reference volumes was closed after 5 seconds from the initiation of the experiment, i.e., when the gas temperature returned to its initial value, it is believed that the adiabatic expansion did not affect the readings of the DPT-1 in Method 2.

Despite the impossibility of recording a reliable pressure decay in the first 5 seconds after initiating the experiment in Method 1 and Method 2 for two different reasons, the application of the two corrections discussed in the *Processing of pressure decay data* Section leads to excellent agreement between the upstream and downstream time lags. Method 2 does not require adjusting the pressure in the reference volume to the anticipated gas expansion in the working volume after initiating the experiment; therefore, it is technically more straightforward to use. Because reliable pressure decay results are available after similar times in both methods, Method 2 is recommended over Method 1 for recording the pressure decay in time-lag experiments.

Nomenclature

Symbols

A	Membrane area [m^2]
C	Specific heat [J/kg K]
c	Gas concentration in the membrane [mol/m^3]
D	Diffusivity coefficient [m^2/s]
L	Membrane thickness [m]
P	Permeability coefficient [Barrer or mol/s m Pa]
p	Pressure [torr or Pa]
R	Universal gas constant [J/mol K]
S	Solubility coefficient [mol/m^3 Pa]
T	Absolute temperature [K]
t	Time [s]
V	Volume [m^3]

Greek symbols

θ	Time lag [s]
γ	Ratio of the specific heats
Δp	Pressure decay/pressure rise [torr/s or Pa/s]

Subscripts

d	Downstream
f	Final value
i	Initial value
m	Measured value
r	Reference volume
u	Upstream
w	Working volume
wd	Working volume change due to the diaphragm displacement

Abbreviations:

APT	Absolute pressure transducer
DPT	Differential pressure transducer
CV	Constant volume
PDMS	Polydimethylsiloxane

References

[1] S.W. Rutherford, D.D. Do, Review of time lag permeation technique as a method for characterisation of porous media and membranes, Adsorption. 3 (1997) 283 – 312. https://doi.org/10.1007/BF01653631.

[2] M. Al-Ismaily, J.G. Wijmans, B. Kruczek, A shortcut method for faster determination of permeability coefficient from time lag experiments, J. Memb. Sci. 423 – 424 (2012). https://doi.org/10.1016/j.memsci.2012.08.009.

[3] E.B. Arkilic, M.A. Schmidt, K.S. Breuer, Gaseous slip flow in long microchannels, J. Microelectromechanical Syst. 6 (1997) 167 – 178. https://doi.org/10.1109/84.585795.

[4] N. Al-Qasas, J. Thibault, B. Kruczek, A new characterization method of membranes with nonlinear sorption isotherm systems based on continuous upstream and downstream time-lag measurements, J. Memb. Sci. 542 (2017). https://doi.org/10.1016/j.memsci.2017.07.039.

[5] P.J. Leszczynski, A Novel Constant Volume System for Determining Transport Properties in Polymeric Membranes, 2023.

Chapter 3

Direct determination of permeability, diffusivity and solubility of gases in membrane based on simultaneous monitoring of pressure rise and decay in a single time-lag experiment

Zheng Cao, Jules Thibault, Boguslaw Kruczek*

Abstract

The time-lag method is the most common approach for evaluating the membrane gas permeability, diffusion and solubility coefficients in a single gas permeation experiment. However, only permeability and diffusivity are determined directly, while the solubility is evaluated from the ratio of permeability and diffusivity. Herein, we present how the conventional time-lag experiment can be used to determine all three transport coefficients directly when, in addition to monitoring the pressure rise in the constant volume downstream from the membrane, the corresponding pressure decay is also monitored in the constant volume upstream of the membrane. The new design of the upstream part of the constant volume (CV) system used in this study allowed pressure decay monitoring. We provide the mathematical fundamentals of the new methods enabled by the new CV system and demonstrate them experimentally using a commercial poly(dimethylsiloxane) PDMS membrane.

Keywords: Membrane characterization, Constant volume systems, Time-lag method, Pressure decay, Differential pressure transducer.

Graphical abstract

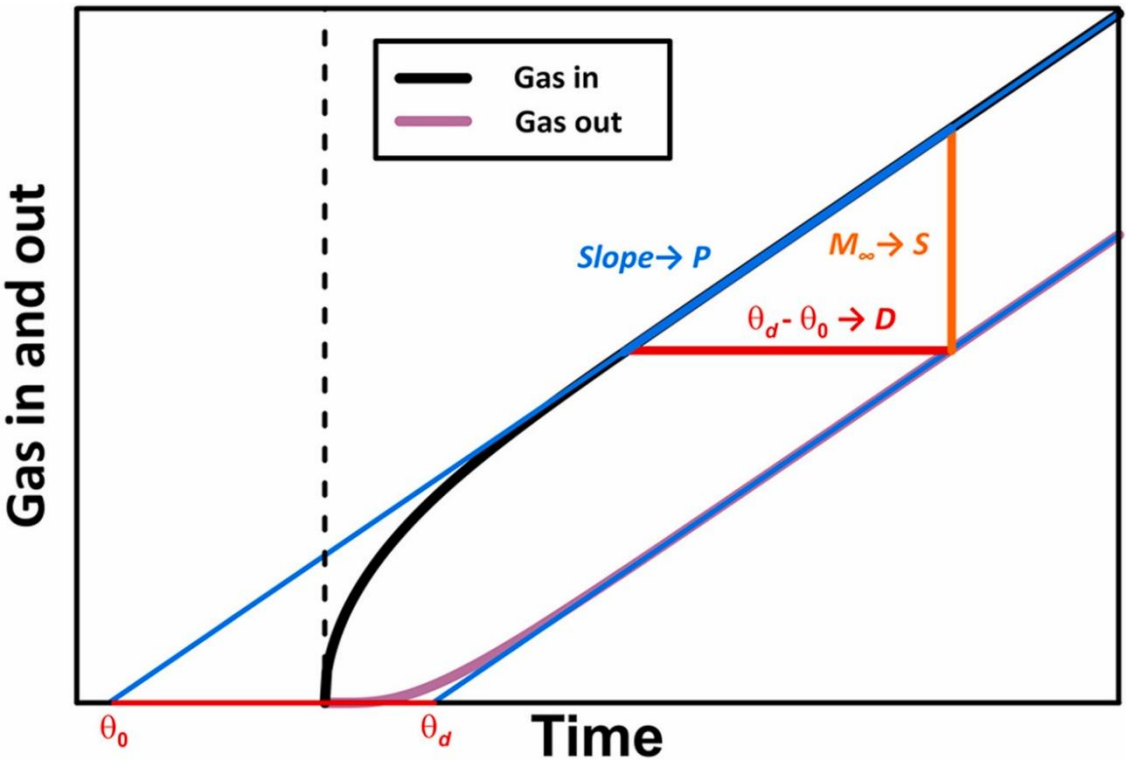

Publication status: Journal of Membrane Science 720(2025) 123741

***Corresponding author**

3.1Introduction

Membrane gas separation became an industrial reality in the late 1970s with Monsanto's first commercial asymmetric hollow membrane modules [1]. Today's prominent membrane-based gas separations include hydrogen recovery [2], natural gas purification [3], and air separation [4]. In addition, olefin/paraffin separation,

ethanol/water separation, and carbon capture applications have expanded the opportunities for gas separation membranes [5]. Despite significant progress in the development of inorganic [6] and mixed matrix membranes (MMMs) [7], commercial gas separation membranes are exclusively prepared using organic polymers. These include polysulfones, cellulose acetates, polyphenylene oxide, aramids, polycarbonates, and polyimides [5]. Developing new materials - organic, inorganic, and composite – remains the central theme of membrane gas separation research. The combination of permeability and permselectivity for a given pair of gases compared to the upper-bound line is the standard metric for assessing new membrane materials [8]. In turn, the permeability (P) and permselectivity for a given pair of gases depend on the respective diffusivity (D) and solubility (S) coefficients of these gases in the membrane material.

The three transport coefficients, P, D, and S, are determined in a single dynamic gas permeation experiment, often referred to as a time-lag experiment. The mathematical basis for the time-lag experiment was first described more than a century ago [9]. The time-lag experiments are generally performed in constant volume (CV) systems. A degassed, homogeneous membrane from the tested material is exposed to a step pressure increase at one (feed) side. The resulting pressure rise at the other (permeate) side of the membrane is monitored in real-time. The tangent of the linear portion of the pressure rise, associated with a constant permeation rate, is directly proportional to P [10]. The extrapolation of that linear portion to the time axis yields a time lag (θ_d), which is related to the diffusivity by:

$$\theta_d = \frac{L^2}{6D} \tag{3.1}$$

where L is the membrane thickness. According to the solution-diffusion model, the ratio of P to D represents S. The linear portion of the pressure response indicates a pseudo-steady state permeation, which is commonly referred to as a steady state.

Alternatively, gravimetric, barometric, and volumetric techniques can determine S directly in gas sorption experiments [11]. The outcome of gas sorption experiments is an adsorption isotherm, i.e., the relation between the gas concentration in the membrane (c) as a function of pressure (p) and solubility is

$$S = \frac{c}{p} \tag{3.2}$$

The solubility might be independent of pressure, like in the case of rubbery polymer membranes, in which Henry's law governs gas sorption. However, typically, *S* depends on *p*. For example, in the case of glassy polymer membranes, which represent most commercial gas separation membranes [5], gas sorption is governed by dual-mode sorption [12]. Also, gas sorption in novel membrane materials, polymeric, inorganic, and mixed matrices does not follow Henry's law and is not necessarily dual-mode sorption. Gas sorption experiments rely on reaching an equilibrium between the gas and the membrane phases, which may require a long time, especially for thick membranes, i.e., when the characteristic length for gas diffusion in a sample is relatively large. On the other hand, monitoring the gas concentration in the membrane as a function of time also allows the direct determination of the gas diffusivity. Knowing *D* and *S*, the gas permeability is evaluated from the product of *D* and *S* [13,14]. Therefore, like the time-lag method, the dynamic sorption/desorption experiments allow determining all three transport coefficients from a single experiment. However, two (*S* and *D*) are determined directly, while the third (*P*) is determined indirectly.

The dynamic sorption/desorption experiments are usually performed using a barometric method called the pressure decay method. This technique introduces a known amount of gas into an evacuated chamber containing the membrane sample, and the pressure decay in the chamber corresponds to gas sorption by the membrane. Therefore, this method relies on the accurate knowledge of the system volume, a sensitive pressure transducer, and maintaining a constant temperature [11].

The protocol of a pressure decay method resembles that of the time-lag method from the perspective of the upstream of the tested membrane. The main difference is that the steady-state permeation is reached in the time-lag method rather than an equilibrium between the gas and the membrane. However, it should be emphasized that the time-lag method relies on the instantaneous equilibrium between the gas and the membrane's upstream interface. Another difference is that the pressure decay method is commonly used in gas sorption/desorption experiments, but its equivalent in gas permeation does not

practically exist, even though the benefits of applying the pressure decay method in membrane characterization were first discussed 30 years ago [15]. Monitoring the upstream pressure decay can offer some unique advantages, particularly when characterizing barrier materials for which reaching the steady state permeation (necessary to determine the time lag) could take not seconds or minutes but hours or even days. Combining the upstream pressure decay with the downstream pressure rise allowed Al-Ismaily et al. to determine P from transient permeation data before reaching a steady state [16]. Immediately after initiating the gas permeation experiment, the membrane behaves as a semi-infinite solid. It can be shown that during that time, the pressure decay (Δp_0) is a linear function of the square root of time [16]:

$$\Delta p_0 = -\frac{2 p_0 SRTA\sqrt{D}}{V_0\sqrt{\pi}}\sqrt{t} \tag{3.3}$$

where p_0 is the upstream (feed) pressure, V_0 is the constant upstream volume, A is the membrane area, T is the absolute temperature, and R is the universal gas constant. Eq. (3) implies that $\Delta p_0 << p_0$. The slope of Δp_0 vs $\sqrt{t}$ is directly proportional to $S\sqrt{D}$, but the intercept from Eq. (3.3) is zero. Therefore, S and D cannot be determined from the initial pressure decay. However, it was shown that laminating the tested membrane with a film of known properties (e.g. silicone rubber) results in an intercept that depends on the tested membrane's S and D [17]. Therefore, the mathematical expression for the intercept yields the second independent equation, thus allowing the determination of D, S, and P from the upstream pressure decay before the gas leaves the tested barrier material. It can also be shown that if the tested membrane is not laminated and the gas emerges from the membrane, the deviation from the initial linear relation given by Eq. (3.3) at any time depends on D but not S [18]. Therefore, D can be evaluated from the observed deviation at the specific time, and knowing D, S can be determined from the initial slope of Δp_0 vs $\sqrt{t}$.

Despite the potential advantages of monitoring the pressure decay in membrane characterization, this approach did not gain much attention in the membrane community. There are two main reasons for that. First, the resolution of the absolute pressure transducers depends on the maximum pressure they can measure. Because the pressure at

the upstream side of the membrane is orders of magnitude greater than that at the permeate side, the pressure rise in the conventional time-lag method can be monitored with an excellent resolution, but not the pressure decay at the upstream side of the membrane. Another challenge when monitoring pressure decay is the temperature drift [19]. The measurements in a CV system assume that the observed pressure rise or decay (dp/dt) depends only on the gas molar flow (dn/dt) into or out of the membrane. It is a reasonable assumption when monitoring the pressure rise starting at high vacuum ($p \approx 0$), but not necessarily when monitoring the pressure decay after initiating a time-lag experiment, which is evident when considering the total derivative from the ideal gas law:

$$\frac{dp}{dt} = \frac{RT}{V}\frac{dn}{dt} - \frac{p}{V}\frac{dV}{dt} + \frac{p}{T}\frac{dT}{dt} \tag{3.4}$$

The second term on the right-hand side is always zero. However, when monitoring the pressure decay, the last term on the right-hand side might not be negligible even when the temperature is controlled because of the magnitude of the feed pressure ($p >> 0$). The resolution problem of absolute pressure transducers can be solved by adopting the concept of a two-tank volume, initially developed by Arkilic et al. [20], commonly used in microfluidics. Al-Ismaily et al. [16] were the first to adopt this concept to measure pressure decay in membrane characterization. However, the time-lag experiments could not be performed at pressures greater than 175 Torr. Moreover, the upstream and downstream time lag ratio did not yield a reasonable value, attributed to a "compression effect." [16]. We have recently solved the problems faced by Al-Ismaily et al. by developing a new generation of the CV system [21], which increased the range of the feed pressure to 2000 Torr and led to the absolute ratio of the time lags for PDMS membrane very close to the expected value of 2.

Like the conventional time-lag technique, the new characterization methods discussed in Refs. [16–18], which rely on the accurate monitoring of the pressure decay, allow the direct determination of two out of three primary gas transport coefficients in the membrane, namely D and P. In this study, we present a new method based on the conventional time lag, which relies on the simultaneous monitoring of pressure rise and decay and allows the direct determination of all three transport coefficients from a single

gas permeation experiment. We first provide the mathematical fundamentals of the new method. Then, we experimentally demonstrate the application of this method in the new CV system using a commercial PDMS membrane. We also discuss how the method proposed in this study and the new generation of CV systems can facilitate the characterization of new membrane materials for gas separation.

3.2 Theoretical background

The governing partial differential equation (PDE) describing the time-lag experiment is the Fick's second law of diffusion:

$$\frac{\partial c(x,t)}{\partial t} = D\frac{\partial^2 c(x,t)}{\partial x^2} \tag{3.5}$$

The corresponding initial and boundary conditions are: $c(x,0)=0;\ c(0,t)=c_0;\ c(L,t)=0.$ Solving the governing PDE, subject to the above initial and boundary conditions, using the separation of variables method leads to:

$$c(x,t) = c_0\left(1-\frac{x}{L}\right) - 2\frac{c_0}{\pi}\times\sum_{n=1}^{\infty}\frac{1}{n}\sin\left(\frac{n\pi x}{L}\right)\exp\left(-\frac{Dn^2\pi^2 t}{L^2}\right) \tag{3.6}$$

Recognizing that $c_0 = p_0 S = p_0\left(P/D\right)$, where p_0 is the upstream pressure after the step change to initiate the experiment, Eq. (3.6) can be rewritten as:

$$c(x,t) = \frac{p_0 P}{D}\left(1-\frac{x}{L}\right) - 2\frac{p_0 P}{\pi D}\times\sum_{n=1}^{\infty}\frac{1}{n}\sin\left(\frac{n\pi x}{L}\right)\exp\left(-\frac{Dn^2\pi^2 t}{L^2}\right) \tag{3.7}$$

Using Fick's first law allows the evaluation of the gas flux anywhere within the membrane:

$$J\left(x,t\right) = -D\frac{dc\left(x,t\right)}{dx} = \frac{p_0 P}{L} + 2\frac{p_0 P}{L}\times\sum_{n=1}^{\infty}\cos\left(\frac{n\pi x}{L}\right)\exp\left(-\frac{Dn^2\pi^2 t}{L^2}\right) \tag{3.8}$$

Evaluating Eq. (3.8) at x = 0 and x = L allows the determination of the time-dependent gas flux in and out of the membrane:

$$J(0,t)=\frac{p_0P}{L}+2\frac{p_0P}{L}\times\sum_{n=1}^{\infty}\exp\left(-\frac{Dn^2\pi^2t}{L^2}\right) \tag{3.9}$$

$$J(L,t)=\frac{p_0P}{L}+2\frac{p_0P}{L}\times\sum_{n=1}^{\infty}(-1)^n\exp\left(-\frac{Dn^2\pi^2t}{L^2}\right) \tag{3.10}$$

The above series solutions simplify to a single-term approximation when the Fourier number (dimensionless time) is relatively large. More specifically, when $Fo=\frac{Dt}{L^2}>0.2$, Eqs. (3.9) and (3.10), become:

$$J(0,t)=\frac{p_0P}{L}+2\frac{p_0P}{L}\exp\left(-\frac{D\pi^2t}{L^2}\right) \tag{3.11}$$

$$J(L,t)=\frac{p_0P}{L}-2\frac{p_0P}{L}\exp\left(-\frac{D\pi^2t}{L^2}\right) \tag{3.12}$$

The difference between the fluxes in and out are:

$$\Delta J(t)=J(0,t)-J(L,t)=4\frac{p_0P}{L}\exp\left(-\frac{D\pi^2t}{L^2}\right) \tag{3.13}$$

As $t\to\infty$, i.e., at steady state, ΔJ approaches to 0. However, in the transient state, when Fo > 0.2, taking the natural logarithm of both sides of Eq. (3.13) leads, after rearrangements, to:

$$\ln\left\{\frac{\Delta J(t)L}{4p_0P}\right\}=-\frac{D\pi^2}{L^2}t \tag{3.14}$$

$\Delta J(t)$ can be evaluated by the differentiation of experimentally measured pressure rise and decay; P can be determined from the steady-state pressure rise or decay, while p_0 and L are known parameters. Therefore, the left-hand side of Eq. (3.14) is known and can be plotted as a function of time, which should yield a straight line with the slope (σ):

$$\sigma=-\frac{D\pi^2}{L^2} \tag{3.15}$$

Knowing σ, D can be evaluated from Eq. (3.15), and it should be the same as D from Eq. (3.1). Also, monitoring the pressure decay also allows the measurement of the upstream time lag (θ_0), which is given by:

$$\theta_0 = -\frac{L^2}{3D} \tag{3.16}$$

The experimentally measured pressure decay also allows another way to determine D. At early times, i.e., before permeating molecules emerge from the permeate interface of the membrane, the membrane behaves as semi-infinite, and the pressure decay is given by Eq. (3.3). In this early transient permeation period, the plot of the pressure decay versus the square root of time should yield a straight line with the slope (Σ_t) given by:

$$\Sigma_t = -\frac{2p_0 SRTA\sqrt{D}}{V_0\sqrt{\pi}} \tag{3.17}$$

On the other hand, when gas permeation reaches a steady state, the upstream pressure becomes a linear function of time, and the corresponding steady-state slope (Σ_{ss}) is given by:

$$\Sigma_{ss} = -\frac{SDp_0 ART}{V_0 L} \tag{3.18}$$

The ratio of the two slopes leads to the following expression:

$$\frac{\Sigma_{ss}}{\Sigma_t} = \frac{\sqrt{\pi}}{2L}\sqrt{D} \tag{3.19}$$

Therefore, the ratio of the two slopes allows for determining D directly from Eq. (3.19).

Eqs. (3.1), (3.15), (3.16) and (3.19) provide four ways to evaluate D from the same time-lag experiment, which should lead to the same value. Although more independent ways to determine a given parameter increase confidence in that parameter, the analysis so far does not go beyond the conventional time-lag method because only D and P are determined directly. S needs to be determined from the ratio of P and D. However, the

accurate measurement of the pressure rise and decay also allows for the direct determination of *S*.

First, we recognize that gas accumulation in the membrane as a function of time, $M(t)$, is related to the fluxes in and out of the membrane:

$$M(t) = A\left\{\int_0^t J(0,t)\,dt - \int_0^t J(L,t)\,dt\right\} \tag{3.20}$$

Substituting Eqs. (3.9) and (3.10) into Eq. (3.20) leads to:

$$M(t) = 2\frac{Ap_0SL}{\pi^2}\left\{\sum_{n=1}^{\infty}\left(\left(-1\right)^n - 1\right)\frac{1}{n^2}\left(\exp\left(-\frac{Dn^2\pi^2 t}{L^2}\right) - 1\right)\right\} \tag{3.21}$$

As $t \to \infty$, i.e. at steady state, $M(t)$ becomes a constant value M_∞:

$$M_\infty = 2\frac{Ap_0SL}{\pi^2}\sum_{n=1}^{\infty} -\frac{\left(\left(-1\right)^n - 1\right)}{n^2} = 2\frac{Ap_0SL}{\pi^2}\left(\frac{\pi^2}{4}\right) = \frac{Ap_0SL}{2} \tag{3.22}$$

Knowing the upstream and downstream volumes of the system and the experimentally measured pressure rise and decay, M_∞ can be evaluated experimentally. In turn, the gas solubility in the membrane becomes:

$$S = \frac{2M_\infty}{p_0LA} \tag{3.23}$$

It should be emphasized that Eq. (3.21) also provides the basis for determining gas diffusivity in the membrane. Dividing both sides of Eq. (3.21) by M_∞ and rearranging the resulting equation leads to:

$$1 - \frac{M(t)}{M_\infty} = \exp\left(-\frac{D\pi^2 t}{L^2}\right) \tag{3.24}$$

Taking the natural logarithm of both sides of Eq. (24) yields:

$$M_{\ln}(t) = \ln\left(1 - \frac{M(t)}{M_{\infty}}\right) = -\frac{D\pi^2 t}{L^2} \tag{3.25}$$

The plot of the LHS of Eq. (3.25) versus time should lead to a straight line with the same slope (σ) as before given by Eq. (3.15), and then D is determined from Eq. (3.16).

3.3 Materials and Methods

3.3.1 Materials

PDMS membranes (SSPM823-010-12"-SSP-M823-Platinum Cured Silicone) were purchased from Interstate Specialty Products (Sutton, MA). They were supplied with a white virgin Teflon backing. According to the supplier, the PDMS membranes had a 0.025" ± 0.002" (0.610 mm ± 0.051 mm) thickness. All experiments were performed using 99.99% pure N_2 from the compressed gas cylinder (Linde Canada Inc., Ottawa, ON).

3.3.2 Apparatus

Figure 3.1 presents the schematic diagram of our novel CV system, which has been recently described in great detail [21]. Here, we focus only on the upstream part of the system, which allows the accurate monitoring of the pressure decay. The upstream volume is divided into the working V-101 and reference V-100 sections, with respective volumes of 89 cm^3 and 96 cm^3. The 96 cm^3 does not include the dead volume (4 cm^3) comprising the upstream part of the membrane cell and tubing up to the remotely operated FCV-7 valve. The working and reference volumes could be connected/separated with another remotely operated valve (FCV-1). The FCV valves comprise a valve body (Swagelok SC-4BK-VCR) and an actuator (Swagelok SS-4BK-VCR-1D & SS-4BK-1C-K10). The bodies of the FV and FCV valves are the same: stainless steel bellows sealed valves, procured from Weston Valve & Fitting LTD, Mississauga, ON. The measurement of the pressure decay due to gas permeation into the membrane relies on a capacitance-based differential pressure transducer DPT1 (CCR Process Products Kanata, Ontario, Canada, MKS698A ±1 Torr, 10^{-6} full-scale resolution, accuracy: 0.05% of reading), which compares a variable pressure in V-101 with a constant pressure in V-100. In addition, the

working and reference volumes are equipped with identical absolute pressure transducers, APT1 and APT4 (CCR Process Products Kanata, Ontario, Canada, MKS627F13TBC1B, 10^{-5} full-scale resolution, accuracy: 0.12% of reading, range: 0 to 2000 Torr). The pressure in the reference volume can be adjusted independently of that in the working volume using a rotary vacuum pump P-400 (CANVACTECH, Ottawa, Ontario, Canada, Edwards RV3, A65201906, ultimate pressure: 1.5×10^{-3} Torr) and compressed gas cylinder TK-400 via FV-6 and FV-3 valves. Except for P-400, a turbomolecular pump P-401 (Edwards Vacuum LLC Sanborn, New York, USA, Edwards TS85D1002, ultimate pressure: < 3.75×10^{-10} Torr) and TK-400, all components of the system in Figure 3.1 are enclosed in a temperature-controlled chamber with an operational range between 273 K and 313 K [22].

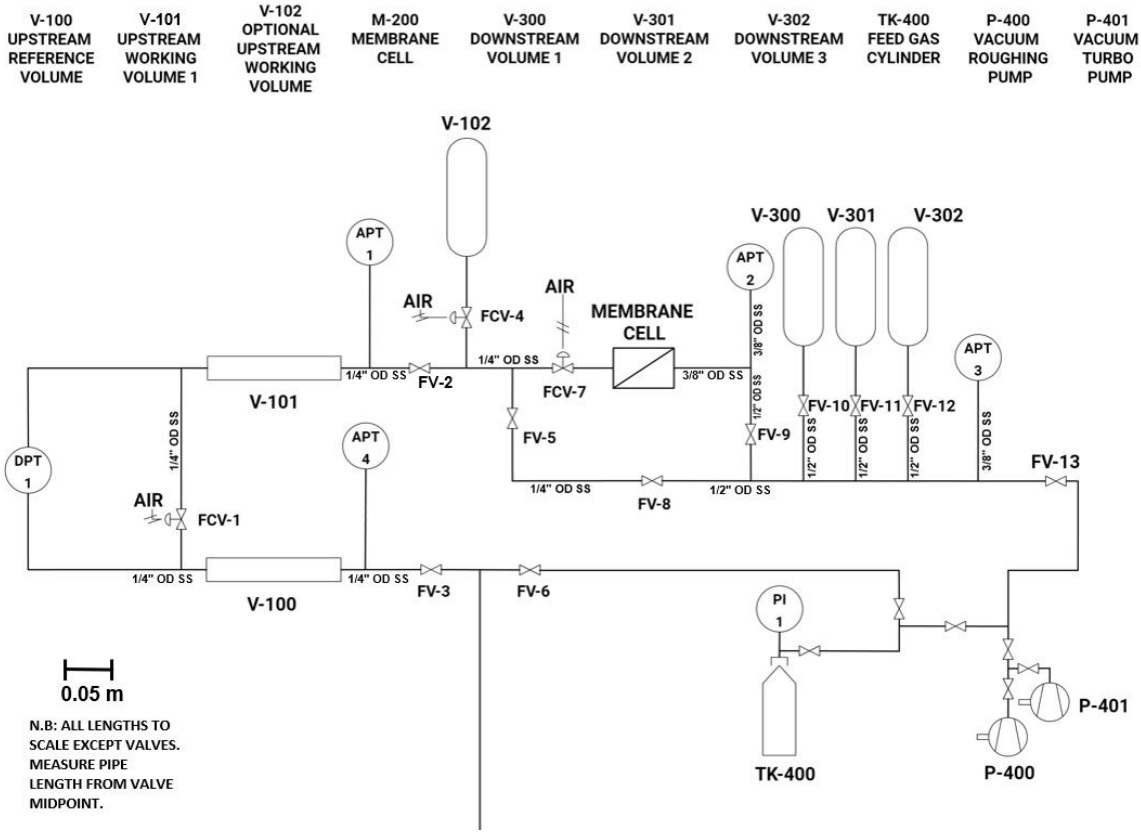

Figure 3.1 A schematic diagram (to the scale) of the novel constant volume (CV) system [21].

3.3.3 Experimental protocol

After installing the membrane inside the cell, the system was extensively evacuated to degas the membrane using two vacuum pumps, P-400 and P-401, and leak tests were performed in the different sections of the system, including the downstream, reference, and working volumes. The observed leak rates (10^{-7} torr/s or lower) were at least four orders of magnitude lower than the measured pressure decay/rise during experiments. After completing the leak tests, the system was evacuated before initiating each experiment. With the membrane cell and the downstream section of the system under vacuum, the reference and working volumes were pressurized to the desired level using TK-400. The remote opening of FCV-7 initiated the experiment, causing gas expansion and a pressure drop in the working volume greater than 1 torr, which is the full range of DPT1. Consequently, the pressure decay could only be monitored using APT1, not DPT1. For DPT1 to monitor the pressure decay, the pressure in the reference volume was reduced by the expected pressure drop in the working volume before the experiment. However, the adiabatic expansion in the working volume led to a sudden decrease in gas temperature. Since the thermal capacity of the gas in the working volume was negligible compared to the thermal capacity of the insulated tubing, the gas temperature quickly returned to its initial level. Due to this phenomenon, the DPT1 readings in the first 5-6 seconds of the experiment were unreliable and had to be discarded [21].

Consequently, the gas permeation experiments began when the working and reference volumes were connected (i.e., FCV-1 was open), making DPT1 unavailable to monitor the experiment's progress. FCV-1 was closed 5 s after FCV-7 was opened. In other words, the progress of the experiments by DPT1 was monitored after 5 s from their initiation. The remote operation of FCV1 and FCV7 ensured excellent repeatability of the experiments [21].

Simultaneously with the pressure decay, the corresponding downstream pressure rise was monitored using two identical 10-Torr absolute pressure transducers, APT2 and APT3 (CCR Process Products Kanata, Ontario, Canada, MKS627F11TBC1B, 10^{-5} full-scale resolution, accuracy: 0.12 % of reading, range: 0 to 10 Torr). The gas accumulated in the downstream configuration that excluded accumulation tanks (V-300, V-301, V302), i.e., in the downstream volume of 81 cm^3. The purpose of not using the accumulation tanks

downstream was to minimize the effect of resistance to gas accumulation, which affects the experimentally measured θ_d [23]. The pressure rise results did not require any processing; the pressure decay results required two corrections described in Ref. [21].

3.4 Results

Figure 3.2 presents an example of the progress of the gas permeation experiment – pressure rise and pressure decay – performed in the CV system shown in Figure 3.1. The experiment was performed with a PDMS membrane (0.610 mm ± 0.051 mm thick) using N_2 at 850 Torr pressure and 30°C. Because the experiment was started when the working and reference volumes were commented, the pressure decay data is available only after 5 seconds from the initiation of the experiment, i.e., when FCV-1 was closed. The pressure decay rate is highest at the beginning of the experiment and gradually decreases as time progresses, reaching a constant rate indicating a steady state. Extrapolating the linear portion of the pressure decay curve to the time axis yields the upstream time lag θ_0 = -99 s. At the same time, right after the initiation of the experiment, there is a negligible pressure rise because it takes time for gas molecules to diffuse across the membrane, which is followed by a gradual increase in the rate of pressure rise until a steady state permeation is attained. The corresponding downstream time lag based on the intercept of the extrapolated linear portion of the pressure rise curve is θ_d = 49 s. Therefore, the corresponding absolute value of the ratio of θ_0 and θ_d is 2.02, which is nearly identical to the theoretical value of 2.

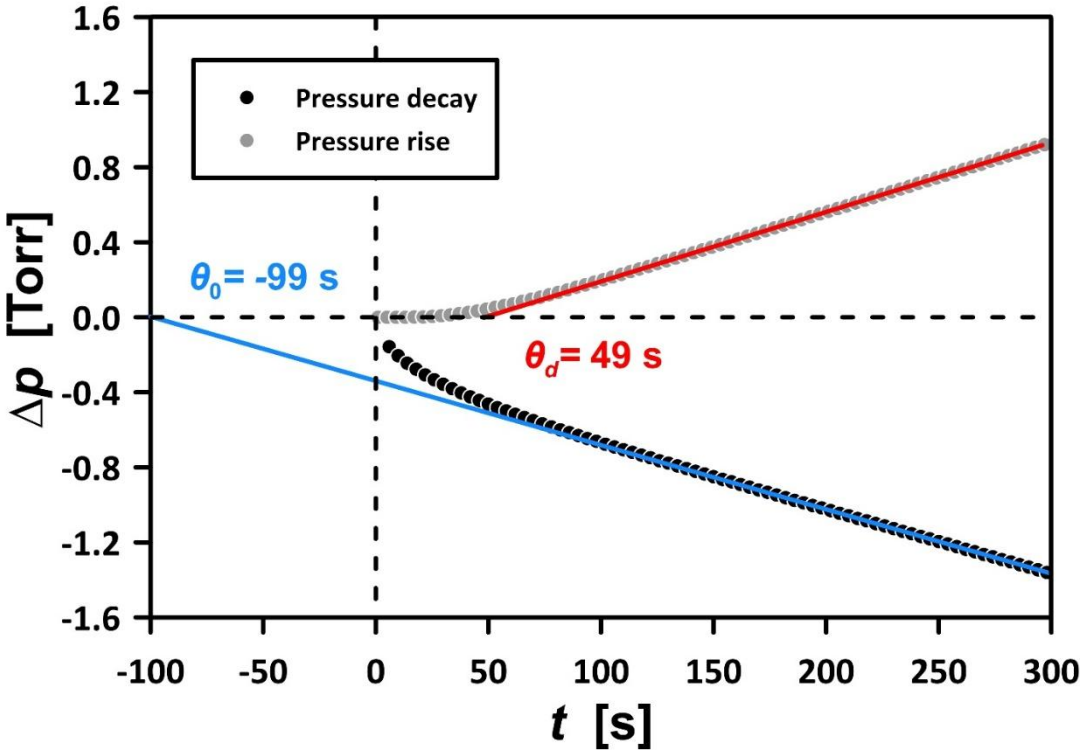

Figure 3.2 An example of the pressure profiles from the N_2 permeation in the CV system using a PDMS membrane of thickness 0.610 ± 0.051 mm. The experiment was conducted at 850 Torr and 30°C.

Using θ_d and θ_0 determined from the experimental pressure rise and decay, the corresponding diffusivity of N_2 in PDMS from Eqs. (3.1) and (3.16) are 1.26×10^{-9} m^2/s and 1.25×10^{-9} m^2/s. Based on the slopes of the downstream pressure rise and the upstream pressure decay, the permeability of N_2 in PDMS is 6.83×10^{-14} mol/s·m·Pa (207 Barrer) and 7.30×10^{-14} mol/s·m·Pa (221 Barrer), respectively. Knowing D and P, the corresponding solubility of N_2 in PDMS from the pressure rise and decay is 5.40×10^{-5} mol/m^3·Pa and 5.83×10^{-5} mol/m^3·Pa, respectively. It is, therefore, evident that D, P, and S from the downstream pressure rise and the upstream pressure decay are very close to each other, which confirms the validity of the experimentally measured pressure decay in our novel CV system.

As shown in Figure 3.2, the rise in pressure after the initiation of the experiment is negligible for the first 40 s because it takes time for the permeating molecules to reach the downstream interface of the membrane. During that time, the membrane behaves as a

semi-infinite solid, and the pressure decay should be governed by Eq. (3.3). Figure 3.3 presents the experimentally measured pressure decay, shown in Figure 3.2, as a function of the square root of time. The inset in Figure 3.3 is the pressure decay portion of Figure 3.2. As expected, Δp_0 is a linear function of $\sqrt{t}$ at early times. Then, the pressure decay rate gradually increases because the permeating molecules leave the membrane, i.e., the membrane is no longer a semi-infinite solid. The slope of the linear portion Δp_0 versus $\sqrt{t}$ represents Σ_t, given by Eq. (3.17), and equals -0.065 Torr/s$^{0.5}$. The corresponding slope of the linear portion of pressure decay in Figure 3.2, used to calculate membrane permeability, represents Σ_{ss}, given by Eq. (3.18), and is equal to 3.4×10^{-3} Torr/s. Therefore, using the ratio of Σ_{ss} and Σ_t, the diffusivity of N_2 in PDMS from Eq. (3.19) is 1.28×10^{-9} m^2/s. This diffusivity, which we will refer to as D by the two-slope method, is very close to the D values from the upstream and downstream time lags, which validates the two-slope method.

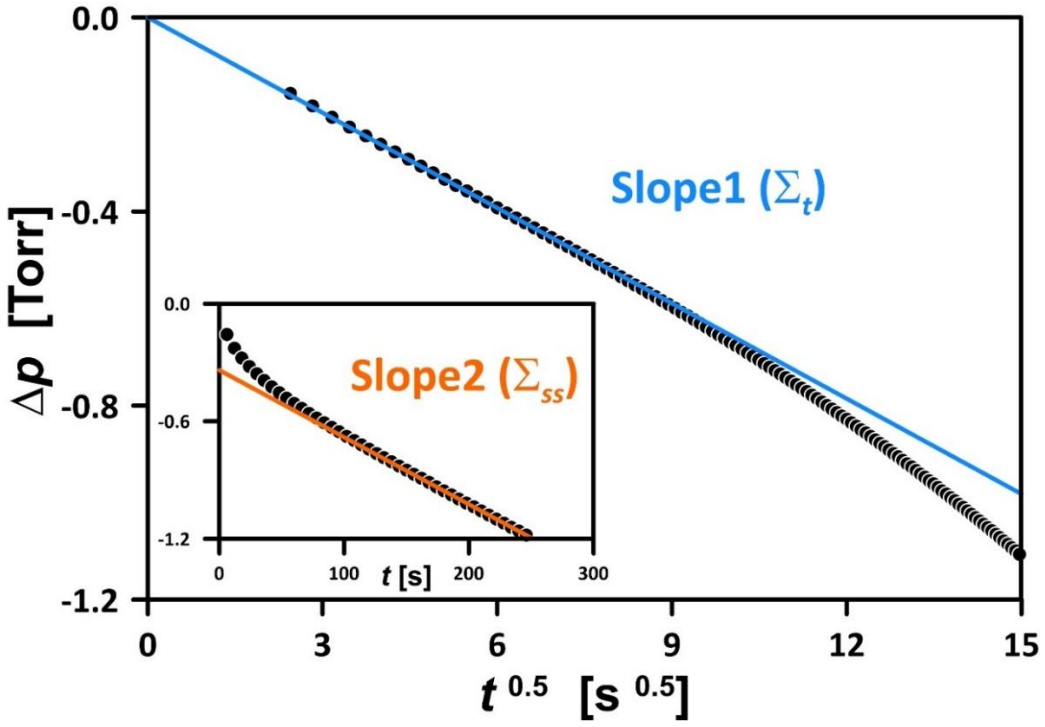

Figure 3.3 Pressure decay of the experiment demonstrated in Figure 3.2 in the square root of the time domain. The inset shows the pressure decay part of Figure 3.2. The N_2 permeation experiment in the CV system using a PDMS membrane of thickness 0.610 ± 0.051 mm at 850 Torr and 30°C.

The direct determination of the solubility of N_2 in PDMS from Eq. (3.23) requires M_∞, i.e., the amount of N_2 dissolved in the membrane at a steady state. The number of moles of N_2 in the membrane at a given time, $M(t)$, can be determined from the pressure decay and pressure rise curves shown in Figure 3.2. The number of moles entering the membrane, $M_0(t)$, is directly related to the pressure decay:

$$M_0(t) = \frac{V_0}{RT}\int_0^t \Delta p_0(t)\,dt = A\int_0^t J(0,t)\,dt \tag{3.26}$$

Similarly, the number of moles leaving the membrane, $M_d(t)$, is directly related to the pressure rise:

$$M_d(t) = \frac{V_d}{RT}\int_0^t \Delta p_d(t)\,dt = A\int_0^t J(L,t)\,dt \tag{3.27}$$

Figure 3.4 presents the plots $M_0(t)$ and $M_d(t)$ using the experimentally measured Δp_0 and Δp_d shown in Figure 3.2. Figure 3.4 resembles Figure 3.2 because M_0 and M_d are directly related to Δp_0 and Δp_d. However, unlike Figure 3.2, the slopes $M_0(t)$ and $M_d(t)$ at a steady state are the same so that the respective linear portions of the curves are parallel. It is because in Eqs. (3.26) and (3.27) rely on the pressure decay and the pressure rise corrected by the respective upstream (V_0) and downstream (V_d) volumes. The gas accumulation in the membrane as a function of time, $M(t)$, is therefore:

$$M(t) = M_0(t) - M_d(t) \tag{3.28}$$

The M_∞ required to calculate S using Eq. (3.23) is represented by the vertical distance between $M_0(t)$ and $M_d(t)$ at a steady state. It is also important to note that the horizontal distance between $M_0(t)$ and $M_d(t)$ at a steady state represents the difference between the downstream and the upstream time lags. Because $M_0(t)$ and $M_d(t)$ are determined from the respective pressure decay (Eq. (3.26)) and pressure rise (Eq. (3.27)) responses, the resulting θ_0 and θ_d in Fig. 5a are identical, as they should, as those in Figure 3.2, and their difference depends on D:

$$\theta_d - \theta_0 = \frac{L^2}{2D} \tag{3.29}$$

The diffusivity of N_2 from Eq. (3.29) represents an arithmetic average diffusivity determined from Eqs. (3.1) and (3.16).

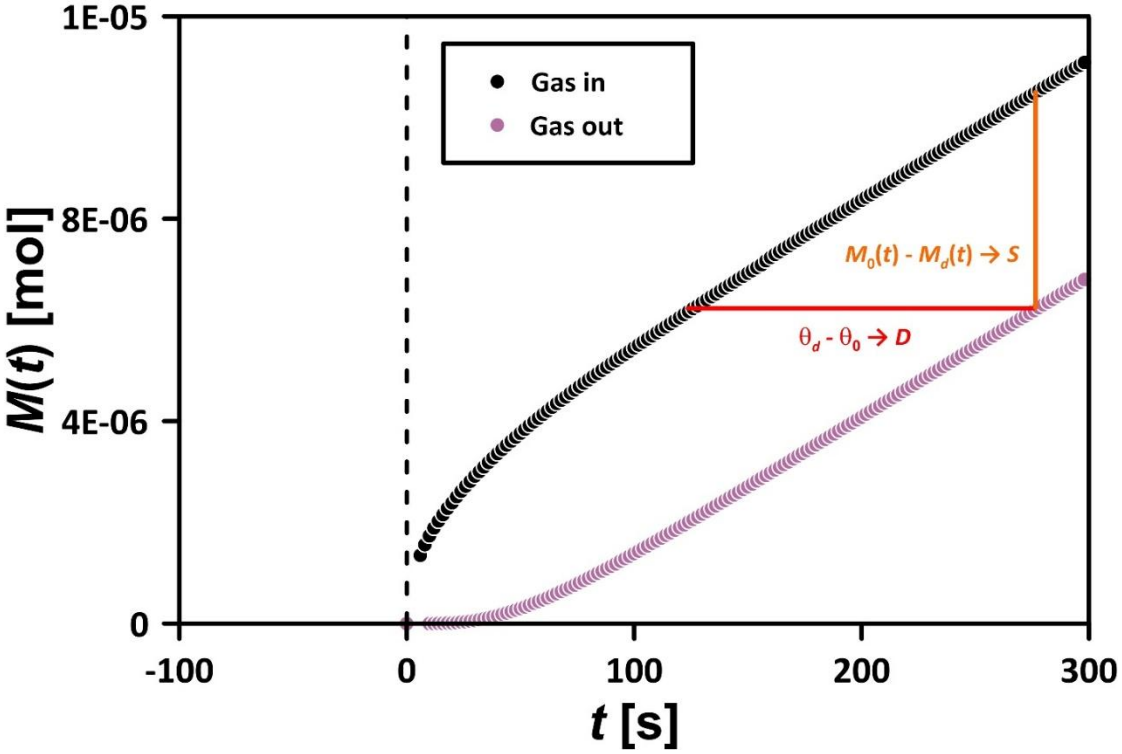

Figure 3.4 The amount of gas entering and leaving the membrane as a function of time determined from $M_0(t)$ and $M_d(t)$ shown in Figure 3.4. for the pressure decay and rise in Figure 3.2. The N_2 permeation experiment in the CV system using a PDMS membrane of thickness 0.610 ± 0.051 mm at 850 Torr and 30°C.

Figure 3.5 presents $M(t)$ as a function of time determined from Figure 3.4. As the time increases, $M(t) \rightarrow M_\infty$, which is identical to the vertical distance between $M_0(t)$ and $M_d(t)$ at a steady state. The value of M_∞ in Figure 3.5 is obtained from the arithmetic average of $M(t)$ after the system reaches the steady state at approximately 200 s. It is important to note that 200 s corresponds to four times the downstream time lag, consistent with a rule of thumb for reaching the steady state permeation [24]. According to Figure 3.5 $M_\infty = 2.35\times10^{-6}$ mol, the corresponding solubility coefficient from Eq. (23) is $S = 5.38$ mol/m^3·Pa.

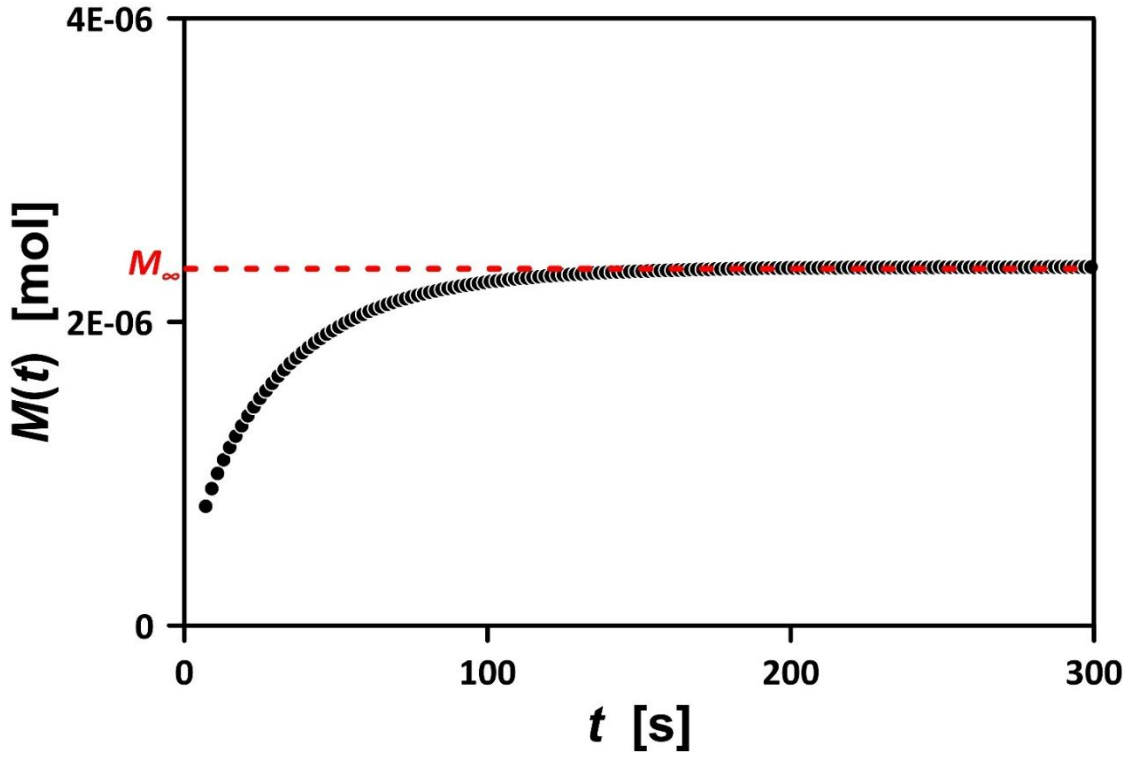

Figure 3.5 Gas accumulation in the membrane as a function of time - determined from $M_i(t)$ and $M_o(t)$ presented in Figure 3.4. The N_2 permeation experiment in the CV system using a PDMS membrane of thickness 0.610 ± 0.051 mm at 850 Torr and 30°C.

Having the experimental value of M_∞ allows the transformation of Eq. (3.21) into Eq. (3.25), as shown in Figure 3.6. It is evident that there is a linear portion in Figure 3.6. The slight upward deviation at the beginning is due to Eq. (3.24) relying on a single-term approximation, which is not valid at short times. Additionally, there is a downward deviation from linearity when Fo > 0.35. As the steady state is approached, the left-hand side of Eq. (3.24) approaches zero. However, the limited resolution of DPT1 results in a systematic error in M_∞ - $M(t)$, which becomes evident when the difference approaches zero. Nevertheless, there is a sufficiently long period in Figure 3.6 during which $M_{ln}(t)$ is a linear function of t with a slope of $\sigma = -0.031\ s^{-1}$, corresponding to a diffusivity $D = 1.14 \times 10^{-9}\ m^2/s$.

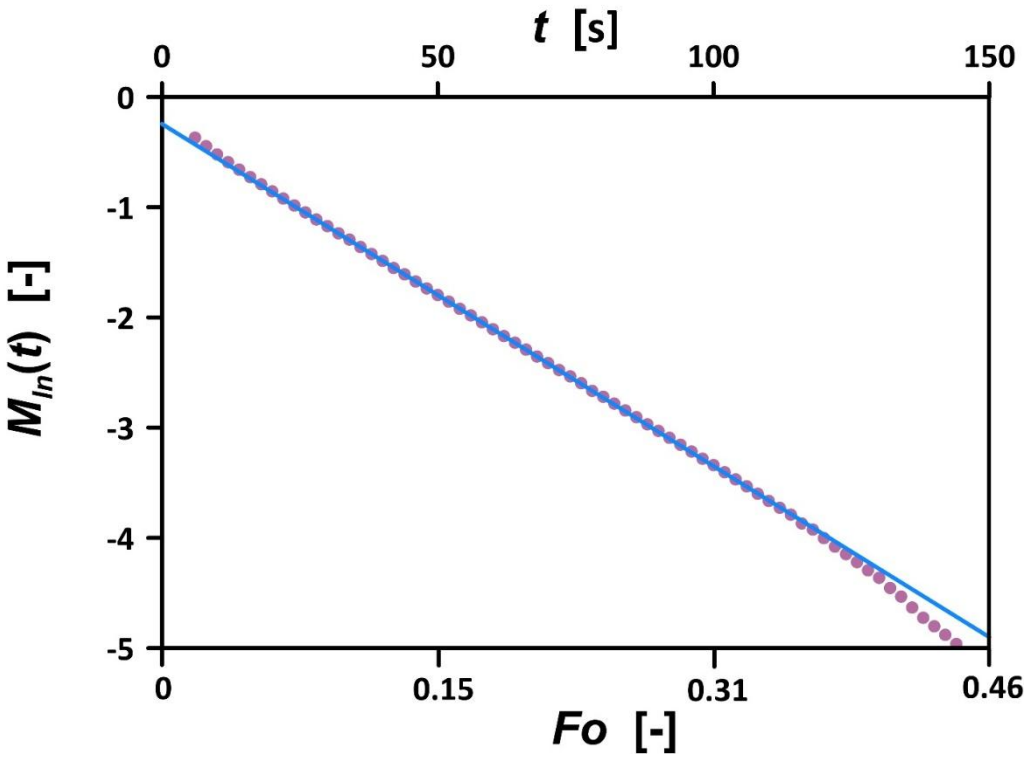

Figure 3.6 Transformation of the results presented in Figure 3.5 using Eq. (3.25). The Fourier number in the lower x-axis is calculated using $D = 1.14 \times 10^{-9}$ m^2/s determined using the slope of the linear portion of the data in this figure. The N_2 permeation experiment in the CV system used a PDMS membrane with a thickness of 0.610 ± 0.051 mm at 850 Torr and 30°C.

3.5 Discussion

Monitoring the pressure decay in addition to the conventional pressure rise during the time lag experiments offers three additional methods for characterizing gas separation membranes. The first and most obvious, which we will refer to as Method 2 (where Method 1 is the time-lag method), is the direct application of the pressure decay, which allows determining D from the upstream time lag and P from the linear portion of the pressure decay, mimicking the conventional membrane characterization using the pressure rise, i.e., Method 1. The second, the two-slope method, which we will refer to as Method 3, uses the linear portion of pressure decay and the early slope of the pressure decay in the square root-of-time domain. The ratio of the two slopes depends only on the

diffusion coefficient. The permeability coefficient in this method is the same as in the first method. These two new methods solely depend on pressure decay. If P, D, and S can be determined solely based on pressure decay using Methods 2 and 3, the permeate side of the membrane could be continuously evacuated, better adhering to one of the two boundary conditions on which the time-lag method relies. Alternatively, the permeate side of the membrane could be connected to an online mass spectrometer, which would be advantageous if the feed were a gas mixture rather than a single gas. Finally, the combined method (Method 4), which relies on both pressure rise and decay, allows for the determination of gas accumulation in the membrane as a function of time. This, in turn, allows the direct determination of the diffusivity and solubility coefficients in a way similar to the dynamic adsorption/desorption experiments used to characterize adsorbents. The resulting P is the product of directly determined D and S.

Table 3.1 summarizes the P, D and S values using the abovementioned methods. Of the four permeability coefficients, three (Methods 1, 2 and 4) are independent values. On the other hand, all four D and S values, i.e., one from each method, are independently determined from the same experiment. In addition, Method 4 offers the arithmetic averages of the transport properties from Methods 1 and 2, which are P = 214 [Barrer], D = 1.26×10^{-9} m^2/s and S = 5.62×10^{-5} [mol/m^3 Pa].

Table 3.1 The summary of N_2 transport coefficients in a PDMS membrane of thickness 0.610 ± 0.051 mm determined from the single gas permeation (time-lag) experiment at 850 Torr and 30 °C.

Method	P [Barrer]	D [m^2/s]	S [mol/m^3 Pa]
1. Conventional pressure rise	207	1.26×10^{-9}	5.40×10^{-5} [(a)]
2. Direct pressure decay	221	1.25×10^{-9}	5.83×10^{-5} [(a)]
3. Pressure decay two-slopes	221[(b)]	1.28×10^{-9}	5.70×10^{-5} [(a)]
4. Combined pressure rise & decay	186[(a)]	1.14×10^{-9}	5.38×10^{-5}

(a) Calculated from $P = DS$
(b) From the pressure decay slope – Method 2

Methods 1-3 rely on the fundamental correlation of the solution diffusion mechanism, i.e.

$$P = DS \tag{3.30}$$

Eq. (3.30) allows for the calculation of S from the ratio of P and D. It also enables the evaluation of P from the product of D and S, which can be compared to the average P from Methods 1 and 2. The P from Method 4 (186 Barrer) is 13% smaller than the average P (214 Barrer). This discrepancy is primarily because the D from Method 4 is 10% smaller than the average D from Methods 1 and 2. As indicated by Eq. (3.25), due to the logarithmic nature of the right-hand of this equation, a small error in M_∞, such as 1%, could translate in a larger error in the slope in Figure 3.6, from which D is evaluated in Method 4.

On the other hand, a 1% error in M_∞ would result in a 1% error in S from Method 4. More importantly, the S from Method 4 does not rely on Eq. (3.30). As previously mentioned, the evaluation of S using Method 4 resembles the determination of S using a barometric method [11]. However, there are some fundamental differences. First, M_∞ in Method 4 represents a steady-state rather than an equilibrium value. At a steady state, for a given feed pressure, while the permeate side is a vacuum, the membrane is "filled" to 50% of its capacity because of the linear concentration profile. If an impermeable layer covered the permeate side of the membrane, the membrane could be filled to 100% of its capacity, which would resemble a typical sorption experiment. However, it can be shown that filling the remaining 50% of the capacity would take a much longer time than reaching the steady state. It is important to acknowledge that in a sorption experiment, a sample (i.e., the membrane) would be exposed to the same pressure conditions on both the feed and permeate sides. As a result, the characteristic length for diffusion inside the membrane would be half of its thickness rather than the entire thickness in the permeation experiment. Still, because of a decreasing concentration gradient for diffusion as the gas accumulates in the sample, reaching the equilibrium would take much longer than reaching a steady state in the permeation cell [25].

Another advantage of determining the solubility coefficient using Method 4 in our CV system is the resolution of the measurement. PDMS or, in general, polymeric membranes do not have high-capacity absorption capacities. Therefore, evaluating the gas solubility coefficient in conventional gas sorption experiments using

gravimetric/barometric/volumetric techniques would require a larger sample, which could increase the characteristic length for diffusion and, consequently, the time to reach the equilibrium concentration in the tested sample [11]. Also, as shown by Eq. (3.23), knowing the experimental M_∞, requires accurate values of p_0, L and A to determine S. There is practically no uncertainty in these values when a membrane is tested in a CV system. The accurate knowledge of L, or, more generally, the characteristic length for diffusion, is even more critical in determining D using Method 4 (Eq. 3.25), as the slope in Figure 3.6 is inversely proportional to the square of membrane thickness.

In this work, we have demonstrated the "multiplication" of membrane characterization methods when the pressure decay and the pressure rise are monitored simultaneously in a conventional time-lag experiment. The importance of using multiple methods (e.g., integral and differential) for analyzing the permeation data from a given time lag experiment was postulated by Beckman et al. [26]. This approach helps detect anomalous diffusion effects. For the rubbery polymers such as PDMS, P, D, and S should be independent of pressure. However, these transport coefficients become pressure-dependent in glassy polymers. Moreover, the more complex membrane materials, including glassy polymer membranes, require additional kinetic and thermodynamic parameters to characterize their performance fully. In this case, the "multiplication" of membrane characterization methods offered by simultaneous monitoring of pressure rise and decay could be advantageous and necessary.

3.6 Conclusions

The time-lag method, the most common way to evaluate membranes D, P and S, is widely used to design and optimize advanced membrane materials in gas separation. The conventional time-lag method, which focuses on the downstream pressure profile, evaluates solubility from the ratio of permeability and diffusivity. In this work, we have provided the theoretical basis and experimentally demonstrated the direct determination of D, P, and S from a single time-lag gas permeation test by simultaneously measuring the upstream pressure decay and downstream pressure rise in a new generation of CV system.

The simultaneous monitoring of pressure decay and pressure rise allows the evaluation of gas accumulation in the membrane as a function of time, and the steady-state gas accumulation allows the direct determination of *S*. Moreover, the time-dependent gas accumulation in the membrane allows direct determination of *D*. Monitoring pressure decay during the time lag experiment also enables a new way of determining *D* from the ratio of two slopes, the early slope of pressure decay in the square root of time domain and the steady state pressure decay. In addition, the entire pressure decay curve mimics the conventional pressure rise curve from which *P* and *D* can be directly evaluated. The *P*, *D*, and *S* of N_2 in the PDMS membrane using these characterization methods were similar, which provided validation of the new methods proposed in this work.

Multiple methods for determining *P*, *D*, and *S* in rubbery polymers might be unnecessary. Still, having several independent values of transport coefficients for a given membrane provides more confidence. However, when it comes to more complex membrane materials, in which Henry's law is not applicable, including glassy polymers, mixed matrix materials, and membranes with anomalous diffusion effects, the conventional time-lag method might be insufficient, and the new methods proposed in this work may become indispensable.

Nomenclature

Symbols

A	Membrane area [m^2]
c	Gas concentration in the membrane [mol/m^3]
D	Diffusivity coefficient [m^2/s]
Fo	Fourier number [-]
L	Membrane thickness [m]
$M(t)$	Gas accumulation in the membrane as a function of time [mol]

$M_{\ln}(t)$	Logarithmic gas accumulation defined by Eq. (25) [-]
M_∞	Gas accumulation in the membrane at the steady state [mol]
P	Permeability coefficient [Barrer or mol/s m Pa]
p	Pressure [torr or Pa]
R	Universal gas constant [J/mol K]
S	Solubility coefficient [mol/m^3 Pa]
T	Absolute temperature [K]
t	Time [s]
V	Volume [m^3]

Greek symbols

θ	Time lag [s]
Δp	Pressure decay/pressure rise [torr/s or Pa/s]
σ	Slope defined by Eq.(15) [1/s]
Σ_t	Slope in the square-root-of-time domain defined by Eq. (17) [torr/s$^{1/2}$ or Pa/s$^{1/2}$]
Σ_{ss}	Slope in the time domain defined by Eq. (18) [torr/s or Pa/s]

Subscripts

d	Downstream
0	Upstream

Abbreviations:

APT	Absolute pressure transducer
DPT	Differential pressure transducer
CV	Constant volume
PDMS	Polydimethylsiloxane

References

[1] L.M. Robeson, Z.P. Smith, B.D. Freeman, D.R. Paul, Contributions of diffusion and solubility selectivity to the upper bound analysis for glassy gas separation membranes, J. Memb. Sci. 453 (2014) 71–83. https://doi.org/10.1016/j.memsci.2013.10.066.

[2] R.W. Baker, Future directions of membrane gas separation technology, Ind. Eng. Chem. Res. 41 (2002) 1393–1411. https://doi.org/10.1021/ie0108088.

[3] R.W. Baker, K. Lokhandwala, Natural gas processing with membranes: An overview, Ind. Eng. Chem. Res. 47 (2008) 2109–2121. https://doi.org/10.1021/ie071083w.

[4] R. Prasad, F. Notaro, D.R. Thompson, Evolution of membranes in commercial air separation, J. Memb. Sci. 94 (1994) 225–248. https://doi.org/10.1016/0376-7388(93)E0193-N.

[5] D.F. Sanders, Z.P. Smith, R. Guo, L.M. Robeson, J.E. McGrath, D.R. Paul, B.D. Freeman, Energy-efficient polymeric gas separation membranes for a sustainable future: A review, Polymer (Guildf). 54 (2013) 4729–4761. https://doi.org/10.1016/j.polymer.2013.05.075.

[6] Q. Wang, R. Zhou, T. Tsuru, Recent Progress in Silicon Carbide-Based Membranes for Gas Separation, Membranes (Basel). 12 (2022). https://doi.org/10.3390/membranes12121255.

[7] A.R. Kamble, C.M. Patel, Z.V.P. Murthy, A review on the recent advances in mixed matrix membranes for gas separation processes, Renew. Sustain. Energy Rev. 145 (2021) 111062. https://doi.org/10.1016/j.rser.2021.111062.

[8] L.M. Robeson, The upper bound revisited, J. Memb. Sci. 320 (2008) 390–400. https://doi.org/10.1016/j.memsci.2008.04.030.

[9] H.A. Daynes, The process of diffusion through a rubber membrane, Proc. R. Soc. London. Ser. A, Contain. Pap. a Math. Phys. Character. 97 (1920) 286–307. https://doi.org/10.1098/rspa.1920.0034.

[10] R.M. Barrer, E.K. Rideal, Permeation, diffusion and solution of gases in organic polymers, Trans. Faraday Soc. 35 (1939) 628–643. https://doi.org/10.1039/tf9393500628.

[11] M. Sadrzadeh, M. Rezakazemi, T. Mohammadi, Fundamentals and Measurement Techniques for Gas Transport in Polymers, Elsevier Inc., 2017. https://doi.org/10.1016/B978-0-12-809884-4.00019-7.

[12] P. Meares, The Diffusion of Gases Through Polyvinyl Acetate, J. Am. Chem. Soc. 76 (1954) 3415–3422. https://doi.org/10.1021/ja01642a015.

[13] W.R. Vieth, K.J. Sladek, A model for diffusion in a glassy polymer, J. Colloid Sci. 20 (1965) 1014–1033. https://doi.org/10.1016/0095-8522(65)90071-1.

[14] D.C. Li, T. Liu, L. Zhao, W.K. Yuan, Solubility and diffusivity of carbon dioxide in solid-state isotactic polypropylene by the pressure - Decay method, Ind. Eng. Chem. Res. 48 (2009) 7117–7124. https://doi.org/10.1021/ie8019483.

[15] X.Q. Nguyen, Z. Brož, F. Vašák, Q.T. Nguyen, Manometric techniques for determination of gas transport parameters in membranes. Application to the study of dense and asymmetric poly(vinyltrimethylsilane) membranes, J. Memb. Sci. 91 (1994) 65–76. https://doi.org/10.1016/0376-7388(94)00019-0.

[16] M. Al-Ismaily, J.G. Wijmans, B. Kruczek, A shortcut method for faster determination of permeability coefficient from time lag experiments, J. Memb. Sci. 423–424 (2012). https://doi.org/10.1016/j.memsci.2012.08.009.

[17] N. Al-Qasas, J. Thibault, B. Kruczek, Analysis of gas transport in laminated semi-infinite solid: Novel method for complete membrane characterization during highly transient state, J. Memb. Sci. 460 (2014). https://doi.org/10.1016/j.memsci.2014.02.024.

[18] N. Al-Qasas, J. Thibault, B. Kruczek, Membrane Characterization Based on the Upstream Pressure Decay in a Dynamic Gas Permeation Test, J. Fluid Flow, Heat Mass Transf. 1 (2014) 57–64. https://doi.org/10.11159/jffhmt.2014.009.

[19] B. Kruczek, S. Lashkari, Challenges in Microflow Measurements in Flow Measurement, Eds. G. U. Beltrán and L. L. Castro Gómez, (2012) 1–34.

[20] E.B. Arkilic, M.A. Schmidt, K.S. Breuer, Gaseous slip flow in long microchannels, J. Microelectromechanical Syst. 6 (1997) 167–178. https://doi.org/10.1109/84.585795.

[21] P. Leszczynski, Z. Cao, H. Wu, J. Thibault, B. Kruczek, MethodsX Determination of time lag by accurate monitoring of pressure decay in a new generation constant volume system, MethodsX. 13 (2024) 102858. https://doi.org/10.1016/j.mex.2024.102858.

[22] P.J. Leszczynski, A Novel Constant Volume System for Determining Transport Properties in Polymeric Membranes, University of Ottawa, 2023.

[23] S. Lashkari, B. Kruczek, Effect of resistance to gas accumulation in multi-tank receivers on membrane characterization by the time lag method. Analytical approach for optimization of the receiver, J. Memb. Sci. 360 (2010). https://doi.org/10.1016/j.memsci.2010.05.043.

[24] R. C. Ll. Jenkins, P.M. Nelson, L. Spirer, Calculation of the transient diffusion of a gas through a solid membrane into a finite outflow volume, Trans. Faraday Soc. 66 (1970) 1391–1401.

[25] J. Crank, The mathematics of diffusion, 2nd ed., Oxford University Press, 1975.

[26] I.N. Beckman, D. Syrtsova, M.G. Shalygin, P. Kandasamy, V. V. Teplyakov, Transmembrane gas transfer: Mathematics of diffusion and experimental practice, J. Memb. Sci. 601 (2020) 117737. https://doi.org/10.1016/j.memsci.2019.117737.

Chapter 4

Impact of the porous support disc of a gas permeation cell on the estimation of the membrane transport properties

Zheng Cao, Boguslaw Kruczek, Jules Thibault*

Abstract

The rapid development of polymeric membranes for gas separation requires an accurate and suitable method for promptly assessing their performance. The time-lag method is one of the most commonly used methods to estimate the permeation parameters (permeability, diffusivity, and solubility) of single gases in membranes. However, a membrane is not evaluated in isolation; it is placed in a permeation cell, which may impact the determination of these parameters. This paper explores the effect of using a porous support disc on estimating the membrane permeation parameters. The impact of a porous disc supporting an ideal membrane was assessed by solving Fick's second law of diffusion. Results clearly show that the membrane thickness, along with the pore size and the porosity of the porous disc, may significantly influence the estimation of the diffusivity and permeability of the membrane using the time-lag method. Interestingly, the observed effect was not dependent on the intrinsic diffusivity of the membrane. The relative diffusivity and relative permeability are strictly a function of the porosity of the porous disc and the ratio of the pore diameter to the membrane thickness. Results can be used to correct the impact of the porous plate and recover the intrinsic membrane properties.

Keywords: Porous support plate; time-lag method; Fick's equation; finite differences; diffusivity, permeability

Graphical abstract

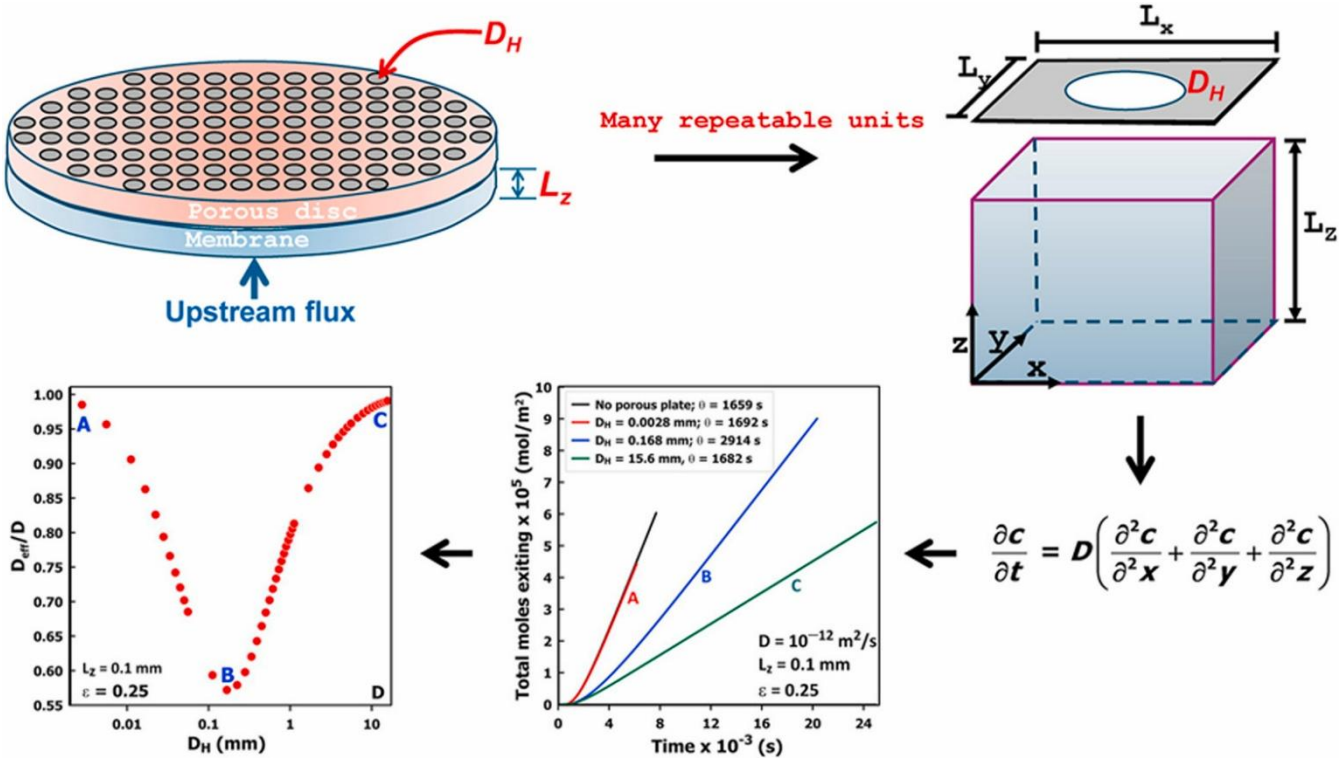

Publication status: Journal of Membrane Science 721(2025) 123831

***Corresponding author**

4.1 Introduction.

The membrane field has witnessed an explosive development in membrane technology for gas separation. To sustain this rapid pace of development, it is paramount to characterize the membranes rapidly for their potential applications. Besides the

physical characterization of the membranes, their performance in terms of solubility, permeability, and diffusivity is undoubtedly the most important. The accurate and timely estimation of permeation parameters is essential for the design and optimization of gas separation processes. There are many methods available to measure the permeation parameters of membranes [1,2]. Still, the most popular is the time-lag method, which measures the time delay between gas concentration changes on either side of the membrane [3]. In the time-lag method, a dynamic gas permeation test is conducted in a pre-evacuated constant-volume system where a step change in gas pressure occurs on one side of the membrane, initiating the experiment, and the downstream pressure rise is recorded as a function of time. The membrane time lag (θ) is determined under steady-state permeation from the intersection of the extrapolated linear portion of the pressure response $\left(dp/dt\right)_{t\to\infty}$ with the time axis. In turn, the diffusivity (D) is inversely proportional to θ [4].

$$D = \frac{L_z^2}{6\theta} \tag{4.1}$$

where L_z is the membrane thickness. Furthermore, the permeability (P) is directly proportional to $\left(dp/dt\right)_{t\to\infty}$. Then, the solubility ($S$) is calculated as the ratio of P and D. Therefore, the time-lag method allows for the estimation of D, P, and S from the single gas permeation experiment [5].

Eq. (1) is the ultimate result of solving the governing partial differential equation – Fick's second law of diffusion, subject to the appropriate initial and boundary conditions. For example, the second boundary condition assumes zero gas concentration at the membrane-permeate interface. However, because the time-lag experiments are typically performed in constant volume (CV) systems and the gas accumulates at the permeate side of the membrane, the gas concentration at the permeate interface of the membrane is a function of time. It is still possible to solve Fick's second law of diffusion analytically when the concentration at the permeate interface, i.e., the second boundary condition, is expressed as a function of time. However, the resulting expression for the time lag loses the simplicity of Eq. (1) [6]. Alternatively, the expression for the time lag given by Eq.

(4.1) can also be corrected to accommodate the increasing gas concentration at the permeate interface [7]. On the other hand, in a properly designed system, the error in diffusivity when using Eq. (1) should not exceed 2% [8], which is small compared to the errors arising from the resolution and accuracy of measuring devices and data analysis in the time-lag method [9].

In principle, Eq. (4.1) applies to membranes where gas sorption is a linear function of pressure (i.e., Henry's law applies), which is the case for rubbery polymers. Yet, it is also used to characterize glassy membranes where dual-mode sorption prevails. Although the effects of dual-mode sorption [10] and partial immobilization of permeating species in the Langmuir sites [11] can be incorporated, the resulting expressions for the time lag are much more complex than Eq. (4.1). Similarly, the time-lag analysis can also be extended to allow variable diffusivity [12,13] and diffusion combined with a reaction [14], which also result in complex expressions for the time lag. However, Eq. (4.1) is widely used regardless of the actual gas transport mechanism in the membrane and the membrane material; the resulting diffusivity is an effective rather than an intrinsic property of the membrane material [15].

Although not explicitly stated, the time-lag method assumes that the membrane constitutes the only resistance to gas transport during the permeation experiment. At the upstream side of the membrane, this assumption implies a perfect step change in pressure to initiate the experiment, which is the case for ideal gases but not for organic vapours [16]. At the permeate side, the absence of resistance to gas transport implies that the location of a pressure transducer to monitor the pressure rise resulting from gas permeation is irrelevant. However, this is not the case [17,18]. Because the permeate receiver is initially at a high vacuum, gas accumulation is governed by Knudsen diffusion, and the corresponding diffusivity is a large but not an infinite value. Knudsen diffusivity is directly proportional to the internal diameter of a conduit, in which gas accumulates, which implies that the smaller the diameter of the tube at the membrane downstream, the greater the resistance effects [19]. These effects are still relatively small, even in 6.35 mm (1/4-inch) tubing, unless the length of tubes in the downstream receiver is considerable. However, they are greatly magnified by the presence of an accumulation tank, which can

be considered resistance-free by itself because of a relatively large Knudsen diffusivity [20]. The resistance to gas accumulation arising from the combination of tubing and an accumulation tank leads to an underestimation of the membrane's time lag and, thus, the overestimation of the membrane diffusivity [21].

The time-lag experiments require the membrane to be securely installed in a membrane permeation cell on proper support to withstand a transmembrane pressure difference. Similar to the resistance to gas accumulation in the downstream receiver, although not explicitly stated, the time-lag method assumes that the membrane support inside the permeation cell does not affect the measured time lag and the gas permeation rate. Figure 4.1 presents a schematic representation of a typical gas permeation cell used to perform time-lag experiments. This figure depicts the location of the porous plate at the downstream side of the permeation cell to maintain the physical integrity of the membrane when subjected to a transmembrane pressure difference. The porous support plate introduces additional flow resistance for gas molecules exiting the membrane. First, the porous support plate is in intimate contact with the membrane on the downstream side, and a gas molecule faces two boundary conditions: uninhibited migration through the holes of the porous plate and gas impermeability with the solid surface of the porous plate. The partial blockage of the migration of gas molecules at the membrane's downstream surface undoubtedly impacts the membrane's estimation of permeation properties. The potential hindrance to the gas transport by the porous plate might not be limited to the CV systems in which the time-lag experiments are typically performed. It may also exist in constant pressure (CP) systems and affect the properties determined using online mass spectrometry [22].

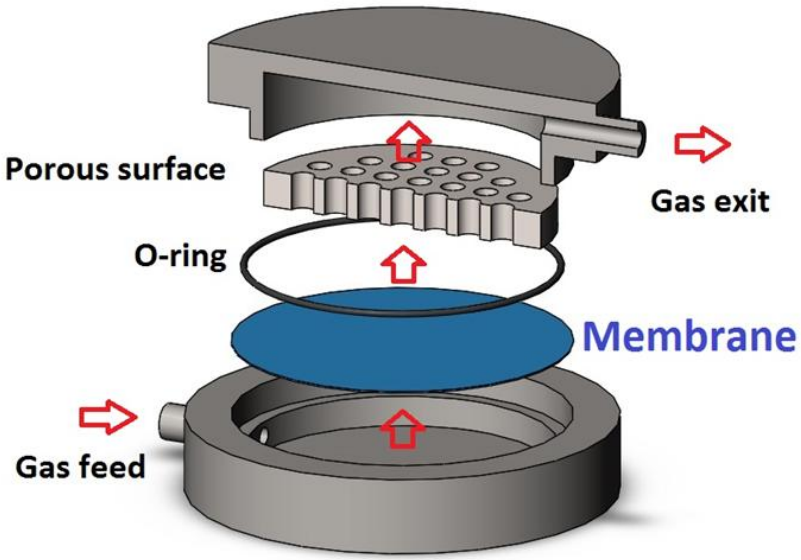

Figure 4.1 Exploded view of a permeation cell for testing gas membranes.

The effect of a porous material in intimate contact with a dense membrane on the transport properties was considered in the past. Indeed, the development of thin film composite membranes and the investigation of the impact of their porous support layer on their permeability have been considered in previous studies [23–26]. Similarly, Davis and Ethier explored how a porous support plate influences water transport during filter cake filtration [27]. Wijmans and Hao introduced a restriction coefficient to account for the decrease in permeability due to the extended path length for diffusion due to the presence of a porous layer [28]. Some researchers used 2D and 3D computational fluid dynamics (CFD) simulations to quantify the impact of the porous layer on the reduction in effective membrane permeability [23,28]. Most of these studies were designed to estimate the membrane permeability upon reaching the steady-state permeation rate. However, to our knowledge, the effect of the membrane support in a gas permeation cell under unsteady state conditions, which affects the experimentally determined time lag of the membrane, has not been previously investigated. Therefore, this paper seeks to evaluate, through numerical simulations, the impact of the porous support plate on the estimation of the membrane diffusivity using the time-lag method and the estimation of the membrane permeability using the steady-state transport rate. As solubility is typically determined

from the ratio of permeability to diffusivity, any error in either of these two parameters will also affect the calculated solubility.

4.2 Methodology

Because the surface pores of the porous support plate are either randomly or uniformly distributed, modeling of the time-lag experiment requires solving the three-dimensional Fick's second law of diffusion (Eq. (4.2)) to determine the variation of the concentration of the migrating species within the membrane as a function of time. In the first attempt to solve this problem, a whole membrane was simulated to accommodate the random surface pore distribution. However, in the case of a thin membrane and larger pore diameters, limitations of the granularity in the membrane discretization and the computational time did not allow for achieving a sufficiently accurate solution. Instead, it was assumed that the pores of the porous plate were uniformly distributed, such that it is possible to consider the membrane made of a large number of identical three-dimensional (3D) repeatable cuboids as illustrated in Figure 4.2. Each cuboid or elementary unit has the same thickness as the membrane and is perfectly aligned to have a circular pore of the support plate at its center. Because of the periodic boundary conditions of the repeatable elementary units, the solution of one elementary unit represents the solution of the whole membrane. Indeed, we can quantitatively infer information about the entire system by analyzing just a small part of a larger domain.

The finite difference method was used to solve Eq. (4.2), which was discretized into a sufficiently large number of mesh points to generate small three-dimensional discrete elements and to ensure mesh independence. The discretized equation for a central mesh point in an explicit form is given by Eq. (4.3). The indices (i,j,k) refer to (x,y,z) directions divided into (NI,NJ,NK) mesh points, respectively. This equation computes, at each time t, the change in the internal concentration at mesh point (i,j,k) during the next time step Δt (i.e. at time $t+\Delta t$). It relies on the concentration at the mesh point (i,j,k) and that of its six neighboring mesh points at time t. Eq. (4.3) is applicable for all internal mesh points that describe the membrane. The solution was obtained using a FORTRAN computer code

written for this project. We assume the dense membrane is isotropic and characterized by constant D and S.

$$\frac{\partial c}{\partial t} = D\left[\frac{\partial^2 c}{\partial x^2} + \frac{\partial^2 c}{\partial y^2} + \frac{\partial^2 c}{\partial z^2}\right] \tag{4.2}$$

$$\frac{c_{i,j,k}^{t+\Delta t} - c_{i,j,k}^{t}}{\Delta t} = D\left[\frac{c_{i-1,j,k}^{t} - 2c_{i,j,k}^{t} + c_{i+1,j,k}^{t}}{\Delta z^2} + \frac{c_{i,j-1,k}^{t} - 2c_{i,j,k}^{t} + c_{i,j+1,k}^{t}}{\Delta y^2} + \frac{c_{i,j,k-1}^{t} - 2c_{i,j,k}^{t} + c_{i,j,k+1}^{t}}{\Delta z^2}\right] \tag{4.3}$$

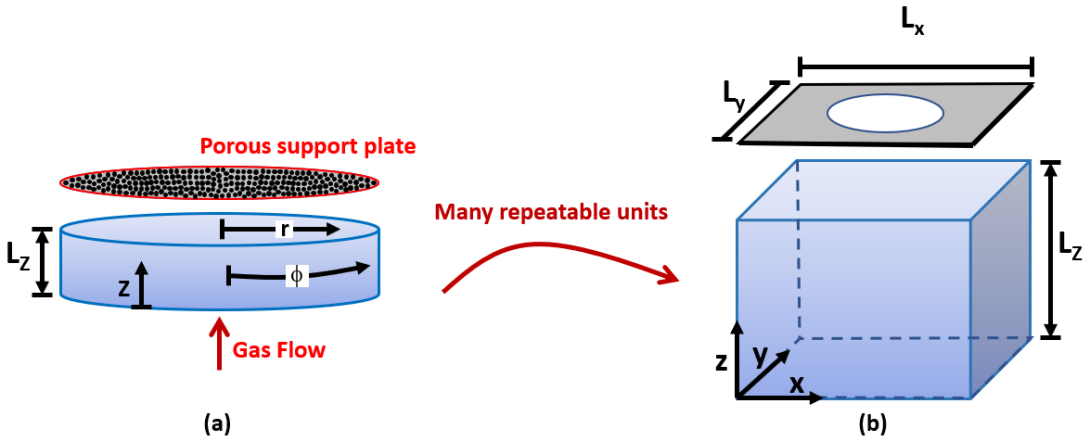

Figure 4.2 Multiple three-dimensional repeatable units can represent a membrane with a porous support plate with uniform hole distribution. An exploded view has been drawn for more clarity.

To completely define the problem, it is necessary to provide the initial condition and six boundary conditions - two for each direction. It is assumed that the initial concentration of the migrating species throughout the membrane is zero (Eq. (4.4)).

$$\text{At } t = 0, \qquad c_{i,j,k}^{t=0} = 0 \qquad \forall i, j, k \tag{4.4}$$

At time zero, a step change in the gas pressure is made at the upstream surface of the membrane, where gas molecules dissolve into the dense membrane and migrate to the permeate side. Eqs. (4.5) and (4.6) define the boundary conditions for the z-direction. Eq.

(4.5) states that the concentration (c) at the upstream interface of the membrane is in instantaneous equilibrium with the concentration (C) of the gas surrounding the membrane, and the ratio of the two concentrations, S, represents dimensionless solubility (Henry's law constant) of the migrating species in the membrane. The boundary condition for the downstream side of the membrane, Eq. (4.6), has two expressions: the top expression applicable for a hole (open space in the support plate) and the bottom expression for an impermeable solid surface. Eq. (4.6) assumes zero gas concentration in the downstream receiver, including the support's porous portion of the support plate. As previously stated, the measurements in the CV system rely on gas accumulation in the downstream receiver. However, in a properly designed system, the level of gas accumulation is low, and the top expression of Eq. (4.6) represents a good approximation. Unlike the top expression, the bottom expression of Eq. (4.6) is the exact boundary condition for the gas molecules that encounter the impermeable solid surface of the porous support plate.

$$\text{At } z = 0, \qquad c^t_{i=1,j,k} = SC^t \qquad \forall j,k \tag{4.5}$$

$$\text{At } z = L_z, \quad \begin{cases} c^t_{i,j,NK} = 0 & \forall j,k \in \text{Hole} \\ \dfrac{\partial c^t_{i,j,NK}}{\partial z} = 0 & \forall j,k \in \text{Solid surface} \end{cases} \tag{4.6}$$

Eqs. (4.7)-(4.10) specify the periodic boundary conditions for the four lateral surfaces of the repeatable cuboid elementary unit, where symmetry conditions prevail.

$$\text{At } x = 0, \qquad \frac{\partial c^t_{i=1,j,k}}{\partial x} = 0 \qquad \forall j,k \tag{4.7}$$

$$\text{At } x = L_x, \qquad \frac{\partial c^t_{i=NI,j,k}}{\partial x} = 0 \qquad \forall j,k \tag{4.8}$$

$$\text{At } y = 0, \qquad \frac{\partial c^t_{i,j=1,k}}{\partial y} = 0 \qquad \forall i,k \tag{4.9}$$

$$\text{At } y = L_y, \qquad \frac{\partial c^t_{i,j=NJ,k}}{\partial y} = 0 \qquad \forall i,k \tag{4.10}$$

The average upstream and downstream fluxes were determined from the concentration gradients at the gas-membrane interfaces, specifically at the upstream and downstream sides, using Eqs. (4.11) and (4.12). Calculating the flux at the upstream surface of the membrane ($k = 1$) is straightforward since the surface concentration is uniform (Eq. (4.11)). However, for the downstream membrane surface ($k = NK$), the flux is zero when the membrane is in contact with the solid surface. When the membrane surface faces a pore of the support plate, the flux may not be perpendicular to the membrane surface at the boundary of the pore. Some lateral contribution to the outgoing flux may occur (second part of Eq. (4.12) in terms of the discretized concentration – see Figure 4.3). In addition, the surface concentration of the membrane aligned with a pore is equal to zero such that the surface concentration ($c_{i,j,k}$) does not appear in Eq. (4.12). In addition, away from the pore boundary, the flux calculated with the lower part of Eq. (4.12) only relies on the last term.

$$J_{z=0} = \frac{1}{L_x L_y} \int_0^{L_y} \int_0^{L_x} -D \left. \frac{\partial c}{\partial z} \right|_{z=0} dx\, dy \tag{4.11}$$

$$J_{z=L_z} = \frac{D}{L_x L_y} \sum_{i=1}^{NI} \sum_{j=1}^{NJ} \begin{cases} 0 & \forall i,j \in \text{Solid surface} \\ \left(\dfrac{c_{i-1,j,k} + c_{i+1,j,k}}{\Delta x} \Delta y \dfrac{\Delta z}{2} \right) + \left(\dfrac{c_{i,j-1,k} + c_{i,j+1,k}}{\Delta y} \Delta x \dfrac{\Delta z}{2} \right) & \\ + \left(\dfrac{c_{i,j,k-1}}{\Delta z} \Delta x \Delta y \right) & \forall i,j \in \text{Hole} \end{cases} \tag{4.12}$$

We assumed that the pores of the support plate do not impose any resistance to the transport of the gas entering them from the membrane. We also assumed convergence to the steady state permeation rate when the average permeation fluxes (J) at the upstream and downstream surfaces were nearly identical, within a tolerance of 0.01%. The downstream average flux allows the calculation of the rate of accumulation of the migrating species in the permeate receiver. Under steady-state permeation, this rate of accumulation remains constant. Extrapolating the constant rate portion of the accumulation curve to the time axis leads to the membrane time lag (θ). This time lag, in turn, allows for the determination of the effective or apparent diffusivity (D_{eff}) using Eq. (4.13), which is similar to Eq. (4.1). If the membrane support does not influence the

downstream gas transport, D_{eff} would be identical to the intrinsic diffusivity D. It is important to restate that the presence of the porous support plate does not change the intrinsic transport properties of the membrane, and the measured transport properties account for the impact of the porous plate. Given that the thickness is squared in Eq. (4.13), an accurate measurement of the thickness is paramount.

$$\theta = \frac{L_z^2}{6D_{eff}} \tag{4.13}$$

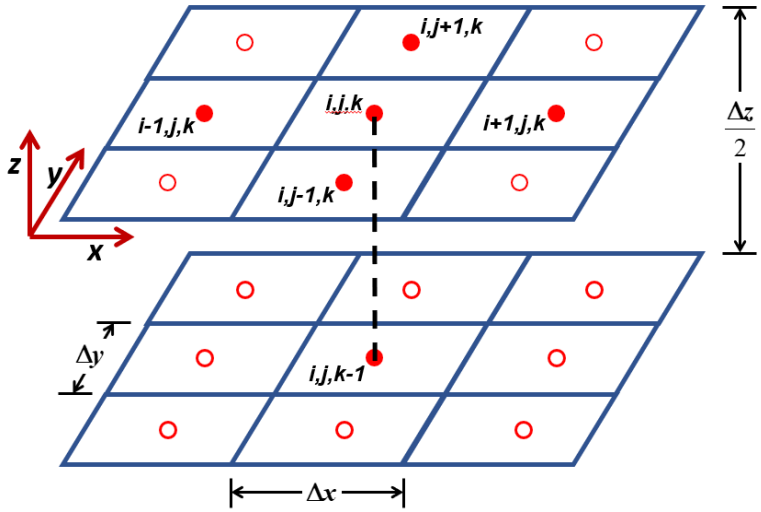

Figure 4.3 Schematic diagram of the discretization points at the permeate interface of the membrane ($k = NK$) in intimate contact with the porous plate.

The steady-state flux allows for the determination of the effective permeability (P_{eff}), as defined by Eq. (14). If the porous support does not influence gas transport, P_{eff} will be the same as P, i.e., the intrinsic permeability of the membrane.

$$P_{eff} = \frac{J\,L_z}{C} \tag{4.14}$$

The diameter of the holes of the porous support plate (D_H), the open fraction area available for permeation (ε), and the membrane thickness (L_z) are adjustable parameters to explore the impact of the porous support plate on the estimated diffusivity and permeability. The porous support plate was assumed to have a flat surface in intimate

contact with the membrane. Eq. (4.6) defines the boundary conditions at the interface between the membrane and the support plate when a mesh element (i,j,NK) aligns with either a hole or a solid surface. It is important to emphasize that, regardless of D_H, we assume no resistance to gas transport in the holes of the support plate, and consequently, the thickness of the support plate is not considered a parameter in this study. Given the near-vacuum on the permeate side of the membrane and the relatively low permeation rate, Knudsen diffusion is the gas transport mechanism in the porous plate support holes. Although for very small D_H the corresponding Knudsen diffusivity might be relatively small, in practice, the support thickness (i.e., the pore length) should not exceed a centimeter, making the resistance effects negligible [19]. The fraction area of the porous plate that covers the membrane and inhibits the free flow of molecules is equal to ($1-\varepsilon$).

4.3 Results and discussion.

In this investigation, the effect of various parameters on the estimation of the diffusivity and permeability of the membrane was evaluated. The investigated parameters included the intrinsic diffusivity of the membrane (D), the membrane's thickness (L_z), the pore diameter of the porous support plate (D_H), and the fraction of the downstream surface of the membrane in contact with the solid surface of the porous plate ($1-\varepsilon$). Before delving into these aspects, the upcoming section aims to validate the numerical finite difference solution - a crucial step in ensuring the accuracy and reliability of computational models.

4.3.1 Validation of the numerical solutions

The validation of the finite difference numerical method is essential to guarantee the accuracy and reliability of the computational simulations conducted in this study. Its purpose is to faithfully capture the underlying physics, minimize errors, and yield trustworthy results. Typically, this validation process relies on analytical benchmark solutions. However, the numerical model was validated using one-dimensional gas permeation due to the absence of benchmark solutions for this three-dimensional problem. In the validation process, the model made two key assumptions: first, a uniform upstream

gas distribution, and second, no flow restriction on the downstream side of the membrane. For this specific scenario, we have an analytical solution represented by Eq. (4.15), which was derived using the method of separation of variables. We then compared the numerically obtained axial concentration profiles at different times with the profiles determined using the analytical solution. Results, as shown in Figure 4.4, demonstrate a perfect fit between the two data sets.

$$c(z,t) = CS\left(1 - \frac{z}{L_z}\right) - \left(\frac{2CS}{\pi}\right)\sum_{n=1}^{\infty}\left[\frac{1}{n}\sin\left(\frac{n\pi z}{L_z}\right)e^{-\left(\frac{Dn^2\pi^2 t}{L_z^2}\right)}\right] \tag{4.15}$$

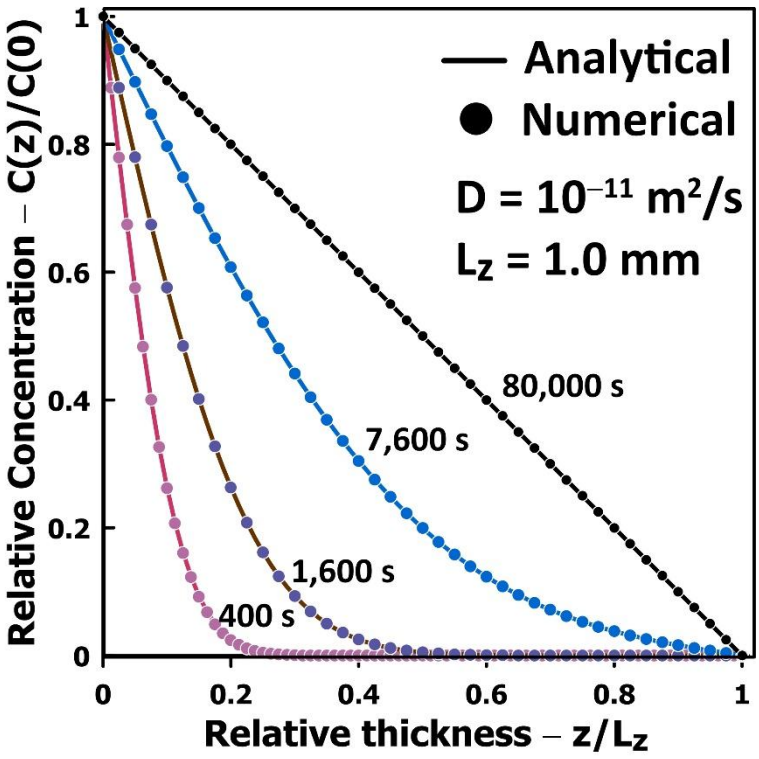

Figure 4.4 Comparison of the analytical and numerical one-dimensional concentration profiles as a function of time for an ideal dense membrane.

To ensure mass conservation, a mass balance considering the entering flux, the outgoing flux, and the mass accumulated within the membrane was also performed and found to be very precise. In addition, it is important to consider the boundary conditions of Eq. (4.12) to ensure convergence of the downstream flux with the upstream flux. Failure

to do so, i.e. considering only the normal concentration gradient, led to a steady-state downstream flux lower than the upstream flux, as illustrated in Figure 4.5. However, the boundary condition of Eq. (4.12) has no effect on the concentration within the membrane. In all the results presented in this investigation, simulations were performed with different mesh sizes to ensure mesh independence.

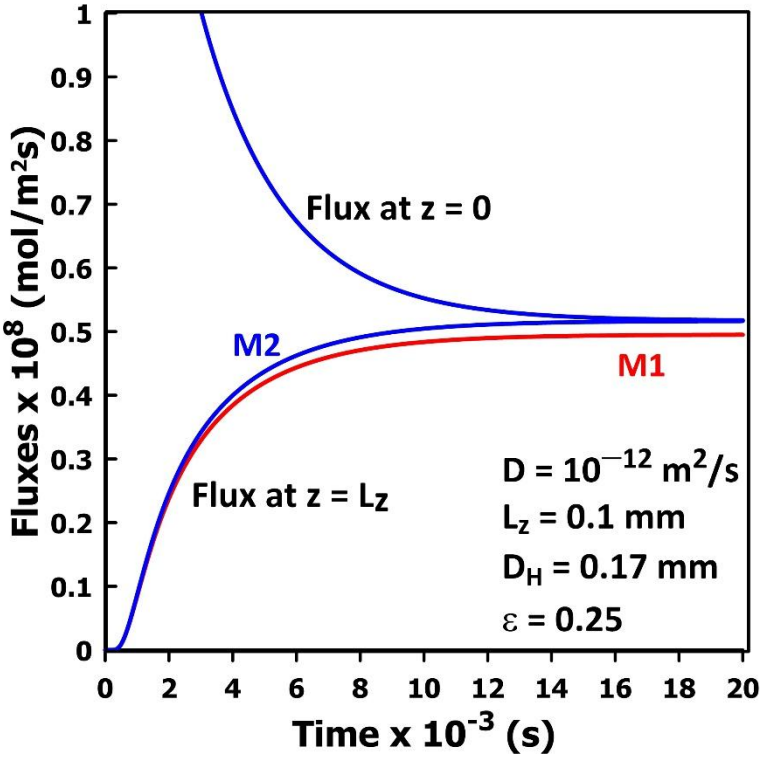

Figure 4.5 Upstream and downstream fluxes as a function of time in the presence of a porous support plate to compare the boundary conditions for evaluating the downstream flux. Method M1 uses the normal gradient only, whereas Method M2 uses the algorithm of Eq. (4.12).

4.3.2 Impact of the membrane diffusivity

We investigated how variations in the intrinsic diffusivity affect the overall transport properties for different membrane thicknesses for a constant area fraction (ε = 0.48) available for permeation. A series of simulations were performed to determine, via the time-lag method, the effective diffusivity for six different intrinsic diffusivity coefficients

and three membrane thicknesses. Results were compared with those of the unobstructed membrane ($\varepsilon = 1.0$). Results of this series of simulations are presented in Figure 4.6a in terms of the relative diffusivity ratio (D_{eff}/D) – the effective diffusivity being estimated via the time-lag method. Figure 4.6b presents the results for the effective permeability obtained from the steady-state permeation rate.

The results of Figure 4.6 emphasize that the relative effective diffusivity and permeability are not affected by the intrinsic diffusivity and permeability of the membrane. These results confirm the findings of Wijmans and Hao for the effective permeability [28]. However, the presence of a porous plate on the downstream surface of the membrane significantly influences the effective diffusivity determined by the time-lag method, and the impact is a function of the membrane thickness. Specifically, as shown in Figure 4.6a, the estimation errors for the effective diffusivity are 28%, 15%, and 8% for membrane thicknesses of 0.1, 0.5, and 1.0 mm, respectively. Thus, the membrane thickness and the fraction area of the porous support plate available for permeation play a significant role in determining the effective diffusivity of the membrane. While the intrinsic diffusivity of the membrane remains unaffected by the presence of the porous support plate, the partial blockage for gas permeation at the downstream surface of the membrane leads to an error in its evaluation.

Results for the estimation of the effective permeability, presented in Figure 4.6b, show that, for a constant ε, the effective permeability increases with an increase in the membrane thickness. The relative permeability is calculated based on the steady-state permeation rate as specified in Eq. (14). Reductions are 32%, 9%, and 5% for membrane thicknesses of 0.1, 0.5, and 1.0 mm, respectively. The effective permeability is, therefore, influenced by the open fraction of the porous plate available for gas permeation and the thickness of the membrane.

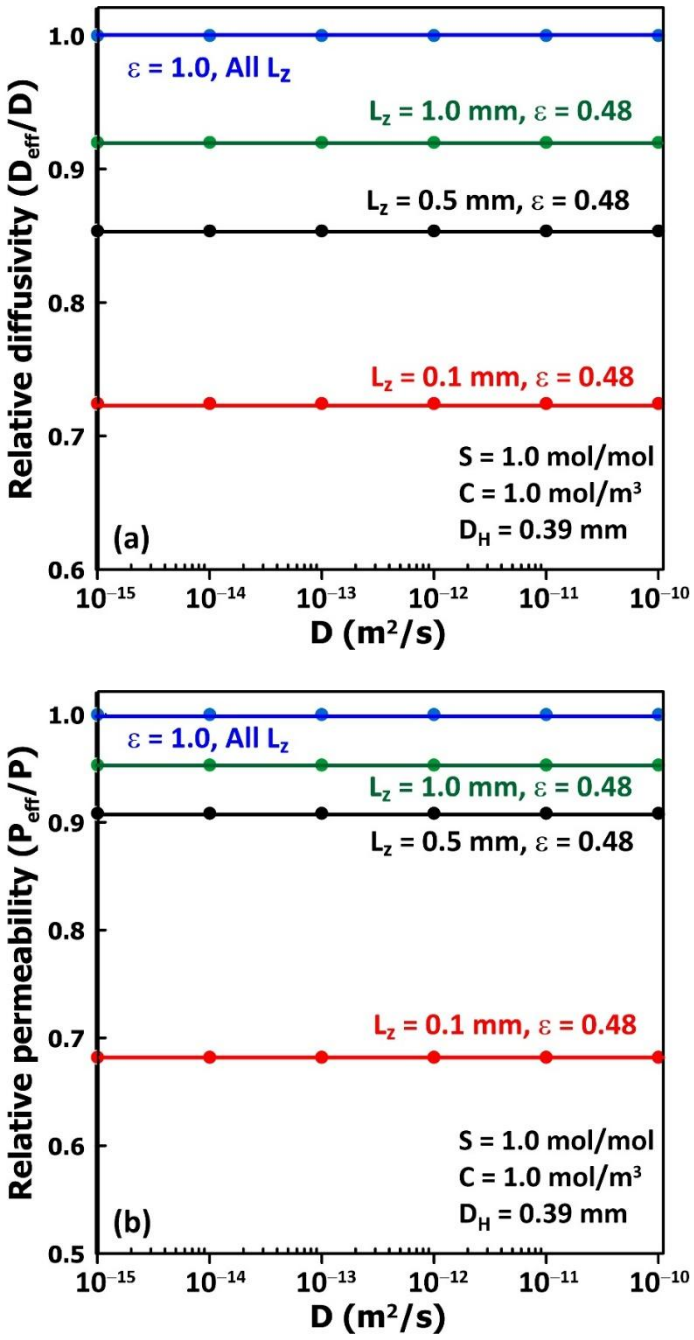

Figure 4.6 (a) Ratio of the effective and intrinsic diffusivity (D_{eff}/D) and (b) the ratio of the effective and intrinsic permeability (P_{eff}/P) as a function of the membrane intrinsic diffusivity for different thicknesses for a constant open fraction of 0.48 of the porous support plate having a pore diameter of 0.39 mm, compared to the permeation of an unobstructed membrane.

4.3.3 Impact of the porous plate surface coverage fraction (1 - ε)

This section delves into the influence of the porous plate coverage fraction. For this case study, an elementary cell unit ($L_x = L_y = 0.5$ mm) was used, and the diameter (D_H) of the centered hole was varied to generate different coverage fractions. The outcomes of this series of numerical simulations are showcased in Figures 4.7a and 4.7b, representing the estimated relative diffusivity and relative permeability, respectively. The relative diffusivity (D_{eff}/D), where D_{eff} is determined using the simulated time lag, is presented in Fig. 7a as a function of the porous plate fraction coverage for seven different membrane thicknesses. These results clearly show a decrease in the effective diffusivity as a function of the porous plate coverage fraction for all seven thicknesses tested. The decrease becomes more significant as the thickness of the membrane decreases from 1 mm to 0.1 mm. However, a further decrease in the membrane thickness progressively leads to a lower error in estimating the relative diffusivity compared to the results of the 0.1-mm thick membrane. For very thin membranes, the rate of decrease of the relative diffusivity is more pronounced at a lower coverage fraction and either decreases more smoothly or increases as the coverage fraction increases. Again, these results highlight the strong and complex impact of the porous plate coverage fraction and membrane thickness on the effective diffusivity. It is important to note that the hole diameter also changed to provide the desired coverage fraction.

The results of the effective permeability are presented in Figure 4.7b. The variation of the relative permeability is more intuitive than that of the estimated diffusivity because it relies strictly on the steady-state permeation rate and is independent of the time required to achieve a steady state. The effective permeability decreases with the coverage fraction, and the decrease is more pronounced for thinner membranes. It is logical to infer that if less area for permeation is available on the downstream side, the relative permeability will decrease and tend to zero as the coverage fraction approaches unity. For very thin membranes, the relative permeability becomes directly proportional to the coverage fraction (see plot in Figure 4.7b for the 0.01-mm membrane). On the other hand, for very thick membranes, the relative permeability remains close to unity for a wider range of the coverage fraction. Still, it will decrease sharply as the coverage fraction tends to unity.

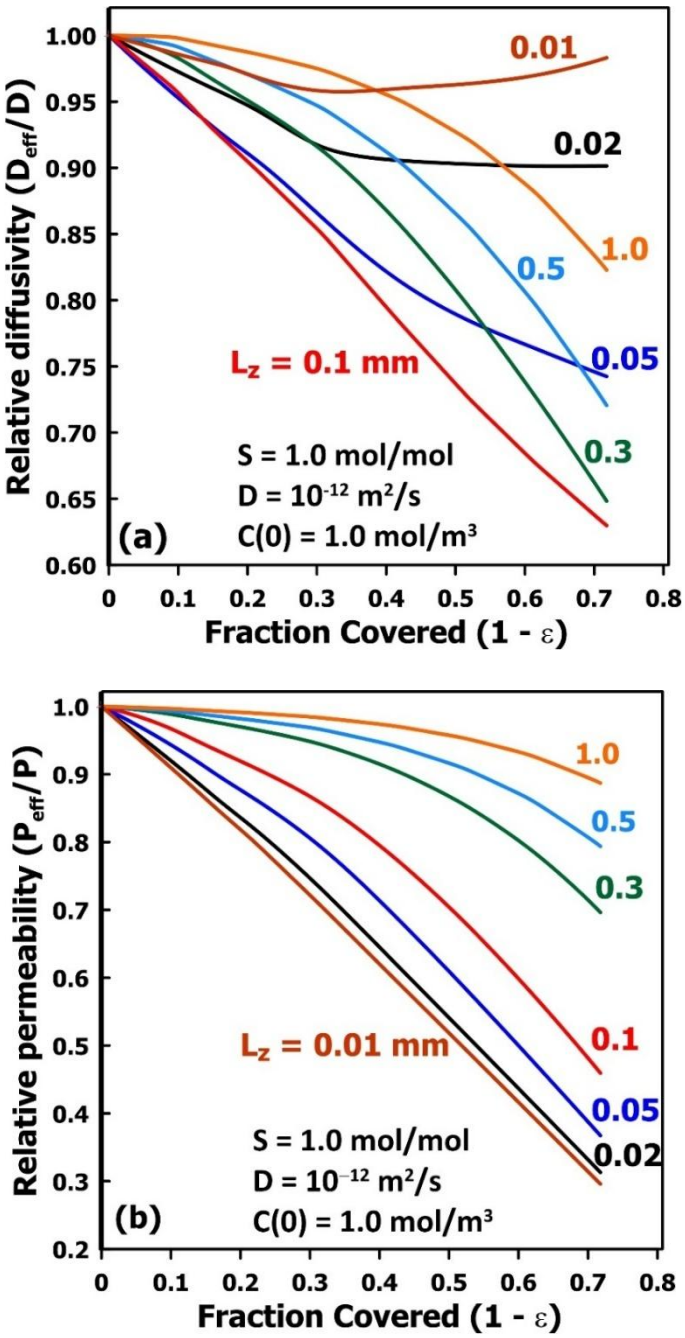

Figure 4.7 Impact of the coverage fraction of the porous support plate on the (a) relative diffusivity and (b) relative permeability for seven membrane thicknesses.

4.3.4 Impact of the membrane thicknesses

To delve deeper into the impact of the membrane thickness on the estimated diffusivity and permeability, we conducted a series of simulations across a broad spectrum of thicknesses for three distinct downstream coverage fractions. The results are presented in Figure 4.8. Figure 4.8a suggests that the effective diffusivity, estimated by the time-lag method, tends to unity for very thin membranes for all coverage areas. It also suggests that the diffusivity would be very accurately estimated for very thick membranes, albeit for unreasonably thick membranes. Between the two extremes of the membrane thickness, the relative diffusivity initially decreases with an increase in the membrane thickness, then goes through a minimum before increasing again. As the coverage fraction increases, the observed minimum in the relative diffusivity is lower and occurs at a higher membrane thickness.

The outcomes for the corresponding estimated permeability are illustrated in Figure 4.8b. For thin membranes, the relative permeability seems to converge proportionally to the downstream surface area available for permeation (ε). As the thickness of the membrane augments, so does the relative permeability, and it is plausible to suggest that it will converge to unity for membranes of substantial thickness. A higher membrane thickness would be required to reach unity at a higher coverage fraction.

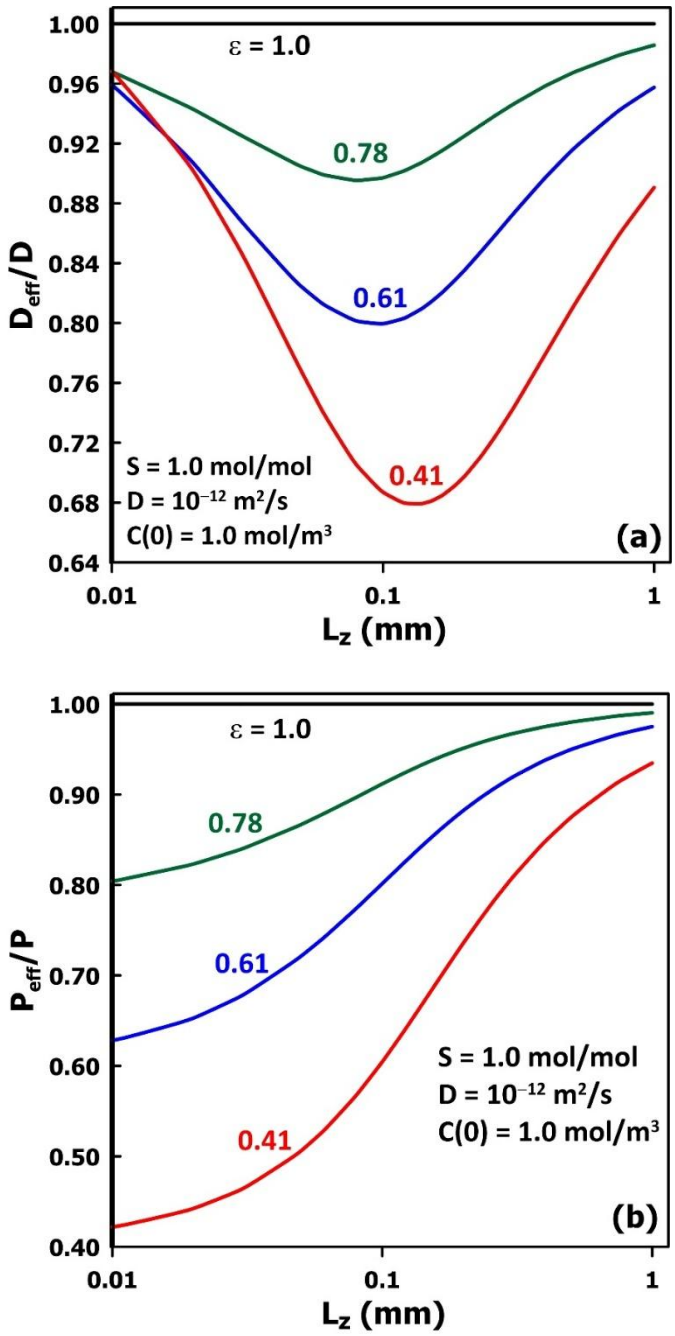

Figure 4.8 Impact of the membrane thickness on (a) the relative diffusivity and (b) the relative permeability for four coverage fractions with a porous plate having a pore diameter of 0.050 mm, 0.044, and 0.036 mm for a plate porosity of 0.78, 0.61, and 0.41, respectively. $L_x = L_y = 0.5$ mm.

4.3.5 Impact of the porous disc pore diameter (D_H)

The findings discussed in the preceding sections considered the effects of the intrinsic diffusivity, the membrane thickness, and the fraction area of the porous support plate available for permeation. The role of the hole diameter of the downstream porous support plate was not explicitly investigated, even though it was modified in some of the results to change the coverage fraction of the porous plate. A series of simulations were performed to determine the effect of the pore diameter (D_H) on the estimated transport properties of the combined membrane-porous plate system for a constant thickness and support plate porosity. To change D_H, the dimensions L_x and L_y of the elementary unit cell were increased while keeping ε constant.

Figure 4.9a presents the results of the relative diffusivity as a function of the support plate pore diameter for two ε values and the membrane without a porous plate. For very small and very large pore diameters, the measured diffusivity leads to the intrinsic diffusivity, as it asymptotically tends to unity. Between these two asymptotic values, the relative diffusivity follows the trend of an inverse Gaussian curve with a minimum D_{eff}/D of 0.57 and 0.73 for a porosity of 0.25 and 0.50, respectively. The minimum occurs at higher values of D_H when ε increases. Figure 4.9b presents the results of the relative permeability as a function of D_H for the same two values of ε. For the two values of the porosity, the permeability of the membrane is accurately estimated for small values of the pore diameter. As the pore diameter is increased, the relative permeability follows the trend of an inverted logistic function decreasing asymptotically to ε, as the hole diameter is increased. As there is a similarity between the logistic function and the cumulative distribution function of a Gaussian distribution, an opportunity to exploit this similarity may exist to find a model to capture these trends. Without delving too deeply into mathematical concepts, the relative permeability of Figure 4.9b corresponds to the probability for the migrating species to permeate through the pores of the porous plate compared to an unobstructed membrane.

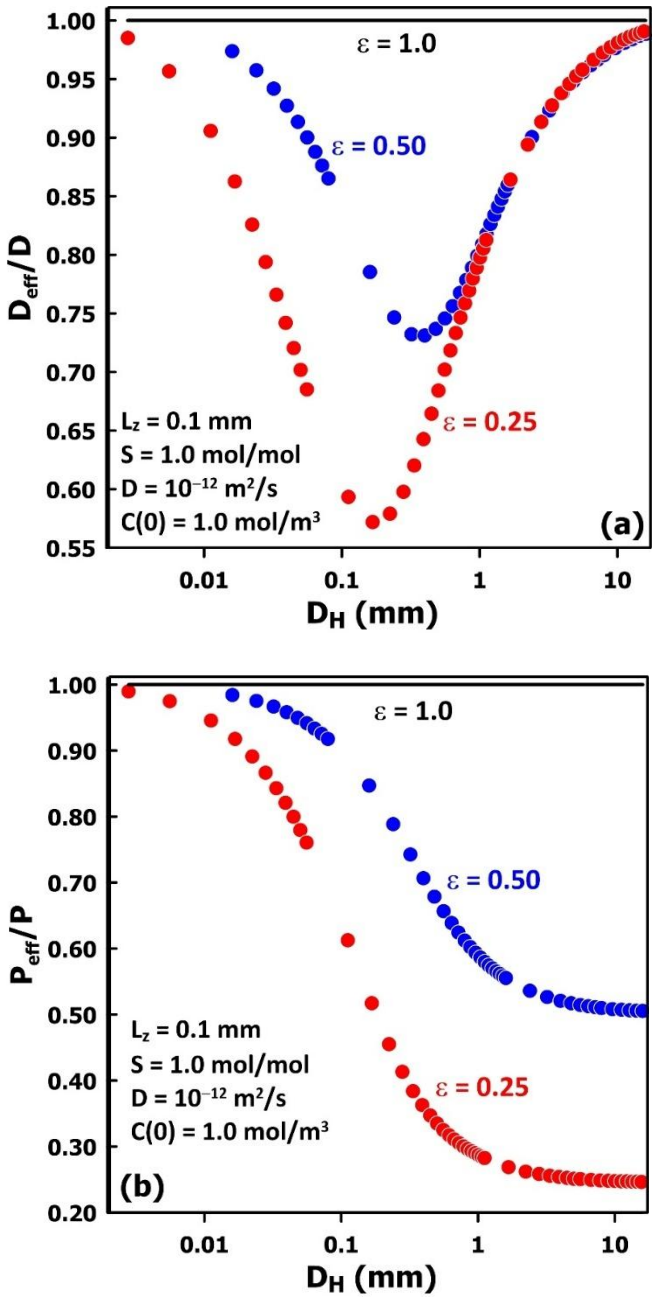

Figure 4.9 Impact of the porous disc hole diameter on (a) the relative diffusivity and (b) the relative permeability for three porous plate coverage fractions with a 0.1-mm thick membrane.

In addition to all the previous results, many simulations were performed to cover a large spectrum of the main variables that can impact the estimation of the relative diffusivity and relative permeability to develop a more general form to represent all the data. After carefully curating all the data, a simple relationship emerged to represent the relative

diffusivity and the relative permeability in a single plot for a constant value of ε. Indeed, by plotting the relative diffusivity and the relative permeability as a function of the ratio of the pore diameter of the porous plate and the membrane thickness, all the data collapse on the same curve, as shown in Figure 4.10.

Figure 4.10a shows that for both very small and very large values of D_H/L_z, the relative diffusivity measured by the time-lag method asymptotically converges to one, which is an accurate estimation of the intrinsic diffusivity of the membrane. Small values of D_H/L_z prevail for small pore diameters of the porous plate and/or thick membranes, whereas large values of D_H/L_z are obtained for large pore diameters of the porous plate and/or thin membranes. Increasing D_H/L_z from the first asymptotic unity value, the variation of the relative diffusivity resembles an inverted Gaussian function going through a minimum before reaching the second asymptotic unity value. The minimum values of the relative diffusivity are approximately 0.86, 0.72, and 0.58 for ε values of 0.72, 0.48, and 0.24, respectively. The values of D_H/L_z at which the minimum occurs fall approximately on the following line:

$$\log_{10}\left(\frac{D_H}{L_z}\right) = 1.06\boldsymbol{\varepsilon} \qquad R^2 = 0.995 \tag{4.16}$$

The intrinsic diffusivity can be calculated with four variables: D_{eff} obtained via the time-lag method, L_z, D_H, and ε. Although it would eventually be possible to derive a mathematical expression to predict the relative diffusivity, the graph of Figure 4.10a provides a simple method for estimating the membrane's intrinsic diffusivity. In the limiting case, when the average pore diameter of the porous support plate is sufficiently small relative to the thickness of the membrane, the time-lag method can be safely used without correction, as the effective diffusivity represents the intrinsic membrane diffusivity. In other cases, a correction factor is required to estimate the intrinsic diffusivity.

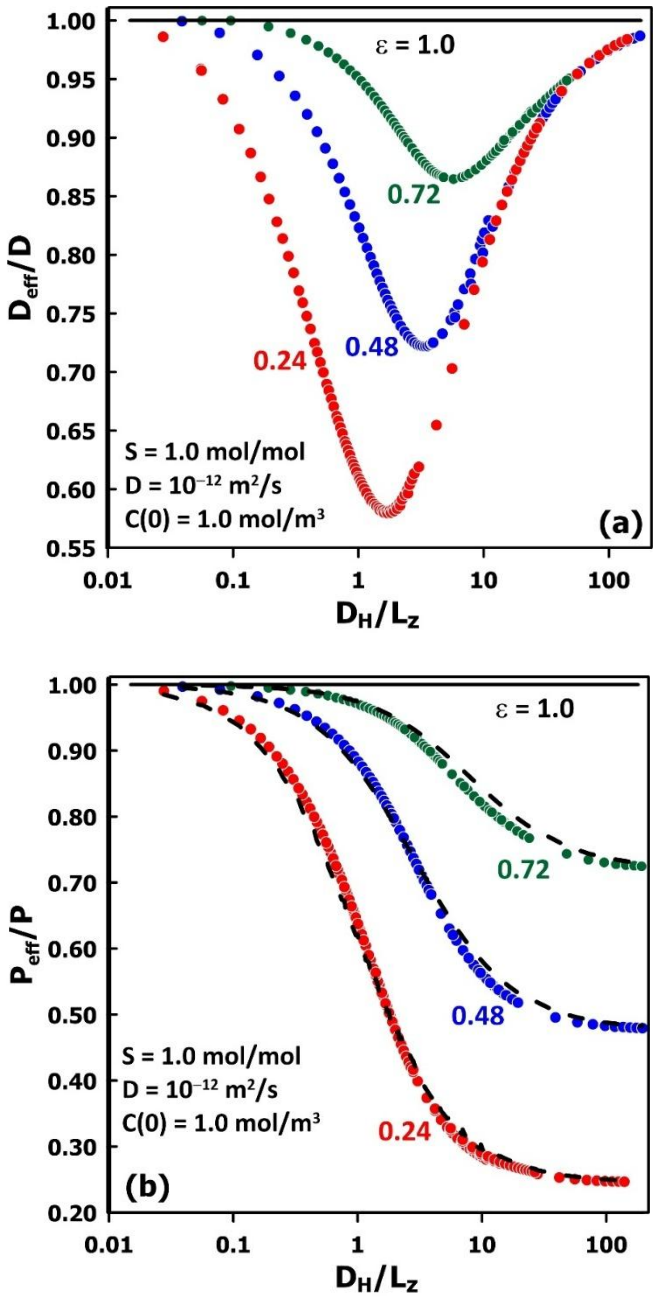

Figure 4.10 The relative diffusivity D_{eff}/D and relative permeability P_{eff}/P as a function of the normalized pore diameter of the porous support plate and the membrane thickness for four values of ε. The dotted lines in (b) are the predictions of the model of Wijmans and Hao [28].

Figure 4.10b presents the results of the relative permeability. The pattern of the relative permeability as a function of the normalized pore diameter is consistent across the three values of ε. The relative permeability is one for small values of D_H/L_z such that the

intrinsic permeability is estimated accurately. As D_H/L_z increases, the relative permeability decreases steadily following the trend of an inverted logistic function and finally reaches asymptotically a minimum value equal to ε. The estimate of the intrinsic permeability is based on four variables: the effective permeability evaluated from the steady-state permeation rate, the membrane thickness, the support plate pore diameter, and the downstream fraction area available for permeation. The asymptotic values of the effective permeability presented in Figure 4.10b were also predicted by Wijmans and Hao [28] and summarized in Eq. (4.17).

$$\begin{aligned} &\varepsilon \to 0: && \frac{P_{eff}}{P} = 0 \\ &\varepsilon \to 1: && \frac{P_{eff}}{P} = 1 \\ &\frac{D_H}{L_z} \to 0: && \frac{P_{eff}}{P} = 1 \\ &\frac{D_H}{L_z} \to \infty: && \frac{P_{eff}}{P} = \varepsilon \end{aligned} \tag{4.17}$$

In addition, the two-coefficient empirical equation (Eq. (4.18)) developed by Wijmans and Hao [28] was used to predict the relative permeability of a membrane supported by a porous support plate. This empirical equation was fitted by the authors using the data of the effective permeability obtained by solving Eq. (4.2) using Ansys Fluent with an average prediction error of 1.8% for a wide range of porosity. The dotted lines of Figure 4.10b show very good agreement with the numerical data obtained in this investigation, which is an additional validation of the accuracy of the numerical algorithm used in this investigation to solve Fick's second law of diffusion. The average prediction errors are 1.38%, 1.06%, and 1.14% for a support plate porosity of 0.24, 0.48, and 0.72, respectively.

$$\frac{P_{eff}}{P} = \frac{\varepsilon + 1.6N_R^{1.1}}{1 + 1.6N_R^{1.1}} \qquad \text{with } \mathrm{N}_R = \frac{2\varepsilon}{1-\varepsilon}\frac{L_z}{D_H} \tag{4.18}$$

Simulations were performed to cover an extensive range of D_H/L_z to tend to the two asymptotic values for the relative diffusivity and relative permeability. The practical range

of the normalized pore diameter D_H/L_z lies approximately between 0.01 and 100, considering typical values of support plate pore diameters (1-500 μm) and membrane thicknesses (5-100 μm).

In the time-lag method, D_{eff} and P_{eff} are calculated independently. Then the effective solubility (S_{eff}) is calculated as the ratio of P_{eff} over D_{eff} . The data of Fig. 10 were used to calculate S_{eff} for the different values of ε. The relative solubility is plotted as a function of the normalized pore diameter (D_H/L_z) as shown in Figure 4.11. For small values of D_H/L_z, the relative solubility is unity as both D_{eff}/D and P_{eff}/P are unity. As D_H/L_z increases, the relative diffusivity decreases more rapidly than the relative permeability, leading to a relative solubility greater than one. For higher values of D_H/L_z, D_{eff}/D starts increasing from its minimum to finally reach unity while P_{eff}/P continues to decrease to reach ε such that S_{eff}/S also asymptotically tends to ε.

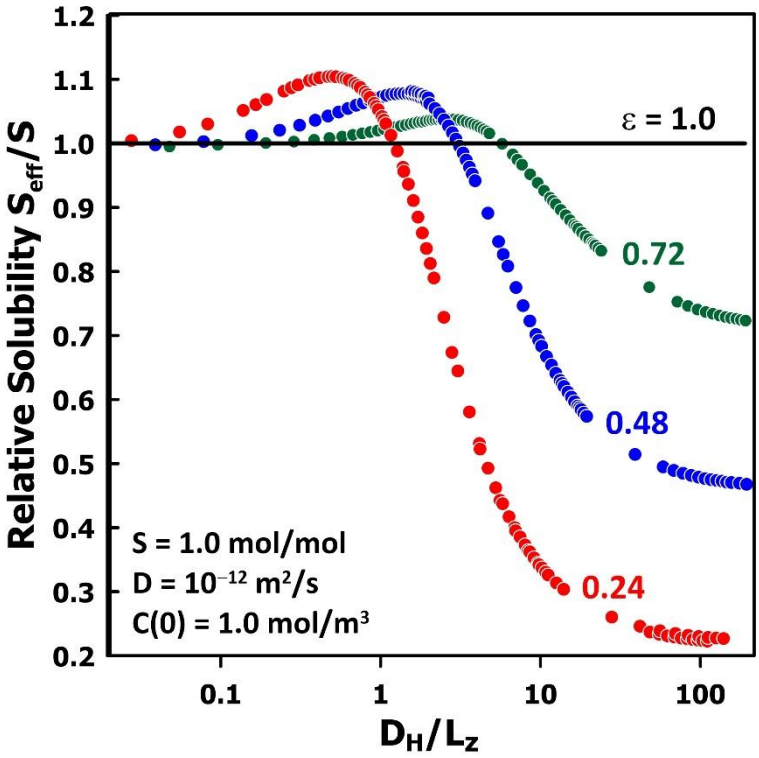

Figure 4.11 The relative solubility S_{eff}/S as a function of the normalized pore diameter (D_H/L_z) of the porous support plate for different values of ε.

4.3.6 Gaining insights from concentration profiles

To better understand how the pore diameter influences the migrating species' relative diffusivity and permeability, the simulations performed to estimate the transport properties as a function of the pore diameter of Figure 4.9 for a membrane thickness of 0.1 mm and a porosity of 0.25 were used. The concentration profiles for the diameters associated with the two asymptotic values and the minimum value were generated. The three x-z concentration profiles for the centerline in the y-direction ($y = L_y/2$) are presented in Figure 4.12. The data points labeled A, B, and C in the plot of the relative diffusivity of Panel D of Figure 4.12 correspond to the three concentration profiles of Panels A, B, and C.

The concentration profile in Panel A reveals that for extremely small pore diameters and/or very thick membranes, both the relative diffusivity and relative permeability equate to unity. It is observed that the concentration profile is almost identical to the concentration profile of an unobstructed membrane, except for a small deviation in the vicinity of the downstream interface. For small pore diameters for a given ε, the pores of the support plate are very close to each other, and the thickness is large enough to allow most molecules to easily converge to the pores even for relatively low ε.

The concentration profile illustrated in Panel B of Figure 4.12 demonstrates that lateral diffusion becomes important as the pore size increases. This is because the pores are larger and more spaced apart given a constant ε, and/or the membrane's thickness is smaller. This significant lateral diffusion causes a delay in achieving a steady state permeation, resulting in a larger time lag and a lower effective diffusivity. A minimum value of the relative diffusivity is attained when the pore size is slightly above the membrane's thickness. Simultaneously, this is where the steady-state permeation rate (relative permeability) declines more rapidly with the increase in the pore size (Figure 4.9).

Beyond its minimum, the relative diffusivity steadily rises to unity as the pore size increases. The concentration profile of Panel C of Figure 4.11 clearly shows that for large pore diameters and/or thin membranes, the lateral diffusion is confined to a relatively

small local region in the vicinity of the pores. The time lag occurs sooner in this case, leading to a progressively higher effective membrane diffusivity. For large pores and/or thin membranes, the membrane is compartmentalized into two subsystems (pores and solid surface), acting almost independently. This is the reason for observing a flat concentration profile with relatively minor diffusive contribution in the vicinity of the edge of the pores.

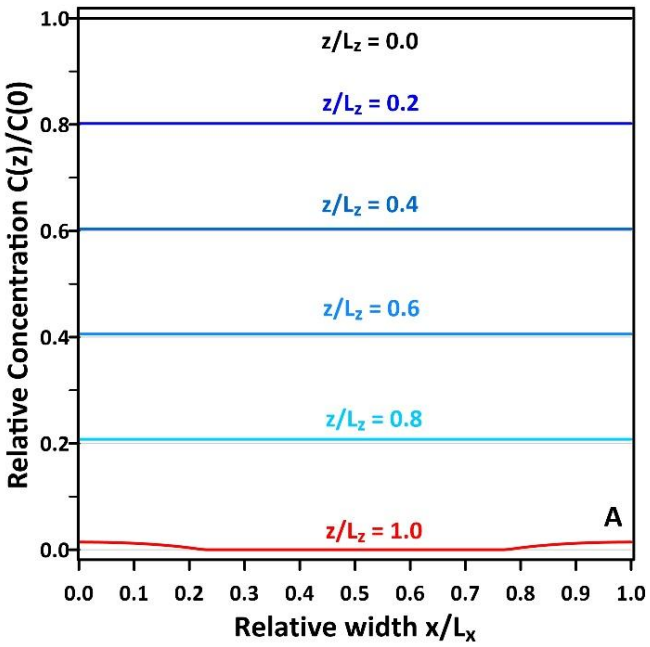
Relative Concentration C(z)/C(0)
1.0
0.8
0.6
0.4
0.2
0.0
z/Lz = 0.0
z/Lz = 0.2
z/Lz = 0.4
z/Lz = 0.6
z/Lz = 0.8
z/Lz = 1.0
A
0.0 0.1 0.2 0.3 0.4 0.5 0.6 0.7 0.8 0.9 1.0
Relative width x/Lx

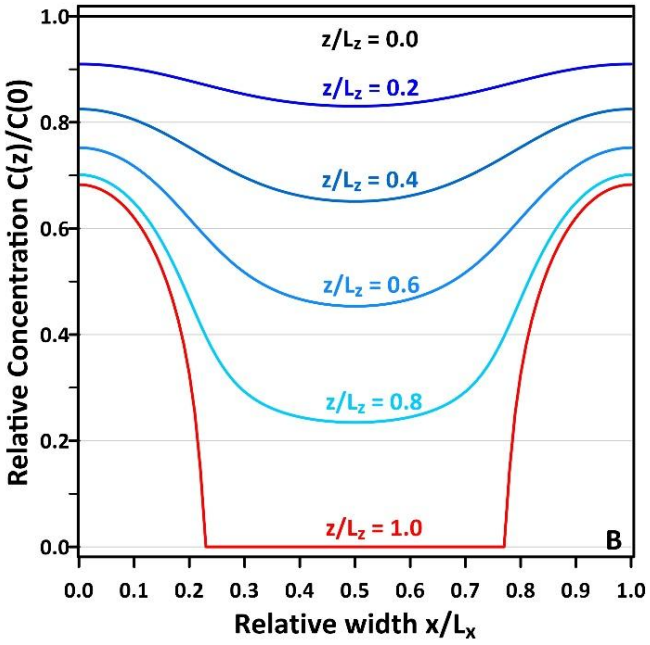
Relative Concentration C(z)/C(0)
1.0
0.8
0.6
0.4
0.2
0.0
z/Lz = 0.0
z/Lz = 0.2
z/Lz = 0.4
z/Lz = 0.6
z/Lz = 0.8
z/Lz = 1.0
B
0.0 0.1 0.2 0.3 0.4 0.5 0.6 0.7 0.8 0.9 1.0
Relative width x/Lx

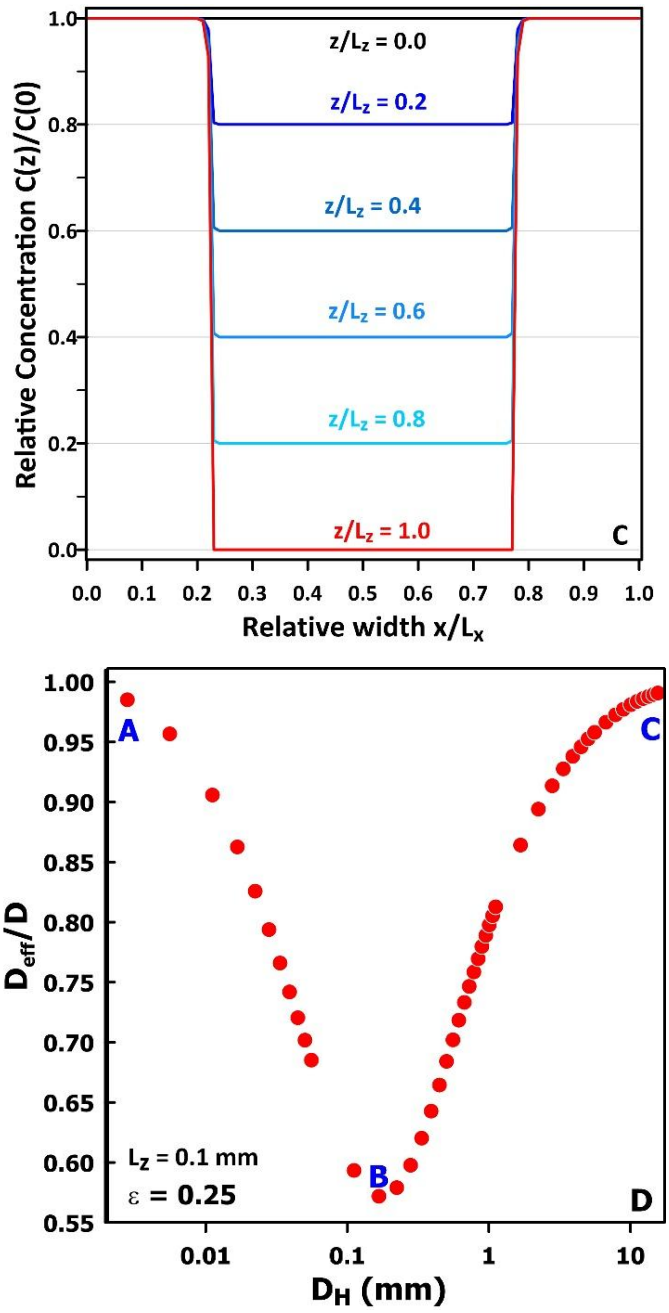

Figure 4.12 *x-z* concentration profiles within an elementary cell unit at the centerline in the *y*-direction ($y = L_y/2$). The three concentration profiles A, B, and C correspond to the three data points labeled A, B, and C in Panel D.

To further illustrate the effect of the porous plate on the estimation of the transport properties, the plots of the gas accumulation on the downstream side of the membrane are plotted in Figure 4.13 and compared with the curve for the unobstructed membrane. The plot for the low values of the normalized pore diameter (D_H/L_z) is essentially identical to the plot of the unobstructed membrane, even for low ε values. As a result, the diffusivity via the time lag and the permeability with the steady state permeation rate (slope of the pressure rise or accumulation plot) are both predicted accurately. As the normalized pore diameter increases, the slope of the pressure rise curve decreases, leading to a decrease in the effective membrane permeability. Slopes of plots A and C are the two asymptotic pressure rise curves for the ε value of 0.25. As D_H/L_z increases, the pressure rise curve spans the area between plots A and C, and the associated effective permeability decreases steadily. The time lag for plot B, corresponding to the minimum relative diffusivity in Panel D, is much higher (lower D_{eff}) than for the asymptotic plots A and C.

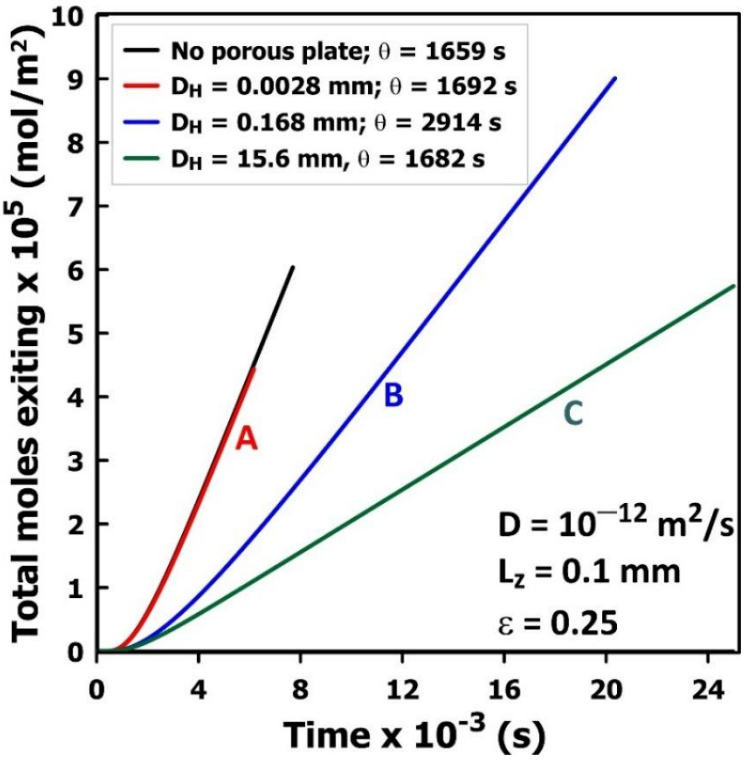

Figure 4.13 Comparison of the downstream gas accumulation as a function of time for a 0.1-mm thick membrane. The plot of a membrane without a porous support disc is compared with the plots for the three pore diameters of Figure 4.12.

4.4 Conclusions

Accurate estimation of the intrinsic transport properties of membranes, including diffusivity, solubility, and permeability, is crucial for designing and optimizing various industrial processes involving gas separation. The time-lag method, a dynamic technique, can yield these three transport parameters from a single gas permeation experiment. However, it is important to consider all the components of a gas permeation cell to ascertain whether the estimated diffusivity and permeability require correction to reflect the membrane's actual transport properties.

In this study, we explored the impact of the porous support located at the membrane's downstream surface. Our findings suggest that the porous support plate can affect the estimation of both the membrane's diffusivity and permeability. Using the time-lag method, the membrane diffusivity is evaluated accurately for very low and very high values of the normalized pore diameter (D_H/L_z). Between the two asymptotic values, the relative diffusivity follows an inverted Gaussian curve with an amplitude inversely proportional to the porosity of the support plate. The relative permeability follows an inverted logistic function going from unity to ε as D_H/L_z increases. Therefore, careful design of the membrane permeation cell and a thorough understanding of these effects are vital for an efficient gas membrane testing system.

Our results demonstrate that using a porous support plate with an average pore diameter significantly smaller than the membrane thickness, coupled with reasonable porosity, enables the accurate determination of membrane transport properties. If this is not the case, it is possible to use the results of this investigation to correct the effective values of the transport properties to estimate their intrinsic values. Is it possible that some of the variations in the estimation of the permeability observed in the multi-lab study on the pure-gas permeation of commercial polysulfone membranes could be attributed to different porous support plates in the gas permeation cell used [29]?

Nomenclature

c Concentration within the membrane at the gas-membrane interface (mol/m^3)

C Concentration in the surrounding gas at the gas-membrane interface (mol/m^3)

D Diffusivity (m^2/s)

D_H Average pore diameter of the porous plate (mm)

J Permeation flux (mol/m^2s)

L Dimensions of the 3D (x, y, z) repeatable unit as per Fig. 2 (m)

NI Number of mesh points in the x-direction

NJ Number of mesh points in the y-direction

NK Number of mesh points in the z-direction

N_R Restriction number

p Pressure (kPa)

P Permeability (m^2/s)

S Solubility ((mol/m^3)/ (mol/m^3))

t Time (s)

x x-direction coordinate (m)

y y-direction coordinate (m)

z z-direction coordinate (m)

Greek symbols

ε Porosity of the support porous disc

θ Time lag (s)

Subscripts

Eff Effective

i Mesh point index in the *x*-direction

j Mesh point index in the *y*-direction

k Mesh point index in the *z*-direction

x *x* direction

y *y* direction

z *z* direction

References

[1] M. Lomax, Permeation of gases and vapours through polymer films and thin sheet - Part I, Polym. Test. 1 (1980) 105–147.

[2] J.K. Jung, Review of Developed Methods for Measuring Gas Uptake and Diffusivity in Polymers Enriched by Pure Gas under High Pressure, Polymers (Basel). 16 (2024). https://doi.org/10.3390/polym16050723.

[3] M. Sadrzadeh, M. Rezakazemi, T. Mohammadi, Fundamentals and Measurement Techniques for Gas Transport in Polymers, Elsevier Inc., 2017. https://doi.org/10.1016/B978-0-12-809884-4.00019-7.

[4] R.M. Barrer, E.K. Rideal, Permeation, diffusion and solution of gases in organic polymers, Trans. Faraday Soc. 35 (1939) 628–643. https://doi.org/10.1039/tf9393500628.

[5] V. Stannett, The transport of gases in synthetic polymeric membranes - An historic perspective, J. Memb. Sci. 3 (1978) 97–115. https://doi.org/10.1016/S0376-7388(00)83016-1.

[6] Z.J. Grzywna, P. Borys, B. Kruczek, On the well-posed problems for diffusion with time dependent boundary condition, Sep. Sci. Technol. 46 (2011). https://doi.org/10.1080/01496395.2011.606864.

[7] P. Taveira, A. Mendes, C. Costa, On the determination of diffusivity and sorption coefficients using different time-lag models, J. Memb. Sci. 221 (2003) 123–133. https://doi.org/10.1016/S0376-7388(03)00252-7.

[8] N. Al-Qasas, J. Thibault, B. Kruczek, The effect of the downstream pressure accumulation on the time-lag accuracy for membranes with non-linear isotherms, J. Memb. Sci. 511 (2016). https://doi.org/10.1016/j.memsci.2016.03.047.

[9] H. Wu, B. Kruczek, J. Thibault, Impact of measuring devices and data analysis on the determination of gas membrane properties, J. Membr. Sci. Res. 4 (2018) 4–14. https://doi.org/10.22079/jmsr.2017.63433.1136.

[10] D.R. Paul, Effect of Immobilizing Adsorption on the Diffusion Time Lag, J Polym Sci Part A-2 Polym Phys. 7 (1969) 1811–1818. https://doi.org/10.1002/pol.1969.160071015.

[11] D.R. Paul, W.J. Koros, Effect of Partially Immobilizing Sorption on Permeability and the Diffusion Time Lag., J Polym Sci Part A-2 Polym Phys. 14 (1976) 675–685. https://doi.org/10.1002/pol.1976.180140409.

[12] H.L. Frisch, The time lag in diffusion, J. Phys. Chem. 61 (1957) 93–95. https://doi.org/10.1021/j150547a018.

[13] J.H. Petropoulos, P.P. Roussis, Study of "non-Fickian" diffusion anomalies through time lags. I. Some time-dependent anomalies, J. Chem. Phys. 47 (1967) 1491–1496. https://doi.org/10.1063/1.1712107.

[14] R.A. Siegel, A laplace transform technique for calculating diffusion time lags, J. Memb. Sci. 26 (1986) 251–262. https://doi.org/10.1016/S0376-7388(00)82110-9.

[15] H. Wu, J. Thibault, B. Kruczek, The validity of the time-lag method for the characterization of mixed-matrix membranes, J. Memb. Sci. 618 (2021) 118715. https://doi.org/10.1016/j.memsci.2020.118715.

[16] E. Favre, N. Morliere, D. Roizard, Experimental evidence and implications of an imperfect upstream pressure step for the time-lag technique, J. Memb. Sci. 207 (2002) 59–72. https://doi.org/10.1016/S0376-7388(02)00039-X.

[17] S. Lashkari, B. Kruczek, Effect of resistance to gas accumulation in multi-tank receivers on membrane characterization by the time lag method. Analytical approach for optimization of the receiver, J. Memb. Sci. 360 (2010). https://doi.org/10.1016/j.memsci.2010.05.043.

[18] P.J. Leszczynski, S. Lashkari, B. Kruczek, Revisiting the Effect of the Resistance to Gas Accumulation in Constant Volume Systems on the Membrane Time Lag, Membranes (Basel). 14 (2024). https://doi.org/10.3390/membranes14080167.

[19] B. Kruczek, H.L. Frisch, R. Chapanian, Analytical solution for the effective time lag of a membrane in a permeate tube collector in which Knudsen flow regime exists, J. Memb. Sci. 256 (2005). https://doi.org/10.1016/j.memsci.2005.02.006.

[20] B. Kruczek, F. Shemshaki, S. Lashkari, R. Chapanian, H.L. Frisch, Effect of a resistance-free tank on the resistance to gas transport in high vacuum tube, J. Memb. Sci. 280 (2006). https://doi.org/10.1016/j.memsci.2006.01.001.

[21] S. Lashkari, B. Kruczek, H.L. Frisch, General solution for the time lag of a single-tank receiver in the Knudsen flow regime and its implications for the receiver's configuration, J. Memb. Sci. 283 (2006). https://doi.org/10.1016/j.memsci.2006.06.015.

[22] S.C. Fraga, M. Monteleone, M. Lanč, E. Esposito, A. Fuoco, L. Giorno, K. Pilnáček, K. Friess, M. Carta, N.B. McKeown, P. Izák, Z. Petrusová, J.G. Crespo, C. Brazinha, J.C. Jansen, A novel time lag method for the analysis of mixed gas diffusion in polymeric membranes by online mass spectrometry: Method development and validation, J. Memb. Sci. 561 (2018) 39–58.

https://doi.org/10.1016/j.memsci.2018.04.029.

[23] G.Z. Ramon, M.C.Y. Wong, E.M.V. Hoek, Transport through composite membrane, Part 1: Is there an optimal support membrane?, J. Memb. Sci. 415–416 (2012) 298–305. https://doi.org/10.1016/j.memsci.2012.05.013.

[24] L. Zhu, W. Jia, M. Kattula, K. Ponnuru, E.P. Furlani, H. Lin, Effect of porous supports on the permeance of thin film composite membranes: Part I. Track-etched polycarbonate supports, J. Memb. Sci. 514 (2016) 684–695. https://doi.org/10.1016/j.memsci.2015.11.043.

[25] H.R. Afshoun, M.P. Chenar, A.F. Ismail, T. Matsuura, Effect of support layer on gas permeation properties of composite polymeric membranes, Korean J. Chem. Eng. 34 (2017) 3178–3184. https://doi.org/10.1007/s11814-017-0215-x.

[26] D.P. Lonsdale, H.K.; Riley, C.R; Lyons, C.R.; Carosella, Transport in Composite Reverse Osmosis Membranes, in: M. Bier (Ed.), Membr. Process. Ind. Biomed., 1971: pp. 101–122. https://doi.org/org/10.1007/978-1-4684-1911-5.

[27] A.M.J. Davis, C.R. Ethier, Transport through materials bounded by porous surfaces, Chem. Eng. Sci. 48 (1993) 1655–1663. https://doi.org/10.1016/0009-2509(93)80125-A.

[28] J.G. Wijmans, P. Hao, Influence of the porous support on diffusion in composite membranes, J. Memb. Sci. 494 (2015) 78–85. https://doi.org/10.1016/j.memsci.2015.07.047.

[29] K.M. Rodriguez, W.N. Wu, T. Alebrahim, Y. Cao, B.D. Freeman, D. Harrigan, M. Jhalaria, A. Kratochvil, S. Kumar, W.H. Lee, Y.M. Lee, H. Lin, J.M. Richardson, Q. Song, B. Sundell, R.Thür, I. Vankelecom, A. Wang, L. Wang, C. Wiscount, Z.P. Smith, Multi-lab study on the pure-gas permeation of commercial polysulfone (PSf) membranes: Measurement standards and best practices, J. Memb. Sci. 659 (2022) 120746. https://doi.org/10.1016/j.memsci.2022.120746

Chapter 5

Effect of feed pressure on transport properties of the membrane via the time-lag method: the case of nitrogen in PDMS

Zheng Cao, Hongchen Wang, Jules Thibault, Boguslaw Kruczek*

Abstract

The time-lag method is commonly used to simultaneously determine the permeability (*P*), diffusivity (*D*), and solubility (*S*) coefficients in a single gas permeation experiment. In the conventional membrane characterization process, these three parameters are typically assumed to remain constant as the pressure applied to the membrane increases. However, possible membrane compaction resulting from the applied pressure may alter the effective gas transport properties. This paper investigates the impact of feed pressure on changes in permeability, diffusivity, and solubility of nitrogen in PDMS membranes of varying thicknesses. We employed a newly designed constant-volume system that enables simultaneous monitoring of the upstream pressure decay and downstream pressure rise during time-lag experiments, allowing for the direct evaluation of *P*, *D*, and *S* under different pressures. The experimental findings revealed that the transport properties of the PDMS membrane decrease as the feed pressure increases. This is the first time the effect of feed pressure has been demonstrated and quantified on diffusivity and solubility.

Keywords: Membrane characterization, Constant volume systems, Time-lag method, PDMS membrane.

Graphical abstract:

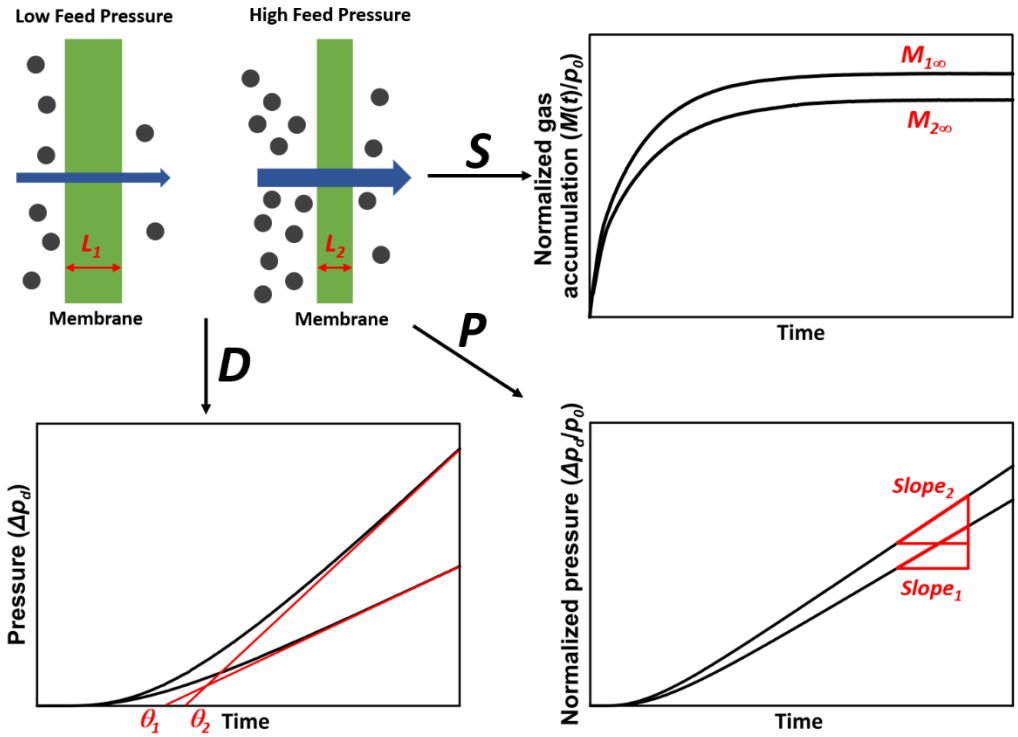

Publication status: Submitted to Journal Membrane of Science

***Corresponding author**

5.1 Introduction

There have been unprecedented advancements in membrane technology for gas separation, driven by the development of novel materials and innovative fabrication techniques. Consequently, efficient and reliable characterization methods are becoming increasingly critical for evaluating the potential of new membrane materials and guiding their practical implementation [1,2]. The standard characterization of membrane materials involves determining the permeability (P), diffusivity (D), and solubility (S) of different gases in a homogeneous membrane (film) fabricated from the tested material. According to the solution-diffusion model, these three transport coefficients are correlated through Eq. (5.1) [3]:

$$P = DS \tag{5.1}$$

The ratio of the permeability coefficients of two different gases is known as the ideal selectivity or permselectivity. Comparing the combination of permeability and permselectivity to the upper-bound line for a given pair of gases is the standard way to evaluate the separation potential of membrane materials [4]. Furthermore, the ideal selectivity is the product of the diffusivity and solubility selectivities, which are the ratios of the corresponding diffusivity and solubility coefficients [3].

A century-old time-lag method enables the determination of P, D, and S from a single dynamic gas permeation experiment performed in a constant-volume (CV) system [5,6].More specifically, the experiment is initiated by a step pressure increase at the feed side of an initially degassed, homogeneous membrane, and the resulting pressure rise at the permeate side is monitored in real time. In a properly designed experiment, the pressure rise eventually becomes a linear function of time with the slope proportional to P. Also, the extrapolation of the linear portion of the pressure rise to the time axis yields a time lag (θ_d), which is related to D by:

$$D = \frac{L^2}{6\theta_d} \tag{5.2}$$

where L is the membrane thickness. Knowing P and D, according to Eq. (5.1), S is calculated as the ratio of P and D.

The validity of Eq. (5.2) and, therefore, the time lag method relies on several key assumptions. One is that P, D, and S coefficients are independent of pressure, or more accurately, of the permeant concentration within the membrane. This assumption generally holds for rubbery membranes operated under relatively low-pressure conditions. Additionally, Eq. (5.2) is based on idealized boundary conditions, where the permeant concentration remains constant at both the feed and permeate interfaces of the membrane, specifically with zero concentration on the permeate side. In reality, however, as the gas enters the membrane, the feed pressure and the corresponding concentration gradually decrease. Conversely, at the permeate interface, the concentration increases over time. Nonetheless, in properly designed time-lag experiments, the error introduced by deviations from the ideal boundary conditions is usually negligible [7,8].

The time-lag method assumes that the membrane is the only resistance to gas transport during the permeation experiment. The implications of this unwritten assumption are a step change in pressure to initiate the time-lag experiment, and that pressure downstream from the membrane is only a function of time, not position. Indeed, unless the time lag experiment is performed using a vapour rather than a gas, the pressure increase to initiate the experiments should occur in a step-wise manner [9]. On the other hand, because the gas accumulates at a high vacuum on the permeate side, the transport downstream from the membrane, i.e., gas accumulation, is governed by Knudsen diffusion, with the corresponding diffusivity directly proportional to the internal tube diameter [10]. In principle, resistance to gas accumulation is inversely proportional to the Knudsen diffusion coefficient. However, when an accumulation tank, effectively resistance-free due to its relatively large internal diameter, is connected to the membrane cell via one or more tubes, this configuration can significantly underestimate the measured time lag. As a result, it may lead to an overestimation of the gas diffusivity in the tested membrane [11–13]. Nevertheless, the impact of gas resistance on the measured time lag can be minimized by using well-designed downstream receivers in the CV system [14].

Additionally, a porous plate is positioned downstream of the membrane to provide mechanical support and help it withstand the pressure gradient during gas permeation tests. While the resistance to gas transport through the porous support is negligible, its presence reduces the effective area available for gas transport at the membrane-porous support interface. This reduction can lead to an underestimation of the experimentally measured P [15,16]. Recently, Cao et al. demonstrated that the membrane thickness, in conjunction with the pore size and porosity of the porous disc, can significantly influence not only the estimation of permeability but also the diffusivity of the membrane using the time-lag method [17]. Interestingly, the observed effect was not dependent on the intrinsic diffusivity of the membrane. The relative diffusivity and relative permeability were strictly a function of the porosity of the porous disc and the ratio of the pore diameter to the membrane thickness.

As previously mentioned, P, D, and S are independent of pressure in the case of rubbery polymers. However, the time-lag method is commonly used for the

characterization of more complex membrane materials, including glassy polymers, polymers with intrinsic microporosity, mixed matrix membranes, and inorganic membranes. In this case, the gas transport properties determined using the time lag method are the effective rather than intrinsic values [18,19]. For example, for glassy polymers, gas sorption follows a dual-mode model. As a result, the effective *S*, *P*, and *D* decrease with feed pressure [20]. However, even for rubbery polymers, gas transport properties may depend on feed pressure.

Stern et al. reported the results of comprehensive studies involving polyethylene (rubbery) dense membranes using a variety of gases ranging from He and N_2 to CO_2 and C_2H_4 at feed pressures up to 60 atmospheres and temperatures ranging from -10 °C to 60 °C. For CO_2 and C_2H_4, which behave as condensable vapours, particularly at high pressures and low temperatures, an increase in permeability with feed pressure, attributed to an increase in solubility of condensable gases with pressure, was observed. On the other hand, for "permanent" gases such as He and N_2, for which permeability was expected to be independent of pressure, the permeability decreased with feed pressure [21]. A similar decrease in permeability of noncondensable gases in a dense poly(dimethylsiloxane) (PDMS) membrane was reported by Merkel et al. [22]. In both cases, the decrease in permeability was relatively small. On the other hand, in the more recent study involving He, N_2, O_2, and PDMS, as the feed pressure increased from 1.3 to 11.8 atm, a 40% to 60% reduction in permeability was observed, depending on the specific gas [23]. This was significantly greater than that reported in Refs. [22,24]

A possible reason for the decrease in permeability with pressure might be compaction of a filter paper, often used between the tested membrane and porous metal support [24]. This argument is supported by the studies of Reinsch et al., who, using an ultrasonic time-domain reflectometry (TDR) technique, observed a decrease in the thickness of asymmetric cellulose acetate membranes in real-time during actual gas separation tests [25]. The observed membrane compaction was attributed to the compaction of the porous support layer under high-pressure conditions. However, the TDR technique cannot differentiate between the compaction occurring in the selective (dense) layer and that in the porous sublayer.

On the other hand, in their respective studies, Merkel et al. [22] and Villaluenga et al [21] attributed a decrease in permeability with pressure to the susceptibility of relatively flexible polymer chains of PDMS to compression under external pressure. Even a slight compression of the polymer matrix would reduce the free volume available for penetrant transport, thereby reducing penetrant diffusion coefficients [26].

PDMS is an example of a highly permeable rubbery polymer because of its high fractional free volume of approximately 0.2 [27,28]. At the same time, PDMS has a distinctive combination of a low Young's modulus (~2 MPa), which allows it to be easily bent and stretched, and a high bulk modulus (~2 GPa), which implies it should maintain its volume under pressure [29,30]. In other words, the free volume of PDMS should not decrease, at least not irreversibly, under low pressures.

This article attempts to answer the question about the possible decrease in free volume of dense PDMS membranes during their testing under different feed pressures. Most of the studies in the literature utilized high feed pressures, which make membrane compaction more likely to occur. However, in this work, we focus on different feed pressures, but lower than 2000 Torr, which would typically be employed to perform membrane characterization using the time-lag method. In addition, previous studies on the effect of feed pressures have focused primarily on P, which is the product of D and S. Therefore, the second question is: if P indeed decreases with pressure, is it because of a decrease in D or S, or both D and S? To avoid possible ambiguity associated with condensable gases, we used N_2 which the perneament gas at ambient temperature and relatively low pressures. The time-lag experiments were performed in a novel CV system that enabled simultaneous monitoring of the pressure rise on the downstream side and the pressure decay on the upstream side of the membrane [23]. The latter feature provided additional methods of determining P, D, and S from the same time-lag experiment [31]. In particular, the simultaneous monitoring of the pressure rise and pressure decay allowed for the direct determination of S, rather than relying only on Eq. (5.1) using the experimental P and D. By investigating the effect of the feed pressure on the transport properties of permanent gas such as N_2 in rubbery PDMS membrane, this article contributes to a fundamental question: *what do we measure in the time-lag method?* As

such, it is a continuation of our previous papers on the effect of the resistance to gas accumulation downstream from the membrane [10–12] and the effect of the porous plate supporting the membrane [17].

5.2 Materials and Methods

5.2.1 Materials

PDMS membranes (SSPM823-010-12"-SSP-M823-Platinum Cured Silicone) of three different thicknesses (0.017", 0.025" and 0.040") were purchased from Interstate Specialty Products (Sutton, MA). We also measured thickness independently using the micrometre calliper, and corresponding values were 0.017" ± 0.002" (0.432 mm ± 0.051 mm), 0.024" ± 0.002" (0.610 mm ± 0.051 mm) and 0.04" ± 0.002" (1.016 mm ± 0.051 mm). Therefore, the manufacturer's and the measured values were in good agreement. In subsequent analysis, we used the membrane thicknesses measured in the lab. All experiments were performed using 99.99% pure N_2 from the compressed gas cylinder (Linde Canada Inc., Ottawa, ON).

5.2.2 Mechanical measurements

Compression of PDMS membranes under external pressure difference was examined using a tensile mechanical tester (TestResources 140 series, Minnesota, USA). The system, shown schematically in Figure 5.1, was equipped with a 5 mm diameter flat compression pin connected to a load cell for force measurement (maximum load of 5 kN). Compression tests were conducted on free-standing membrane samples with a diameter of 5 mm, matching the diameter of the compression pin. Displacement was recorded using a high-resolution linear variable differential transformer (LVDT) with a measurement range of ±1270 μm and a linearity of ±3 μm. The tests were conducted under a peak load of 150 N at a constant displacement rate of 0.1 mm/min.

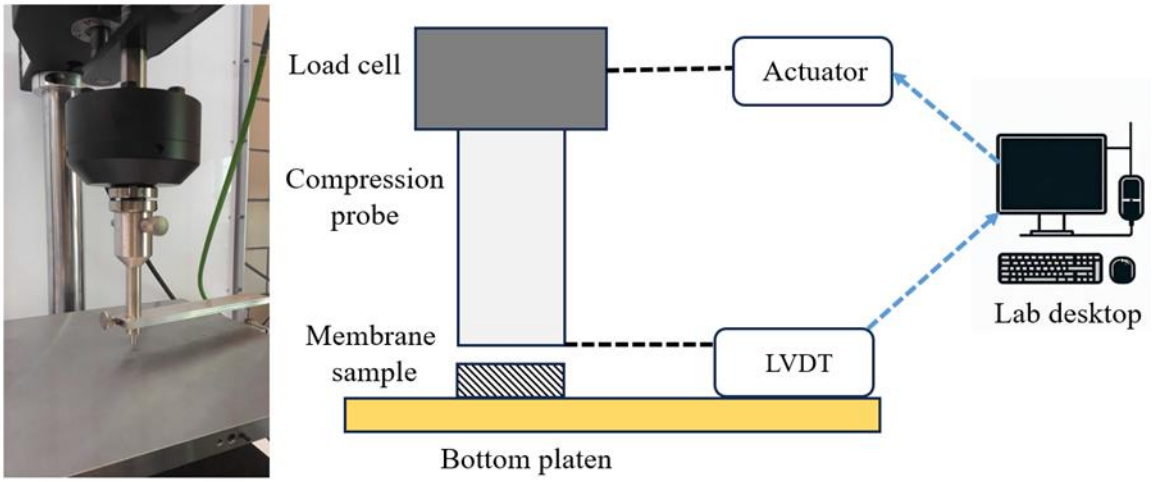

Figure 5.1 A schematic diagram of the tensile testing machine.

5.2.3 CV system apparatus.

Figure 5.2 presents the schematic diagram of the CV system. The system consists of three parts: the membrane cell, the downstream receiver, and the downstream receiver. A detailed description of the system's components and operation can be found in Leszczynski et al. [23].

The gas permeation cell used in this study is schematically shown in Figure 5.3A. To preserve the membrane's physical integrity under an applied pressure differential, a porous support plate is installed at the downstream side. Figure 5.3B details the internal assembly, where the PDMS membrane is fixed to the bottom plate via a metal ledge and remains in full contact with the porous support. The system is sealed from the atmosphere by a rubber ring compressed at the periphery between the cell's upper and lower sections. The porous support has a pore size, D_H = 40 μm, a porosity, ε = 75%, and the total active membrane area A = 0.00132 m². Therefore, even for the thinnest membrane with the thickness, L = 432 μm, $D_H/L < 0.1$, and the effect of porous support on the gas transport properties of the PDMS membranes by the time-lag method, should be negligible [17].

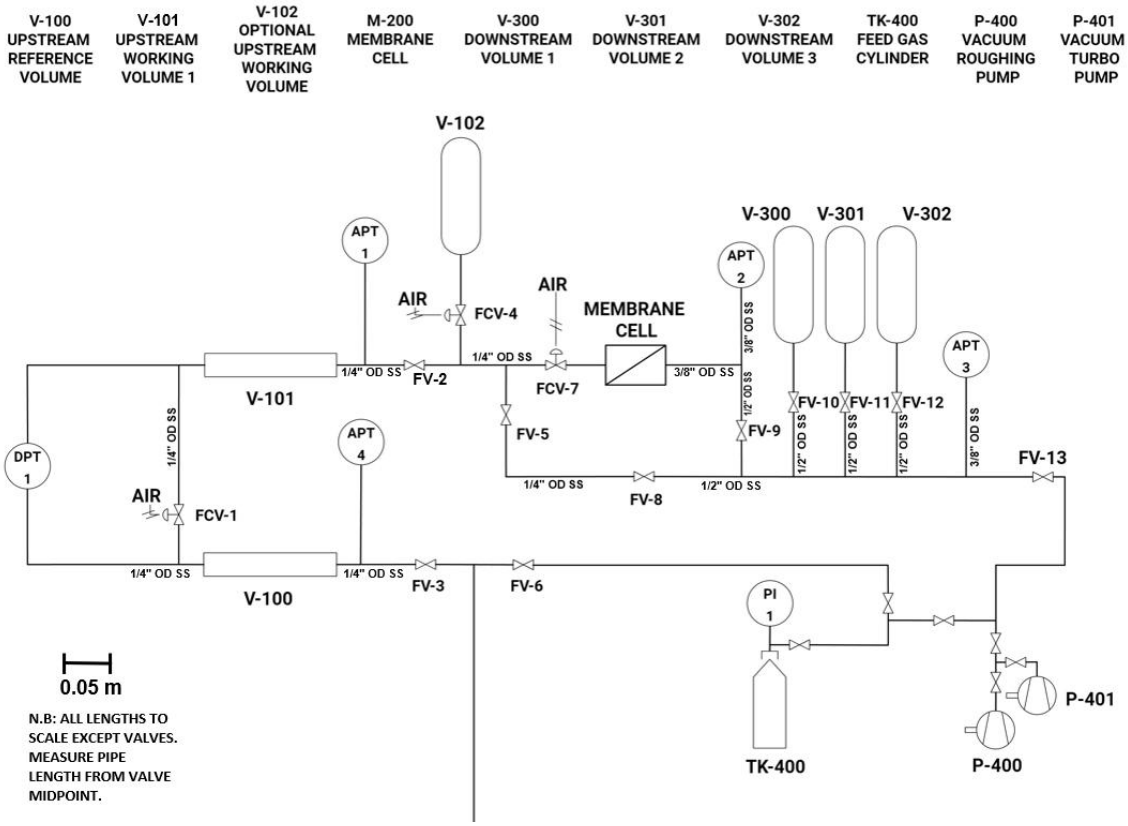

Figure 5.2 A schematic diagram (to the scale) of the CV system for simultaneous monitoring of pressure rise and pressure decay during time-lag experiments [23].

The downstream receiver, i.e., the volume between the membrane cell and the valves FV-8 and FV-13, could be varied by including any combination of the accumulation tanks V-300, V-301, and V-302. However, to minimize the effects of the resistance to gas accumulation, all experiments were performed without any of the accumulation tanks, so that the volume of the downstream receiver, 81 cm^3, consisted solely of the volume of the tubing. It is essential to note that all tubing downstream was either 3/8-inch (9.5 mm) or 1/2-inch (12.7 mm) stainless steel tubes. The absence of gas accumulation resistance was confirmed by statistically identical readings of two pressure transducers, APT 1 and APT 3 (CCR Process Products, Kanata, Ontario, Canada, MKS627F11TBC1B), which monitored the pressure rise. These transducers featured a full-scale resolution of 10^{-5}, an accuracy of 0.12% of reading, and a measurement range of 0 to 10 Torr.

The upstream receiver, i.e., the volume between the membrane cell and the valves FV-5 and FV-6, was divided into the working volume V-101 (89 cm^3 between FCV-7, FCV-4, and FCV-1) and the reference volume V-100 (96 cm^3 between FCV-1 and FV-6). The pressure decay due to gas permeation into the membrane was measured using a capacitance-based differential pressure transducer DPT1 (CCR Process Products, Kanata, Ontario, Canada, MKS698A ±1 Torr, 10^{-6} full-scale resolution, accuracy: 0.05% of reading), by comparing a variable pressure in V-101 with a constant pressure in V-100. The working and reference volumes were also equipped with identical absolute pressure transducers, APT1 and APT4 (CCR Process Products, Kanata, Ontario, Canada, MKS627F13TBC1B, 10^{-5} full-scale resolution, accuracy: 0.12% of reading, range: 0 to 2000 Torr), to confirm the pressure decay measurements made by the DPT1.

The entire CV system, except a rotary vacuum pump, P-400 (CANVACTECH, Ottawa, Ontario, Canada, Edwards RV3, A65201906, ultimate pressure: $1.5x10^{-3}$ Torr), a turbomolecular pump P-401 (Edwards Vacuum LLC Sanborn, New York, USA, Edwards TS85D1002, ultimate pressure: < $3.75x10^{-10}$ Torr) and a gas cylinder TK-400, was enclosed in a temperature-controlled chamber with an operational range between 273 K and 313 K, but experiments were performed at 303 K.

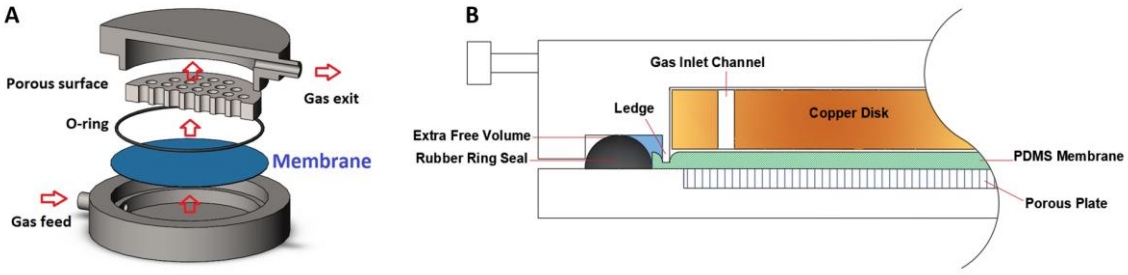

Figure 5.3 Schematic representation of the gas permeation cell for time-lag experiments. (A) The exploded view of the permeation cell schematic diagram [17]. (B) Internal structure diagram of the cell.

5.2.4 Experimental protocol

The details of the experimental protocol are described in Refs. [23,31]. In summary, after installing a membrane in the cell, both the upstream and downstream receivers were thoroughly evacuated using a P-400 pump. This evacuation lasted at least 48 hours whenever the membrane cell was opened, and a minimum of 6 hours between the tests using the same membrane. During evacuation, leak tests were periodically conducted in various sections of the system to ensure complete degassing. The final leak rates were consistently at or below 10^{-7} torr/s, which were several orders of magnitude lower than the pressure decay or rise observed during the actual experiments. Before the experiment, with FCV-7 closed, the pressures in the working and reference volumes were set to the desired value. The experiment was initiated by opening FCV-7 while the working and reference volumes were connected, i.e., FCV-1 was open. Although the dead volume upstream (~4 cm^3 between the membrane cell and FCV-7) was small, the resulting expansion in the upstream pressure for any feed pressure exceeded 1 Torr, i.e., the full range of DPT1. With FCV-1 open, the expansion in the working and reference volumes was the same, so that DPT-1 read zero. In every experiment, FCV-1 was closed after 5 seconds from opening FCV-7. In other words, the progress of pressure decay started to be monitored 5 seconds after the initiation of the experiment. Remote operation of FCV1 and FCV7 from a computer ensured excellent repeatability of the experiments.

For each membrane thickness, at least three different coupons were tested. Moreover, for each coupon at a given feed pressure, at least one repeated experiment was performed. The membranes were tested at four different feed pressures: 850 Torr, 1150 Torr, 1550 Torr, and 1850 Torr. The downstream pressure rise data did not require any processing; however, the upstream pressure decay data required two corrections described in Ref. [23].

5.2.5 Analysis of the experimental results

The simultaneous monitoring of both pressure rise and pressure decay during the time-lag experiments enabled multiple methods for determining P, D, and S from a single experimental run. The mathematical basis of the equations presented in this section is described elsewhere [23].

Method 1 is the conventional time-lag method, and the corresponding variables P, D, and S will be denoted using subscript 1. In this method, P_1 is evaluated from the steady-state rate of the pressure rise $\left(dp_d/dt\right)_s$:

$$P_1 = \frac{V_d L}{p_0 ART} \times \left(\frac{dp_d}{dt}\right)_s \tag{5.3}$$

where V_d is the volume of the downstream receiver (i.e., 81 cm^3), p_0 is the feed pressure after the initiation of the experiment, A is the membrane area, R is the universal gas constant, and T is the absolute temperature. The diffusivity D_1 is evaluated using Eq. (2) based on the downstream time lag (θ_d). The solubility S_1 is obtained from the ratio of P_1 and D_1.

Method 2, for which the transport coefficients are assigned the subscript 2, is a "mirror" image of Method 1, based on the pressure decay in the upstream receiver. Consequently,

$$P_2 = -\frac{V_u L}{p_0 ART} \times \left(\frac{dp_u}{dt}\right)_s \tag{5.4}$$

where V_u is the volume of the upstream receiver, which is the sum of the working volume and the dead volume (i.e., 89 cm^3 + 4 cm^3 = 93 cm^3), and $\left(dp_u/dt\right)_s$ is the linear, i.e., the steady-state portion of the pressure decay. The diffusivity D_2 is determined from the corresponding upstream time lag (θ_u) [32]:

$$D_2 = -\frac{L^2}{3\theta_u} \tag{5.5}$$

Finally, the solubility S_2 is the ratio of P_2 and D_2.

Method 3, referred to as the two-slope method, is also based solely on the upstream pressure decay. At the early stages of the experiment, specifically before the gas emerges from the membrane to the downstream receiver, the membrane behaves as a semi-infinite solid. Consequently, the pressure decay is given by [33]:

$$\frac{dp_u}{dt} = -\frac{2p_0 SRTA\sqrt{D}}{V_u\sqrt{\pi}}\sqrt{t} \tag{5.6}$$

Therefore, the pressure decay is directly proportional to the square root of time, with the slope (Σ_t) given by:

$$\Sigma_t = -\frac{2p_0 SRTA\sqrt{D}}{V_u\sqrt{\pi}} \tag{5.7}$$

According to Eq. (5.4), the steady-state slope in the upstream receiver is given by:

$$\left(\frac{dp_u}{dt}\right)_s = \Sigma_s = -\frac{p_0 PART}{V_u L} \tag{5.8}$$

Consequently, substituting Eq. (5.1) into Eq. (5.8), the diffusivity in Method 3, D_3, can be evaluated by rearranging the ratio of Eq. (5.7) and Eq. (5.8):

$$D_3 = \frac{4}{\pi}\left(L\frac{\Sigma_s}{\Sigma_t}\right)^2 \tag{5.9}$$

The permeability in Method 3 is the same as that in Method 2, because it is evaluated from Equation (5.4), i.e., $P_3 = P_2$. The corresponding solubility is the ratio of P_2 and D_3.

Method 4 relies on both the pressure rise and the pressure decay. Recognizing that the difference between the rate of gas entering and leaving the membrane represents gas accumulation, it can be shown that the time-dependent accumulation, $M(t)$, is given by:

$$M(t) = 2\frac{Ap_0 SL}{\pi^2}\left\{\sum_{n=1}^{\infty}\left((-1)^n - 1\right)\frac{1}{n^2}\left(\exp\left(-\frac{Dn^2\pi^2 t}{L^2}\right) - 1\right)\right\} \tag{5.10}$$

It can also be shown that as $t \to \infty$, i.e. at steady state, $M(t)$ becomes a constant value M_∞ given by:

$$M_\infty = \frac{Ap_0 SL}{2} \tag{5.11}$$

Therefore, Method 4 allows for the direct determination of solubility, S_4, based on the experimental M_∞:

$$S_4 = \frac{2M_\infty}{p_0 LA} \tag{5.12}$$

Furthermore, it can be shown that the time-dependent relative gas accumulation $M(t)/M_\infty$, is a function of diffusivity, which we refer to as D_4:

$$1 - \frac{M(t)}{M_\infty} = \exp\left(-\frac{D_4 \pi^2 t}{L^2}\right) \tag{5.13}$$

The above equation can be linearized by taking the logarithm of both sides, and the resulting slope is directly proportional to D_4. Therefore,

$$D_4 = \frac{-L^2}{\pi^2 t} \ln\left(1 - \frac{M(t)}{M_\infty}\right) \tag{5.14}$$

Knowing S_4 and D_4, the permeability in Method 4, as per Eq. (5.1), is the product of S_4 and D_4.

5.3 Results

5.3.1 Effect of pressure on the membrane thickness

Figure 5.4 presents the stress-strain curves for the three thicknesses of PDMS membranes used in this work. The stress-strain curves were derived from the raw tensile test data by converting the measured force-displacement values (force/cross-sectional area vs. displacement/initial thickness). Figure 5.4A shows the curves for the entire range of tensile load of the instrument (0-8000 kPa), which exceeds the standard pressure range for gas separation processes. For example, for O_2/N_2 separation, the typical range of feed pressures to which membranes are exposed is 100 kPa to 1500 kPa (700–10000 Torr) [34]. However, in this work, the highest pressure at which the time-lag tests were performed was 1850 Torr (246 kPa). Therefore, Figure 5.4B focuses on the results within the pressure range of 0 to 600 kPa. Within this range, a linear relationship between stress and strain is evident. However, the slope of this relationship varies with membrane thickness: the thicker the membranes, the lower the slope. This indicates that thicker membranes are

more susceptible to compaction under a given load (i.e., pressure). For example, at the highest feed pressure, corresponding to a stress of 246 kPa, the strain (defined as the percentage reduction in thickness) is approximately 3% for the thinnest membrane (0.432 mm). In contrast, the thickest membrane (1.016 mm) shows a strain of nearly 5%.

Using the linear regressions shown in Figure 5.4B, Table 5.1 summarizes the absolute thicknesses of the membranes at the loads corresponding to the feed pressures used in the time-lag experiments. The observed compactions vary from 6 μm for the thinnest membrane at the lowest feed pressure to 35 μm for the thickest membrane at the highest feed pressure. It is important to emphasize that, unlike a tensile testing machine (Fig. 1), in which the PDMS samples could expand radially under load (to retain their total volume), in the membrane cell, the radial expansion is limited by the metal seal. Additionally, the pores of the support plate are likely too small to accommodate the PDMS membrane, particularly given the highest feed pressure of only 1850 Torr. Therefore, the exact thickness of PDMS membranes, which is required for the calculation of *P*, *D* and *S,* is unknown. Nevertheless, it is safe to assume that the actual membrane thickness during gas permeation tests should be between the nominal value (i.e., under zero pressure) and the value corresponding to the strain under a given load (feed pressure).

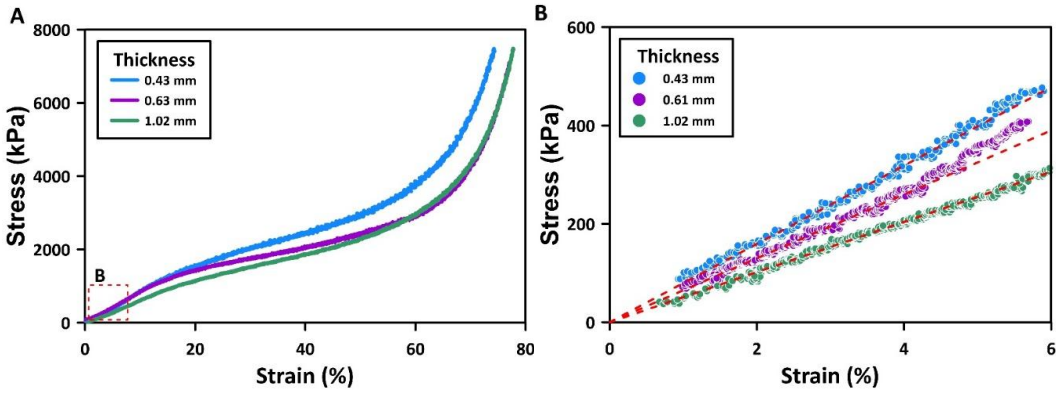

Figure 5.4 The stress-strain curves of the PDMS membranes tested in this work. (A) The entire stress range: 0 to 8000 kPa. (B) The focused stress range: 0 to 600 kPa. The dashed lines indicate the linear regressions for different membrane thicknesses in the focused range.

Table 5.1 The summary of the estimated thicknesses of the PDMS membranes at the loads corresponding to the feed pressures used in the time-lag experiments, based on Figure 5.4B.

Applied stress	Feed pressure	Minimum thickness of PDMS membrane [mm]		
kPa	Torr	0.017 inch	0.024 inch	0.040 inch
0	0	0.432	0.610	1.016
113	850	0.426	0.599	0.995
153	1150	0.424	0.595	0.988
206	1550	0.421	0.591	0.978
246	1850	0.418	0.587	0.971

5.3.2 Effect of pressure on *P*, *D*, and *S*

To illustrate the effect of feed pressure (p_0) on the transport properties of N_2 in PDMS, we will consider the results from one example of the membrane tested at four different pressures and analyzed using the four methods described in Section 5.2.5. In principle, regardless of the method, the effect should be the same. Nevertheless, the applications of four different methods, enabled by the simultaneous monitoring of pressure rise and pressure decay, increase confidence in the reported transport properties.

Figure 5.5 presents the downstream pressure rise (i.e., the conventional time-lag experiments) in the experiments using a 0.024-inch PDMS membrane, performed at feed pressures of 850, 1150, 1550, and 1850 Torr. As expected, the slope of the steady-state portion of the pressure rise curves increases with the feed pressure. It can also be observed that the resulting time lag increases with the feed pressure. This effect is more clearly visible in the inset of Figure 5.5, which focuses on the time axis between 45 and 55 seconds. The results from Figure 5.5 are summarized in Table 5.2, in which D, P, and S, i.e., D_1, P_1, and S_1, are evaluated using Eqs. (2), (3), and (1), respectively. The calculated diffusivity, permeability, and thus solubility depend on the membrane thickness used. For each transport coefficient, two extreme values are provided: one based on the pressure-dependent values listed in Table 5.1, i.e., minimum thickness (Min. L), and the other based on the nominal thickness (Nom. L) of 0.610 mm (i.e., the maximum thickness).

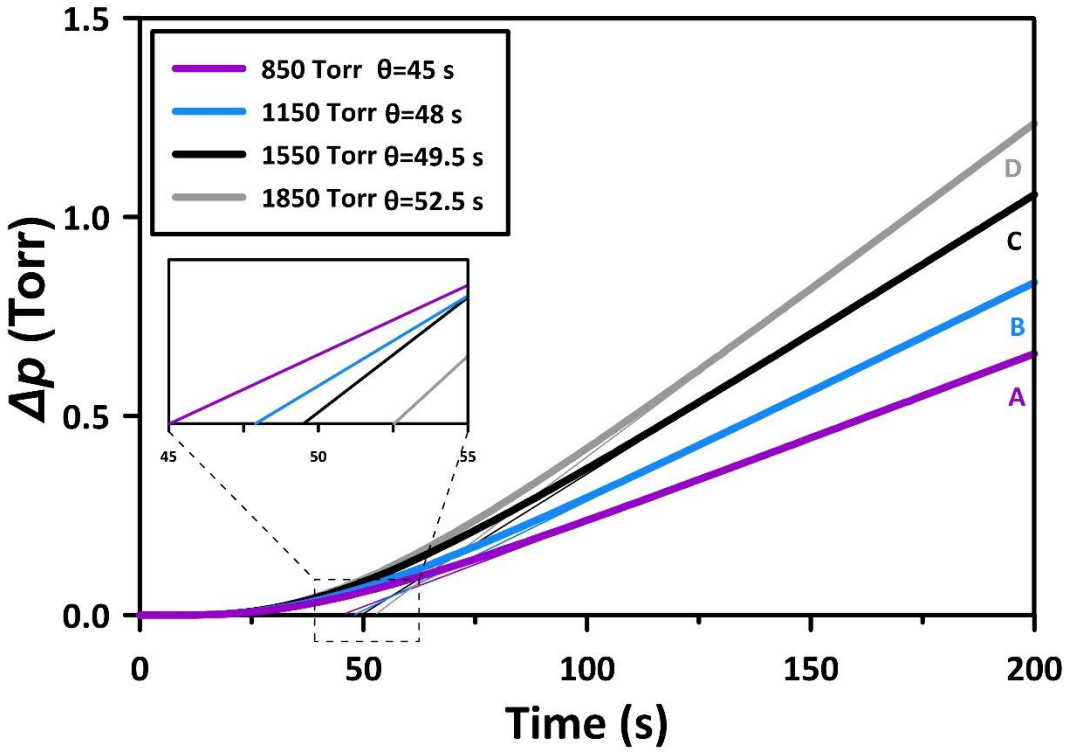

Figure 5.5 The effect of feed pressure using the conventional time-lag method using N_2. Experiments were performed using a 0.024-inch PDMS membrane at 303 K and four different pressures (850, 1150, 1550, and 1850 Torr).

Table 5.2 Summary of the analysis of the results from the conventional time-lag method, presented in Figure 5.5. The transport properties were calculated using the minimum thickness (Min. L) and nominal thickness (Nom. L).

Pressure [Torr]	P_1 [Barrer]		$D_1 \cdot 10^9$ [m^2/s]		$S_1 \cdot 10^5$ [mol/m^3 Pa]	
	Min. L	Nom. L	Min. L	Nom. L	Min. L	Nom. L
850	215	219	1.33	1.38	5.42	5.32
1150	206	211	1.23	1.29	5.60	5.46
1550	200	206	1.18	1.25	5.69	5.52
1850	187	194	1.09	1.18	5.72	5.51

Although the slope of the pressure rise increased with the feed pressure, the permeability decreased, regardless of whether the actual or nominal thickness was used to calculate P_1. Because the nominal thickness is constant and greater than the minimum

thickness, it follows from Eq. (5.3) that P_1 based on the nominal thickness is greater than P_1 based on the minimum thickness, with the difference between the two increasing with the feed pressure. It is important to note that although the minimum thickness decreased by 2% between the pressures of 850 and 1850 Torr, the corresponding decrease of P_1 between these two pressures was 13%. As the membrane was installed directly on the porous support with a filter paper in between, the observed decrease in permeability could indicate some membrane compaction caused by the applied feed pressure. Additionally, as the feed pressure p_0 increased, the time lag also increased, leading to a corresponding decrease of diffusivity D_1 as calculated using Eq. (5.2). Similar to permeability P_1, the value of D_1 based on the nominal thickness was higher than that based on the minimum thickness, as dictated by Eq. (5.2). Although because permeability decreased, a decrease in diffusivity with p_0 could expected, the magnitude of this decrease (17% between 850 and 1850 Torr) was greater than the corresponding decrease in P_1. As a result, the solubility S_1 calculated using Eq. (5.1) increased with pressure. This outcome is counterintuitive because if the membrane were compacted, one would expect not only a reduction in penetrant mobility (i.e. diffusivity) but also a decrease, or at least no increase, in the number of available Henry's sites (i.e., the solubility). The solubility would increase with pressure only for a condensable penetrant [24]. However, N_2, even at the highest feed pressure (1850 Torr) and 303 K, should behave close to an ideal gas. Thus, the condensation of the penetrant can be safely rejected as a reason. At the same time, the increase in S_1 with feed pressures is relatively small compared to the observed decreases in P_1 and D_1 and might as well arise from the experimental errors in P_1 and D_1 from which S_1 was calculated.

Figure 5.6 presents the pressure decay curves corresponding to the pressure rise shown in Figure 5.5. Table 5.3 summarizes the analysis based on these pressure decay curves. The N_2 transport properties, D_2, P_2, and S_2, were evaluated using Eqs. (5.5), (5.4), and (5.1), respectively. Like for D_1, P_1, and S_1, the transport properties were calculated using Min. L and the Nom. L. The results in Tables 5.2 and 5.3 are very similar, which verifies the validity of monitoring pressure decay in the time-lag experiments using our CV system. At the same time, like S_1, S_2 increases with the feed pressure.

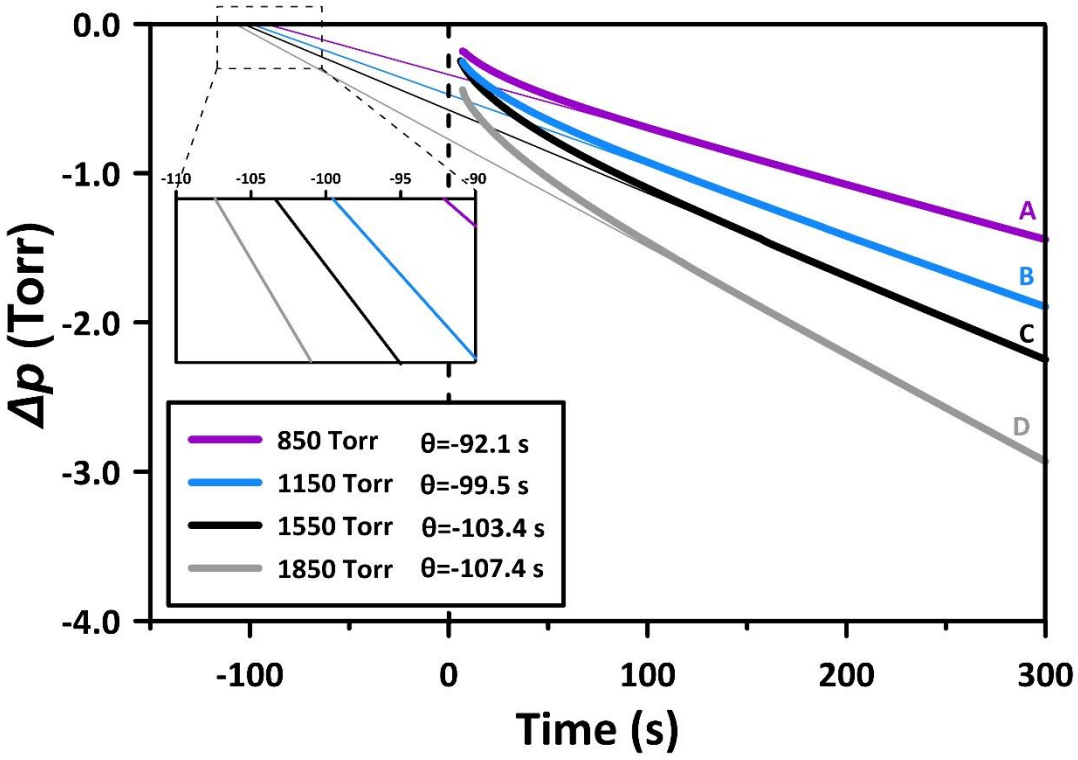

Figure 5.6 The effect of feed pressure using the time-lag method based on pressure decay in the upstream receiver. Experiments were performed using a 0.024-inch PDMS membrane at 303 K and four different pressures (850, 1150, 1550, and 1850 Torr).

Table 5.3 Summary of the analysis of the results from the time-lag method based on the pressure decay in Figure 5.5. The transport properties were calculated using the minimum thickness (Min. *L*) and nominal thickness (Nom. *L*).

Pressure [Torr]	P_2 [Barrer]		$D_2 \cdot 10^9$ [m^2/s]		$S_2 \cdot 10^5$ [mol/m^3 Pa]	
	Min. *L*	Nom. *L*	Min. *L*	Nom. *L*	Min. *L*	Nom. *L*
850	213	217	1.30	1.35	5.49	5.39
1150	208	213	1.19	1.25	5.87	5.73
1550	197	203	1.13	1.20	5.86	5.68
1850	191	198	1.07	1.15	5.98	5.75

Figure 5.7 presents the effect of feed pressure on the pressure decay shortly after the experiment's initiation, plotted as a function of the square root of time. During this

initial phase, the membrane is expected to behave as a semi-infinite solid. Under such conditions, the pressure decay should follow Eq. (5.6) with the slope (Σ_t) given by Eq. (5.7). The data clearly show a linear relationship between the pressure decay and the square root of time. As p_0 increases, Σ_t also increases, which is consistent with Eq. (5.7) since Σ_t is directly proportional to p_0. Additionally, the duration of the linear region in the pressure decay curve shortens with increasing feed pressure. This occurs because higher p_0 accelerates transport across the membrane, causing permeant molecules to exit the membrane more quickly. In other words, the time span during which the membrane behaves as a semi-infinite solid becomes shorter. Using Σ_t along with Σ_s calculated from Eq. (5.8), diffusivity D_3 was evaluated from Eq. (5.9). It is important to note that Σ_s was also used to calculate P_2 using Eq. (5.4). Consequently, the two-slope method uses the permeability from the upsteam time-lag method, i.e., $P_3 = P_2$. With both permeability and diffusivity known, the solubility S_3 was then calculated using Eq. (5.1).

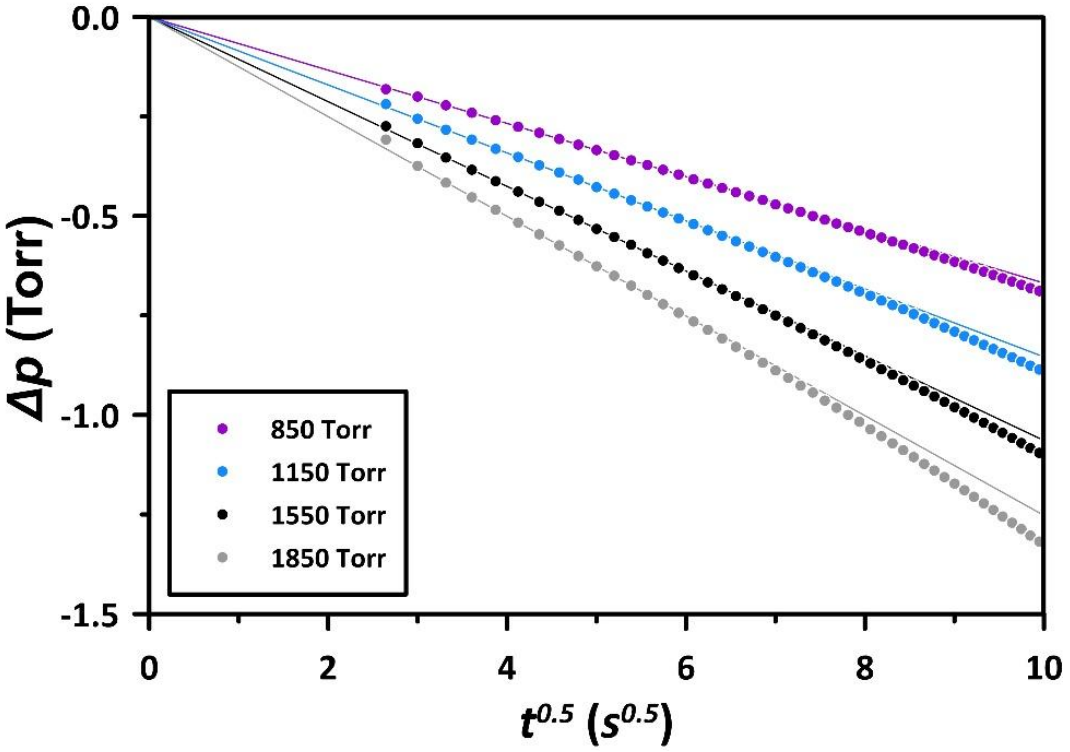

Figure 5.7 The effect of feed pressure on the pressure decay shortly after the initiation of the experiment as a function of the square root of time. Experiments were performed using a 0.024-inch PDMS membrane at 303 K and four different pressures (850, 1150, 1550, and 1850 Torr).

Table 5.4 summarizes the analysis based on the two-slope method. In general, the transport properties in Table 4 are comparable to those in Tables 5.2 and 5.3, which validates the use of the two-slope method. However, although D_3 decreases with an increase in p_0, this decrease is relatively smaller than that for D_1 and D_2. As a result, an increase in S_3 with feed pressure is not as apparent as for S_1 and S_2. It should be emphasized that the solubility in Methods 1-3 is evaluated from the ratio of permeability and diffusivity, i.e., indirectly.

Figure 5.8 presents the effect of feed pressure on the gas accumulation, $M(t)$, normalized by p_0, as a function of time. As time increases, $M(t)/p_0$ increases and eventually becomes constant, corresponding to the normalized steady-state gas accumulation in the membrane M_∞/p_0. In turn, the solubility S_4 was evaluated directly from M_∞/p_0 using Eq. (5.11). It is evident from Figure 5.8 that M_∞/p_0 and thus S_4 decrease with p_0. The calculated values of S_4 at different feed pressures are summarized in Table 5.5. At the lowest feed pressure of 850 Torr, S_4 is comparable to S_1, S_2, and S_3. However, due to different trends in the feed pressure, S_4 becomes increasingly smaller than the indirectly determined S_1-S_3, with the difference reaching 15% at 1850 Torr.

Table 5.4 Summary of the analysis of the results using the two-slope method. The transport properties were calculated using the minimum thickness (Min. L) and nominal thickness (Nom. L).

Pressure [Torr]	$P_3 = P_2$ [Barrer]		$D_3 \cdot 10^9$ [m^2/s]		$S_3 \cdot 10^5$ [mol/m^3 Pa]	
	Min. L	Nom. L	Min. L	Nom. L	Min. L	Nom. L
850	213	217	1.24	1.28	5.77	5.66
1150	208	213	1.17	1.23	5.93	5.78
1550	197	203	1.12	1.19	5.90	5.72
1850	191	198	1.08	1.16	5.94	5.71

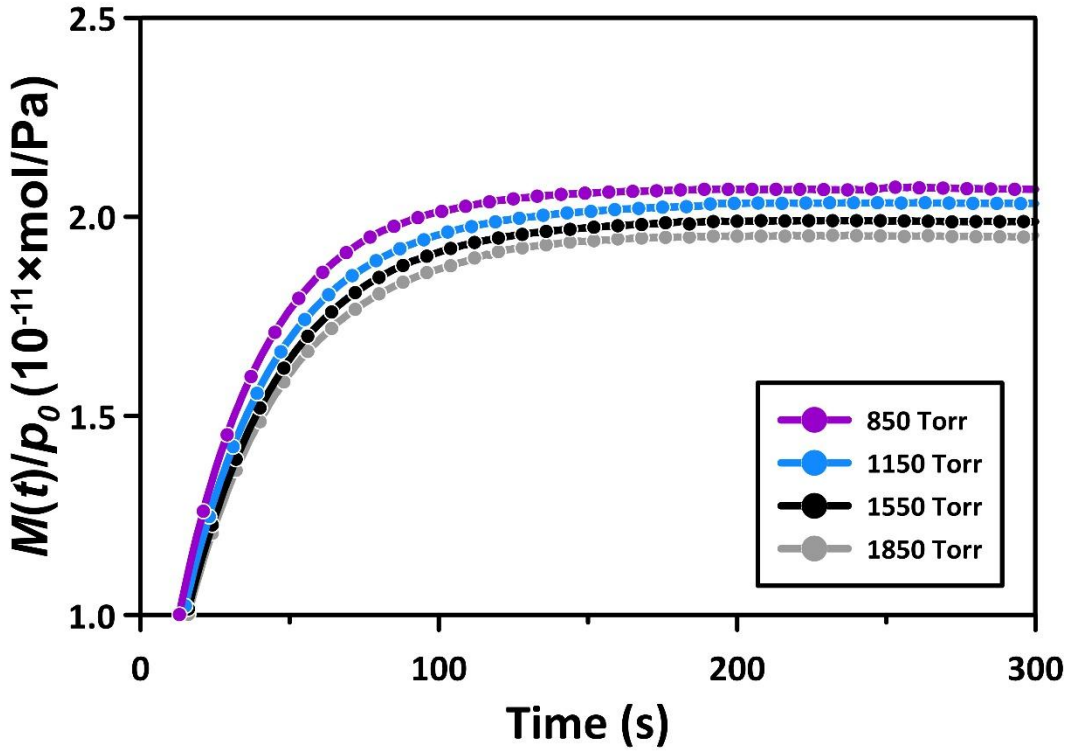

Figure 5.8 The effect of feed pressure on the normalized gas accumulation in the membrane as a function of time. Experiments were performed using a 0.024-inch PDMS membrane at 303 K and four different pressures (850, 1150, 1550, and 1850 Torr).

The accumulation method implies that the gas accumulation $M(t)$ follows Eq. (5.10), and consequently, the relative gas accumulation $M(t)/M_\infty$ follows Eq. (5.13). To validate this, Eq. (5.13) was linearized by taking the natural logarithm of both sides. The transformed experimental data are shown in Figure 5.9. The clear linear relationship in the plot $\ln(1 - M(t)/M_\infty)$ confirms the validity of the gas accumulation method and demonstrates its successful implementation in our CV system. Moreover, the slopes observed in Figure 5.8 were used to calculate diffusivity D_4 from Eq. (5.14), which states that D_4 is directly proportional to the slope. It is clear that as feed pressure increases, the slope becomes less negative, and thus D_4 decreases with increasing p_0. Table 5 summarizes the values of D_4 calculated using Eq. (5.14) for both the minimum and nominal membrane thicknesses. The effect of p_0 on D_4 mirrors the trends observed for D_1-D_3. However, for a given p_0, D_4 is generally smaller than the other diffusivity values, particularly D_1 and D_2.

Using D_4 and S_4, the permeability P_4 was calculated using Eq. (5.1), and the corresponding values at different feed pressures are summarized in Table 5. Because both S_4 and D_4 decrease with increasing p_0, P_4 also decreases with the feed pressure, which is consistent with the trend observed for P_1 and P_2. However, for a given p_0, P_4 is smaller than the corresponding P_1 and P_2. This is the consequence of a decrease in S_4 with p_0. It is important to emphasize that P_4, being derived from Eq. (5.1), is determined indirectly. Therefore, it is analogous to S_1-S_3, which are also evaluated indirectly using the same equation.

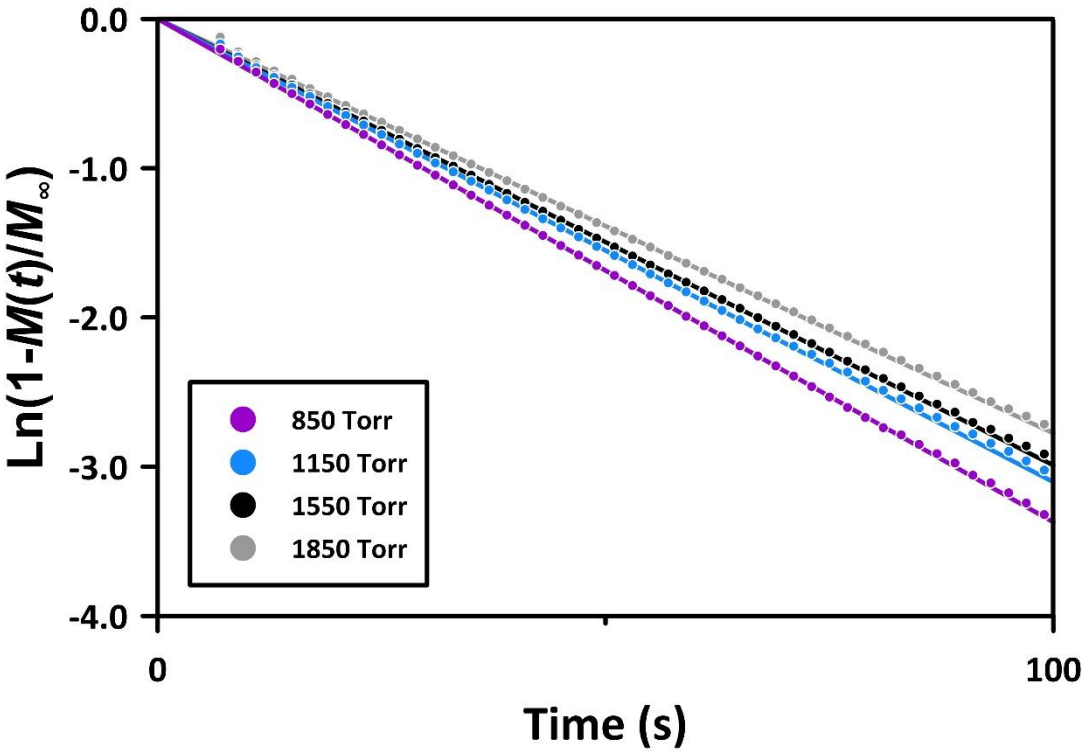

Figure 5.9 The effect of feed pressure on relative gas accumulation in the membrane as a function of time. Experiments were performed using a 0.024-inch PDMS membrane at 303 K and four different pressures (850, 1150, 1550, and 1850 Torr).

Table 5.5 Summary of the analysis of the results from the gas accumulation method, which relies on simultaneous monitoring of pressure rise and decay in time-lag experiments. The transport properties were calculated using the minimum thickness (Min. L) and nominal thickness (Nom. L).

Pressure [Torr]	P_4 [Barrer]		$D_4 \cdot 10^9$ [m^2/s]		$S_4 \cdot 10^5$ [mol/m^3 Pa]	
	Act. L	Nom. L	Act. L	Nom. L	Act. L	Nom. L
850	200	204	1.23	1.27	5.48	5.38
1150	176	180	1.11	1.17	5.28	5.15
1550	162	167	1.06	1.13	5.12	4.96
1850	145	151	9.69	1.05	5.02	4.84

The simultaneous monitoring of the pressure rise and pressure decay in time-lag experiments allows the determination of three independent permeabilities (P_1, $P_2 = P_3$, and P_4), along with four independent diffusivities and solubilities. This raises an important question: which method yields the most reliable values? Method 4 stands out, as it was the only approach to exhibit a decrease in solubility with increasing pressure. Given the observed decrease in permeability and diffusivity with feed pressures in all methods, which suggests some membrane compaction, the latter should also be evident in some decrease in the number of sorption (Henry's) sites, i.e., a decrease in membrane solubility. This suggests that monitoring gas accumulation in the membrane over time may be the most reliable method. However, one can arrive at this conclusion regardless of the observed effect of feed pressure on solubility.

As pressure rises in the downstream receiver and decays in the upstream receiver, the pressure gradient across the membrane gradually decreases. Although this decrease is generally negligible, it still slightly lowers the steady-state slopes observed in the downstream and upstream receivers. The resulting error in P_1 and P_2 is generally minimal, often just a fraction of a percent, and can be considered negligible. However, the impact on the time-lag parameters (θ_d and θ_u) is more pronounced. Because these values are derived by extrapolating the linear portion of the pressure response curves to the time axis, even a slight underestimation of the slope leads to a significant decrease in θ_d and θ_u (with θ_u becoming a smaller negative value). This, in turn, causes an overestimation of the

respective D_1 and D_2. Therefore, there is more confidence in P_1 and P_2 than in the corresponding D_1 and D_2.

Considering S_4, it is based on the difference between the gas flux entering the membrane and the gas flux exiting the membrane under steady state, or more precisely, under pseudo-steady state. As indicated above, due to the decrease in the pressure gradient across the membrane, both fluxes may decrease over time; however, their difference from which the solubility is evaluated (i.e., M_∞) should remain relatively constant. The same argument could be used before the steady-state permeation is reached, that is, to the time-dependent gas accumulation $M(t)$. Consequently, one should be confident about the ratio $M(t)/M_\infty$, which provides the basis for the determination of D_4. Additionally, plotting the experimental results into the linearized form of Eq. (5.13) yields perfect straight lines in Figure 5.9. Therefore, we are highly confident about the directly determined S_4 and D_4.

If S_4 and D_4 better reflect the solubility and diffusivity of the penetrant in the membrane than those from the other method, the product of S_4 and D_4, i.e., P_4, should also be reliable. However, at any feed pressure, P_4 is smaller than P_1 and P_2, which we consider reliable. This discrepancy may stem from various experimental errors, which certainly exist in our CV system [8]. However, more fundamentally, it illustrates the risk of blindly applying Eq. (5.1) to estimate one of the three basic transport properties from the other two.

5.3.3 Effect of membrane thickness on *P*, *D*, and *S*

Building on the previous discussion, among the three independent methods for determining P, the values obtained directly from the respective pressure rise and pressure decay, namely P_1 and P_2, are considered reliable. This holds true despite potential underestimation caused by the decreasing pressure gradient across the membrane. Therefore, in the following discussion, we will use the arithmetic average of P_1 and P_2 to represent the membrane permeability. However, for S, we consider that the solubility based on the steady-state gas accumulation in the membrane, i.e., S_4, is the most reliable, because it does not require Eq. (5.1) and the prior knowledge of P and D. Although D can

be determined directly, i.e., without relying on Eq. (5.1), in four different ways, we will consider D_4 in the following discussion primarily because it is associated to S_4 and is determined directly from the slope (Figure 5.9). In Tables 5.2-5.5, two sets of *P*, *D*, and *S* were presented: one based on the minimum thickness at a given pressure and the other based on the constant nominal thickness. By definition, *P* and *D,* based on the minimum thickness, were greater than based on the nominal thickness, while for *S,* the opposite was true. Although the differences increased with the feed pressure, they did not exceed 3%. In the following discussion, the presented *P*, *D*, and *S* are based on the nominal membrane thickness, which minimizes the effect of feed pressure on the transport properties.

For a given feed pressure, three independent membranes of the same nominal thickness were tested. Each coupon was tested as follows. The tests started at the lowest feed pressure (850 Torr). After completing the test and the necessary evacuation, the next test was performed at an increased feed pressure of 1150 Torr. This protocol was continued until the highest feed pressure of 1850 Torr was reached. The tests were then repeated, starting with the highest feed pressure and progressing to the lowest. Consequently, each coupon was tested twice at a given feed pressure, and *P*, *D*, and *S* in Figs. 5.10-5.12 represent the average of six values, and the error bars represent the corresponding standard deviations.

Figure 5.10 presents the combined effect of membrane thickness and feed pressure on the N_2 permeability of PDMS membranes. Consistent with the results obtained for the sample membrane shown in Tables 5.2 and 5.3, for any membrane thickness, the permeability decreases with increasing feed pressure. Moreover, for a given feed pressure, the permeability decreases with the membrane thickness. In other words, if a decrease in permeability with feed pressure results from membrane compaction, the results suggest that thicker membranes are more prone to compaction under a given feed pressure. This is consistent with the results shown in Figure 5.4. At the same time, it is essential to emphasize that because the seal in the membrane cell restricts possible membrane expansion in the radial direction, the results in Figure 5.4 should be treated qualitatively, rather than quantitatively. In other words, the membrane compaction, i.e., a decrease in free fractional volume under pressure, is likely much lower than the strain in Figure 5.4.

It is also essential to emphasize that any possible membrane compaction under pressure is reversible, as the permeabilities at a given feed pressure in the step-up and the repeated step-down experiments are similar. The repeatability of permeabilities at the same pressures for the same and different membrane coupons is manifested by relatively small error bars in Figure 5.10, never exceeding 10% of the average value. Interestingly, the size of the error bars generally increases with membrane thickness. For the thinnest membranes, the error margins are typically around 1%.

Figure 5.11 presents the combined effect of membrane thickness and feed pressure on the N_2 diffusivity in PDMS membranes. Similarly to permeability, for a given membrane thickness, the diffusivity decreases with the feed pressure. On the other hand, the effect of membrane thickness on the diffusivity is less straightforward. For 0.432 mm and 0.610 mm membranes, the diffusivity is consistently higher in the thinner membrane, presumably due to the lower compaction, at all feed pressures. Yet, when the thickest membrane (1.016 mm) is considered, the trend becomes ambiguous. Contrary to the notion that membrane compaction increases with thickness, the diffusivity in the thickest membrane is either comparable or even higher than that in the 0.432 mm membrane. Unlike the pattern observed in Figure 5.10, there is no clear relationship between the membrane thickness and the size of the error bars in Figure 5.11. The error margins generally remain below 10%, regardless of thickness.

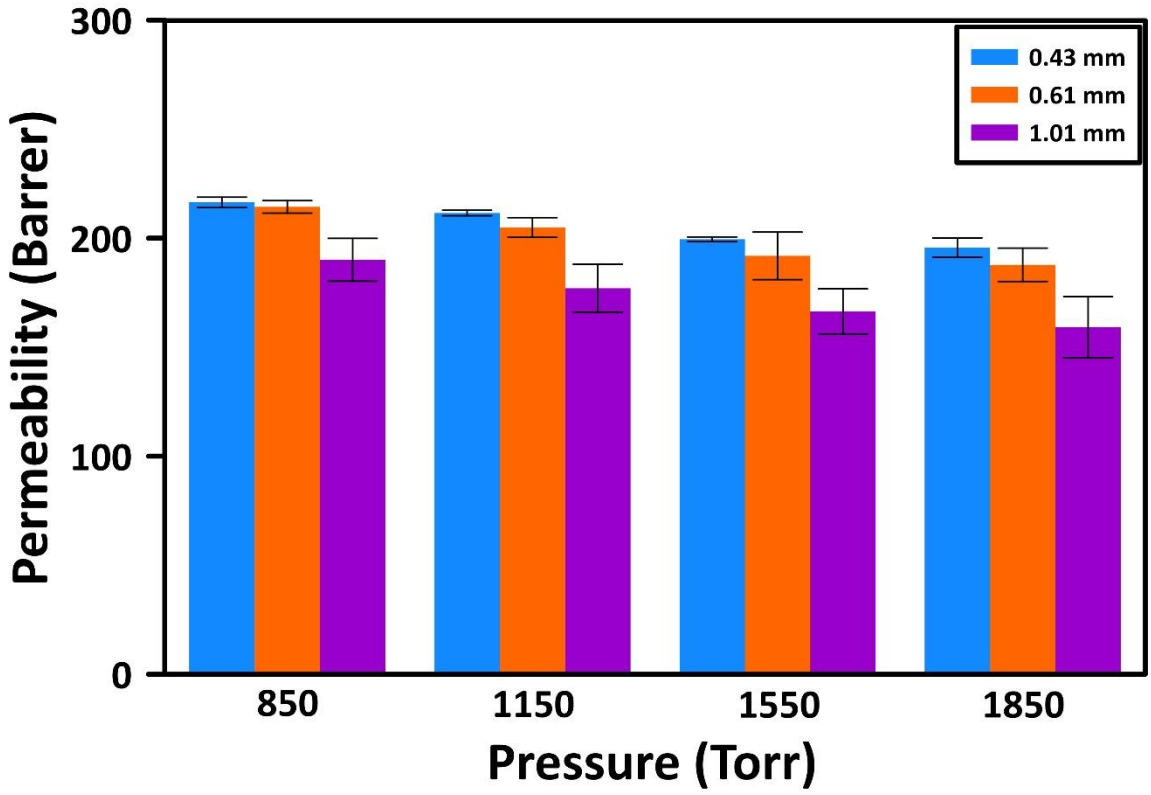

Figure 5.10 The combined effect of membrane thickness and feed pressure on permeability (arithmetic average of P_1 and P_2) of N_2 in PDMS membranes. All experiments were performed at 303 K, and the provided permeabilities and corresponding error bars represent averages and standard deviations from three coupons of the same nominal thickness, tested twice at a given feed pressure.

Figure 5.12 presents the combined effect of membrane thickness and feed pressure on the solubility of N_2 in PDMS membranes. The solubility decreases with increasing feed pressure for any given membrane thickness. However, while the solubility of N_2 in the thickest PDMS membrane is statistically smaller than that in the 0.432 and 0.610 mm membranes, the solubilities of N_2 for these two thinner membranes are statistically indistinguishable at the same feed pressure. Consequently, assuming that membrane compaction leads to a decrease in solubility, Figure 5.12 does not support the notion that for a given feed pressure, the thicker membranes are more compacted. The error bars shown in Figure 5.12, each less than 4%, are smaller than those in Figs. 5.10 and 5.11.

This may indicate a smaller influence of experimental errors on the directly determined solubility compared to other values indirectly determined from *P* and *D*.

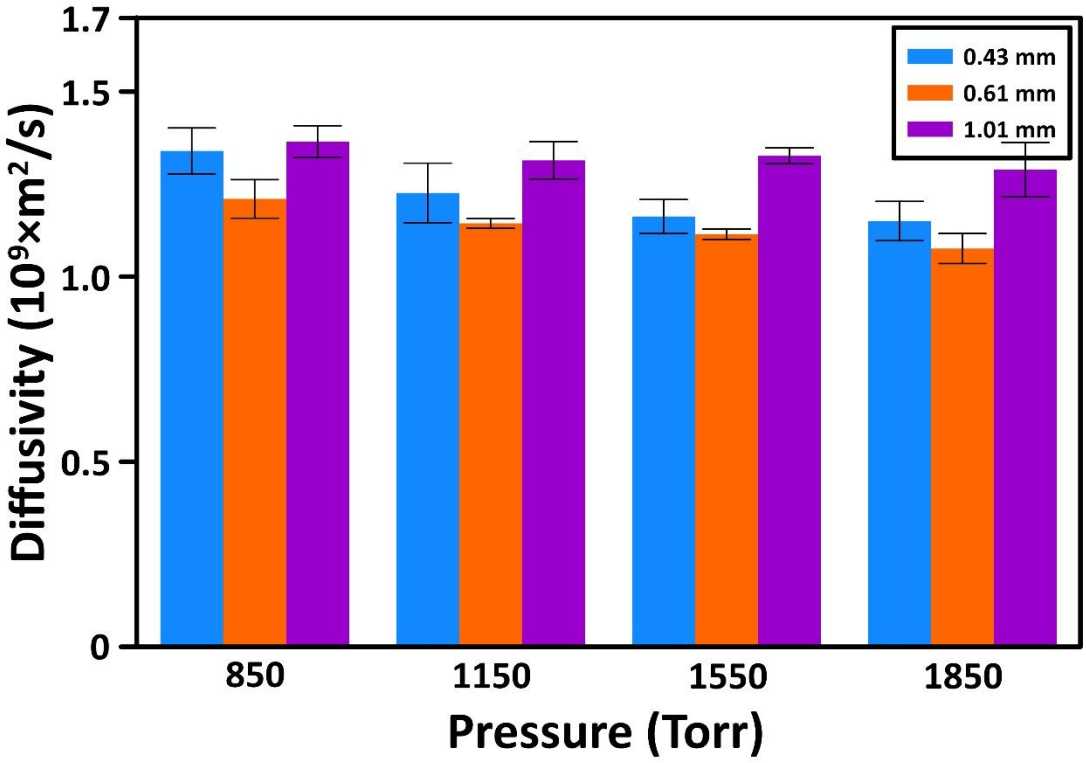

Figure 5.11 The combined effect of membrane thickness and feed pressure on diffusivity (D_4) of N_2 in PDMS membranes. All experiments were performed at 303 K, and the provided permeabilities and corresponding error bars represent averages and standard deviations from three coupons of the same nominal thickness, tested twice at a given feed pressure.

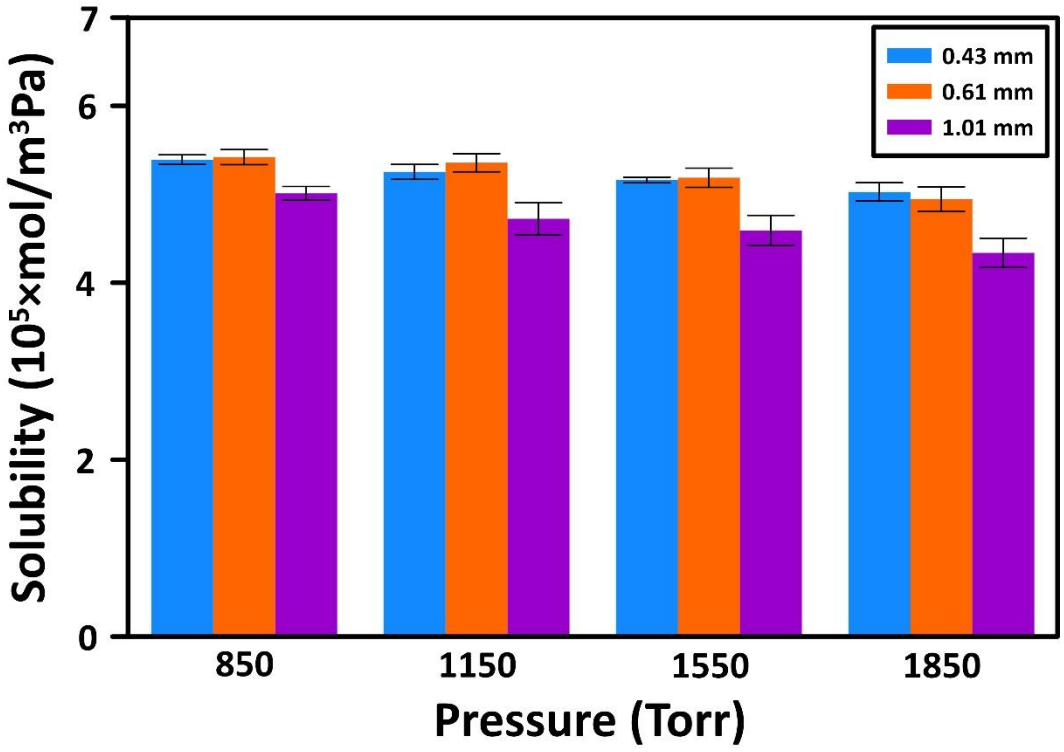

Figure 5.12 The combined effect of membrane thickness and feed pressure on solubility (S_4) of N_2 in PDMS membranes. All experiments were performed at 303 K, and the $^{-1}$provided permeabilities and corresponding error bars represent averages and standard deviations from three coupons of the same nominal thickness, tested twice at a given feed pressure.

5.4 Discussion

According to Merkel et al., the permeability of N_2 in PDMS decreases linearly with the applied pressure gradient and the corresponding slope, m_p = -0.0035 atm^{-1} [22]. Based on the data reported by Villaluenga and Tabe-Mohammadi for N_2 in PDMS, their m_p would range between -0.057 and -0.038 atm^{-1} [21], which is an order of magnitude greater (considering the absolute value) than that reported by Merkel et al. In the current study, based on Figure 5.9, the corresponding m_p depends on the membrane thickness, and is even greater than that reported by Villaluenga and Tabe-Mohammadi, ranging from -0.218 atm^{-1} for the 1.01 mm-thick to -0.086 atm^{-1} for the 0.43 mm-thick PDMS membrane. It is important to emphasize that the properties of the PDMS membrane, including the

susceptibility to compaction under pressure, depend on the degree of cross-linking density of the polymer [22]. Also, the membranes in the current study and those of Villaluenga and Tabe-Mohammadi were tested in CV systems, in which the permeate site of the membrane was essentially under high vacuum during gas permeation tests. The membranes in the Merkel et al. study were tested under constant pressure (CP), with the permeate side of the membrane at atmospheric pressure, which could contribute to the differences in m_p. However, despite significant differences in m_p across different studies, the compaction of PDMS under the pressure gradient is undeniable. As previously stated, PDMS has a fractional free volume of approximately 0.2 [27,28], and its compaction implies some decrease in this value. It is beyond the scope of this study to estimate this decrease under different feed pressures. However, any decrease in the fractional free volume of PDMS was reversible. Our testing protocol, in which each coupon was tested from the lowest to the highest pressure, followed by repeating the experiments in the reverse order, i.e, from the highest to the lowest pressure, indicated excellent repeatability of the membrane performance at a given feed pressure, thus confirming the recovery of the fractional free volume.

As indicated by Eq. (1), the permeability is a product of diffusivity and solubility of the gas in the membrane. As previously noted, even a slight reduction in the fractional free volume resulting from membrane compaction would reduce the penetrant diffusion coefficient [26]. Indeed, this study confirmed experimentally for the first time a decrease in the diffusivity of N_2 in PDMS under increasing feed pressures. Assuming a linear decrease in diffusivity with feed pressure, in the same way as was done for permeability, the corresponding slope, m_d, based on Fig. 10, varies from -0.132 atm^{-1} for the 0.43 mm membrane to -0.076 atm^{-1} for the 1.01 mm membrane. Therefore, the absolute values of m_d are smaller than those of m_p, which suggests that membrane compaction also affects the solubility of N_2 in PDMS. Accordingly, based on Figure 5.11, the corresponding coefficient of decrease in solubility with pressure, $m_{s,}$ ranges from -0.102 atm^{-1} for the 1.01 mm membrane to -0.051 atm^{-1} for the 0.43 mm membrane. Therefore, although the absolute values of m_s are slightly lower than those of m_d, it is evident that membrane compaction also decreases gas solubility along with the permeant mobility in the PDMS membrane.

As previously stated, transport properties, including the solubility, were determined independently, i.e., without reliance on Eq. (5.1), and the product of the respective diffusivity and solubility slightly deviates from the directly measured permeability. This indicates that all *P*, *D*, and *S* are associated with some experimental errors. However, these errors do not undermine the observed reversible compaction of PDMS and the fact that this compaction, based on the experimental values of *P*, *D*, and *S,* increases with the feed pressure.

Figure 5.4 could suggest that membrane compaction, for a given feed pressure, increases with membrane thickness. However, as already stated, the stress-strain relation, shown in Figure 5.4, was obtained in the system in which the membrane samples could expand radially, which was not likely to occur in the actual membrane cell during gas permeation tests (Figure 5.3). Still, based on the N_2 permeability results, as shown in Figure 5.10, one could conclude that the thicker the membrane, the greater the compaction at a given feed pressure. However, this observation was not supported by diffusivity and solubility results shown in Figures 5.11 and 5.12, respectively. It does not mean that this relationship between membrane thickness and compaction does not exist, but rather that, because of inherent experimental errors, it cannot be affirmatively confirmed.

5.5 Conclusions

The effect of feed pressures on nitrogen permeability, diffusivity, and solubility in commercial PDMS membranes of different thicknesses was systematically investigated using a novel CV system. The simultaneous monitoring of pressure rise and pressure decay allowed, in addition to determining *P*, *D*, and *S* from the conventional time-lag method based on the pressure rise in the downstream receiver, three extra sets of *P*, *D*, and *S* from the same experiment, which included the direct determination of *S* based on the steady-state gas accumulation in the membrane.

For a given membrane thickness, *P* and *D* decreased with increasing feed pressure, regardless of the method used to analyze the experimental results. As the feed pressure increased from 850 to 1850 Torr, *P* and *D* decreased up to 25%, depending on the membrane thickness. A decrease in *P* and *D* with increasing feed pressure indicates

membrane compaction. For the solubility determined indirectly from the ratio of P and D, a slight increase was observed with increasing feed pressure. It was not expected, given the membrane compaction under pressure. However, the solubility determined from the steady-state gas accumulation in the membrane decreased with feed pressure. More specifically, a 7-15% decrease in S was observed, depending on the membrane thickness, when the feed pressure increased from 850 to 1850 Torr.

As indicated by the ex-situ stress-strain experiments using the samples of PDMS membranes utilized in gas permeation experiments, for a given stress, the strain increased with the sample thickness, suggesting more significant compaction of the thicker membranes. However, this trend was observed only for P, not for D and S. Therefore, the current study cannot affirmatively conclude that compaction is affected by the membrane thickness. On the other hand, despite a relatively low feed pressure, reversible compaction of PDMS membranes, based on the directly measured P, D, and S, was demonstrated, and it was proven that it increases with the applied feed pressures. Moreover, for the first time, the compaction was demonstrated not only based on P, but also based on its components, i.e., D and S.

Nomenclature

Symbols

A	Membrane area [m^2]
c	Gas concentration in the membrane [mol/m^3]
D	Diffusivity coefficient [m^2/s]
J	Gas flux [mol/m^2 s]
L	Membrane thickness [m]
m	Coefficient of decrease in transport property (P, D, S) with pressure [atm^{-1}]
$M(t)$	Gas accumulation in the membrane as a function of time [mol]

M_∞	Gas accumulation in the membrane at the steady state [mol]
$M_{\ln}(t)$	Logarithmic gas accumulation defined by Eq. (25) [-]
P	Permeability coefficient [Barrer or mol/s m Pa]
p	Pressure [Torr or Pa]
p_0	Feed pressure [Torr or Pa]
R	Universal gas constant [J/mol K]
S	Solubility coefficient [mol/m^3 Pa]
T	Absolute temperature [K]
t	Time [s]
V	Volume [m^3]

Greek symbols

θ	Time lag [s]
Δp	Pressure decay/pressure rise [torr/s or Pa/s]

Subscripts

d	Downstream
e	Effective property
i	Intrinsic property
u	Upstream
0	Upstream
∞	Steady state

References

[1] C.Z. Liang, T.S. Chung, J.Y. Lai, A review of polymeric composite membranes for gas separation and energy production, Prog Polym Sci 97 (2019). https://doi.org/10.1016/j.progpolymsci.2019.06.001.

[2] D.F. Sanders, Z.P. Smith, R. Guo, L.M. Robeson, J.E. McGrath, D.R. Paul, B.D. Freeman, Energy-efficient polymeric gas separation membranes for a sustainable future: A review, Polymer (Guildf) 54 (2013) 4729–4761. https://doi.org/10.1016/j.polymer.2013.05.075.

[3] J.G. Wijmans, R.W. Baker, The solution-diffusion model: a review, J Memb Sci 107 (1995) 1–21. https://doi.org/10.1016/0376-7388(95)00102-I.

[4] L.M. Robeson, The upper bound revisited, J Memb Sci 320 (2008) 390–400. https://doi.org/10.1016/j.memsci.2008.04.030.

[5] H. A. Daynes, The process of diffusion through a rubber membrane, Proc. R. Soc. Lond. A97:286–307 (1920). https://doi.org/10.1098/rspa.1920.0034.

[6] R.M. Barrer, E.K. Rideal, Permeation, Diffusion and Solution of Gases in Organic Polymers., Transactions of the Faraday Society 35 (1939) 628. https://doi.org/https://doi.org/10.1039/tf9393500628.

[7] N. Al-Qasas, J. Thibault, B. Kruczek, The effect of the downstream pressure accumulation on the time-lag accuracy for membranes with non-linear isotherms, J Memb Sci 511 (2016) 119–129. https://doi.org/10.1016/j.memsci.2016.03.047.

[8] H. Wu, B. Kruczek, J. Thibault, Impact of measuring devices and data analysis on the determination of gas membrane properties, Journal of Membrane Science and Research 4 (2018) 4–14. https://doi.org/10.22079/jmsr.2017.63433.1136.

[9] E. Favre, N. Morliere, D. Roizard, Experimental evidence and implications of an imperfect upstream pressure step for the time-lag technique, J Memb Sci 207 (2002) 59–72. https://doi.org/10.1016/S0376-7388(02)00039-X.

[10] B. Kruczek, H.L. Frisch, R. Chapanian, Analytical solution for the effective time lag of a membrane in a permeate tube collector in which Knudsen flow regime exists, J Memb Sci 256 (2005) 57–63. https://doi.org/10.1016/j.memsci.2005.02.006.

[11] B. Kruczek, F. Shemshaki, S. Lashkari, R. Chapanian, H.L. Frisch, Effect of a resistance-free tank on the resistance to gas transport in high vacuum tube, J Memb Sci 280 (2006) 29–36. https://doi.org/10.1016/j.memsci.2006.01.001.

[12] S. Lashkari, B. Kruczek, Effect of resistance to gas accumulation in multi-tank receivers on membrane characterization by the time lag method. Analytical approach for optimization of the receiver, J Memb Sci 360 (2010) 442–453. https://doi.org/10.1016/j.memsci.2010.05.043.

[13] S. Lashkari, B. Kruczek, H.L. Frisch, General solution for the time lag of a single-tank receiver in the Knudsen flow regime and its implications for the receiver's configuration, J Memb Sci 283 (2006) 88–101. https://doi.org/10.1016/j.memsci.2006.06.015.

[14] P.J. Leszczynski, S. Lashkari, B. Kruczek, Revisiting the Effect of the Resistance to Gas Accumulation in Constant Volume Systems on the Membrane Time Lag, Membranes (Basel) 14 (2024). https://doi.org/10.3390/membranes14080167.

[15] G.Z. Ramon, M.C.Y. Wong, E.M.V. Hoek, Transport through composite membrane, Part 1: Is there an optimal support membrane?, J Memb Sci 415–416 (2012) 298–305. https://doi.org/10.1016/j.memsci.2012.05.013.

[16] L. Zhu, W. Jia, M. Kattula, K. Ponnuru, E.P. Furlani, H. Lin, Effect of porous supports on the permeance of thin film composite membranes: Part I. Track-etched polycarbonate supports, J Memb Sci 514 (2016) 684–695. https://doi.org/10.1016/j.memsci.2015.11.043.

[17] Z. Cao, B. Kruczek, J. Thibault, Impact of the porous support disc of a gas permeation cell on the estimation of the membrane transport properties, J Memb Sci 721 (2025). https://doi.org/10.1016/j.memsci.2025.123831.

[18] H. Wu, J. Thibault, B. Kruczek, The validity of the time-lag method for the characterization of mixed-matrix membranes, J Memb Sci 618 (2021). https://doi.org/10.1016/j.memsci.2020.118715.

[19] H. Wu, J. Thibault, B. Kruczek, On the limitation of the time-lag method for characterizing mixed-matrix membranes embedding filler particles of different permeability, J Memb Sci 663 (2022). https://doi.org/10.1016/j.memsci.2022.121074.

[20] N. Al-Qasas, J. Thibault, B. Kruczek, A new characterization method of membranes with nonlinear sorption isotherm systems based on continuous upstream and downstream time-lag measurements, J Memb Sci 542 (2017) 91–101. https://doi.org/10.1016/j.memsci.2017.07.039.

[21] J.P.G. Villaluenga, A. Tabe-Mohammadi, Effects of Pressure Ratio and Pressure Difference on the Gas Permeation Properties of Rubbery and Glassy Membranes., 23 (2003).

[22] T. C. Merkel, V. Bondar, K.Nagai, B. D. Freeman, Yu. P. Yampolskii, Gas Sorption, Diffusion, and Permeation in Poly(dimethylsiloxane), Macromolecules 32 (1999) 8427–8440. https://doi.org/https://doi.org/10.1021/ma990685r.

[23] Peter Leszczynski, Zheng Cao, Haoyu Wu, Jules Thibault, Boguslaw Kruczek, Determination of time lag by accurate monitoring of pressure decay in a new generation constant volume system, MethodsX 102858 (2024). https://doi.org/10.1016/j.mex.2024.102858.

[24] S.A. Stern, S.M. Fang, R.M. Jobbins, Permeation of Gases at High Pressures, Journal of Macromolecular Science, Part B 5 (1971) 41–69. https://doi.org/10.1080/00222347108212520.

[25] V.E. Reinsch, A.R. Greenberg, S.S. Kelley, R. Peterson, L.J. Bond, A new technique for the simultaneous, real-time measurement of membrane compaction and performance during exposure to high-pressure gas, J Memb Sci 171 (2000). https://doi.org/10.1016/S0376-7388(00)00307-0.

[26] W.J. Koros, S.K. Burgess, Z. Chen, Polymer Transport Properties, in: Encyclopedia of Polymer Science and Technology, Wiley, 2015: pp. 1–96. https://doi.org/10.1002/0471440264.pst376.pub2.

[27] Y. Yampolskii, Polymeric gas separation membranes, Macromolecules 45 (2012) 3298–3311. https://doi.org/10.1021/ma300213b.

[28] G. Consolati, D. Nichetti, F. Quasso, Probing the Free Volume in Polymers by Means of Positron Annihilation Lifetime Spectroscopy, Polymers (Basel) 15 (2023). https://doi.org/10.3390/polym15143128.

[29] D. Armani, C. Liu, N. Aluru, Re-configurable fluid circuits by PDMS elastomer micromachining, in: Technical Digest. IEEE International MEMS 99 Conference. Twelfth IEEE International Conference on Micro Electro Mechanical Systems (Cat. No.99CH36291), IEEE, 1999: pp. 222–227. https://doi.org/10.1109/MEMSYS.1999.746817.

[30] R. Moučka, M. Sedlačík, J. Osička, V. Pata, Mechanical properties of bulk Sylgard 184 and its extension with silicone oil, Sci Rep 11 (2021). https://doi.org/10.1038/s41598-021-98694-2.

[31] Z. Cao, J. Thibault, B. Kruczek, Direct determination of permeability, diffusivity and solubility of gases in membrane based on simultaneous monitoring of pressure rise and decay in a single time-lag experiment, J Memb Sci 720 (2025). https://doi.org/10.1016/j.memsci.2025.123741.

[32] S.W. Rutherford, D.D. Do, Adsorption dynamics measured by permeation and batch adsorption methods, 2000.

[33] M. Al-Ismaily, J.G. Wijmans, B. Kruczek, A shortcut method for faster determination of permeability coefficient from time lag experiments, J Memb Sci 423–424 (2012) 165–174. https://doi.org/10.1016/j.memsci.2012.08.009.

[34] L.N. Sridhar, R.K. Gupta, M. Bhardwaj, Barrier properties of polymer nanocomposites, Ind Eng Chem Res 45 (2006) 8282–8289. https://doi.org/10.1021/ie0510223.

Chapter 6

From Raw Data to Reliable Insights: Membrane Characterization via Time Lag and Data Reconciliation

Zheng Cao, Boguslaw Kruczek, Jules Thibault*

Abstract

The time-lag method is a widely adopted experimental technique for evaluating membrane transport properties. It directly measures permeability (P) and diffusivity (D), with the solubility (S) subsequently calculated from the ratio of P/D. To achieve a robust characterization of membrane transport behavior, five distinct approaches, based on the latest generation of our constant-volume (CV) system, were employed: the upstream time-lag method, the downstream time-lag method, the two-slope method, the solution-diffusion model, and the accumulation method. Each method yields independent estimates of P, D, and/or S.

To determine the most probable values of the transport properties across the different methods, a data reconciliation technique was employed. This approach minimizes an objective function that accounts for all sources of variation, both from experimental measurements and model-based predictions. Each term in the objective function is weighted according to its precision. While measured variables typically come with known levels of uncertainty, assessing the precision of model-based estimates is more challenging. To address this, a Monte Carlo procedure was used to assign appropriate weights to the model-based estimates. A gradient descent optimization

algorithm was then applied to converge on the most accurate estimates of *P*, *D*, and *S*. The reconciled results yielded statistically robust estimates of *P*, *D*, and *S*, validated against the original experimental data. This work establishes comprehensive and reliable protocols for membrane characterization, confirming that data reconciliation effectively resolves inconsistencies and improves the accuracy of extracted transport properties.

Keywords: Membrane characterization, Constant volume system, Upstream and downstream time-lag methods, Data reconciliation.

Publication status: To be submitted

***Corresponding author**

6.1 Introduction

The membrane-based gas separation industrial technology has expanded significantly since the late 1970s, with key applications now encompassing hydrogen recovery, natural gas purification, air separation, and emerging areas such as olefin/paraffin separation, ethanol dehydration, and carbon capture [1-5]. To enhance its separation performance, the ongoing development of novel membrane materials—spanning organic polymers, inorganic frameworks, and hybrid composites—continues to drive research in this field. A critical standard for evaluating new membranes is their performance relative to Robeson's upper bound, which defines the trade-off between permeability and permselectivity for specific gas pairs [6]. These transport properties are fundamentally governed by the diffusivity (*D*) and solubility (*S*) coefficients of the permeating gases within the membrane material. Accurately characterizing these parameters remains central to advancing membrane technology for enhanced separation efficiency and industrial applicability.

Among the various techniques for characterizing membrane transport properties, the time-lag method remains the most widely used approach due to its simplicity [7]. This method involves conducting a dynamic gas permeation experiment in a pre-evacuated constant volume (CV) system, by monitoring the pressure rise at the permeate side over time when the test is initiated by an ideal step change in feed pressure. The time lag (θ) is determined by extrapolating the linear steady-state portion of the downstream pressure to its intersection with the time axis, and is used to calculate the diffusivity (D) [8]. Furthermore, permeability (P) is directly proportional to the steady-state flux obtained from the steady-state downstream pressure slope, and solubility (S) is calculated from the ratio of P and D. The main advantage of the time-lag method is its simplicity; meanwhile, it enables the estimation of D, P, and S from a single gas permeation experiment.

Recently, our research group designed and manufactured a new CV system that enables the accurate monitoring of the upstream pressure decay, in addition to the downstream pressure rise [9]. The availability of the new CV system has given rise to additional methods for estimating P, D, and S. Currently, to determine the transport properties (P, D, and S) of the membrane, the new CV system can provide additional distinct methods: the downstream time-lag method, the upstream time-lag method, the two-slope method, the dual time-lag method, and the accumulation method [10]. These methods are described in more detail in the Methodology section.

While the time-lag method is widely employed, its underlying assumptions are often not explicitly stated. A critical assumption in solving Fick's second law of diffusion is the boundary condition of no gas accumulation at the membrane-permeate interface. However, in practical CV systems where permeate side gas accumulation occurs, this assumption becomes invalid as the permeate concentration becomes time-dependent [11]. This phenomenon leads to a reduction in the effective driving force across the membrane, which consequently causes deviations in measured time lags - specifically an underestimation of the downstream time lag (θ_d) and overestimation of the absolute upstream time lag (θ_u). Al-Qasas et al. demonstrated that these errors can be maintained below 2% through careful system design [11].

An additional significant source of experimental deviation stems from instrumentation limitations. Upstream pressure measurements demand particularly high resolution, as transducer accuracy is linked to its maximum pressure range. To address this, our new CV system employs a dual-sensor approach: a differential pressure transducer (DPT) between a working and a reference volume to precisely quantify gas flux into the membrane, and lower-range absolute pressure transducers for monitoring upstream pressure rise [9]. While this configuration substantially improves measurement resolution, inherent deviations remain unavoidable [9]. Furthermore, temperature fluctuations introduce additional deviations. The deviation from ideal gas law assumptions during pressure monitoring can be quantified using Eq. (6.1) [10]:

$$\frac{dp}{dt} = \frac{RT}{V}\frac{dn}{dt} - \frac{p}{V}\frac{dV}{dt} + \frac{p}{T}\frac{dT}{dt} \tag{6.1}$$

The first term on the right-hand side indicates the gas flow through the membrane, and the second term is always zero. The third term indicates the pressure change due to a potential temperature drift, which can be considered negligible at the permeate side ($p \approx 0$). However, when monitoring the pressure decay, the last term on the right-hand side might not be negligible even when the temperature is well controlled because of the magnitude of the feed pressure ($p >> 0$). A temperature variation leads to extra deviation for upstream results.

Additionally, the membrane is typically supported by a porous plate to maintain its structural integrity during permeation tests. While gas transport resistance through the support plate is negligible, its presence reduces the effective transport area at the membrane interface, causing systematic underestimation of measured permeability (P). Recent work by Cao et al. [12] revealed that the porous support's geometry (pore size and porosity) and its ratio to the membrane thickness significantly affect both permeability and diffusivity (D) determinations via the time-lag method. Notably, these effects were found to be independent of the membrane's intrinsic diffusivity, with relative D and P being solely governed by the support's porosity and the ratio of the pore diameter and membrane thickness. These findings indicate the potential source of deviation from the porous support.

Another universal assumption in the time-lag experiment is that the applied pressure does not compact membranes during testing, and in other words, *P*, *D*, and *S* are independent of the applied feed pressure. However, this is valid for only rubbery polymers at moderate pressures. Our recent work observed that when external pressure is applied to the membrane, not only will the effective thickness decrease, but it will also cause a reduction in the intrinsic *P*, *D*, and *S* values [13]. This is explained by the available free volume degradation, when the flexibility of the molecular chains is limited as the membrane is compacted. The compaction effect will cause extra deviations in the membrane characterization.

The time-lag method fundamentally assumes membrane properties (*P*, *D*, and *S*) remain pressure-independent during testing. Our recent findings [13] demonstrate that the applied feed pressure induces membrane compaction, producing two concurrent effects: (1) reduction in effective membrane thickness, and (2) degradation of intrinsic transport parameters (*P*, *D*, and *S*). This phenomenon arises from a reduction in polymer free volume and restricted chain mobility under compression. These pressure-dependent variations may introduce systematic errors in transport parameter determination, with the deviation magnitude that depends on both pressure level and polymer rigidity.

In this study, additional distinct methods were employed to determine the permeability (*P*), diffusivity (*D*), and/or solubility (*S*) coefficients. Given the measurement uncertainties and potential deviations associated with each technique, a critical question arises: *What are the most probable values for P, D, and S?* Thus, data reconciliation has been used to estimate the most appropriate permeation parameters. In data reconciliation, both the reliability of data measurements and the accuracy of each estimation method are taken into consideration [14]. The optimization to find the most representative values of the transport properties is achieved by minimizing an objective function that considers the level of confidence of the various measurements and the analytical models of time-lag experiments. Weighting factors for all model-based terms were established through Monte Carlo simulations, where input parameters were varied within their experimental uncertainty ranges following Gaussian distributions. This approach not only quantifies

parameter uncertainties but also should provide statistically robust estimates of *P*, *D*, and *S* by accounting for both instrument precision and model limitations.

6.2 Methodology

As outlined in the introduction, the downstream time-lag method is a well-established technique for estimating the permeability (*P*), diffusivity (*D*), and solubility (*S*) coefficients of membranes in single-gas permeation experiments conducted using a constant-volume (CV) system [15]. The newly developed CV system enhances experimental capabilities by enabling the accurate monitoring of the upstream pressure decay, in addition to the downstream pressure rise [9]. This advancement has paved the way for additional analytical methods to determine *P*, *D*, and *S*. A shared assumption across these methods is that the penetrant gas diffuses through a homogeneous membrane according to the solution-diffusion model, as described by Eq. (2). This equation states that the ideal permeability is the product of the diffusivity and solubility, which is typically valid for rubbery polymers.

$$P = DS \tag{6.2}$$

Each estimation method yields its own set of values for *P*, *D*, and S. To determine the most reliable estimates of these transport properties, a data reconciliation approach is used. Data reconciliation accounts for uncertainties in both the measured process variables and the predictive accuracy of each model used to estimate the transport properties. This section begins by presenting the equations used to extract transport properties from the upstream pressure decay and the downstream pressure rise, as observed in time-lag experiments conducted with the new CV system. It then outlines the construction of the objective function used within the data reconciliation framework, which integrates the measured process variables and the distinct analytical models to optimize the estimates of *P*, *D*, and *S*.

6.2.1 Different models to extract *P*, *D*, and *S* from time-lag experiments

6.2.1.1 Downstream time-lag method

In the classical time lag, used by numerous researchers, the membrane separates a pressurized upstream chamber from a downstream chamber. Both chambers and the membrane are completely evacuated. The experiment is initiated by admitting the selected gas at the desired pressure in the upstream chamber. The downstream chamber, initially under vacuum or low pressure, starts to accumulate gas as it permeates through the membrane. Its accumulation in the downstream chamber is monitored over time. The characteristic time lag, referred here as the downstream time lag (θ_d), is the intercept with the time axis of the extrapolation of the linear portion of the pressure rise curve. θ_d provides a direct measure of D via Eq. (6.3), while the steady-state permeation rate yields P, as calculated by Eq. (6.4). This method offers a straightforward and integrated means of characterizing membrane transport properties [15]. In Eq. (6.3), L is the membrane thickness.

$$\theta_d = \frac{L^2}{6D} \tag{6.3}$$

$$Slope_d = \left(\frac{dp_d}{dt} \right)_{t \to \infty} = \frac{p_0 ARTP}{V_d L} \tag{6.4}$$

In Eq. (6.4), A is the membrane area, p_d is the downstream pressure rise, p_0 is the feed pressure, T is the membrane temperature, R is the universal gas constant, and V_d is the downstream chamber volume. Eq. (6.4) is the equation of the slope of the linear portion of the permeate pressure rise after steady state has been reached. The estimation of the slope is dependent on the time-dependent pressure profile recorded by the downstream pressure transducer. Once D and P have been determined, S is determined by the ratio of P over D as given in Eq. (6.1).

6.2.1.2 Upstream time-lag method

Similarly, the upstream time lag (θ_u), calculated from the pressure decay profile, can provide an additional estimate of D, as given by Eq. (6.5).

$$\theta_u = -\frac{L^2}{3D} \tag{6.5}$$

Akin to the downstream time-lag method, the same mass balance can be performed for the pressure decay to calculate the steady-state permeation rate and determine an additional estimate of *P*.

$$Slope_u = \left(\frac{dp_u}{dt}\right)_{t\to\infty} = \frac{p_0 ARTP}{V_u L} \tag{6.6}$$

In Eq. (6.6), V_u is the upstream volume, and p_u is the upstream pressure.

In our experiments, the simultaneous monitoring of the pressure decay with great accuracy was achieved by splitting the upstream volume into a working and reference volumes and monitoring pressure decay using a differential pressure transducer between the two volumes. This apparatus may cause additional variance of the method compared to the downstream time-lag method, especially at the initiation of the experiment.

In both time-lag methods, permeability is determined from the slope of the linear region of the pressure-versus-time curve, while diffusivity is determined from the time-lag coefficients (θ) obtained by extrapolating this linear portion to the time axis. These estimations rely on the assumption of ideal boundary conditions, specifically, that the concentration at the upstream side of the membrane remains constant, and that the concentration at the permeate side is zero throughout the permeation experiment. However, in practical CV systems, estimating *P* and *D* from upstream pressure decay and downstream pressure rise is only feasible when these ideal assumptions are not strictly upheld [11]. Gas accumulation reduces the pressure gradient, leading to a reduction in flux. This effect shortens the downstream time lag (θ_d) and increases the absolute value of the upstream time lag ($|\theta_u|$). Jenkins et al. [16] conducted a series of numerical investigations to investigate the deviations caused by this phenomenon. Their findings indicate that diffusivity can be overestimated by more than 4% at the permeate side, even in well-designed systems. Moreover, the deviation in upstream time lag can be substantially greater, constrained by the accuracy of the extrapolation method.

To minimize errors caused by this effect, it is essential to carefully select the analytical window used for time-lag determination. Specifically, using a shorter and earlier linear extrapolation window reduces the impact on the measured time lags. However, a sufficient transient period must precede the linear region to ensure that gas permeation has reached a steady state [11]. Recent studies indicate that steady-state permeation is typically achieved before $3\theta_d$, and recommend performing linear extrapolation within the time range of $3\theta_d$ to $4\theta_d$ to minimize deviations.

6.2.1.3 Two-slope method

Analytical methods based on pressure decay generally follow a similar experimental protocol to the time-lag method for characterizing membrane behavior, whether upstream or downstream. However, a key distinction lies in their operational principles: the time-lag method relies on reaching steady-state permeation, whereas pressure decay analysis captures valuable information during the transient phase, which can also be used to assess membrane transport properties. Immediately after the initiation of the permeation, the membrane behaves as a semi-infinite solid ($0 < Fo < 0.2$), during which the pressure decay (Δp_u) exhibits a linear relationship with the square root of time [17]:

$$\Delta p_u = -\frac{2 p_0 SRTA\sqrt{D}}{V_u\sqrt{\pi}}\sqrt{t} \tag{6.7}$$

where Δp_u is the upstream (feed) pressure decrease, V_u is the constant upstream volume, A is the membrane area, T is the absolute temperature, and R is the universal gas constant. The slope of Δp_u vs $\sqrt{t}$ is directly proportional to $S\sqrt{D}$, and the intercept of which is zero. The constant slope of this transient period ($Slope_t$) is given by:

$$Slope_t = \frac{dp_u}{d\sqrt{t}} = -\frac{2 p_0 SRTA\sqrt{D}}{V_0\sqrt{\pi}} \tag{6.8}$$

The diffusivity can be obtained by taking the ratio of Eq. (6.6) and Eq. (6.8), which leads to:

$$\frac{Slope_u}{Slope_t} = \frac{\sqrt{\pi}}{2L}\sqrt{D} \tag{6.9}$$

Similar to the previous methods, P can be evaluated from the steady-state slope described in Eq. (6). Once both P and D are known, S can be determined from the solution-diffusion model, as defined in Eq. (2). This method combines two distinct slopes, one from the steady-state period and another from the transient phase of the pressure decay profile, to directly evaluate diffusivity. Accordingly, we refer to this method as the two-slope method.

6.2.1.4 Dual time-lag method

As previously mentioned, a key advantage of the new CV system is its ability to simultaneously record both the upstream pressure decay and the downstream pressure rise. This dual-monitoring capability enables a novel analytical approach: combining upstream and downstream time-lag data to achieve a more robust and comprehensive characterization of diffusivity. Due to its integrated measurement strategy, this technique is referred to as the dual time-lag method, as it unifies the traditional upstream and downstream methodologies into a single, cohesive framework.

The gas flux entering ($J(0,t)$) and leaving ($J(L,t)$) the membrane can be evaluated by applying Fick's first law of diffusion to the concentration profile within the membrane. This profile is derived from a solution obtained via separation of variables, expressing concentration as a function of both time and spatial position:

$$J\left(0,t\right) = \frac{p_0 P}{L} + 2\frac{p_0 P}{L}\exp\left(-\frac{D\pi^2 t}{L^2}\right) \tag{6.10}$$

$$J\left(L,t\right) = \frac{p_0 P}{L} - 2\frac{p_0 P}{L}\exp\left(-\frac{D\pi^2 t}{L^2}\right) \tag{6.11}$$

Next, Eqs. (10) and Eq. (11) are integrated to determine the number of moles of gas molecules entering and exiting the membrane, denoted as $M_{in}(t)$ and $M_{out}(t)$, respectively.

These quantities are directly correlated with the upstream pressure decay and the downstream pressure rise.

$$M_{in}(t) = \frac{V_u \Delta p_u}{RT} = A\int_0^t J(0,t)\,dt \tag{6.12}$$

$$M_{out}(t) = \frac{V_d \Delta p_d}{RT} = A\int_0^t J(L,t)\,dt \tag{6.13}$$

Once steady-state conditions are achieved, Eqs. (12) and (13) can be simplified and expressed in their reduced forms as shown in Eqs. (14) and (15).

$$M_{in}(t) = \frac{V_u \Delta p_u}{RT} = A\int_0^t J(0,t)\,dt \tag{6.14}$$

$$M_{out}(t) = \frac{V_d \Delta p_d}{RT} = A\int_0^t J(L,t)\,dt \tag{6.15}$$

As illustrated in Figure 6.1, once steady-state conditions are reached and the numbers of moles entering and exiting the membrane are equal ($M_{in}(t_{in}) = M_{out}(t_{out})$), the horizontal distance between the upstream and downstream time lags reflects the difference between θ_u and θ_d. This time offset is used to calculate D, as defined in Eq. (6.16).

$$\theta_d - \theta_u = \frac{L^2}{2D} \tag{6.16}$$

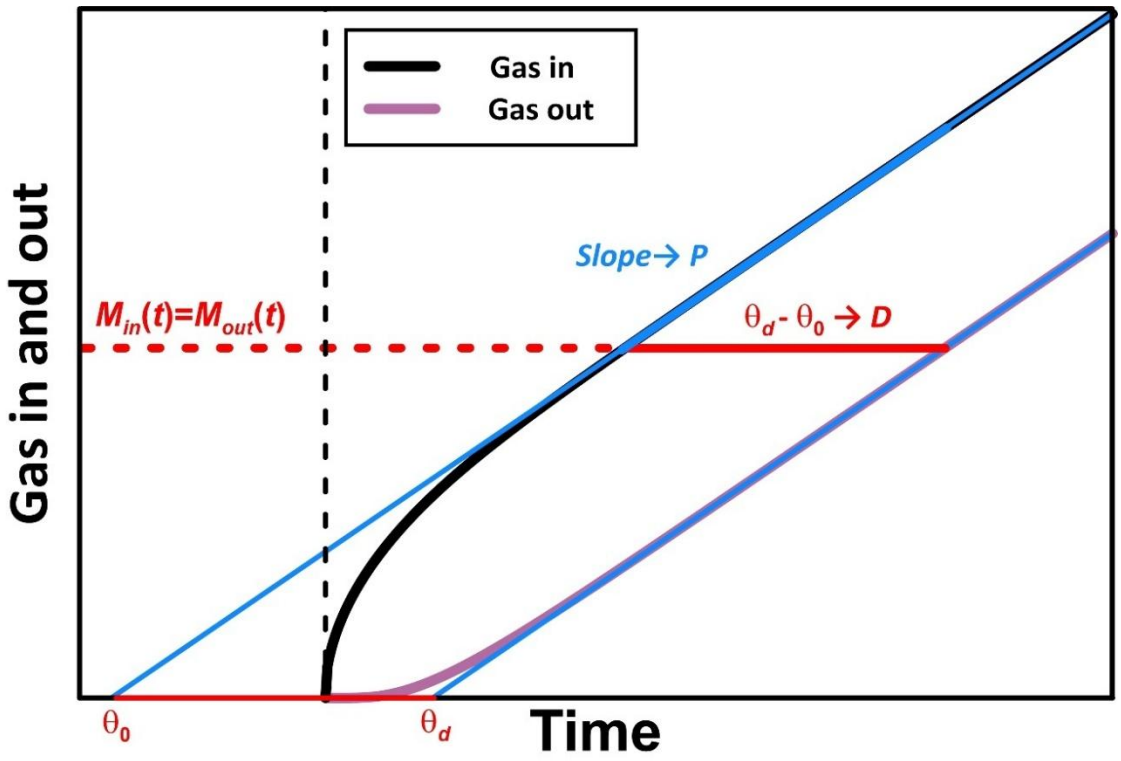

Figure 6.1 Schematic representation of the dual time-lag method based on the absolute gas flux entering the membrane and the gas flux exiting the membrane under steady state conditions.

6.2.1.5 Accumulation method

In our earlier work, we presented a new characterization method for directly determining *D* and *S* based on the gas accumulation in the membrane as a function of time [10]. This innovative approach, implemented through our modified CV system, uniquely combines simultaneous monitoring of upstream pressure decay and downstream pressure rise in a single permeation experiment to evaluate the gas uptake rate of the membrane material. Unlike conventional techniques that derive *D* directly and, subsequently, calculate *S* as *P*/*D*, our accumulation-based method provides a direct evaluation of *S* and *D* through measurement of gas accumulation rate as a function of time in the membrane material.

First, we recognize that gas accumulation in the membrane as a function of time, $M(t)$, is related to the fluxes in and out of the membrane:

$$M\left(t\right)=M_{in}(t)-M_{out}(t)=A\left\{\int_{0}^{t}J\left(0,t\right)dt-\int_{0}^{t}J\left(L,t\right)dt\right\} \tag{6.17}$$

When $Fo > 0.2$, substituting Eq. (6.10) and Eq. (6.11) into Eq. (6.17) leads to:

$$M(t)=\frac{Sp_0LA}{2}\left[1-\exp\left(-\frac{D\pi^2t}{L^2}\right)\right] \tag{6.18}$$

As $t \to \infty$, i.e. at steady state, $M(t)$ becomes a constant value M_∞:

$$M_\infty=\frac{Ap_0SL}{2} \tag{6.19}$$

M_∞ can be evaluated experimentally or graphically by determining the vertical distance between the summation of the number of moles entering and leaving the membrane. The gas solubility can be directly determined by:

$$S=\frac{2M_\infty}{p_0LA} \tag{6.20}$$

Once M_∞ has been determined, this method also provides an additional means to characterize D. Dividing both sides of Eq. (6.18) by M_∞ and rearranging the resulting equation, we obtain:

$$1-\frac{M\left(t\right)}{M_\infty}=\exp\left(-\frac{D\pi^2t}{L^2}\right) \tag{6.21}$$

Taking the natural logarithm of both sides of Eq. (6.21) yields:

$$M_{\ln}\left(t\right)=\ln\left(1-\frac{M\left(t\right)}{M_\infty}\right)=-\frac{D\pi^2t}{L^2} \tag{6.22}$$

The diffusivity can be determined from the slope (σ) of Eq. (6.22) as:

$$\sigma = -\frac{D\pi^2}{L^2} \tag{6.23}$$

6.2.2 Constructing and solving the objective function for data reconciliation

Within the data reconciliation framework, the objective function consists of two primary components: the measured process variables and the predictive models for transport properties. Each component will be examined individually in the following sections.

6.2.2.1 Measured variables

Each time-lag experiment conducted using the CV system involves several process variables that influence the estimation of the transport properties. The six main variables are the upstream gas pressure (p_0), the temperature (T), the upstream chamber volume (V_u), the downstream chamber volume (V_d), the membrane area (A), and the membrane thickness (L). These variables appear throughout the governing equations and are essential for calculating P, D, and S. The variables are measured or estimated to the best of our knowledge. While these variables are measured or estimated to the best of our ability, each carries a degree of uncertainty. The data reconciliation approach accounts for this uncertainty by allowing the variables to adjust within their confidence bounds to satisfy the global objective function. The data reconciliation method recognizes this fact and allows these variables to vary to satisfy the global objective function. As a result, the first component of the objective function comprises the six measurement terms, as defined in Eq. (24). Variables marked with a caret (^) indicate those subject to modification by the optimization algorithm to minimize the objective function. Each term is affected by the inverse of the variance of the variable. A variable with high measurement precision will have a low variance, resulting in a strong weighting that keeps its optimized value close to the measured one. Conversely, variables with greater uncertainty (higher variance) are given more flexibility to deviate from their initial estimates during optimization.

$$J_1 = \frac{1}{\sigma_{p_0}^2}(\hat{p}_0 - p_0)^2 \tag{6.24a}$$

$$J_2 = \frac{1}{\sigma_T^2}(\hat{T} - T)^2 \tag{6.24b}$$

$$J_3 = \frac{1}{\sigma_{V_d}^2}(\hat{V}_d - V_d)^2 \tag{6.24c}$$

$$J_4 = \frac{1}{\sigma_{V_u}^2}(\hat{V}_u - V_u)^2 \tag{6.24d}$$

$$J_5 = \frac{1}{\sigma_A^2}(\hat{A} - A)^2 \tag{6.24e}$$

$$J_6 = \frac{1}{\sigma_L^2}(\hat{L} - L)^2 \tag{6.24f}$$

6.2.2.2 Models to calculate *P*, *D*, and *S*

Data reconciliation is most effective when a variable can be estimated using multiple independent methods or measurements. This redundancy enables the detection and correction of inconsistencies and errors, resulting in more reliable and coherent results. In the absence of alternative calculation pathways, reconciliation lacks the necessary cross-validation to enhance precision. Fortunately, the introduction of the new CV system, which allows for the determination of upstream and downstream time lags, provides sufficient redundancy to implement data reconciliation effectively for estimating membrane transport properties. The equations presented in Section 6.2.1 can be reformulated as distinct objective functions.

For the downstream time lag (θ_d), Eq. (6.25a) defines J_7, which corresponds to Eq. (6.3). It is desired to maintain the estimation of D as close as possible to its value determined via the downstream time-lag method. This will be the case for all terms of the objective function. Similarly, for the upstream time lag (θ_u), J_8 represents Eq. (6.5) and is

defined by Eq. (6.25b). The permeability coefficient (P) can be estimated using the slope of the steady-state permeation rate, specifically for the downstream pressure rise (Eq. (6.25c) defining J_9, which is a reformulation of Eq. (6.4)), and the downstream pressure decay (Eq. 6.25d defining J_{10} based on Eq. (6.6)).

Eq. (6.9) can provide a means to estimate D, as represented by J_{11} in Eq. (6.25e). The slope of the pressure decay has already been calculated in Eq. (6.25c). However, the slope of the pressure decay as a function of the square root of time must be evaluated prior to the point at which molecules begin exiting the membrane, beyond which the infinite solid assumption no longer holds.

In the dual time-lag method, Eq. (6.16) is reformulated as J_{12} (Eq. (6.25f)). To compute the difference (θ_d - θ_u), the time-axis distance corresponding to the same steady flux was averaged over ten data points.

For the accumulation method (J_{13}, Eq. (6.20), and Eq. 6.25g), the vertical distance between the negative upstream pressure decay and the downstream pressure rise curves under steady-state conditions, and converted into the total moles accumulated, evaluates the number of moles that are present in the polymeric membrane (M_∞). As a result, the solubility (S) can be estimated. The accumulation method can also provide an additional means to estimate D. Indeed, the slope of the natural logarithm of the fraction of the number of moles that remained to be absorbed to reach saturation, as described in Eqs. (6.22)-(6.23), is directly proportional to D. Eq. (6.23) has been reformulated to define J_{14}, given by Eq. (6.25h).

The relationship $P = DS$ (Eq. (6.1)), which is valid for gas permeation following the solution-diffusion mechanism, is used in Eq. (6.25i) to define J_{15} [18]. Finally, Eq. (6.25j) defines J_{16}, which specifies that the ratio of the upstream time lag to the downstream time lag is equal to two for rubbery polymers. In this investigation, gas permeation experiments were conducted using polydimethylsiloxane (PDMS), which is a rubbery polymer and, therefore, the relationship described by J_{16} prevails.

$$J_7 = \frac{1}{\sigma_7^2}\left(\hat{D} - \frac{L^2}{6\theta_d}\right)^2 \tag{6.25a}$$

$$J_8 = \frac{1}{\sigma_8^2}\left(\hat{D} - \frac{L^2}{3|\theta_u|}\right)^2 \tag{6.25b}$$

$$J_9 = \frac{1}{\sigma_9^2}\left(\hat{P} - \frac{V_d L}{p_0 ART}\left(\frac{dp_d}{dt}\right)_{t\to\infty}\right)^2 \tag{6.25c}$$

$$J_{10} = \frac{1}{\sigma_{10}^2}\left(\hat{P} - \frac{V_u L}{p_0 ART}\left(\left|\frac{dp_u}{dt}\right|\right)_{t\to\infty}\right)^2 \tag{6.25d}$$

$$J_{11} = \frac{1}{\sigma_{11}^2}\left(\hat{D} - \frac{(2L)^2}{\pi}\left(\frac{Slope_u}{Slope_t}\right)^2\right)^2 \tag{6.25e}$$

$$J_{12} = \frac{1}{\sigma_{12}^2}\left(\hat{D} - \frac{L^2}{2(\theta_d - \theta_u)}\right)^2 \tag{6.25f}$$

$$J_{13} = \frac{1}{\sigma_{13}^2}\left(\hat{S} - \frac{2M_\infty}{p_0 LA}\right)^2 \tag{6.25g}$$

$$J_{14} = \frac{1}{\sigma_{14}^2}\left(\hat{P} - \hat{D}\hat{S}\right)^2 \tag{6.25h}$$

$$J_{15} = \frac{1}{\sigma_{15}^2}\left(\hat{P} - \hat{D}\hat{S}\right)^2 \tag{6.25i}$$

$$J_{16} = \frac{1}{\sigma_{16}^2}\left(\frac{|\theta_u|}{\theta_d} - 2\right)^2 \tag{6.25j}$$

All individual terms from J_1 to J_{16} collectively define the global objective function, as presented in Eq. (26). This function is optimized by adjusting nine independent variables to simultaneously minimize all 16 individual terms. To determine the variance of each

objective term from J_7 to J_{16}, Monte Carlo simulations were conducted. In these simulations, the first six variables were randomly varied according to a normal distribution, constrained by their respective standard deviations. A total of 1000 simulations were performed, and the resulting standard deviations of each model output were calculated and incorporated into the global objective function.

$$\text{Find} \begin{Bmatrix} \hat{p}_0 & \hat{T} & \hat{V}_d & \hat{V}_u & \hat{A} \\ \hat{L} & \hat{P} & \hat{D} & \hat{S} & \end{Bmatrix} \text{to minimize} \sum_{i=1}^{14} J_i \tag{6.26}$$

6.3 Results and discussion.

6.3.1 Ideal gas permeation experiment.

In this section, we evaluate the performance of the data reconciliation algorithm under ideal conditions using a simulated gas permeation experiment, referred to as File 1. Figure 6.2 displays the upstream pressure decay and downstream pressure rise curves for this illustrative case, represented by solid lines. Table 6.1 summarizes the data reconciliation results for this ideal experiment in its first two rows. It lists nine variables subject to adjustment by the optimization routine: six measured variables (p_0, T, V_d, V_u, A, and L) and three transport parameters (P, D, and S). The first row presents the original measured values along with estimates of the transport properties derived using the downstream time-lag method. The second row shows the values of these nine variables after applying data reconciliation. The reconciled values closely match the initial measurements and property estimates, with a total sum of squares for the 16 objective function terms of just 0.43. This minimal deviation indicates that the initial parameters, including the transport properties P, D, and S, remained virtually unchanged, thereby confirming the consistency and theoretical reliability of the five analytical approaches. These findings demonstrate that the models produced highly accurate estimates of the transport parameters, thereby validating the effectiveness of the data reconciliation algorithm. It can be confidently applied to the analysis of actual gas permeation experiments when both upstream pressure decay and downstream pressure rise are available.

The ideal permeation experiment assumes ideal boundary conditions—specifically, a constant upstream pressure and a downstream concentration maintained at zero throughout the entire permeation. To assess the impact of more realistic conditions, the same scenario was simulated using the same nine parameters, but with dynamic boundary conditions where both the upstream and downstream pressures varied as a function of the time-dependent permeation flux through the membrane. The resulting pressure decay and rise curves are shown in Figure 6.2 as red dashed lines. Notably, introducing realistic boundary conditions produced no significant deviation in the pressure profiles. The relatively small pressure variations on both sides of the membrane had no discernible effect on the estimation of the transport properties.

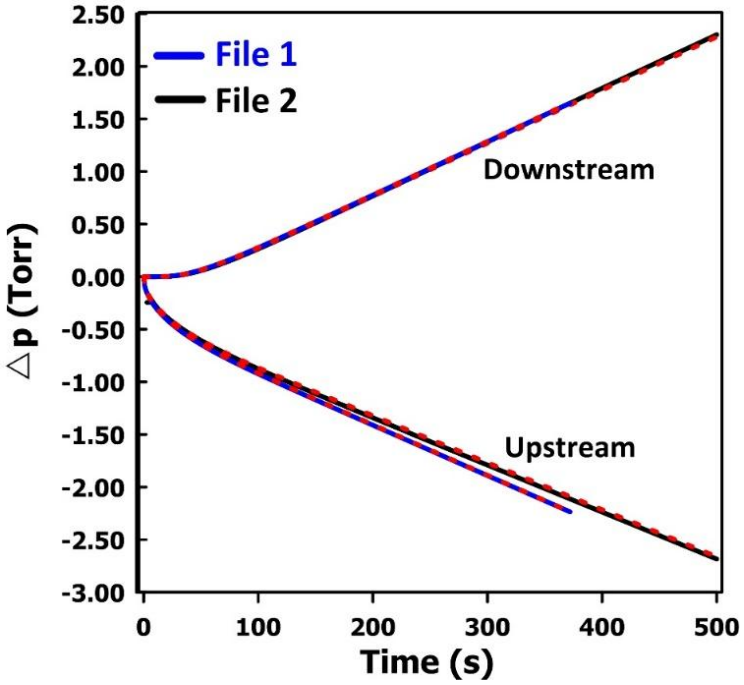

Figure 6.2 Typical pressure decay and pressure rise during a time-lag experiment.

6.3.2 Data reconciliation of real gas permeation experiments

Data reconciliation was applied to estimate nine initial variables—six measured quantities and three transport properties—for each of nine gas permeation experiments conducted using the CV system. For each experimental file (Files 2–10), the first row of Table 6.1 presents the measured values and the initial estimates of the transport properties,

which serve as the starting point for the reconciliation process. The initial estimates of P, D, and S are predicted from the original experimental time lags. The second row displays the reconciled values of these same variables following optimization. Additionally, Table 6.1 includes the corresponding values of the objective function, as defined in Eq. (6.26).

We begin by examining the results of File 2, as its nine initial measurements and transport properties (listed in Table 6.1) were used to simulate the ideal upstream pressure decay and downstream pressure rise curves discussed in the previous section. This setup allows for a direct comparison between ideal and experimental pressure profiles under identical conditions. Figure 1 reveals that the experimental downstream pressure rise curve aligns almost perfectly with the curve simulated using the initial parameters under ideal conditions (File 1). Furthermore, the simulated pressure rise curves for Files 1 and 2, generated using reconciled parameters and realistic boundary conditions, also match the experimental data precisely. These findings reaffirm that minor deviations from ideal boundary conditions have no significant impact on the estimation of transport properties. The downstream pressure rise remains accurately predicted by the analytical model. To reconcile the experimental data from File 2, the objective function defined in Eq. (6.26) was minimized. This process led to slight adjustments in the upstream and downstream volumes. Additionally, the permeability and solubility values, initially estimated using the downstream time-lag method, decreased by 3% and 8%, respectively, while the diffusivity remained virtually unchanged. In contrast, Figure 6.2 shows a noticeable difference between the upstream pressure decay curves of the simulated (File 1) and experimental (File 2) data. Interestingly, when real boundary conditions are incorporated into the simulation, the resulting pressure decay curves are identical to both the experimental curve from File 2 and the ideal simulation from File 1.

Table 6.1 Results of 10 permeation experiments for the estimation of P, D, and S. The first row of each file comprises the six measurements and the estimated values of P, D, and S based on the downstream time lag. File 1 is the simulated file with ideal boundary conditions, and Files 2–10 are experimental files.

File	p_0 (Torr)	T (K)	V_u (m^3)	V_d (m^3)	A (m^2)	L (m)	P (m^2/s)	D (m^2/s)	S (-)	ΣJ_i
1	1.15E+03	3.03E+02	8.60E-05	8.10E-05	1.32E-03	6.05E-04	1.64E-10	1.28E-09	1.28E-01	4.33E-01
	1.15E+03	3.03E+02	8.60E-05	8.10E-05	1.32E-03	6.05E-04	1.64E-10	1.29E-09	1.27E-01	
2	1.15E+03	3.03E+02	8.60E-05	8.10E-05	1.32E-03	6.05E-04	1.64E-10	1.28E-09	1.28E-01	7.08E+00
	1.15E+03	3.03E+02	8.77E-05	7.91E-05	1.32E-03	6.03E-04	1.59E-10	1.27E-09	1.18E-01	
3	8.58E+02	3.03E+02	1.00E-04	8.10E-05	1.32E-03	9.95E-04	1.77E-10	1.21E-09	1.47E-01	2.82E+02
	8.58E+02	3.03E+02	1.03E-04	7.73E-05	1.32E-03	9.42E-04	1.57E-10	9.67E-10	1.39E-01	
4	1.16E+03	3.03E+02	1.00E-04	8.10E-05	1.32E-03	9.88E-04	1.58E-10	1.23E-09	1.29E-01	5.18E+01
	1.16E+03	3.03E+02	1.03E-04	7.73E-05	1.32E-03	9.79E-04	1.48E-10	1.14E-09	1.28E-01	
5	1.16E+03	3.03E+02	1.00E-04	8.10E-05	1.32E-03	9.78E-04	2.00E-10	1.10E-09	1.81E-01	1.64E+00
	1.16E+03	3.03E+02	1.03E-04	7.76E-05	1.32E-03	9.78E-04	1.90E-10	1.10E-09	1.69E-01	
6	1.84E+03	3.03E+02	1.00E-04	8.10E-05	1.32E-03	9.71E-04	1.17E-10	1.06E-09	1.11E-01	3.26E+02
	1.84E+03	3.03E+02	1.05E-04	7.37E-05	1.32E-03	9.17E-04	1.01E-10	7.98E-10	1.35E-01	
7	1.15E+03	3.03E+02	8.70E-05	8.10E-05	1.32E-03	5.99E-04	1.65E-10	1.29E-09	1.28E-01	1.47E+01
	1.15E+03	3.03E+02	8.65E-05	8.15E-05	1.32E-03	5.95E-04	1.64E-10	1.29E-09	1.18E-01	
8	1.53E+03	3.03E+02	8.90E-05	8.10E-05	1.32E-03	4.32E-04	1.53E-10	1.10E-09	1.40E-01	1.32E+00
	1.53E+03	3.03E+02	8.75E-05	8.26E-05	1.32E-03	4.32E-04	1.56E-10	1.04E-09	1.44E-01	
9	1.53E+03	3.03E+02	9.00E-05	8.10E-05	1.32E-03	5.91E-04	1.63E-10	1.18E-09	1.38E-01	6.39E+01
	1.53E+03	3.03E+02	8.98E-05	8.12E-05	1.32E-03	5.70E-04	1.57E-10	1.09E-09	1.42E-01	
10	1.85E+03	3.03E+02	1.00E-04	8.10E-05	1.32E-03	9.71E-04	1.38E-10	1.07E-09	1.29E-01	1.89E+02
	1.85E+03	3.03E+02	9.99E-05	8.11E-05	1.32E-03	9.39E-04	1.41E-10	1.08E-09	1.12E-01	

Table 6.1 shows that, for most experiments, the measured values of the six process variables remained largely unchanged during the data reconciliation process. This suggests that the original measurements were reasonably accurate. However, in a few cases, the measured values underwent substantial adjustments in an effort to optimize both the six measurements and the three transport parameters to minimize the objective

function. These large and implausible changes indicate potential issues with the corresponding permeation experiments and are typically associated with elevated objective function values. This is exemplified by File 6, which exhibits the highest objective function value. Figure 6.3 displays the upstream pressure decay and downstream pressure rise curves for the File 6 experiment (solid lines), alongside the simulated curves (dashed lines) generated using the reconciled values of the six measurements and three transport parameters under realistic boundary conditions. Remarkably, the reconciliation of File 6, using all nine adjustable parameters, resulted in a near-perfect match with the experimental pressure curves. The algorithm leveraged the flexibility in the measured process variables to minimize the objective function. In this case, the reconciled volume of the upstream chamber and the membrane thickness were reduced by 10% and 5.6%, respectively. Since these variables can typically be measured with relatively high precision, such deviations strongly suggest that an error occurred during the permeation experiment. The primary cause of the observed deviation in this experiment is its limited duration, as it was terminated after only three time lags according to the downstream time-lag method.

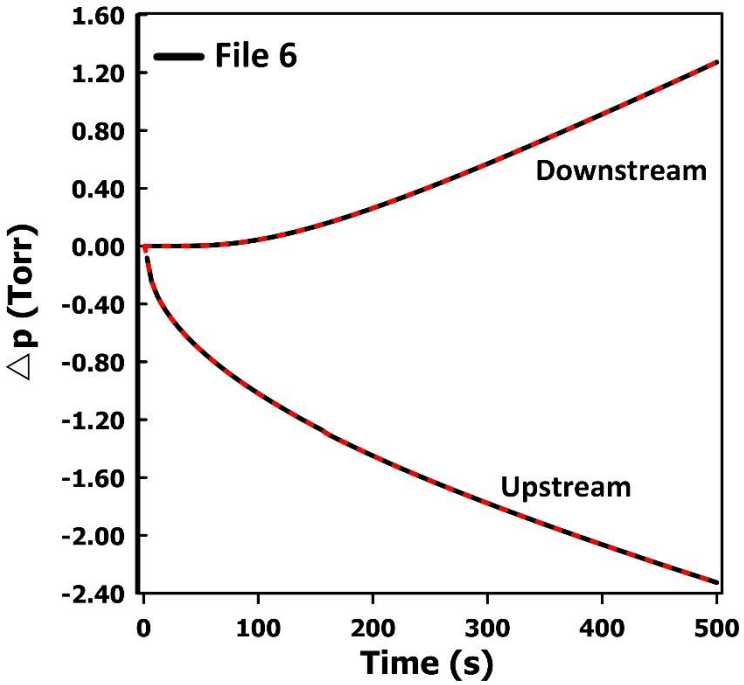

Figure 6.3 Experimental pressure decay and pressure rise (solid lines) as a function of time compared to the simulated ones (dashed lines) using the nine reconciled variables for File 6 and real boundary conditions.

To better visualize and evaluate the performance of data reconciliation across the permeation experiments, Figure 6.4 presents the ratio of the reconciled value to the originally estimated value for each of the 16 terms in the objective function. For the six measured variables, this ratio reflects the reconciled value divided by the original measurement. For the ten model-based estimations (terms J_7 to J_{16}), each is similarly expressed as a ratio. For example, the ratio for J_7, i.e. $\hat{D} / (L^2 / 6\theta_d)$, illustrates the ratio of the reconciled diffusivity and the model used for its estimation for that specific model term. These ratios serve as indicators of the accuracy of both the measurements and the estimation models. When most values cluster near the unity line, it suggests a high-quality permeation experiment with a low objective function value, thereby increasing confidence in the estimated transport parameters. This pattern is observed in Files 1, 2, 5, 7, and 8. In contrast, Files 3, 6, and 10 exhibit more erratic behavior, with ratios deviating significantly from unity and corresponding to higher objective function values. The plots in Figure 4 offer valuable insights into the reliability of the experimental data. For instance, the ratio associated with J_7 highlights the potential error in estimating diffusivity when relying solely on the downstream time-lag method. Additionally, it is hypothesized that these ratios may act as a distinctive fingerprint for assessing the quality and reliability of a given gas permeation experiment.

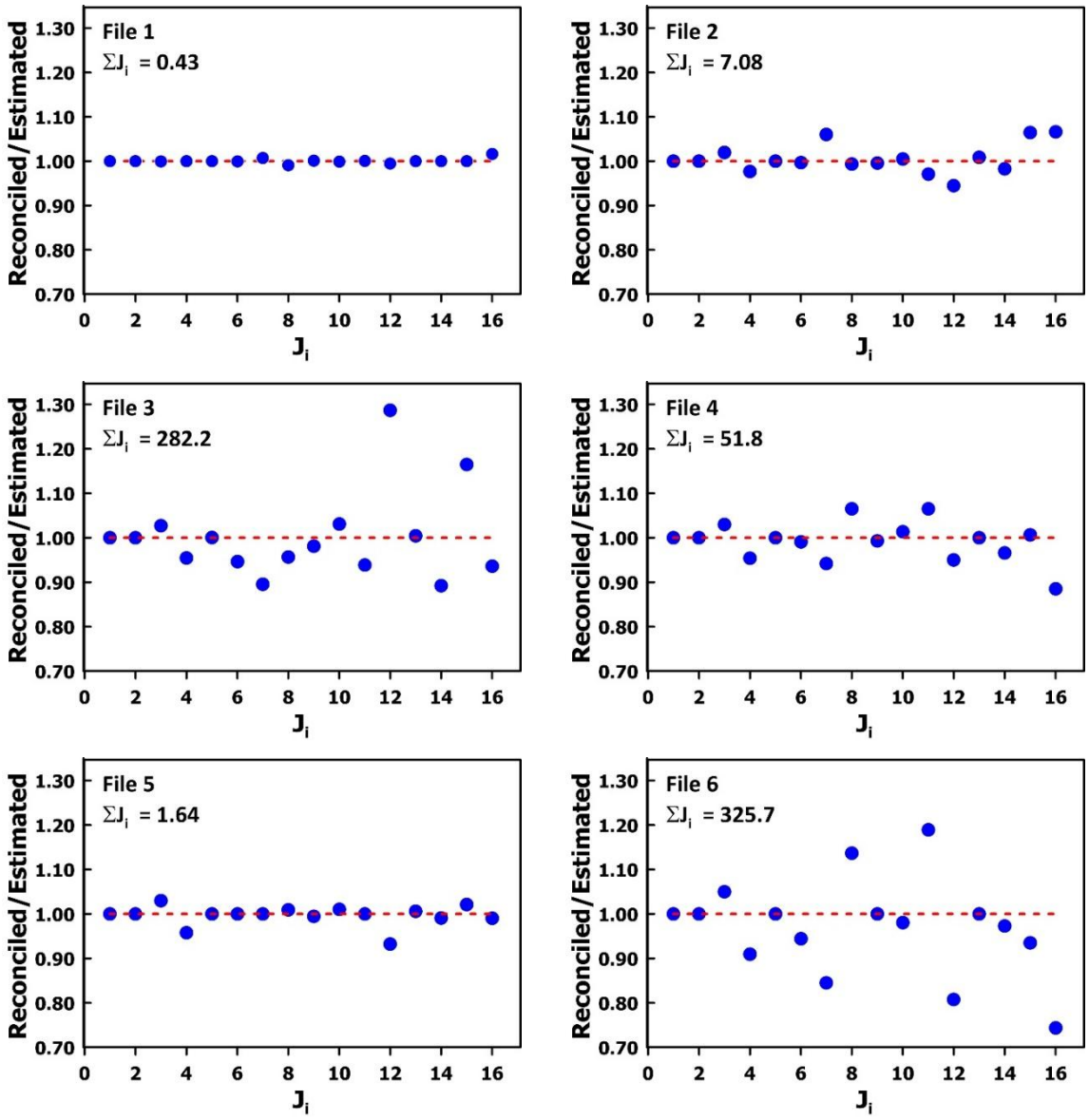
File 1
ΣJi = 0.43
File 2
ΣJi = 7.08
File 3
ΣJi = 282.2
File 4
ΣJi = 51.8
File 5
ΣJi = 1.64
File 6
ΣJi = 325.7
Reconciled/Estimated
Ji
0.70
0.80
0.90
1.00
1.10
1.20
1.30
0
2
4
6
8
10
12
14
16

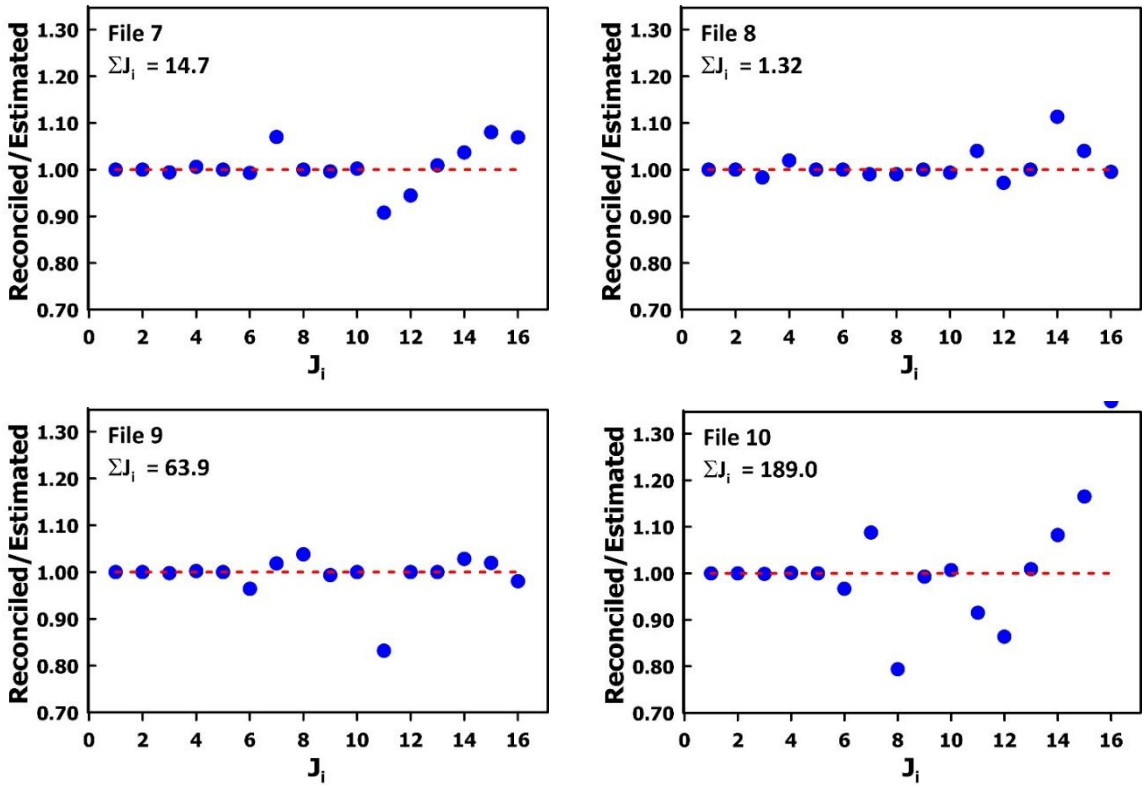

Figure 6.4 The ratio of converged value over the estimated value for each of the 16 individual terms of the objective function, comprised of the 6 measurements and 10 model-based estimations.

6.4 Conclusion

In this investigation, the data reconciliation technique was used to identify the most probable values of the membrane transport properties (*P*, *D*, and *S*) in the time-lag experiment. Through simultaneous monitoring of the upstream pressure decay and downstream pressure rise in a novel constant-volume system, five approaches were considered, each providing independent estimates of the transport parameters. The data reconciliation approach considered uncertainties from both experimental measurements and model assumptions, yielding statistically robust values for *P*, *D*, and *S*. The objective function was composed of six terms for experimental measurements and eight terms for the estimation methods. The weighting factors of each measurement term can be easily determined, whereas the Monte Carlo simulation was used to determine the weighting

factors for each method model. And the optimization of the measurements and the transport properties is achieved by minimizing the overall objective function.

The key motivation of this work is the significant enhancement in the reliability and precision of the extracted transport parameters using alternative methods combining upstream and downstream results in time lag experiments. The reconciliation process yielded statistically robust, consolidated values for *P*, *D*, and *S*, resolving inconsistencies inherent in using any single method alone. Furthermore, the analysis provided a powerful diagnostic tool by inspecting the individual objective functions. The adjustments during optimization and the final objective function value serve as direct indicators of individual experiment quality, successfully identifying specific experimental file errors.

The comprehensive protocol for membrane characterization validated by the power of data reconciliation not only delivers more trustworthy values but also establishes a generalizable methodology for uncertainty quantification and quality control in permeation experiments. It is potentially applicable to more complex membrane systems, promising a significant advancement in the accuracy and reliability of material characterization.

Appendix A

A.1 Analytical solutions for the upstream and downstream time lag

The local concentration of the permeating species $C(x,t)$ within the membrane, as a function of time (t) and position (x), evolves according to Fick's second law of diffusion (Eq. A.1), which governs gas permeation through the membrane via diffusion.

$$\frac{\partial C}{\partial t} = D\frac{\partial^2 C}{\partial x^2} \tag{A.1}$$

Prior to the start of the experiment, the membrane is evacuated under high vacuum, resulting in a uniform initial concentration of zero throughout. The experiment commences with an instantaneous pressure increase that remains constant in the upstream chamber, thereby imposing a fixed boundary condition at the upstream interface ($x = 0$).

Meanwhile, the downstream pressure ($x = L$) is maintained at zero. These conditions form the basis for the initial and boundary assumptions outlined in Eq. (A.2).

$$IC: C(x,0) = 0 \tag{A.2a}$$

$$BC1: C(0,t) = p_0 \cdot S \tag{A.2b}$$

$$BC2: C(L,t) = 0 \tag{A.2c}$$

The solution of Eq. (A.1) subjected to the initial and ideal boundary conditions in Eq. (A.2) can be obtained by separation of variables. The solution (Eq. A.3) gives the concentration profile as a function of time (t) and distance in the membrane (x).

$$C(x,t) = p_0 S\left(1-\frac{x}{L}\right) - \frac{2p_0 S}{\pi} \times \sum_{n=1}^{\infty} \frac{1}{n} \sin\left(\frac{n\pi x}{L}\right) \exp\left(-\frac{Dn^2\pi^2 t}{L^2}\right) \tag{A.3}$$

To determine the corresponding fluxes at both interfaces, Fick's first law can be used, as expressed by Eq. (A.4).

$$J = -D\frac{\partial C}{\partial x} \tag{A.4}$$

The analytical solutions for the gas fluxes at the upstream interface ($x = 0$) and downstream interface ($x = L$) are given in Eqs. (A.5) and (A.6).

$$J_u = J(0,t) = \frac{Dp_0 S}{L} + \frac{2Dp_0 S}{L} \times \sum_{n=1}^{\infty} \exp\left(\frac{-n^2\pi^2 Dt}{L^2}\right) \tag{A.5}$$

$$J_d = J(L,t) = \frac{Dp_0 S}{L} + \frac{2Dp_0 S}{L} \times \sum_{n=1}^{\infty} \cos(n\pi) \exp\left(\frac{-n^2\pi^2 Dt}{L^2}\right) \tag{A.6}$$

To determine the time lags, the pressures on the upstream and downstream sides can be calculated by conducting a mass balance in each chamber by integrating their fluxes with time, as expressed in Eqs. (A.7) and (A.8).

$$p(0,t) - p_0 = -\frac{ART}{V_u} \int_0^t J(0,t)\, dt \tag{A.7}$$

$$p(L,t)-0=-\frac{ART}{V_d}\int_0^t J\left(L,t\right)dt \tag{A.8}$$

The expressions for the upstream pressure and downstream pressure as a function of time were derived as:

$$\Delta p_u = p(0,t)-p_0 = -\frac{p_0 ARTP}{V_u L}\left[t+\frac{L^2}{3D}+\frac{2L^2}{\pi^2 D}\times\sum_{n=1}^{\infty}\left(\frac{-1}{n^2}\right)\exp\left(-\frac{Dn^2\pi^2 t}{L^2}\right)\right] \tag{A.9}$$

$$\Delta p_d = p(L,t)-0 = -\frac{p_0 ARTP}{V_d L}\left[t-\frac{L^2}{6D}+\frac{2L^2}{\pi^2 D}\times\sum_{n=1}^{\infty}\frac{(-1)^{n+1}}{n^2}\exp\left(-\frac{Dn^2\pi^2 t}{L^2}\right)\right] \tag{A.10}$$

After the steady-state has been achieved ($t\to\infty$), the transient terms in Eqs. (A.9) and (A.10) become negligible, and the above equations can be simplified to the following linear equations:

$$\lim_{t\to\infty}\Delta p_u = -\frac{p_0 ARTP}{V_u L}\left(t+\frac{L^2}{3D}\right) \tag{A.11}$$

$$\lim_{t\to\infty}\Delta p_d = -\frac{p_0 ARTP}{V_d L}\left(t-\frac{L^2}{6D}\right) \tag{A.12}$$

The intercepts of the extrapolating line from the linear portions of Eqs. (A.11) and (A.12) with the time axis, lead to upstream and downstream time lags. The upstream (θ_u) and downstream (θ_d) time lags are directly proportional to the membrane effective diffusivity (*D*), as shown in Eqs. (6.3) and (6.5).

A.2 Derivation of the solution-diffusion model from Fick's first law

The solution-diffusion model describes the transport of a chemical species through a dense polymer membrane. The model describes the membrane permeation as a process where molecules first dissolve into the membrane material and then diffuse to the permeate side under the impetus of a concentration gradient. The expression of the solution-diffusion model, which is given in Eq. (2), was obtained from Fick's first law of

diffusion given in Eq. (A.4). At steady state, it is possible to integrate Fick's first law (Eq. (A.13)) and obtain the relationship for *P* of Eq. (A.14).

$$J = -D\frac{dc}{dx} = -D\frac{\Delta c}{\Delta x} = -D\frac{c_0 - c_L}{0 - L} = D\frac{c_0}{L} = D\frac{Sp_0}{L} = DS\frac{p_0}{L} \tag{A.13}$$

$$P = DS = \frac{J\,L}{p_0} \tag{A.14}$$

It is also possible to derive Eq. (A.14) in terms of concentration.

Nomenclature

Symbols

A	Membrane area [m^2]
c	Gas concentration in the membrane [mol/m^3]
D	Diffusivity coefficient [m^2/s]
J	Objective function
F	Overall objective function value
Fo	Fourier number [-]
L	Membrane thickness [m]
$M(t)$	Gas accumulation in the membrane as a function of time [mol]
M_∞	Gas accumulation in the membrane at the steady state [mol]
$M_{\ln}(t)$	Logarithmic gas accumulation defined by Eq. (6.25) [-]
P	Permeability coefficient [Barrer or mol/s m Pa]
p	Pressure [Torr or Pa]
p_0	Feed pressure [Torr or Pa]

R	Universal gas constant [J/mol K]
S	Solubility coefficient [mol/m^3 Pa]
T	Absolute temperature [K]
t	Time [s]
V	Volume [m^3]

Greek symbols

θ	Time lag [s]
σ	Weighting factor
Δp	Pressure decay/pressure rise [torr/s or Pa/s]

Subscripts

d	Downstream
e	Effective property
i	Intrinsic property
in	Entering membrane
out	Leaving membrane
u	Upstream
0	Upstream
∞	Steady state

References

[1] L.M. Robeson, Z.P. Smith, B.D. Freeman, D.R. Paul, Contributions of diffusion and solubility selectivity to the upper bound analysis for glassy gas separation membranes, J. Memb. Sci. 453 (2014) 71–83. https://doi.org/10.1016/j.memsci.2013.10.066.

[2] R.W. Baker, Future directions of membrane gas separation technology, Ind. Eng. Chem. Res. 41 (2002) 1393–1411. https://doi.org/10.1021/ie0108088.

[3] R.W. Baker, K. Lokhandwala, Natural gas processing with membranes: An overview, Ind. Eng. Chem. Res. 47 (2008) 2109–2121. https://doi.org/10.1021/ie071083w.

[4] R. Prasad, F. Notaro, D.R. Thompson, Evolution of membranes in commercial air separation, J. Memb. Sci. 94 (1994) 225–248. https://doi.org/10.1016/0376-7388(93)E0193-N.

[5] D.F. Sanders, Z.P. Smith, R. Guo, L.M. Robeson, J.E. McGrath, D.R. Paul, B.D. Freeman, Energy-efficient polymeric gas separation membranes for a sustainable future: A review, Polymer (Guildf). 54 (2013) 4729–4761. https://doi.org/10.1016/j.polymer.2013.05.075.

[6] L.M. Robeson, The upper bound revisited, J. Memb. Sci. 320 (2008) 390–400. https://doi.org/10.1016/j.memsci.2008.04.030.

[7] M. Sadrzadeh, M. Rezakazemi, T. Mohammadi, Fundamentals and Measurement Techniques for Gas Transport in Polymers, Elsevier Inc., 2017. https://doi.org/10.1016/B978-0-12-809884-4.00019-7.

[8] R.M. Barrer, E.K. Rideal, Permeation, diffusion and solution of gases in organic polymers, Trans. Faraday Soc. 35 (1939) 628–643. https://doi.org/10.1039/tf9393500628.

[9] Leszczynski P., Cao Z., Wu H., Thibault J., and Kruczek B. (2024). Determination of time lag by accurate monitoring of pressure decay in a new generation constant volume system. MethodsX 13, 102858. https://doi.org/10.1016/j.mex.2024.102858.

[10] Z. Cao, J. Thibault, B. Kruczek, Direct determination of permeability, diffusivity and solubility of gases in membrane based on simultaneous monitoring of pressure rise and decay in a single time-lag experiment, J Memb Sci 720 (2025). https://doi.org/10.1016/j.memsci.2025.123741.

[11] N. Al-Qasas, J. Thibault, B. Kruczek, The effect of the downstream pressure accumulation on the time-lag accuracy for membranes with non-linear isotherms, J. Memb. Sci. 511 (2016). https://doi.org/10.1016/j.memsci.2016.03.047.

[12] Z. Cao, B. Kruczek, J. Thibault, Impact of the porous support disc of a gas permeation cell on the estimation of the membrane transport properties, J Memb Sci 721 (2025). https://doi.org/10.1016/j.memsci.2025.123831.

[13] Z. Cao, H. Wang, J. Thibault, B. Kruczek, Effect of feed pressure on the membrane thickness and membrane transport properties via the time-lag method, J Memb Sci.

[14] K. Pouliot, J. Thibault, A. Garnier, and G. Acuna Leiva. "K_La Evaluation during the Course of Fermentation Using Data Reconciliation Techniques." Bioprocess Engineering (Berlin, West) 23, no. 6 (2000): 565–573. https://doi.org/10.1007/s004490000198.

[15] Daynes, H.A. (1920). The Process of Diffusion through a Rubber Membrane. Proc. R. Soc. A Math. Phys. Eng. Sci. 97, 286–307.

[16] Jenkins, R.C.L., Nelson, P.M., Spirer, L. (1970). Calculations of the Transient Diffusion of Gas through a Solid Membrane into a Finite Outflow Volume, Transactions of the Faraday Society, 66, 1391-1401.

[17] Al-Ismaily M., Wijmans J.G., Kruczek B. (2012). A shortcut method for faster determination of permeability coefficient from time lag experiments, J. Memb. Sci. 423–424. https://doi.org/10.1016/j.memsci.2012.08.009.

[18] Phan B.K., Shen K.-H., Gurnani R., Tran H., Lively R., Ramprasad R. (2024). Gas permeability, diffusivity, and solubility in polymers: Simulation-experiment data fusion and multi-task machine learning. npj Computational Materials, 10:186, 1-11. https://doi.org/10.1038/s41524-024-01373-9.

Chapter 7

Monte Carlo simulations for the estimation of the effective permeability of mixed-matrix membranes

Zheng Cao, Boguslaw Kruczek, Jules Thibault*

Abstract

Recent years have seen an explosive development of mixed-matrix membranes (MMMs) for a myriad of applications. In gas separation, it is desired to concurrently enhance the permeability, selectivity, and physicochemical properties of the membrane. To help achieve these objectives, experimental characterization and predictive models can be used synergistically. In this investigation, a Monte Carlo (MC) algorithm is proposed to rapidly and accurately estimate the relative permeability of ideal MMMs over a wide range of conditions. The difference in diffusivity coefficients between the polymer matrix and the filler particle is used to adjust the random progression of the migrating species inside each phase. The solubility coefficients of both phases at the polymer-filler interface are used to control the migration of molecules from one phase to the other in a way to achieve progressive phase equilibrium at the interface. Results for various MMMs were compared with the results obtained with the finite difference method under identical conditions, where the results from the finite difference method are used in this investigation as the benchmark method to test the accuracy of the Monte Carlo algorithm.

Results were found to be very accurate (in general < 1% error) over a wide range of polymer and filler characteristics. The MC algorithm is simple and swift to implement and provides an accurate estimation of the relative permeability of ideal MMMs. The MC method can easily be extended to investigate more readily non-ideal MMMs with particle agglomeration, interfacial void, polymer chain rigidification and/or pore blockage, and MMMs with any filler geometry.

Keywords: mixed-matrix membrane (MMM); relative permeability; solubility; Monte Carlo simulations; Finite difference simulations

Publication status: Membranes 12(2022) 1053

***Corresponding author**

7.1 Introduction

In the last 40 years, membrane technology for gas separation has seen tremendous growth in the number of industrial applications where, in many cases, it can now compete advantageously with conventional unit operations, such as distillation, absorption and adsorption. More recently, mixed-matrix membranes (MMMs), where a filler is incorporated within the matrix of a polymeric membrane, have seen tremendous research interest and an increase in the number of potential applications [1]. MMMs have been proposed in order to modify the characteristics of the membrane to improve the desired performance, making use of the advantages stemming from the synergistic characteristics of both the polymeric and inorganic membranes. The last decade has seen significant development in MMMs with numerous applications: gas separation with functionalized fillers [2], ethanol dehydration [3], ABE solvent separation [4,5], treatment of oil sands produced water [6], water desalination [7], embedding environmentally friendly nanoclay palygorskite for flux enhancement and fouling reduction [8] and many others. The main benefits of MMMs are the process intensification and the performance enhancement by

the presence of suitable fillers while preserving the economic and processing convenience of the polymer [9].

The most common use of MMMs in gas separation and solvent pervaporation has targeted the change in the permeability and selectivity of the membranes. For instance, to improve the permeability of the membrane, it is possible to incorporate higher-performance nanoporous or high-permeability fillers where preferential diffusion paths are created within the MMM. On the other hand, if the purpose of the membrane is to act as a barrier material, impermeable fillers can be embedded in the polymer matrix to increase the tortuosity and reduce the membrane's effective permeability. The permeability of the polymer, the filler and the MMM is the product of their respective diffusivity and solubility. It has been clearly shown through correlations and numerical analysis that the relative effective permeability of a MMM is impacted by the relative permeability of the two phases (filler and polymer) and not by their individual relative diffusivity and relative solubility [10]. This is contrary to the results presented by Singh et al. [11], who argued that both the diffusivity ratio and the solubility ratio should be considered separately. Most empirical models and numerical models used for the estimation of the relative permeability of MMMs, considered ideal MMMs assuming the absence of interfacial voids and rigidified polymeric regions at the interface with the filler, in addition to assuming that the filler is uniformly distributed in the polymer matrix and the polymer does not penetrate the pores of the fillers. It is obvious that, in practice, most MMMs are not ideal, and the effective permeability may be different. Nevertheless, it is important to estimate the effective permeability of ideal MMMs such that any deviations from ideality observed experimentally can be better assessed and understood. Many analytical models are available in the literature and have been extensively used by many researchers. However, these models are limited to fillers of simple geometrical shapes, most often spherical. Numerical techniques such as the finite differences method (FDM) [4,12] and finite element method (FEM) [11,13] have been extensively used to calculate the relative permeability of MMMs and are considered to be the actual values.

To manufacture and optimize a MMM with the desired properties for a specific gas separation, it is paramount to gain a deeper understanding of the transport properties of

these MMMs. The synergy of modelling and experimentation can play an essential role in attaining these objectives. In the past decade, our group has used numerical simulations to determine the effective permeability of ideal MMMs embedding filler particles having different diffusivity and/or solubility than the host polymer, thereby decreasing or enhancing the effective permeability of the MMM. These numerical simulations were performed by solving the three-dimensional second Fick's law of diffusion using the FDM. The FDM requires complex coding and significant computation time. In search of a more straightforward simulation method to implement, we have opted for a Monte Carlo (MC) algorithm. The principle of an MC simulation is to approximate the expected value of a random variable by an average over a large number of measurements. There are different scales at which simulations of the diffusion process can be performed, going from the atomistic scale [14-16] by considering a very tiny evaluation space-domain to the macroscopic scale by solving the Fick's second law of diffusion for the whole membrane using a suitable solver for partial differential equations [4]. Atomistic simulations consider stretching, bending and torsional motion of the polymer chain and permeating molecules, which allows studying adsorption and diffusion locally. This degree of granularity is not useful for estimating the relative permeability of MMMs. As an intermediate between these two opposing scales, this investigation proposes to use an MC approach to indirectly solve Fick's second law of diffusion by simply considering the Brownian motion of molecules within an MMM. The MC algorithm is much easier to implement and should provide the same level of accuracy akin to more conventional solutions of the diffusion process.

7.2 Methodology

7.2.1 Definition of the simulation domain

In this investigation, it is assumed that the MMM is ideal, implying that all solid filler particles, having identical shape, geometry, and orientation, are uniformly distributed within the polymer matrix. In addition, the polymer/particle interface is considered ideal, and the permeability and solubility coefficients for both the polymer and the filler particles are assumed constant. The two-phase MMM is subdivided into a

number of elementary units. Each elementary unit consists of a polymer matrix with a centrally-located solid particle schematically presented in Figure 7.1. The solid volume fraction of an elementary unit is identical to the volume fraction of the entire MMM. It has been shown that the effective permeability of an elementary unit is identical to the permeability of the entire MMM [10,17]. As a result, to solve numerically for the effective permeability of MMMs, it is only necessary to consider one elementary unit. For all finite difference (FD) and Monte Carlo (MC) simulations, in Cartesian coordinates, the three-dimensional elementary unit of dimensions $L_x \times L_y \times L_z$ is discretized into a grid $n_x \times n_y \times n_z$ finite volumes. The solid filler particle of dimensions $x_F \times y_F \times z_F$ located at the center of the elementary unit has a diffusivity coefficient (D_F) and a solubility coefficient (S_F), whereas, for the polymer in the elementary unit surrounding the filler, they are D_p and S_p, respectively.

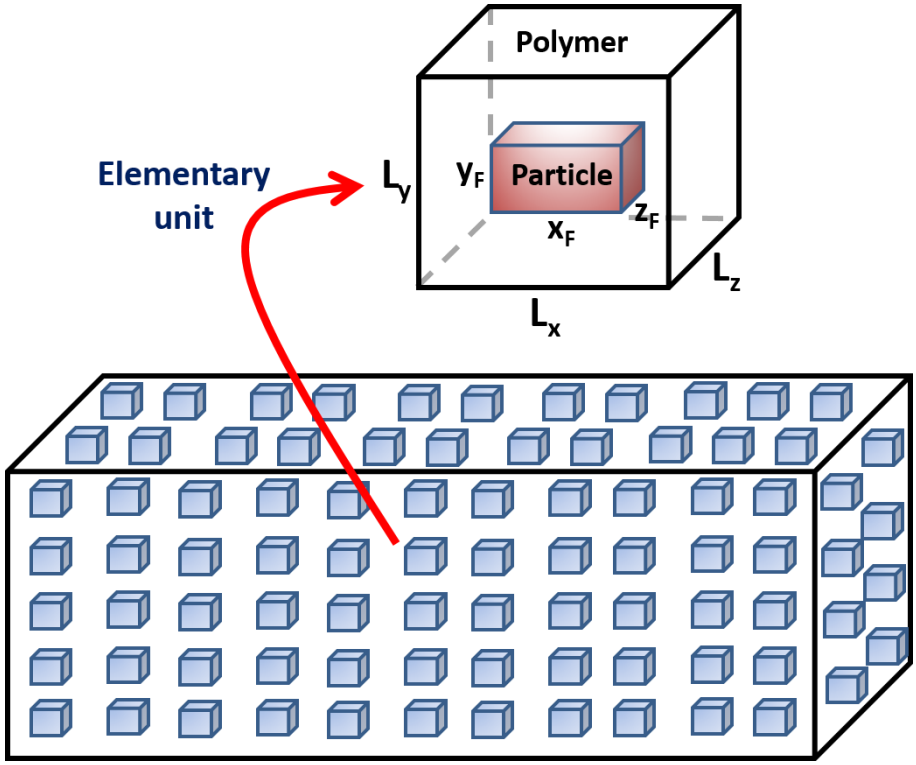

Figure 7.1 Schematic diagram of a section of a MMM consisting of a myriad of identical elementary units, each comprised of a centrally-located filler particle embedded in the polymer matrix.

The initial and boundary conditions need to be defined to solve this problem. For providing the boundary conditions, the filler particle is assumed to be a cuboid, as defined in the previous paragraph. For the initial condition, that is, before the concentration step change on one side of the membrane occurs at time $t = 0$, a nil concentration is assumed throughout the membrane (Eq. 1). For the boundary conditions in Cartesian coordinates, twelve relations are required to completely define the problem: six boundary conditions at the periphery of the polymeric elementary unit and six boundary conditions at the polymer-solid interfaces. Eq. (2) provides the boundary conditions on the upstream and downstream sides of the membrane (the y-axis is the permeation direction). It is assumed that at the onset of permeation, a step change in the gas pressure or concentration is applied to the upstream side of the membrane ($y = 0$), whereas the gas pressure on the downstream side of the membrane ($y = L_y$) is kept under perfect vacuum. The resulting concentrations in the membrane at both surfaces are simply the product of the neighboring gas pressure or concentration and the solubility S_P of the polymer. Because all elementary units are identical, symmetry conditions prevail at the other four faces of the polymer parallelepiped, as expressed in Eq. (3) for $BC_{3\text{-}6}$. These are periodic boundary conditions since the MMM is formed of a large number of identical elementary units. At the filler particle-polymer interface, it is assumed that equilibrium between the two phases prevails at each of the six faces of the nanoparticle (see $BC_{7\text{-}12}$ in Eq. (4)). Even though Eq. (4) applies for cuboid particles aligned with the membrane surface, similar boundary conditions can easily be defined for other particle geometry. More details on the derivation and solution of these equations can be found in Wu et al. [18-19]. The results obtained by the FDM are considered true values and will be used as the benchmark for evaluating the accuracy of the results obtained by the Monte Carlo simulations.

$$\text{IC:} \quad C_{i,j,k}^{t<0} = 0 \qquad \forall i,j,k \tag{7.1}$$

$$\begin{aligned} &\text{BC}_1\text{: } C_{i,y=0,k} = \frac{p_0}{RT} S = \text{c}_0\text{S} \qquad \forall i,k \\ &\text{BC}_2\text{: } C_{i,y=L_y,k} = 0 \qquad\qquad\quad \forall i,k \end{aligned} \tag{7.2}$$

$$\mathrm{BC}_{3\text{-}6}: \quad \left.\frac{\partial C}{\partial x}\right|_{x=0} = \left.\frac{\partial C}{\partial x}\right|_{x=L_x} = \left.\frac{\partial C}{\partial z}\right|_{z=0} = \left.\frac{\partial C}{\partial z}\right|_{z=L_z} = 0 \tag{7.3}$$

$$\begin{aligned}
&\mathrm{BC}_7: C^{Filler}_{(L_x-x_p)/2,y,z} = \frac{S_p}{S_F} C^{Polymer}_{(L_x-x_p)/2,y,z} && \forall\left[\left(\frac{(L_y-y_p)}{2} \le \mathrm{y} \le \frac{(L_y+y_p)}{2}\right)\bigcap\left(\frac{(L_z-z_p)}{2} \le \mathrm{z} \le \frac{(L_z+z_p)}{2}\right)\right] \\
&\mathrm{BC}_8: C^{Filler}_{(L_x+x_p)/2,y,z} = \frac{S_p}{S_F} C^{Polymer}_{(L_x+x_p)/2,y,z} && \forall\left[\left(\frac{(L_y-y_p)}{2} \le \mathrm{y} \le \frac{(L_y+y_p)}{2}\right)\bigcap\left(\frac{(L_z-z_p)}{2} \le \mathrm{z} \le \frac{(L_z+z_p)}{2}\right)\right] \\
&\mathrm{BC}_9: C^{Filler}_{x,(L_y-y_p)/2,z} = \frac{S_p}{S_F} C^{Polymer}_{x,(L_y-y_p)/2,z} && \forall\left[\left(\frac{(L_x-x_p)}{2} \le \mathrm{x} \le \frac{(L_x+x_p)}{2}\right)\bigcap\left(\frac{(L_z-z_p)}{2} \le \mathrm{z} \le \frac{(L_z+z_p)}{2}\right)\right] \\
&\mathrm{BC}_{10}: C^{Filler}_{x,(L_y+y_p)/2,z} = \frac{S_p}{S_F} C^{Polymer}_{x,(L_y+y_p)/2,z} && \forall\left[\left(\frac{(L_x-x_p)}{2} \le \mathrm{x} \le \frac{(L_x+x_p)}{2}\right)\bigcap\left(\frac{(L_z-z_p)}{2} \le \mathrm{z} \le \frac{(L_z+z_p)}{2}\right)\right] \\
&\mathrm{BC}_{11}: C^{Filler}_{x,y,(L_z-z_p)/2} = \frac{S_p}{S_F} C^{Polymer}_{x,y,(L_z-z_p)/2} && \forall\left[\left(\frac{(L_x-x_p)}{2} \le \mathrm{x} \le \frac{(L_x+x_p)}{2}\right)\bigcap\left(\frac{(L_y-y_p)}{2} \le \mathrm{y} \le \frac{(L_y+y_p)}{2}\right)\right] \\
&\mathrm{BC}_{12}: C^{Filler}_{x,y,(L_z+z_p)/2} = \frac{S_p}{S_F} C^{Polymer}_{x,y,(L_z+z_p)/2} && \forall\left[\left(\frac{(L_x-x_p)}{2} \le \mathrm{x} \le \frac{(L_x+x_p)}{2}\right)\bigcap\left(\frac{(L_y-y_p)}{2} \le \mathrm{y} \le \frac{(L_y+y_p)}{2}\right)\right]
\end{aligned} \tag{7.4}$$

7.2.2 Monte Carlo algorithm

The MC method was developed during the Manhattan Project for modelling neutron diffusion during the fission process and is now used in a myriad of applications in numerous fields of study [20-22]. In this investigation, the dynamic MC simulations are used to model the dynamic behavior of molecules permeating through a MMM, where all molecules are subjected to Brownian diffusion or random walk diffusion. In this investigation, the implementation of the MC was performed using two different methods. In the first method, referred to as MC1, the displacement of molecules occurs in a cubic lattice, where a molecule can only jump from the current mesh element (i,*j*,*k*) to one of the six neighboring meshes (Figure 7.2). In the second method, referred to as MC2, the displacement of molecules can occur in any direction with a jump proportional to the local relative diffusivity. The relative diffusivity is calculated as the diffusivity of the phase where the molecule under consideration is currently located, divided by the highest diffusivity of the system, i.e. the diffusivity of the polymer or the filler particle. In MC1, the molecules are located only within one of the mesh volume elements. In contrast, for MC2, molecules can assume any location within the elementary unit and their (*x*,*y*,*z*) coordinates are recorded throughout their migration through the membrane. To avoid

redundancy, the description of the MC method will be focused on the cubic lattice method (MC1), and only minor differences for the second method will be provided. It is important to mention that it is not possible for the macroscopic aspect of the MC, as used in this investigation, to determine the effective membrane permeability directly. Instead, the relative membrane permeability ($P_r = P_e/P_P$), that is, the ratio of the effective permeability of the MMM over the permeability of the neat polymeric membrane, is determined by performing the identical MC simulation and comparing the steady-state permeation flux of a MMM with the steady-state flux of an identical membrane without the presence of a filler particle. Since the diffusivity, solubility and permeability of the neat membrane are usually known or can be more easily determined experimentally, the effective permeability of the MMM can therefore be estimated. In this investigation, the results of a MC simulation for a MMM will always be compared with the results of a neat membrane under identical conditions.

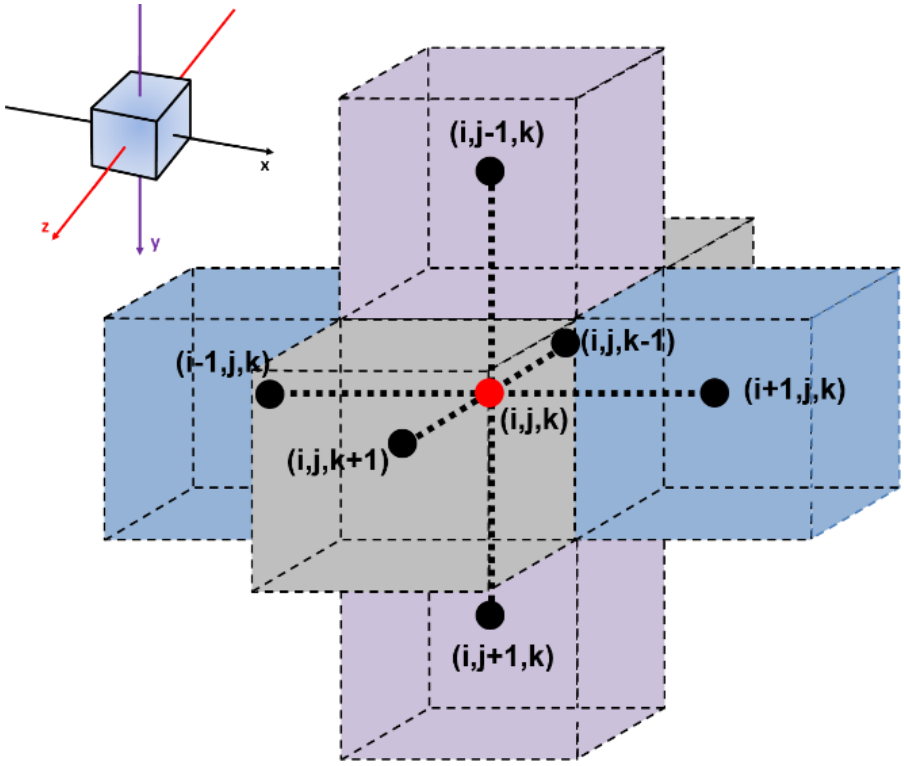

Figure 7.2 The central mesh element (*i*,*j*,*k*) surrounded by its six neighboring mesh elements as used in cubic lattice for the MC and the FD methods (Adapted from [18-19]).

Simulations were performed with a MMM having a nil initial concentration of molecules throughout the membrane. At the onset of the dynamic permeation experiment, a step change in the gas pressure or gas concentration on the upstream side of the membrane is applied, which leads to a sudden increase in the number of molecules diffusing into the upstream surface layer of the membrane. It is assumed that there is an instantaneous equilibrium at the upstream interface. To maintain the concentration of molecules constant at the upstream interface of the membrane, it will be reset to the same value after each iteration, which will naturally set the flux of molecules entering the membrane. In gas permeation in a dense membrane, two main steps are considered: (1) the sorption of gases in the membrane material and (2) the diffusion of gas molecules from a region of higher chemical potential (concentration) to a region of lower chemical potential. MC simulation can create the permeation of molecules through the membrane due to the Brownian movement of molecules. Naturally, molecules move in a random walk from the upstream region (higher concentration) to the downstream region of the membrane (lower concentration). In MC simulations, each molecule within the membrane is subjected to a displacement at each iteration to mimic the molecule's Brownian diffusion.

After discretizing the elementary unit with a large number of meshes, providing the values of the membrane characteristics and process variables and populating the upstream surface layer with a sufficiently large number of molecules, each iteration follows the same procedure as follows: (Figure 7.3 shows the pseudocode of the MC algorithm):

(a) All members of the current population are, in turn, subjected to a random move in one of the six adjoining meshes (Figure 7.2) such that a molecule will potentially move to an adjacent mesh. To consider the difference in the diffusivity coefficient between the two phases of the MMM, the probability of a molecule adopting the suggested move is made equal to the ratio of the diffusivity at the current mesh location and the maximum diffusivity value as expressed in Eq. (7.5).

$$IF\ \mathrm{RN} < \frac{D_{Current\ Mesh}}{Max(D_F, D_P)} THEN\ Move\ accepted \tag{7.5}$$

If the random number (*RN*) is smaller than the diffusivity ratio, the move is considered. A move is always suggested, but not necessarily realized, depending on some additional considerations when the molecule under consideration is currently located within the phase having the lowest diffusivity. For instance, assuming a diffusivity ratio of 0.1, if the molecule is located in the phase with the lowest diffusivity, the probability of moving to a neighboring mesh slot is 0.1. If a molecule is currently located in the phase having the highest diffusivity, the move is always accepted, provided a few additional conditions are satisfied.

(b) Indeed, when a move of a molecule is accepted, this particular move is subjected to two additional conditions to be realized.

(i) If a molecule is currently located at one of the four lateral faces perpendicular to the *x*- and *z*-direction of the elementary unit and the move brings that molecule outside the elementary unit, then this molecule simply re-enters the elementary unit directly on the opposite face in order to satisfy the four symmetrical periodic conditions in the *x*- and *z*-directions [23].

(ii) Since it is assumed that equilibrium prevails at the polymer-solid interface, if the suggested random move is from phase 1 to phase 2 (Figure 7.4), the move will be accepted if it favors the attainment of the equilibrium between the two phases. If the two solubility coefficients differ, a discontinuity in concentration will prevail at the polymer-solid interface. If the current ratio of concentration C_2/C_1 already exceeds the solubility ratio S_2/S_1, the move is not performed (Eq. 7.6). If the ratio of concentration following the move remains smaller than the solubility ratio, the move is performed (Eq. 7.7). Finally, if the concentration ratio before the move is smaller than the solubility ratio whereas it becomes greater after the move, the probability of accepting the move is calculated as given

in Eq. (7.8). It is important to point out that the interface equilibrium cannot be specified directly, but must be attained progressively through molecule random walk. Eqs. (7.6)-(7.8) ensure that the system is always trying to achieve equilibrium.

$$\text{IF } \frac{C_2}{C_1} \geq \frac{S_2}{S_1} \text{ THEN } \textit{No Move} \tag{7.6}$$

$$\text{ELSE IF } \frac{C_2+1}{C_1-1} \leq \frac{S_2}{S_1} \text{ THEN } \textit{Move} \tag{7.7}$$

$$\text{ELSE IF } \left(\frac{C_2}{C_1} < \frac{S_2}{S_1} \text{ AND } \frac{C_2+1}{C_1-1} > \frac{S_2}{S_1}\right) \text{ THEN } \text{Prob}_{\text{Move}} = \frac{\frac{S_2}{S_1} - \frac{C_2}{C_1}}{\frac{C_2+1}{C_1-1} - \frac{C_2}{C_1}} \tag{7.8}$$

(c) When all the members of the current molecule population have been considered in one given iteration, the population is updated. First, the number of molecules in the upstream surface layer is reset to its original number to satisfy the equilibrium condition between the constant surrounding gas pressure and the polymer surface of the MMM. Resetting the original number of molecules automatically calculates the flux of molecules entering the membrane at each iteration. Because the Brownian motion is purely a random process, it is possible to encounter a negative flux for some iterations. Secondly, all the molecules that exited the downstream side of the membrane allow the calculation of the instantaneous permeation flux of molecules leaving the membrane. At each iteration, the molecules added or removed from the upstream membrane surface layer and the molecules exiting the downstream side serve to update the current population of molecules.

(d) The above procedure is followed for a given number of iterations or until molecules' average inlet and outlet fluxes are the same, i.e., the steady-state permeation is attained. The final results are then printed. The relative permeability of the MMM is calculated by dividing the steady-state permeation

flux obtained for the MMM by the permeation flux of the neat membrane under identical conditions, implying that the conditions of Eq. (5) are considered in calculating the flux of the neat membrane even if a filler is absent.

(e) The above procedure pertains to the lattice MC. In the case of the second method alluded to earlier (MC2), the only difference is in calculating the displacement of the molecules permeating through the membrane. In the lattice MC, the molecules can jump from the central cubic mesh to one of the six neighboring meshes. In the second method, the molecules can move in any direction by randomly choosing a displacement in the three directions and calculating the new coordinates of a given molecule. In this method, a move is always accepted, but the distance travelled by one molecule is adjusted via the diffusivity ratio of the two phases, similar to what was performed in the lattice MC. All the other considerations, such as the periodic symmetrical conditions and the polymer-solid equilibrium interface, remain the same. For the latter two considerations and the upstream surface population, the number of molecules in each cubic mesh of the MMM is calculated and used in the same way as in the lattice MC.

```
Start
Set D_F , D_P , S_F , S_P
Calculate D_ref = Max(D_F ,D_P)
Discretize elementary unit: n_x, n_y, n_z
Define filler dimensions: x_F, y_F, z_F
Initialize upstream surface population: NSURF
NPOP = NSURF
For i = 1 to NITER
  For j = 1 to NPOP
    Get RN
    Select potential move
    Get RN
    IF (RN <  D_mesh/Max(D_F ,D_P))  THEN
      IF (Lateral move out of filler) THEN Enter other side
      IF (At polymer-filler interface) THEN Apply Eqs. (6)-(8)
    ELSE No Move
    END IF
  NEXT j
  Add/Remove Molecules in first layer to reach population NSURF
  Remove from population molecules leaving downstream
  Calculate the input and output fluxes
  Calculate new NPOP
NEXT i
PRINT final results
End
```

Figure 7.3 Computer pseudocode of the MC algorithm proposed in this investigation.

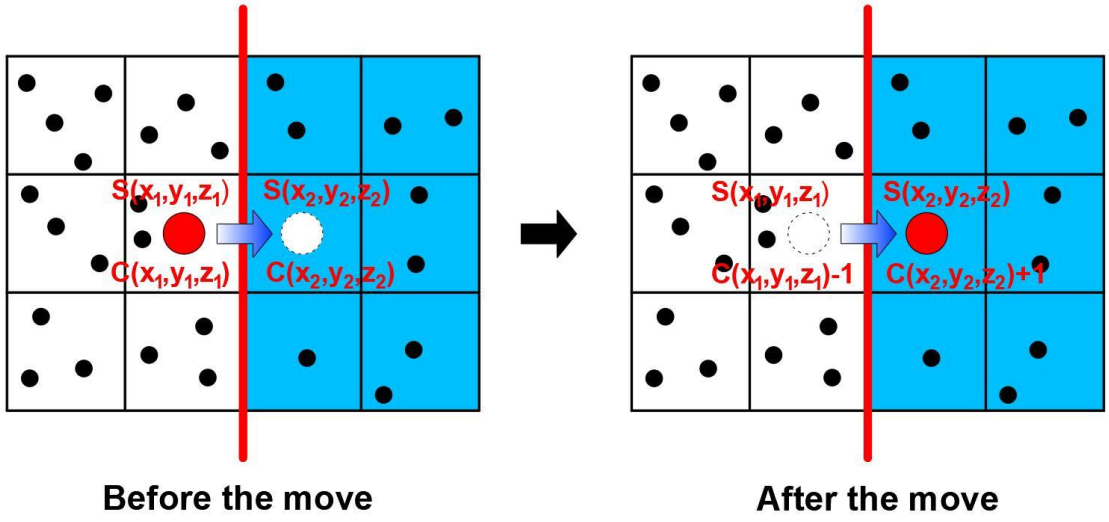

Figure 7.4 Schematic diagram of the potential migration of one molecule across the polymer-solid interface from phase 1 to phase 2 in an MMM.

The computer codes to perform MC and FD simulations were written in the FORTRAN programming language. When memory permitted, simulations were performed using a DELL Lattitude 5500 laptop computer with an Intel Core i7-8665U CPU at 1.90 GHz and 16 GB installed RAM. For larger problems, the CAC cluster Frontenac at Queen's University (Kingston, Canada) was used, which comprised a wide variety of computers with large memory ranging from 128 GB to 2 TB. The advantage of the cluster is the possibility of submitting many simulations with larger populations at the same time.

7.3 Results and discussion

The MC simulation is pretty robust in determining the relative permeability of MMMs because the migration flux for a particular MMM is compared with the flux of the neat polymeric membrane under identical conditions. Indeed, this procedure provides the relative effective permeability of the MMM and not the actual effective permeability. It is, therefore, not necessary to have the exact time scale to obtain this information as it is assumed that the same time is elapsed for each iteration. To explore the ability of the MC simulation to provide the relative permeability of the MMM, a series of tests were

performed and compared to the same results obtained with the FD method, which is assumed to provide the actual value of the MMM permeability and relative permeability.

Figure 7.5 presents the inlet and outlet fluxes obtained during a typical MC simulation using method MC1. The initial population is nil throughout the membrane. At time zero, the first upstream surface layer is populated with a given number of molecules that is reset to a constant value at each iteration. The output flux is nil until some molecules from the higher upstream concentration migrate through the membrane to emerge at the downstream side of the membrane and eventually leading to an average constant outlet flux. The initial input flux is very high at the beginning because of the large gradient of molecules in the meshes close to the upstream surface of the membrane. There are initially very few molecules in the downstream portion of the membrane to create a backflow of molecules to the upstream portion of the membrane via the natural Brownian motion to significantly reduce the net flow of molecules entering the upstream membrane surface. As the population of molecules progressively builds up with the number of iterations, the average input flux stabilizes to reach a constant value equal to the output flux under steady-state conditions. The solid line in Figure 7.5 represents the moving average of the instantaneous input and output fluxes, the instantaneous fluxes represented by the light color plots. Figure 7.5 shows that the instantaneous flux varies significantly due to the random nature of the Brownian motion. The inlet flux varies much more than the output flux because of the much larger number of molecules present at the upstream membrane interface. For some iterations, the instantaneous input flux is negative because of the random walk-backflow of molecules to the first upstream membrane layer. Since equilibrium exists between the surrounding gas and the upstream surface layer, the probability of molecules leaving the first layer to satisfy the equilibrium condition is not nil. The flux variation on the membrane's downstream side is not as severe because the number of molecules is significantly less than on the upstream side. The MC simulation more realistically represents the phenomenon occurring in an actual gas permeation process across a membrane. In contrast, the solution to Fick’s second law of diffusion by FD assumes a direct permeation path from the upstream to the downstream sides of the membrane using diffusion coefficients smaller than the ones associated with the random walk diffusion.

The two MC methods, MC1 and MC2, discussed in Section 7.2.2, are compared under identical conditions for the same MMM having a cubic nanoparticle of different sizes. The plot of the relative steady-state flux or relative permeability of the MMM for three different levels of discretization is presented in Figure 7.6 and compared with the results obtained with the FD method. The two MC methods gave nearly identical results for the three levels of discretization. In addition, these results show that the accuracy of the MC methods is excellent, with an average error of 0.008 in the estimation of the relative permeability and a maximum error of 0.015 at the higher volume fraction. In addition, the method is not sensitive to the discretization level, at least for cubic filler particles. In most of the results presented in this work, a 41×41×41 discretization grid was used to ensure maximum accuracy under all conditions.

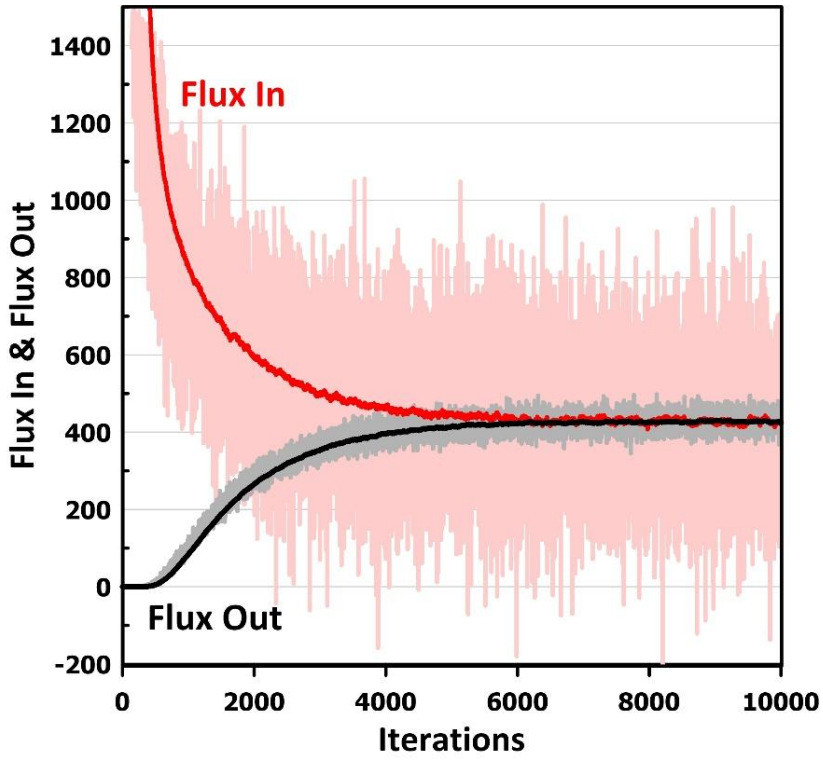

Figure 7.5 The plot of the typical fluxes of molecules at the upstream and downstream sides of the MMM using the lattice MC (MC1). The light color plots represent the instantaneous fluxes, whereas the solid lines represent the moving average fluxes. Lattice: 41×41×41; $(x_F,y_F,z_F) = (27,27,27)$; $D_F = D_P = 1\times10^{-11}$ m^2/s; $S_F = 0.10$, $S_P = 0.50$.

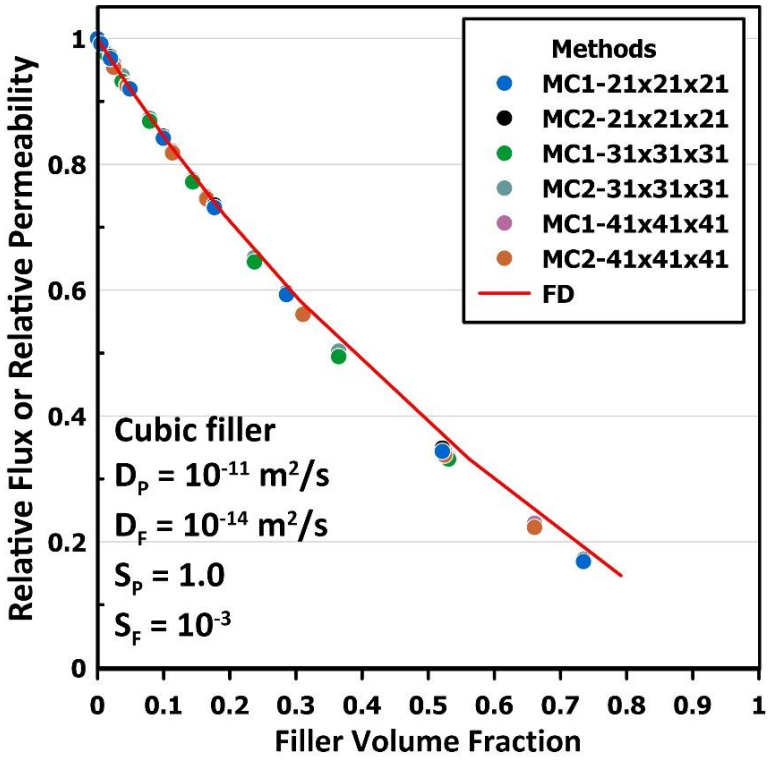

Figure 7.6 The plot of the relative steady-state flux or relative permeability of a MMM with a cubic filler particle of different sizes for the two MC methods: the lattice MC (MC1) and the continuous displacement MC (MC2). Three different discretization meshes were used for comparison, and the results were compared with the results of the FD method under identical conditions.

Figure 7.7 presents the results obtained for MMMs with an impermeable cuboid filler as a function of the filler volume fraction for both the MC and FD methods. In each of the four series of simulations, the thickness (y_F) of the cuboid filler remained constant while the other two dimensions of the filler ($x_F = z_F$) were progressively increased to augment the filler volume fraction and, as a result, the filler projected area. The four different values of the filler thickness were 5, 15, 25 and 35, defined on a three-dimensional grid of 41×41×41. The other two dimensions were varied from 5 to 37 by increments of 4. The results of Figure 7.7 clearly show that the MC method can predict the relative permeability of the MMM very accurately for the first three thicknesses, even when only two cubic mesh volumes ($x_F = z_F = 37$) are available around the filler for the

molecules to permeate to the downstream side of the membrane. Indeed, the absolute value of the error (AE), defined in Eq. (7.9), are 0.006, 0.006, 0.008 and 0.022, respectively for thicknesses 5, 15, 25 and 35. For the thicker filler (y_F = 35), the average AE for the estimation of the relative permeability of the MMM is about three times higher than for the other three thicknesses. This latter situation is obviously an extreme case since the thickness of the particle represents 85% of the thickness of the elementary unit. In general, and based on these results, it can be concluded that MC simulations can be used with confidence for the estimation of the relative permeability of MMMs.

$$AE = \left| P_{r,MC} - P_{r,FD} \right| \tag{7.9}$$

The results of Figure 7.7 highlight a very important aspect concerning estimating the relative permeability of ideal MMMs. There exists a significant difference in the values of the relative permeability for an identical filler volume fraction. The most popular correlations for the estimation of the relative permeability of MMMs use the volume fraction of the filler as the main model parameter and, therefore, cannot account for the significant variations observed in the results in Figure 7.7. This is the case for the well-known correlations of Maxwell [24], Lewis et al. [25] and Pal [26], which assume that the filler particle can be considered spherical. This is not the case, for instance, when thin impermeable Montmorillonite platelets are used as fillers in the polymer. The Montmorillonite platelets act as a barrier material, and their associated MMMs have been considered in food packaging [12]. Wu et al. [18-19] have recently proposed a general correlation for predicting the relative permeability of MMMs embedding impermeable fillers of various shapes based on geometrical parameters of the filler rather than purely on the void fraction. At the same time, the simplicity and accuracy of the MC simulation can certainly contribute advantageously to estimating the relative permeability of MMMs for various filler geometries, as is the case for the results in Figure 7.7.

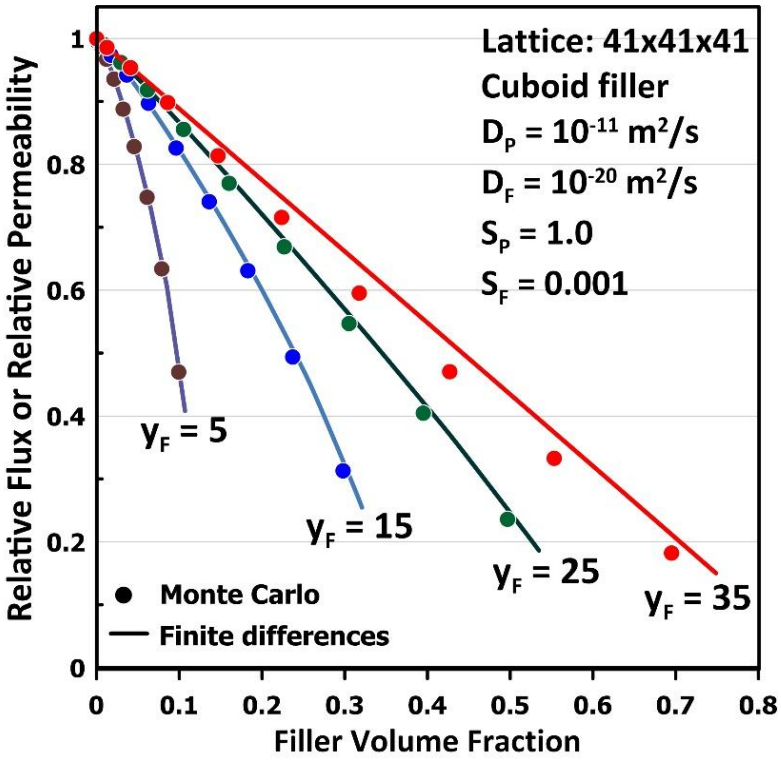

Figure 7.7 The plot of the relative steady-state flux or relative permeability of a MMM with an impermeable cuboid filler for four different thicknesses (y_F) on lattice discretization of 41×41×41. The other two dimensions ($x_F = z_F$) were increased to augment the filler volume fraction. Results were compared with the results of the FD method under identical conditions.

A series of simulations was performed with cubic filler particles ($x_F = y_F = z_F$) of different sizes to change the filler volume fraction and for different solubility coefficients of the filler. At the same time, all other parameters remained the same. Figure 7.8(a) presents the results for the filler having a lower permeability than that of the polymer matrix, such that the filler is acting partially as a barrier material. Figure 7.8(b) presents the results for the filler having a higher permeability than that of the polymer matrix, such that the filler contributes to enhancing the effective permeability of the MMM by providing a preferential path for permeation. The results obtained with the MC simulations are compared to those obtained by the FD method. These results clearly show that the MC method can accurately predict the relative permeability of MMMs over a wide range of the solubility coefficient. Indeed, the average AE for the prediction of the relative

permeability for the results of Figure 7.8(a) are 0.002, 0.007, 0.011 and 0.009, respectively, for the filler having a relative solubility of 0.01, 0.10, 0.20 and 0.50. Relative solubility is defined as the ratio of the filler solubility over the solubility of the polymer. The average AE for the prediction of the relative permeability for the results of Figure 7.8(b) are 0.017, 0.036, 0.040 and 0.077, respectively, for the filler having a relative solubility of 2, 5, 10 and 20.

It is easier to perform MC simulations when the solubility coefficient of the filler is lower or not much higher than the solubility of the polymer matrix because the steady-state population inside the elementary unit remains at a reasonable level. When using a three-dimensional lattice grid of 41×41×41, it is recommended to have a constant upstream surface population for each cubic mesh of 40 and more to achieve a representative steady-state concentration profile. However, when the filler has a high solubility, a larger number of molecules will accumulate within the filler due to the attainment of equilibrium. As a result, the total population of molecules within the elementary unit will increase and may exceed the memory allocation currently available on many computers. When the solubility of the filler is high, the size of the filler particle that may be considered is restricted. Figure 7.9 presents the plot of the population of molecules as a function of the number of iterations for a cubic filler with a solubility twice that of the polymer. This graph shows that for lower filler volume fractions, the population stabilizes below the upper memory limit. It is possible to reduce the lattice grid to a lower number of three-dimensional mesh volumes to accommodate higher filler solubility. However, this restriction is temporary as the size of memory available on most computers constantly increases.

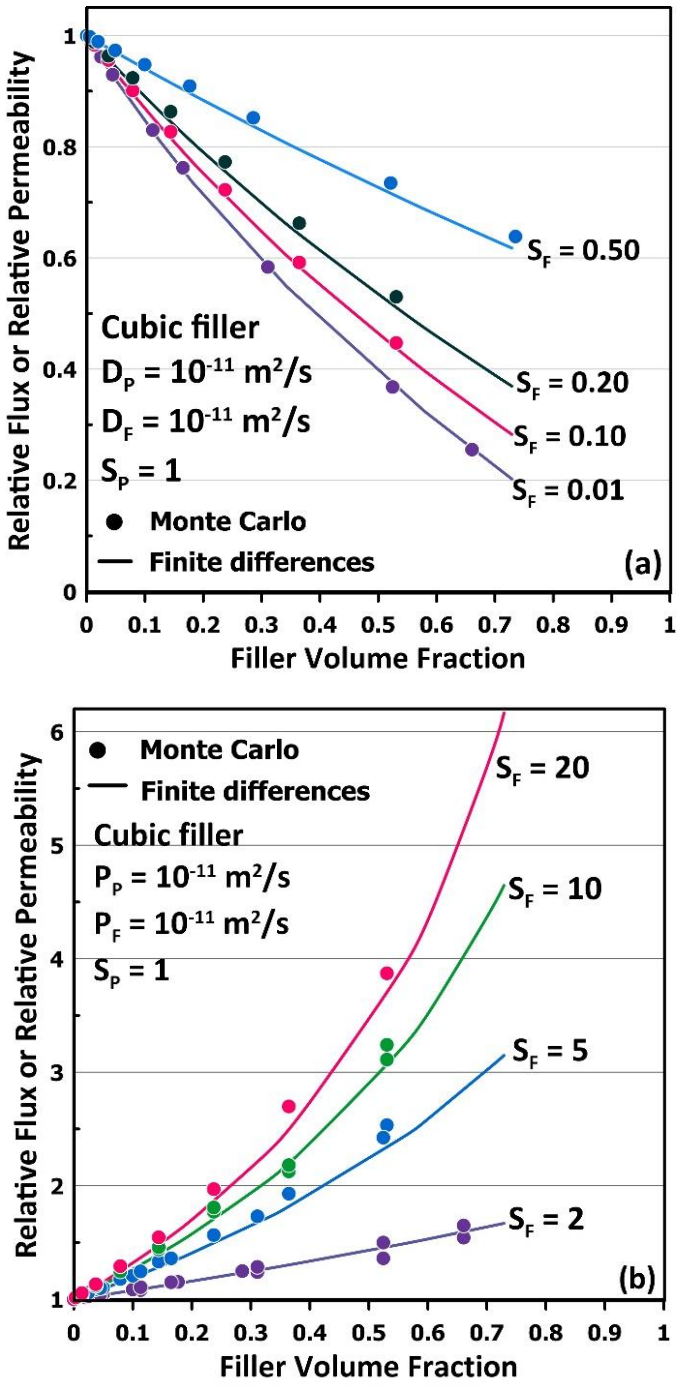

Figure 7.8 The plot of the relative steady-state flux or relative permeability of a MMM with a cubic filler particle for (a) four different filler solubility coefficients lower than the solubility of the polymer and (b) four different filler solubility coefficients higher than the solubility of the polymer. Results are compared with the results of the FD method under identical conditions.

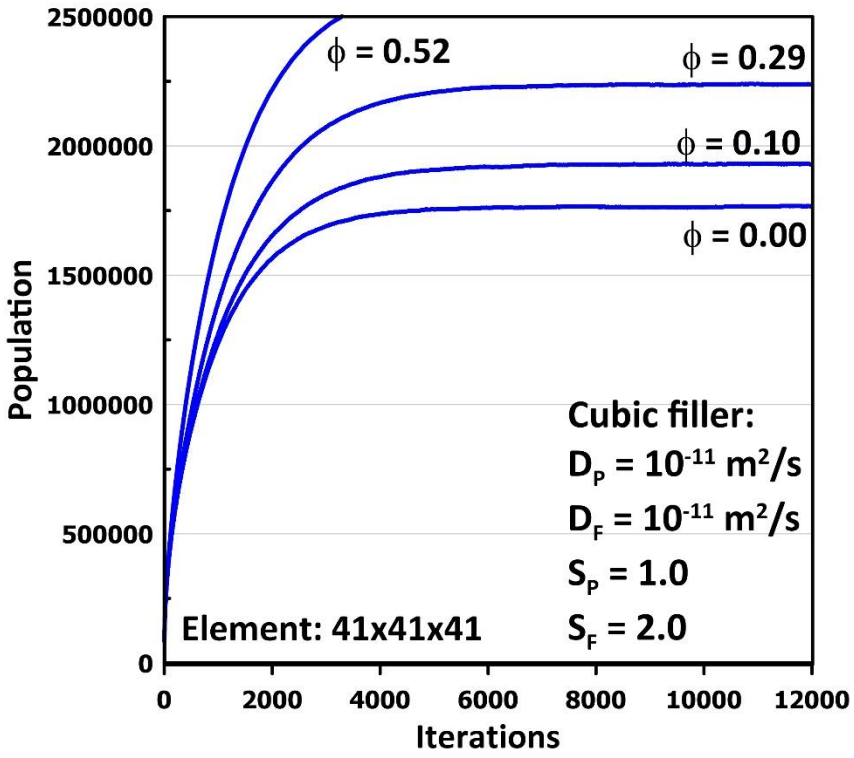

Figure 7.9 The plot of the population of molecules as a function of the number of iterations for different sizes of a cubic filler for the case where the solubility coefficient of the filler is twice the one of the polymers.

MC simulations also allow access to the concentration profile within the MMM. Figure 7.10 presents the instantaneous steady-state concentration profile for a neat polymeric membrane and a MMM with an impermeable cubic filler (19×19×19) embedded in a lattice of an elementary element (41×41×41). This concentration profile is the cross-section of the median *z*-plane of the MMM. Figure 7.10 shows a clear concentration profile and concentration gradient despite the random nature of the permeation process. It is important to point out that this steady-state concentration profile is captured at one particular instant, and the number of molecules in each mesh volume will vary from one instant to another. To attain a very well-defined concentration profile, one would need to use a much larger molecule population, provided the memory allocation and the time of computation are not excessive. Another approach is to take a moving average of the number of molecules over a period of time for each mesh volume of the elementary unit when the steady state has been achieved.

The results presented in this section were obtained assuming ideal MMMs. However, for most fabricated MMMs, it is very difficult to achieve an ideal membrane because of various factors impeding this objective. The most cited reasons for not achieving ideality are particle agglomeration, polymer-filler interfacial void, polymer chain rigidification, pore blockage and method of fabrication. It is very common in designing an MMM to assume ideality, as it is impossible to forecast the defects that the fabricated membrane may suffer. The estimated performance of a MMM, obtained via popular correlations [24-26] for simple filler geometry or numerically by MC or FD for more complex filler geometry, is critical because it serves as a baseline in order to investigate the reasons for deviating from ideality. There are many papers where actual MMM performance was opposite to what was expected, and allowed researchers postulating as to the cause of the observed discrepancies [27]. For example, Ahn et al. [28] investigated the relative permeability of MMMs prepared from polysulfone embedding various amounts of spherical nonporous fumed silica nanoparticles. They measured the relative permeability of six different gases as a function of the filler void fraction and compared their results with the Maxwell correlation [24]. Since these nonporous fumed silica nanoparticles are impermeable, they act as a barrier material, and the relative effective permeability should decrease as a function of the filler volume fraction. However, this was not the case, and the relative permeability increased with the filler volume fraction. They explained this discrepancy by a substantial change in the free volume in the polymer phase caused by the introduction of silica nanoparticles. In fact, they claimed that the diffusion coefficient of the polymeric phase increased with the amount of silica embedded in the polymeric phase due to the increase in the free volume. The Maxwell correlation was used as a baseline to measure the degree of discrepancy in the relative permeability. We believe that another reason to explain this discrepancy could be due to a polymer-filler interfacial void that would enhance the diffusion coefficient around the silica nanoparticles, leading to an enhancement of the permeability. The next phase of our research will use MC simulations with three phases to explain some discrepancies that are commonly observed in the literature, such as interfacial void and polymer chain rigidification. The effect of agglomeration could also be easily studied.

This is where a numerical tool like the one presented in this work becomes essential. It is simply not possible to rely on currently existing correlations.

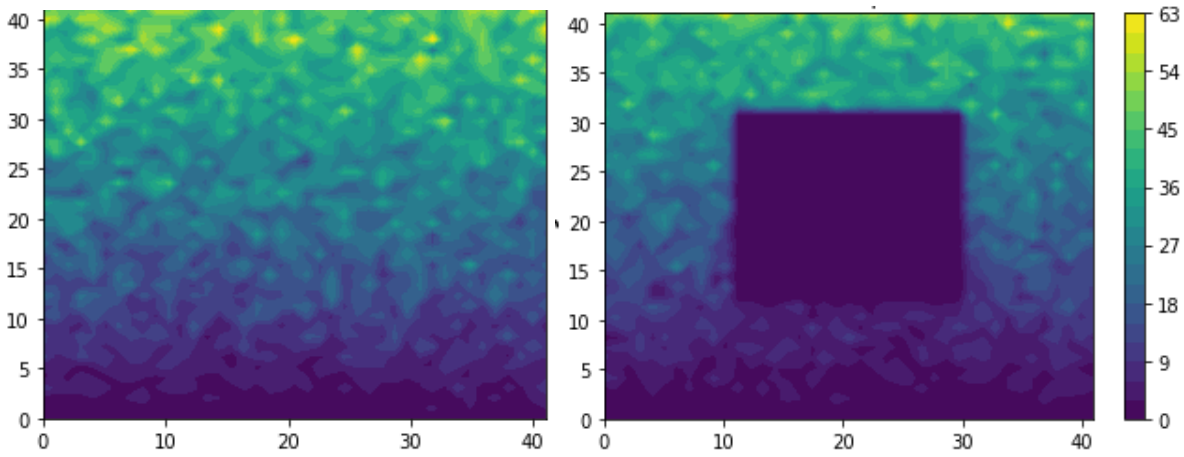

Figure 7.10 The plot of the instantaneous steady-state concentration profile for a neat polymeric membrane (left) and a MMM (right) with an impermeable filler (19×19×19) in an elementary unit (41×41×41). The x-y profile was obtained at the median z-direction.

7.4 Conclusions

This investigation considers the Monte Carlo simulation as a tool for estimating the relative permeability of ideal mixed-matrix membranes over a wide range of polymer and filler parameters. Monte Carlo simulation offers a flexible and accurate approach to estimating the relative permeability of MMMs up to high filler volume fractions. The results are comparable to those obtained by solving Fick's second law of diffusion by finite differences. The ease of coding the MC algorithm compared to finite differences or finite elements is an enviable advantage. It was found that the MC algorithm is relatively insensitive to the scale of the grid discretization, provided that the number of molecules considered is sufficiently high. Both MC methods, MC1 and MC2, gave nearly identical results. The current MC solution uses the relative diffusivity for adjusting the migration of a given molecule in the different phases of the MMM, and the relative solubility to reach the equilibrium at the polymer-solid interface.

The power and memory of the current computers allow tackling important engineering problems. Some of the memory limitations encountered in this investigation will surely be resolved in the future, allowing us to consider more complex problems. We are currently extending the MC simulations to consider non-ideal MMMs in an attempt to gain a better understanding of the discrepancies observed in the literature.

Nomenclature

c	Concentration of the permeating gas surrounding the MMM (mol/m^3)
C	Concentration of the permeating gas inside the MMM (mol/m^3)
D	Diffusivity coefficient (m^2/s)
L	Dimension of one side of the elementary unit (m)
n	Number of the division of the elementary unit along a particular axis
p	Pressure of the permeating gas in the surrounding of the MMM (Pa)
P	Permeability (m^2/s)
R	Ideal gas constant (Pa m^3/(mol K))
S	Solubility coefficient ((mol/m^3)/(mol/m^3))
t	Time (s)
T	Temperature (K)

Subscripts:

e	Effective
F	Filler phase
i	Index for mesh point in the x-direction
j	Index for mesh point in the y-direction
k	Index for mesh point in the z-direction

P	Polymer phase
r	Relative
x	x-coordinate (m)
y	y-coordinate (m)
z	z-coordinate (m)
0	Initial
1	Phase 1
2	Phase 2

Abbreviations:

AE	Absolute value of the error
BC	Boundary condition
FD	Finite differences
IC	Initial condition
MC	Monte Carlo
RN	Random number

References

[1] Salahshoori I, Seyfaee A, Babapoor A. Recent advances in synthesis and applications of mixed matrix membranes. Synthesis and Sintering. 2021, 1, 1–27. https://doi.org/10.53063/synsint.2021.116.

[2] Decknik J, Sumby CJ, Janiak C. Enhancing Mixed-Matrix Membrane Performance with Metal−Organic Framework Additives. Cryst. Growth Des. 2017, 17, 4467−4488. DOI: 10.1021/acs.cgd.7b00595.

[3] Gnus M, Dudek G, Turczyn R. The influence of filler type on the separation properties of mixed-matrix membranes. Chemical Papers 2018, 72, 1095–1105. https://doi.org/10.1007/s11696-017-0363-9.

[4] Azimi H, Ebneyamini A, Tezel FH, Thibault J. Separation of Organic Compounds from ABE Model Solutions via Pervaporation Using Activated Carbon/PDMS Mixed Matrix Membranes. Membranes 2018, 8, 40. DOI:10.3390/membranes8030040.

[5] Liu W, Ban Y, Liu J, Wang Y, Hu Z, Wang Y, Li Q, Yang W. ZIF-L based mixed matrix membranes for acetone-butanol-ethanol (ABE) recovery from diluted aqueous solution. Separation and Purification Technology, 2021, 276, 119085. https://doi.org/10.1016/j.seppur.2021.119085.

[6] Liang H, Zou C, Tang W. Development of novel polyether sulfone mixed matrix membranes to enhance antifouling and sustainability: Treatment of oil sands produced water (OSPW). J Taiwan Institute of Chem Eng. 2021, 118, 215-222. https://doi.org/10.1016/j.jtice.2020.12.022.

[7] Feng B, Xu K, Huang A. Synthesis of graphene oxide/polyimide mixed matrix membranes for desalination. RSC Adv., 2017, 7, 2211-2217. DOI: 10.1039/c6ra24974d.

[8] Yang L, Zhang Q, Wang Q, Ding W, Zhang K. Organo-Functionalization: An Effective Method in Enhancing the Separation and Antifouling Performance of Thin-Film Nanocomposite Membranes by Improving the Uniform Dispersion of Palygorskite Nanoparticles. Membranes 2021, 11, 889. https://doi.org/10.3390/membranes11110889.

[9] Hamid MRA, Jeong H-K. Recent advances on mixed-matrix membranes for gas separation: Opportunities and engineering challenges. Korean J Chem Eng 2018, 35, 8, 1577-1600. DOI: 10.1007/s11814-018-0081-1.

[10] Ebneyamini A, Azimi H, Tezel FH, Thibault J. Modelling of mixed-matrix membranes: Validation of the resistance-based model. J. Memb. Sci. 2017, 543, 361–369. DOI: 10.1016/j.memsci.2017.08.064.

[11] Singh T, Kang D-Y, Nair S. Rigorous calculations of permeation in mixed-matrix membranes: Evaluation of interfacial equilibrium effects and permeability-based models. Journal of Membrane Science 2013, 448 160–169. http://dx.doi.org/10.1016/j.memsci.2013.08.010.

[12] Zamanian, M., Sadrnia, H., Khojastehpour, M., Hosseini, F., Kruczek, B., Thibault, J. Barrier Properties of PVA/TiO_2/MMT Mixed-Matrix Membranes for Food Packaging. J. Polym. Environ., 2021, 29(5), 1396-1411.

[13] Monsalve-Bravo GM, Bhatia SK. Extending effective medium theory to finite size systems: Theory and simulation for permeation in mixed-matrix membranes. J Membr. Sci. 2017, 531, 148–159. http://dx.doi.org/10.1016/j.memsci.2017.02.029.

[14] Wang S, Lu L, Wu D, Lu X, Cao W, Yang T, Zhu Y. Molecular Simulation Study of the Adsorption and Diffusion of a Mixture of CO_2/CH_4 in Activated Carbon: Effect of Textural Properties and Surface Chemistry. J. Chem. Eng. Data 2016, 61, 4139−4147. DOI: 10.1021/acs.jced.6b00554.

[15] Dutta RC, Bhatia SK. Transport Diffusion of Light Gases in Polyethylene Using Atomistic Simulations. Langmuir 2017, 33, 936−946. DOI: 10.1021/acs.langmuir.6b04037.

[16] Wei W, Liu J, Jiang J. Atomistic Simulation Study of Polyarylate/Zeolitic-Imidazolate Framework Mixed-Matrix Membranes for Water Desalination. ACS Appl. Nano Mater. 2020, 3, 10022−10031. https://dx.doi.org/10.1021/acsanm.0c02004.

[17] Ebneyamini A, Azimi H, Tezel FH, Thibault J. Mixed-matrix membranes applications: Development of a resistance-based model. J. Memb. Sci. 2017, 543, 351–360. DOI: 10.1016/j.memsci.2017.08.065.

[18] Wu H, Zamanian M, Kruczek B, Thibault J. Gas Permeation Model of Mixed-Matrix Membranes with Embedded Impermeable Cuboid Nanoparticles. Membranes, 2020, 10, 422; doi:10.3390/membranes10120422.

[19] Wu H, Kruczek B, Thibault J. A generalized model for the prediction of the permeability of mixed-matrix membranes using impermeable fillers of diverse

geometry. Journal of Membrane Science 641 (2022) 119951. doi.org/10.1016/j.memsci.2021.119951.

[20] Brandimarte P. Handbook in Monte Carlo Simulation: Applications in Financial Engineering, Risk Management, and Economics. Wiley ebook 978-1-118-59451-3 (2014).

[21] Mode CJ. Applications of Monte Carlo Methods in Biology, Medicine and Other Fields of Science. London: IntechOpen; 2011 440 p. Available from: https://www.intechopen.com/books/105 doi: 10.5772/634.

[22] Sin G, Espuna A. Editorial: Applications of Monte Carlo Method in Chemical, Biochemical and Environmental Engineering. Frontiers in Energy Research. 2020, 8:68. https://doi.org/10.3389/fenrg.2020.00068.

[23] Belova IV, Murch GE, Fiedler T, Ochsner A. The Lattice Monte Carlo Method for Solving Phenomenological Mass and Heat Transport Problems. Diffusion Fundamentals 2017, 4, 15.1-15.23.

[24] Maxwell, JC. A Treatise on Electricity and Magnetism, 1st Ed.; Clarendon Press: London, UK, 1873.

[25] Lewis TB, Nielsen LE. Dynamic Mechanical Properties of Particulate-Filled Composites. J. Appl. Polym. Sci. 1970, 14, 1449–1471. DOI.org/10.1002/app.1970.071040604.

[26] Pal R. New Models for Thermal Conductivity of Particulate Composites. J. Reinf. Plast. Compos. 2007, 26, 643–651. https://doi.org/10.1177/0731684407075569.

[27] Wolf C, Angellier-Coussy H, Gontard N, Doghieri and Guillard V. How the shape of fillers affects the barrier properties of polymer/nonporous particles nanocomposites: A review. 2018, 556, 393-418. https://doi.org/10.1016/j.memsci.2018.03.085.

[28] Ahn J, Chung W-J, Pinnau I and Guiver MD. Polysulfone/silica nanoparticle mixed-matrix membranes for gas separation. Journal Membrane Science. 2008, 314, 123-133. doi:10.1016/j.memsci.2008.01.031.

Chapter 8

Leveraging Electrical Network Models for Solving Fick's Second Law of Diffusion in Membrane Gas Permeation

Zheng Cao, Boguslaw Kruczek, Jules Thibault*

Abstract

The permeation of gases through non-porous membranes is a fundamental process with wide-ranging applications, from gas separation and fuel cell technology to respiratory physiology. Governed by Fick's second law of diffusion, the mathematical modeling of such transport processes often becomes analytically and computationally challenging, especially in heterogeneous, mixed matrix, or multilayered systems. To navigate these complexities, this study revisits and expands upon the use of electrical analogies as an intuitive and powerful modeling approach rooted in mid-20th-century analog computing. By leveraging the mathematical equivalence between diffusion and electrical conduction, we construct an equivalent electrical network that mirrors the transient behavior of gas permeation across membranes. In this framework, concentration gradients are represented as voltage differences, diffusive fluxes as electrical currents, and diffusional resistances as circuit resistances. While traditional applications of electrical analogies have largely focused on steady-state phenomena, our approach enables dynamic analysis and offers conceptual clarity and computational efficiency. This methodology not only simplifies the solution of Fick's second law of diffusion but also reinforces the enduring relevance of analogical thinking in modern engineering practice. Comparative results demonstrate that

the equivalent electrical circuit closely aligns with both analytical and finite difference solutions, validating its effectiveness and accuracy.

Keywords: Electrical analogy, Membrane gas permeation, Fick's law of diffusion, Finite differences, Mixed matrix membranes

Publication status: To be submitted

***Corresponding author**

8.1 Introduction

The permeation of gases across membranes is a fundamental process in numerous scientific and engineering applications, including gas separation, fuel cells, and respiratory physiology. When the membrane is non-porous, this phenomenon is governed by Fick's second law of diffusion, which describes the temporal evolution of concentration profiles in a diffusing medium. Analytical and numerical solutions to this type of partial differential equation can be complex, particularly in heterogeneous or multilayered systems. In addition, experimental determination of transport parameters may be difficult to obtain for these complex systems. To address these challenges, engineers and scientists have resorted to analogies as a powerful and intuitive modeling in addition to an experimental approach. Indeed, analogies have been instrumental in linking engineering principles with the aim of comprehending the underlying phenomena across different engineering fields. For example, the Chilton-Colburn j-factor analogy is one of several theoretical constructs that express the similarity between momentum, heat, and mass transfer in fluid systems, especially under turbulent flow conditions [1,2]. These analogies are useful because they enable engineers to estimate difficult-to-measure quantities, such as mass transfer coefficients from more easily measured heat or momentum data [3,4]. There are indeed scientific studies where researchers use mass transfer experiments to infer heat transfer parameters, and vice versa, often leveraging the

analogy between heat and mass transfer. Heat and mass transfer often follow similar mathematical formulations (e.g., Fourier's law vs. Fick's law), allowing one to be studied via the other. For instance, mass transfer experiments (e.g., using naphthalene sublimation or electrochemical methods) can be easier to control and measure than direct heat transfer setups [5-8].

Historically, one analogy that has been the most prevalent in engineering is the electrical analogy. Up to 1980, analog computers were still widely used to simulate complex process dynamics, especially in engineering and scientific research. These computers used electrical circuits to model differential equations and allowed users to visualize and interact with these equations in a hands-on way, making abstract mathematical concepts more tangible. Analog computers were marvels of mid-20th-century engineering, especially for simulating complex process dynamics like fluid flow, mechanical vibrations, chemical reactions, or control systems, before digital methods took over. Engineers could tweak parameters live and observe system behavior instantly. Analog computers were discarded or sent to museums. Despite the disappearance of analog computers, the use of electrical analogy remains omnipresent in engineering education to help comprehend intuitively complex phenomena. It is being successfully applied to a wide range of engineering problems, including thermal conduction, thermal radiation, process control, and acoustics.

Electrical analogies can exploit the mathematical equivalence between diffusion and electrical conduction, enabling the translation of mass transport problems into equivalent electrical circuits. In this framework, concentration gradients correspond to voltage differences, diffusive fluxes to electrical currents, and diffusional resistances to electrical resistances. This analogy facilitates the application of well-established circuit analysis techniques to solve diffusion problems, offering both conceptual clarity and computational efficiency. Equivalent electrical circuits have been used for many years to explain heat and mass transfer. For example, Yagi and Kunii have used an electrical equivalent circuit to represent heat transfer in a packed bed [9], and Kim and Yeo used them to examine the dynamic analysis of thermal bridges in buildings [10]. Zueco et al. used electrical equivalent circuits in fluid flow problems [11]. Aït-Idir et al. used an

equivalent electrical circuit to study the oxygen transport in a polymer electrolyte membrane fuel cell [12].

The great majority of studies using an equivalent electric circuit used it as a method to illustrate the physical phenomena for steady-state or simple dynamic problems. In this paper, we extend the electrical analogy approach to model the permeation of gases through non-porous membranes. By constructing an equivalent electrical circuit that mirrors the diffusion process, we demonstrate how Fick's second law of diffusion can be solved with greater ease and insight.

8.2 Methodology

8.2.1 Electrical equivalent for a neat membrane (1D)

The similarity of the unsteady-state heat and mass transfer equations with Ohm's law allows us to solve a transport phenomenon problem using an equivalent dynamic electric circuit. The iterative solution of the electric circuit of Figure 8.1 can be used to solve for the permeation of a chemical species across a homogeneous membrane when proper electrical equivalences with the mass transfer equation are used. To solve the electrical circuit of Figure 1 from the initial ground state to the steady state to represent the permeation of a chemical species across a neat membrane (one-dimensional solution), the following procedure is followed.

(a) The domain of solution is divided into N elementary electrical circuits, as shown in Figure 1. Each elementary circuit comprises two resistances R_n and one capacitor C_n, corresponding respectively to the total resistance and the capacitance of the n^{th} elementary circuit. In terms of the solution of the mass transfer problem, the total resistance $2R_n$ of an elementary circuit is equal to $(\Delta y/AD_nS_n)$ as shown in Table 1, with Δy being the thickness of the corresponding membrane layer ($\Delta y = L_y/N$), A the area of the membrane considered, D_n the diffusivity of the n^{th} layer of the membrane, and S_n its solubility. The accumulated charge in the capacitor is proportional to the concentration of the chemical species, with the capacitance being equal to $(A\Delta yS_n)$.

(b) All voltages (V_n and U_n), currents ($I_{n,1}$, $I_{n,2}$, and $I_{n,3}$), and accumulated charges (Q_n) of all elementary circuits are initially set to zero. At time $t = 0$, the surface voltage V_1 or the input voltage of the first elementary circuit is set to the equivalent surface concentration that would prevail at the surface of the membrane, typically equal to C_0S_1 or p_0S_1/RT. At the same time, the voltage at the downstream side of the membrane, i.e., the output voltage V_{N+1} of the N^{th} elementary circuit, is set to zero, which corresponds to a perfect vacuum at the permeate side of the membrane. For the one-dimensional solution of a neat membrane, the initial condition and the two boundary conditions define the problem to be solved.

(c) At each integration time step Δt, the currents in the three branches of each elementary circuit are calculated using Ohm's law (Eqs. 8.1-8.3), which then allows us to calculate the increase in the accumulated charge at each iteration using Eq. (8.4).

$$I_{n,1} = \frac{V_n - U_n}{R_n} \tag{8.1}$$

$$I_{n,2} = \frac{U_n - U_{n+1}}{R_n + R_{n+1}} \tag{8.2}$$

$$I_{n,3} = I_{n,1} - I_{n,2} \tag{8.3}$$

$$\frac{dQ_n}{dt} = I_{n,3}^t \quad \Rightarrow \quad \mathrm{Q}_n^{t+\Delta t} = \mathrm{Q}_n^t + I_{n,3}^t \Delta t \tag{8.4}$$

(d) The temporal increase in the accumulated charge in the capacitor provides the new value of voltage U_n at the center of each elementary electrical circuit via Eq. (8.5).

$$U_n^{t+\Delta t} = \frac{Q_n^{t+\Delta t}}{C_n} \tag{8.5}$$

With the new values of voltage U_n, the input voltage V_n of each elementary circuit can be calculated via Eq. (8.6) with V_1 remaining fixed.

$$V_n^{t+\Delta t} = \frac{R_{n-1}R_n}{R_{n-1} + R_n}\left[\frac{U_{n-1}^{t+\Delta t}}{R_{n-1}} + \frac{U_n^{t+\Delta t}}{R_n}\right] \quad \textit{for } n = 2 \textit{ to } N \tag{8.6}$$

This procedure is repeated a large number of integration time steps Δt until a steady state has been achieved. The currents $I_{1,1}$ and $I_{N,2}$ correspond to the instantaneous fluxes at the upstream and downstream surfaces of the membrane, respectively.

Table 8.1 Equivalences between heat transfer, mass transfer, and electrical circuits.

Heat transfer	Mass transfer	Electrical circuit
$q = Ak\frac{\Delta T}{\Delta y}\ \left(\frac{J}{s}\right)$	$J = ADS\frac{\Delta C}{\Delta y} = AP\frac{\Delta C}{\Delta y}\ \left(\frac{mol}{s}\right)$	$I = \frac{\Delta V}{R}\ \left(\frac{V}{\Omega}\ or\ Ampere\right)$
$Acc = A\Delta y\rho C_P(T - T_{ref})\ \ (J)$	$Acc = A\Delta ySC\ \ (mol)$	$Acc = \text{Charge} = Q = CV\ \ (C)$
$C = A\Delta y\rho C_P\ \ (\frac{J}{^oC})$	$C = A\Delta yS\ \ (m^3)$	C
$R = \frac{\Delta y}{Ak}\ \left(\frac{^oC\ s}{J}\right)$	$R = \frac{\Delta y}{ADS} = \frac{\Delta y}{AP}\ \left(\frac{s}{m^3}\right)$	R

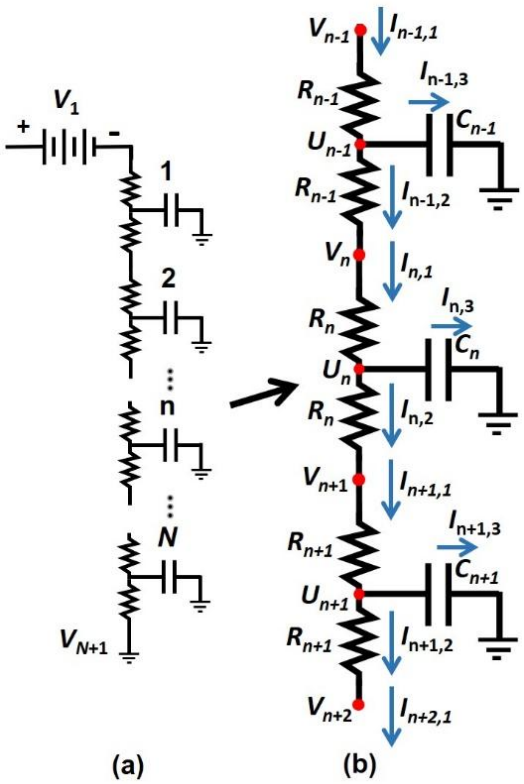

Figure 8.1 Equivalent electrical circuit for a neat membrane corresponding to the one-dimensional solution of Fick's second law of diffusion. The membrane is divided into N elementary circuits.

8.2.2 Electrical equivalent for a three-dimensional membrane

The one-dimensional equivalent electrical circuit used to represent the dynamic permeation of a chemical species through a neat homogeneous membrane can be easily extended to a three-dimensional (3D) electrical network, such as for solving Fick's second law of diffusion for mixed matrix membranes (MMMs) (Figure 8.2(a)), which are used as a three-dimensional case study in this investigation. For this illustrative example, it is assumed that MMMs are ideal, implying that all solid filler particles, having identical shape, geometry, and orientation, are uniformly distributed within the polymer matrix. In addition, the polymer/particle interface is considered ideal, and the permeability and solubility coefficients for both the polymer and the filler particles are assumed constant. The two-phase MMM is subdivided into a number of elementary units. Each elementary unit consists of a polymer matrix with a centrally located solid particle, schematically presented in Figure 8.2(a). The solid volume fraction of an elementary unit is identical to the volume fraction of the entire MMM. It has been shown that the effective permeability of an elementary unit is identical to the permeability of the entire MMM [13,14]. As a result, to solve numerically for the effective permeability of MMMs, it is only necessary to consider one elementary unit. In Cartesian coordinates, the three-dimensional elementary unit of dimensions $L_x \times L_y \times L_z$ is discretized into a grid comprised of $N_x \times N_y \times N_z$ discrete volumes. The solid filler particle of dimensions $x_F \times y_F \times z_F$ located at the center of the elementary unit has a diffusivity coefficient D_F and a solubility coefficient S_F, whereas, for the continuous polymeric phase in the elementary unit surrounding the filler, they are D_p and S_p, respectively.

Each 3D discrete volume of the elementary unit of the membrane can be represented by the electric circuit of Figure 8.2(b). There are now six branches, two for each dimension, connected to the center point of the discrete volume. All six resistances $R_{i,j,k}$ of the discretized volume (i,j,k) are identical, but may vary from one discrete volume to another. For instance, the resistances of a discrete volume representing the polymer will be different from that of the filler particle. Each capacitance $C_{i,j,k}$ may also vary from one discrete volume to another when the volume $(\Delta x \Delta y \Delta z)$ and solubility $(S_{i,j,k})$ are different.

The resistance and capacitance of a discrete volume are specified using the equivalent mass transfer variables of Table 8.1. Each interior discrete volume is subjected to the following procedure. At each integration time step Δt, the currents in the six branches of each discrete volume are calculated using Ohm's law, and used to calculate the excess current $I_{i,j,k,C}$ going to the capacitor, as per Eq. (8.7). The subscripts 1 and 2 are associated with the currents entering and leaving using the two branches in the x-direction, respectively. Similarly, subscripts 3 and 4, and 5 and 6 are associated with the y- and z-directions, respectively.

$$\begin{aligned} I_{i,j,k,C} &= I_{i,j,k,1} - I_{i,j,k,2} + I_{i,j,k,3} - I_{i,j,k,4} + I_{i,j,k,5} - I_{i,j,k,6} \\ &= \frac{U_{i,j,k} - U_{i-1,j,k}}{R_{i-1,j,k} + R_{i,j,k}} - \frac{U_{i+1,j,k} - U_{i,j,k}}{R_{i,j,k} + R_{i+1,j,k}} + \frac{U_{i,j,k} - U_{i,j-1,k}}{R_{i,j-1,k} + R_{i,j,k}} - \frac{U_{i,j+1,k} - U_{i,j,k}}{R_{i,j,k} + R_{i,j+1,k}} \\ &+ \frac{U_{i,j,k} - U_{i,j,k-1}}{R_{i,j,k-1} + R_{i,j,k}} - \frac{U_{i,j,k+1} - U_{i,j,k}}{R_{i,j,k} + R_{i,j,k+1}} \end{aligned} \tag{8.7}$$

The excess current $I_{i,j,k,C}$ for the discrete volume (i,j,k) is the current that flows to the capacitor and, therefore, allows the calculation of the increase in the accumulated charge at each iteration using Eq. (8.8).

$$\frac{dQ_{i.j.k}}{dt} = I^{t}_{i,j,k,C} \quad \Rightarrow \quad \mathrm{Q}^{t+\Delta t}_{i,j,k} = \mathrm{Q}^{t}_{i,j,k} + I^{t}_{i,j,k,C}\Delta t \tag{8.8}$$

As per Eqs. (8.5)-(8.6) for the 1D electric circuit, the voltage at the center of each discrete volume $U_{i,j,k,}$ and, subsequently, the voltages $V_{i,j,k}$ at the interface between two discrete volumes can be calculated, allowing for another iteration to be executed, until a steady state has been achieved.

Eq. (8.7) is valid for all interior discrete volumes. For a complete solution, the initial and boundary conditions must be defined. For the initial condition, that is, before the concentration or pressure step change on the feed side of the membrane occurs at time $t = 0$, a nil voltage (concentration) prevails throughout the membrane (Eq. (8.9)). For the boundary conditions in Cartesian coordinates, six relations are required at the six surfaces of the repeatable elementary unit to completely define the problem. Eq. (8.10) provides the boundary conditions on the upstream and downstream sides of the membrane (the y-axis is the permeation direction). It is assumed that at the onset of permeation, a step

change in the gas pressure or concentration is applied to the upstream side of the membrane ($y = 0$), whereas the gas pressure at the downstream side of the membrane ($y = L_y$) is kept under a perfect vacuum. The resulting concentrations in the membrane at both surfaces are simply the product of the neighboring gas pressure or concentration and the solubility of the polymer. Because all repeatable elementary units are identical, symmetry conditions prevail at their other four faces as expressed in Eq. (8.11) for $BC_{3\text{-}6}$. These are periodic boundary conditions since the MMM is formed of a large number of identical elementary units.

$$\text{IC:} \quad V_{i,j,k}^{t<0} = U_{i,j,k}^{t<0} = 0 \qquad \forall i,j,k \tag{8.9}$$

$$\begin{aligned} &\text{BC}_1: V_{i,j=1,k} = \frac{p_0}{RT} S_{i,1,k} = \mathrm{c}_0 S_{i,1,k} \qquad \forall i,k \\ &\text{BC}_2: V_{i,j=N_y+1,k} = 0 \qquad \forall i,k \end{aligned} \tag{8.10}$$

$$\begin{aligned} &\text{BC}_3: \quad I_{i=1,j,k,1} = 0 \qquad \forall j,k \\ &\text{BC}_4: \quad I_{i=N_x,j,k,2} = 0 \qquad \forall j,k \\ &\text{BC}_5: \quad I_{i,j,k=1,5} = 0 \qquad \forall i,j \\ &\text{BC}_6: \quad I_{i,j,k=N_z,6} = 0 \qquad \forall i,j \end{aligned} \tag{8.11}$$

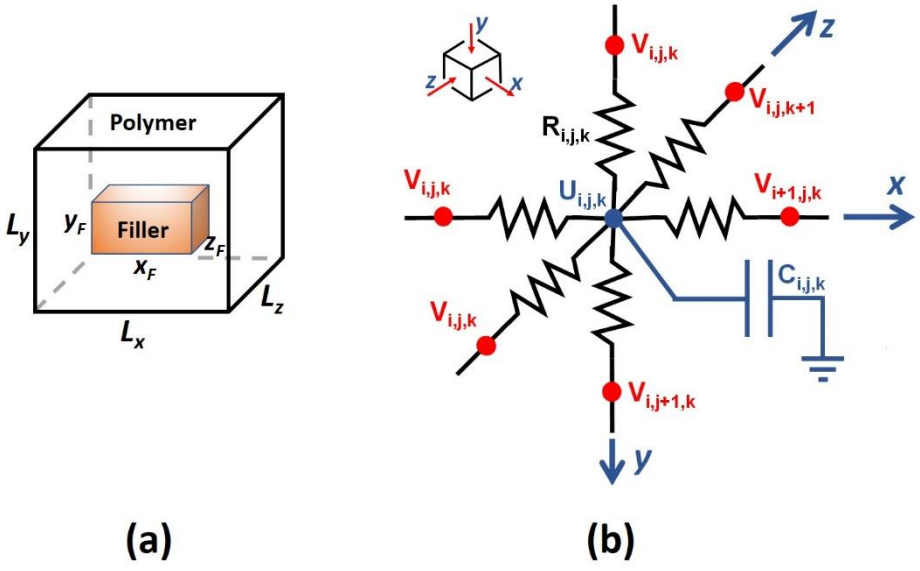

Figure 8.2 Electrical circuit configuration of a discrete volume necessary to solve the three-dimensional solution of Fick's second law of diffusion, such as for a mixed matrix membrane shown in (a).

8.2.3 Three-dimensional finite difference method

For 1D solutions, it is possible to compare the prediction of the equivalent electric circuit with analytical solutions. For 3D solutions, there are no known analytical solutions. As a result, to assess the precision of the solutions of the 3D electrical network comprised of a large number of elemental electrical circuits of Figure 8.2(b), solutions of the same problem obtained with the finite difference method will be used. More details on the derivation, the boundary conditions, and the solution of Fick's second law of diffusion via the finite difference method can be found in Ref: [15,16]. The results obtained by the finite difference method are used as the benchmark for evaluating the accuracy of the results obtained by the electrical circuit analogy.

8.3 Results and Discussion

8.3.1 Neat membrane (1D solution)

To explore the accuracy for simulating the dynamic permeation of a chemical species across a neat polymeric membrane via the equivalent electrical circuit of Figure 8.1, results are compared with an analytical solution (Eq. (8.12)) and presented in Figure 8.3(a). When the resistances and the capacitances of the electric circuit are calculated based on their equivalence to the mass transfer equation (Table 8.1), the profile of the voltage as a function of time across the electrical network of Figure 8.1 provides directly, without any back substitution, the concentration profile across the membrane at the same time, as shown in the concentration plots of Figure 8.3(a). The concentration profile is predicted very accurately throughout the permeation process.

Figure 8.3(b) presents the instantaneous membrane inlet and outlet fluxes obtained during the simulation of a gas permeating through a non-porous membrane using the electric circuit analogy. The fluxes at the feed and permeate sides of the membrane are obtained directly by the sum of the input and output current densities of the electrical network. The initial upstream flux is high because of the large voltage difference prevailing at the onset of the permeation experiment. As the voltage progressively

increases throughout the membrane, the input flux decreases until a constant permeation rate is achieved. On the other hand, the output flux remains nil until some molecules from the higher upstream concentration migrate through the membrane to emerge at the downstream side of the membrane and eventually leading to an average constant outlet flux equal to the constant permeation rate. The dotted line in Figure 8.3(b) represents the instantaneous input and output fluxes calculated with the analytical solution given in Eqs. (8.13)-(8.14). The equivalent electric circuit can provide an accurate prediction of the dynamic concentration profiles and the corresponding input and output fluxes when the equivalence between mass transfer and the electric circuit of Table 1 is implemented.

$$C(x,t) = C_0 S\left(1 - \frac{x}{L_y}\right) - \left(\frac{2C_o S}{\pi}\right) \sum_{n=1}^{\infty} \frac{1}{n} sin\left(\frac{n\pi x}{L_y}\right) e^{-\left(\frac{Dn^2\pi^2 t}{L_y^2}\right)} \tag{8.12}$$

$$J_u = J(0,y) = \frac{DC_0 S}{L_y} + \left(\frac{2DC_o S}{L_y}\right) \sum_{n=1}^{\infty} e^{-\left(\frac{Dn^2\pi^2 t}{L_y^2}\right)} \tag{8.13}$$

$$J_d = J(L_y,t) = \frac{DC_0 S}{L_y} + \left(\frac{2DC_o S}{L_y}\right) \sum_{n=1}^{\infty} \cos(n\pi)\, e^{-\left(\frac{Dn^2\pi^2 t}{L_y^2}\right)} \tag{8.14}$$

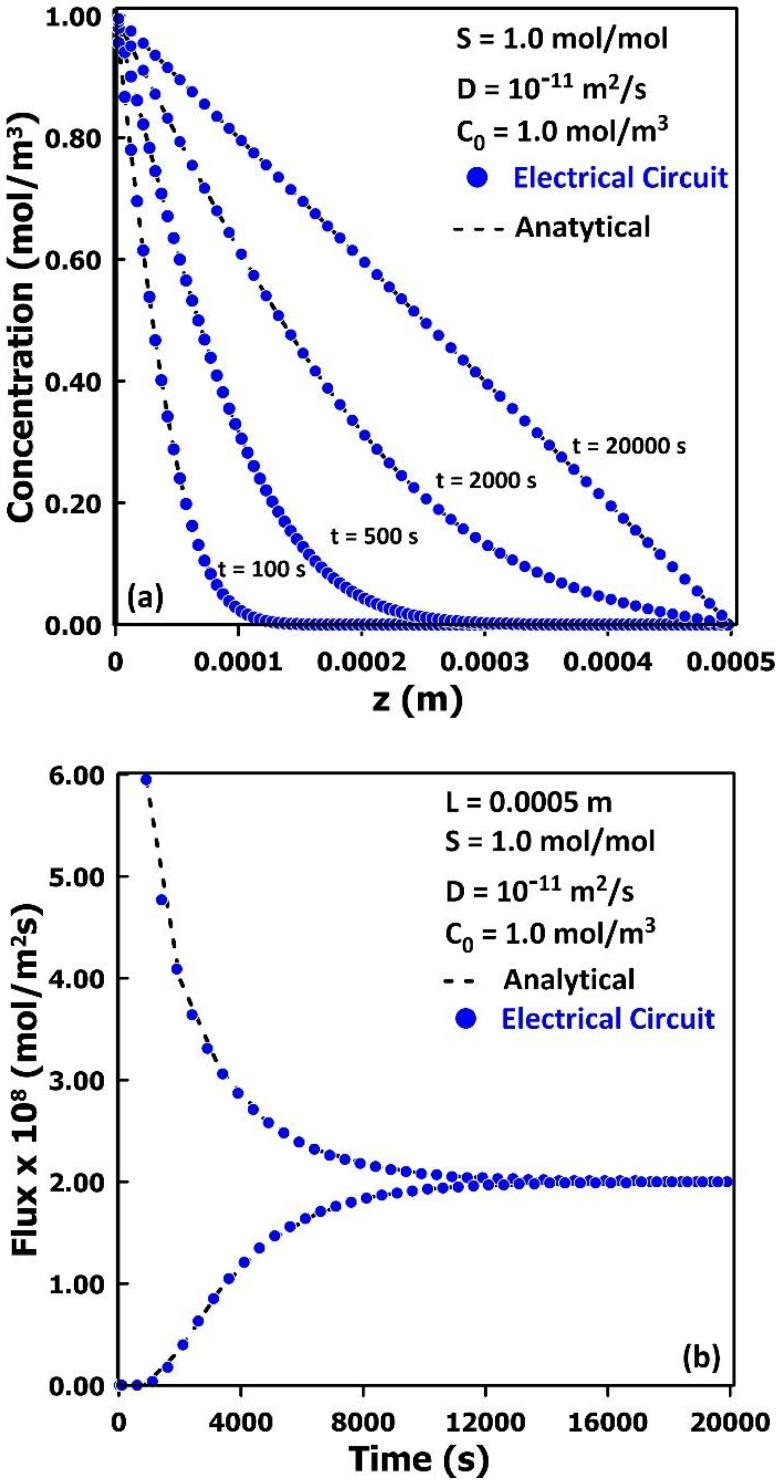

Figure 8.3 Comparison of the analytical solution and the numerical solution obtained using the electrical circuit for (a) the concentration profile across the membrane at four different times, and (b) the upstream and downstream fluxes as a function of time.

8.3.2 Mixed matrix membrane (3D solution)

The ability of the electric circuit analogy for solving Fick's second law of diffusion for three-dimensional systems has been assessed by considering the gas permeation within a MMM. The solid filler particles of different geometries are typically embedded within the matrix of a polymeric membrane. In a MMM, filler particles play a crucial role in enhancing the membrane's performance beyond what the polymer alone can achieve. Fillers like zeolites, metal-organic frameworks (MOFs), or silica can act as molecular sieves, allowing certain molecules to pass while blocking others, thereby boosting separation efficiency. Some fillers create additional pathways to augment or reduce the tortuosity of diffusion, thereby modifying the permeability of molecules through the membrane. In this section, the electric circuit of Figure 8.2 will first be used to predict the permeability of a MMM acting as a barrier material with a filler having a relatively low permeability ($P_F = 10^{-18}$ m^2/s) compared to the permeability of the polymer matrix ($P_p = 10^{-12}$ m^2/s). In the absence of a three-dimensional analytical solution for a MMM, the identical problem was also solved using the finite difference method, and the results are used to assess the precision of the electrical equivalency results.

A series of simulations was performed using spherical and cubic filler particles of different sizes. Results of these simulations are presented in Figure 8.4, where the relative membrane permeability is plotted as a function of the filler volume fraction. The relative permeability is defined as the ratio of the effective permeability of the MMM and that of the pure polymeric membrane, expressed as P_{eff}/P_p. Figure 8.4(a) compares the relative permeability of MMMs containing spherical fillers, as calculated with three different approaches: the equivalent electrical network, the finite difference method, and the Maxwell equation (Maxwell, 1873). The Maxwell equation was derived for the estimation of the relative permeability of a dispersion of spheres in a continuous phase of permeabilities P_F and P_P, respectively, as given in Eq. (8.15). The Maxwell equation is recommended for a filler volume fraction of up to approximately 0.25, but results show that it predicts with relatively good precision the relative permeability for much higher volume fractions. Results clearly show that the three methods provide essentially the same

results for the estimation of the relative permeability, with higher deviations in the estimation with the Maxwell equation at higher filler volume fractions. Figure 8.4(b) presents similar results for an MMM with cubic fillers. Both simulations of the electrical circuit analogy and the finite difference method give identical results over a large range of the filler volume fraction. The relative permeability is also predicted very well with the Maxwell equation.

$$\frac{P_{eff}}{P_p} = \frac{P_F + 2P_p - 2\phi(P_p - P_F)}{P_F + 2P_p + \phi(P_p - P_F)} \tag{8.15}$$

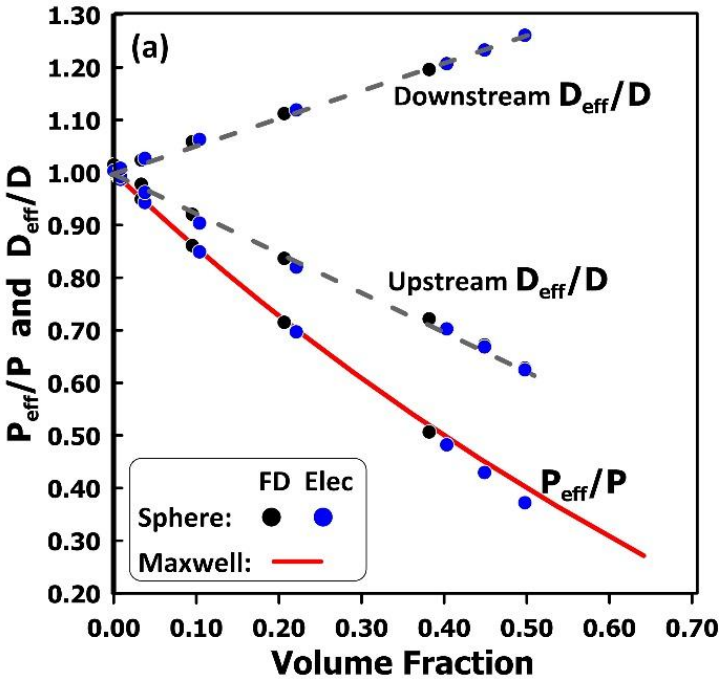

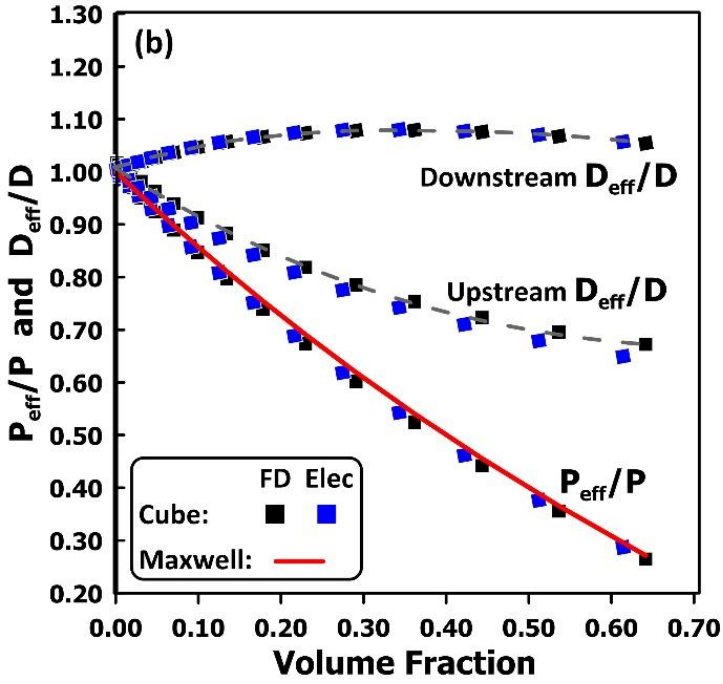

Figure 8.4 Comparison of the electrical circuit analogy, the finite difference method, and the Maxwell equation for the estimation of the relative permeability of a MMM with (a) spherical and (b) cubic fillers as a function of the filler volume fraction. Also plotted are the relative diffusivity of the MMM based on the upstream and downstream time-lag methods.

In gas permeation experiments, the time-lag method (Daynes, 1920) can be used to determine the membrane diffusivity by monitoring the transient permeation rate of a gas through a non-porous membrane [17]. As in the simulations performed in this investigation, the upstream side of the membrane is suddenly pressurized while the downstream remains under or near vacuum. As gas begins to permeate into the downstream chamber, the pressure increase is monitored. Under a steady permeation rate, the slope of the downstream pressure rise curve is extrapolated to the time axis, and this intercept provides the downstream time lag (θ_d). The effective diffusion coefficient (D_{eff}) can be calculated using Eq. (8.16). With the proper apparatus and monitoring devices, it is now possible to measure accurately the pressure decay in the upstream reservoir, which allows to determine the upstream time lag (θ_u) and, as a result, the effective diffusivity using Eq. (8.17). Estimations of the relative diffusivity determined with the upstream and

downstream time lags are presented in Figure 8.4 as a function of the filler volume fraction for the MMMs with spherical and cubic filler particles. Results show that the time-lag method for a neat polymeric membrane ($\phi = 0$) returns the exact value that was used in the simulations. As the volume fraction is increased, the relative diffusivity estimated using the downstream time lag increases linearly for the MMM with spherical fillers, whereas it increases to a lesser extent for the cubic fillers and passes through a maximum at a volume fraction of approximately 0.30. The relative diffusivity estimated via the upstream time lag shows the opposite behaviour, where it decreases with the volume fraction. The two time-lag methods provide different estimates for the same MMM with different patterns for different particle geometries. The estimation is obviously wrong. It has been shown in an earlier work that a good estimate of the effective diffusivity for MMMs using the downstream time-lag method becomes accurate with a larger number of repeatable layers of filler particles in the direction of permeation [18,19]. The permeability of MMM is estimated very accurately for a single repeatable elementary unit, but this is not the case for the estimation of the diffusivity. This discrepancy is beyond the scope of this investigation, as it aims to clearly show that the equivalent electrical circuit is able to accurately predict process variables with an accuracy akin to the finite difference method.

$$D_{eff} = \frac{L_y^2}{6\theta_d} \tag{8.16}$$

$$D_{eff} = \frac{L_y^2}{3\theta_u} \tag{8.17}$$

To further assess the ability of the equivalent electrical circuit to solve Fick's second law of diffusion for different filler particle shapes, a series of simulations was performed with MMMs incorporating square plate fillers of different thicknesses. Results for the estimation of the relative permeability are presented in Figure 8.5 and compared with those obtained with the finite difference method. The projected area of the three simulated square plates covers 12.5%, 25.0%, and 56.2% of the surface area of the repeatable elementary unit. Results show that nearly identical relative permeability of MMMs was obtained with the two simulation methods. Because the fillers have a relatively low permeability, it is normal that the relative permeability decreases with the volume fraction

and the projected area of the filler. These MMMs act as barrier materials. If the permeability of the filler particle were higher than that of the continuous polymeric phase, the relative permeability would be above unity and increase with the volume fraction.

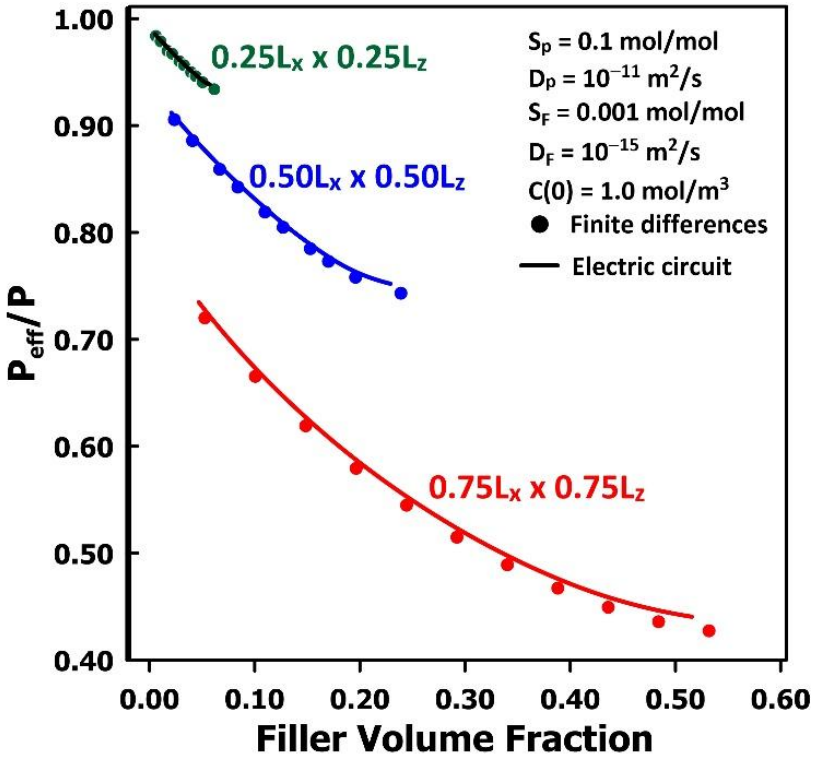

Figure 8.5 The comparison of the relative permeability of mixed matrix membranes for three different filler particles as a function of the filler volume fraction, calculated with the equivalent electrical circuit and finite differences.

For each of the fillers of Figure 8.5, the relative diffusivity of one repeatable elementary unit was determined using the upstream and downstream time-lag methods for comparison purposes. Estimates of the relative diffusivity obtained with the equivalent electric circuit, presented in Figure 8.6, are nearly identical to the values determined using the finite difference method, showing that the electrical network is a viable method to solve for Fick's second law of diffusion. The pattern observed for the relative diffusivity depends on the volume fraction, the geometry of the filler particles, the permeability of the filler, and the number of repeatable unit layers stacked on top of each other. This topic, with its observed discrepancies in the use of the time-lag method for MMMs, evidently

deserves to be fully investigated. The results nevertheless demonstrated that the equivalent electrical circuit is a good method to solve for Fick's second law of diffusion for gas permeation through membranes.

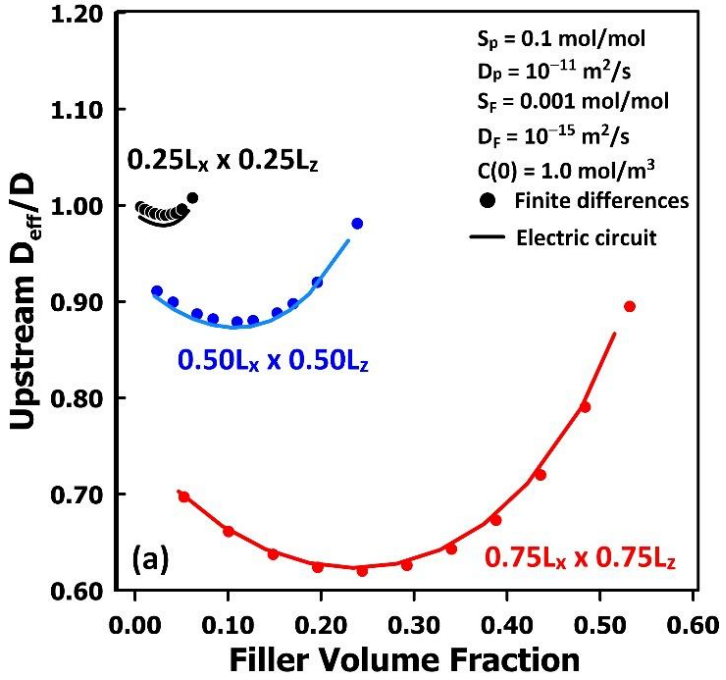

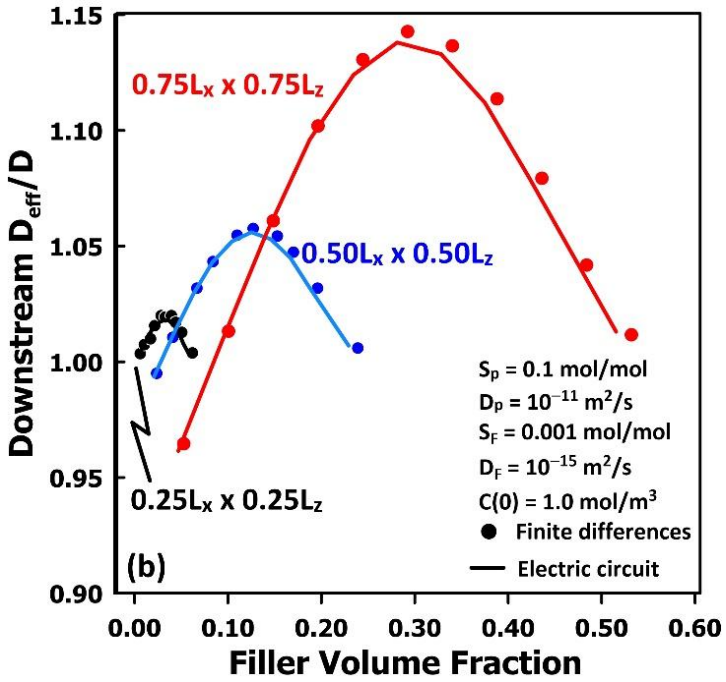

Figure 8.6 The comparison of the upstream (a) and downstream (b) relative diffusivity of mixed matrix membranes as a function of the filler volume fraction, calculated with the equivalent electrical circuit and finite differences.

The instantaneous input and output fluxes were calculated using both simulation methods for one of the MMMs for which the results were presented in Figures 8.5 and 8.6. The fluxes for the electrical circuit are directly evaluated with the average current density at the upstream and downstream sides of the repeatable elementary unit. The fluxes obtained by the finite difference method are evaluated using Fick's first law of diffusion with the average concentration gradient at the upstream and downstream sides of the elementary unit. The results of Figure 8.7 show that the fluxes are identical for both methods of solution.

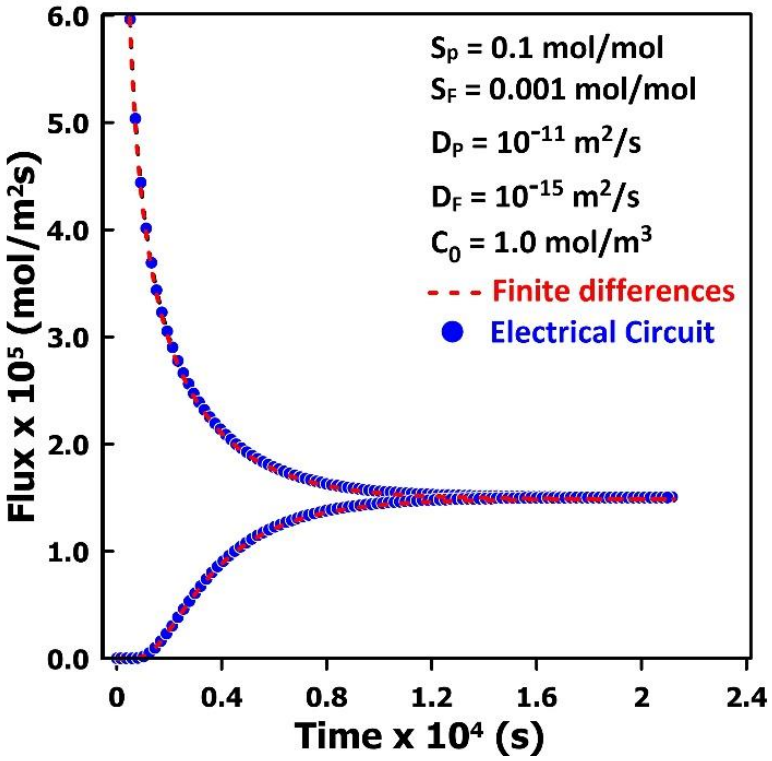

Figure 8.7 Comparison of the finite difference method and the electrical analogy for the estimation of the upstream and downstream fluxes for a mixed matrix membrane incorporating a nearly-impermeable cuboid. Solutions were obtained for a 50-nm cubic elementary unit with a nanoparticle of dimensions $0.5L_x \times 0.92L_y \times 0.5L_z$.

8.3.3 Stability and accuracy evaluation

Through a series of numerical simulations, it was found that the integration time step Δt for solving the three-dimensional electrical circuit to ensure a stable solution was identical to the time step required for the solution of Fick's second law of diffusion using the finite difference method. For the solution of three-dimensional parabolic partial differential equations, such as the heat equation or Fick's second law of diffusion, numerical stability is a key concern when applying the finite difference method. For explicit schemes, the time step Δt must satisfy a stringent condition known as the Courant–Friedrichs–Lewy (CFL) condition to avoid instability [20]. Specifically, the time step must be sufficiently small in relation to the spatial grid sizes Δx, Δy, and Δz. This criterion is given in Eq. (8.18) for the three-dimensional solution [21]. In this investigation, the integration time step was chosen as 25% of its minimal value for stability for all simulations.

$$\Delta t < \frac{1}{2D_{\max}\left[\frac{1}{\Delta x^2}+\frac{1}{\Delta y^2}+\frac{1}{\Delta z^2}\right]} \tag{8.18}$$

In Eq. (8.18), D_{max} is the maximum value of the diffusion coefficient within the domain of solution. Violating this bound leads to growing errors and non-physical results. On the other hand, implicit methods allow for larger time steps and are unconditionally stable, but at the cost of higher computational effort.

In addition to stability, the level of discretization of the domain of solution is also an important factor in ensuring an accurate solution. Typically, one performs simulations with different levels of discretization to ascertain that the solution is not dependent on the space discretization. The results of Figure 8.8 show the estimation of the relative diffusivity for a neat membrane, using the upstream time-lag method, as a function of the number of mesh points in the *y*-direction. The prediction errors in the estimation of the relative diffusivity, using the electrical network method, are very low even for 10 mesh points, and become independent of the mesh size with approximately 20 mesh points (Error less than 0.4%). On the other hand, the method of finite differences leads to significant prediction errors (17% for 10 mesh points). The main reason for this lack of

precision of the finite difference method is due to the evaluation of the concentration gradient at the upstream surface of the membrane, especially when the experiment is initiated. The concentration gradient is used to calculate the flux as well as the decrease in pressure in the upstream reservoir. As a result, the pressure decay curve is shifted, which leads to the erroneous estimation of the upstream diffusivity. The solution with the equivalent electric circuit does not suffer from this limitation because the input flux, via the input current, is evaluated directly without having to take a derivative. It would be possible to use smaller mesh sizes near the upstream surface to achieve higher precision of the derivative, but at the expense of higher computation time. The prediction errors for the estimation of the diffusivity with the downstream time-lag method obtained via the finite difference method are negligible, even for a smaller mesh size, because the concentration gradient is smooth and always relatively low.

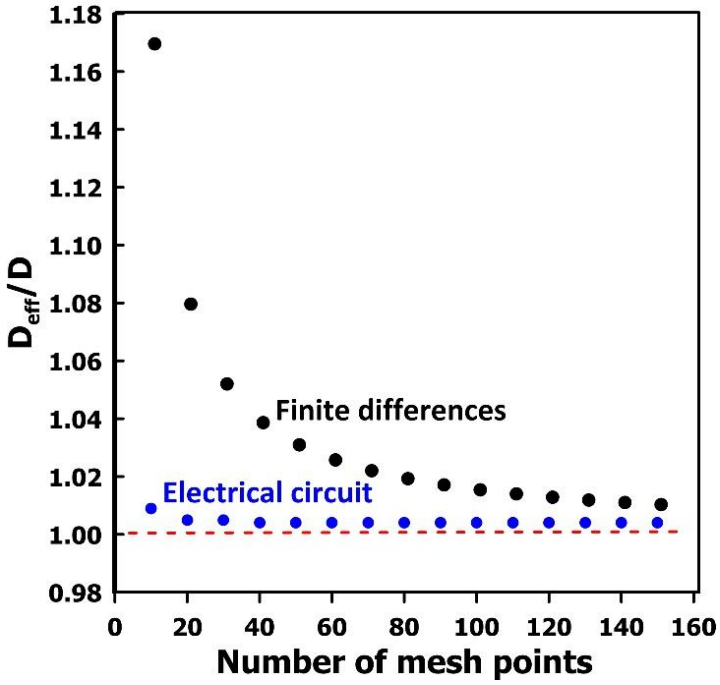

Figure 8.8 Comparison of the estimation of the diffusivity of a neat membrane as a function of the number of mesh points. The estimation is obtained using the upstream time-lag method for the electrical circuit and the finite difference methods.

A series of simulations was performed to assess how the estimation of the effective permeability of MMMs is impacted by the mesh size. The MMMs with the larger square

plate of Figure 8.5 were simulated with three different numbers of mesh points: 41, 81, and 121 in each direction, while keeping the same square plate proportion ($0.75L_x \times 0.75L_z$) of the filler of varying thickness. Results of the relative permeability as a function of the filler volume fraction, obtained with the electrical circuit method and the finite difference method, are presented in Figure 8.9. The three plots obtained with the electrical circuit method are perfectly superimposed, which shows that the relative permeability is independent of the level of discretization of the domain of solution in the range of the mesh size investigated. On the other hand, the finite difference method led to three different plots of the relative permeability. As the mesh size is decreased, the plot of the relative permeability approaches the plots of the results of the electrical circuit method. It is hypothesized that, at the limit, the results of the finite difference method would give the same predictions as for the electrical circuit. It is important to mention, however, that closer results were obtained with the other two smaller square plates and for the spherical and cubic filler particles. The fact that the equivalent electrical circuit network is much less impacted by the discretization level leads to recommending its use to solve the type of problems encountered in this investigation. It provides accurate results and requires fewer computer resources.

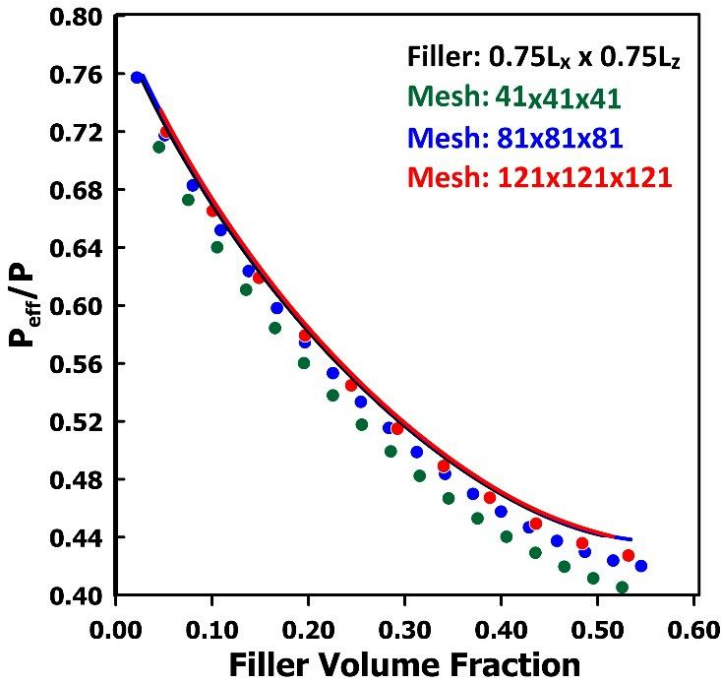

Figure 8.9 The comparison of the relative permeability of a mixed matrix membrane in Figure 8.5 as a function of the filler volume fraction, calculated with the equivalent electrical circuit and finite differences with different levels of discretization.

8.3.4 General Discussion

There are several advantages to resorting to electrical analogy to solve unsteady-state heat and mass transfer problems:

(a) With its simpler concept, electrical circuits are often easier to analyze and code. Engineers can leverage well-established electrical principles like Ohm's Law and Kirchhoff's Law. There exists a straightforward equivalence between heat and mass transfer and the laws of electricity.

(b) The equations to solve for Fick's second law of diffusion are relatively simple to code and solve, much simpler than for the finite difference method and the finite element method. In addition, there exist robust tools and software for electrical circuit analysis that can be adapted for solving heat and mass transfer problems efficiently. In

this investigation, each unit cell was solved recursively using the explicit solution as a function of time, akin to the finite difference solution, until steady state was achieved.

(c) It offers conceptual clarity by providing intuitive parallels between electrical resistance and mass/thermal resistance, voltage and concentration/temperature difference, and current and mass/heat flow.

(d) As many heat and mass transfer problems may involve nonlinear behavior, electrical analogies can be easily adapted to represent them accurately. It was the case in this investigation for the solution of the mixed matrix membranes, where different diffusivity and solubility coefficients were used for the polymer and the filler particles. Indeed, different resistances and capacitances were used.

(e) As the resistance and capacitance of each discrete 3D volume can be specified independently, it would be possible to have the diffusivity and solubility represented by nonlinear variables and behave differently along different directions (anisotropic). For instance, it would be possible to have a capacitance modeled to follow a Langmuir isotherm.

(e) Via the electrical analogy, the upstream and downstream fluxes are calculated directly and more accurately than with the finite difference method, where the flux is calculated from the concentration gradient at both surfaces of the membrane, which may lead to greater prediction errors.

(f) The equivalent electrical circuit is less sensitive to the level of discretization, such that it is possible to use a smaller number of mesh points in each direction, and as a result, less computation time.

8.4 Conclusion

This study demonstrates the effectiveness of using an equivalent electrical network to model the transient diffusion of gases across non-porous membranes. By translating Fick's second law of diffusion into an electrical circuit framework, we offer a novel yet intuitive approach that simplifies the analysis of mass transfer phenomena, particularly in complex, mixed matrix, and multilayered systems. The analogy between electrical

conduction and molecular diffusion not only provides conceptual clarity but also enables the use of well-established circuit analysis techniques to solve time-dependent transport problems.

While electrical analogies have long been employed to illustrate mostly steady-state behavior in heat and mass transfer, our extension to dynamic systems underscores their broader applicability and relevance. This approach opens new avenues for both theoretical modeling and experimental design, especially in cases where direct measurement of transport parameters is impractical. Moreover, it reinforces the pedagogical value of analogical reasoning in engineering education, bridging abstract mathematical formulations with tangible physical insights.

Future work may explore the integration of this method with digital simulation tools, the modeling of reactive or multi-component systems, and the development of experimental setups that physically embody the proposed electrical analogs. Ultimately, the enduring utility of electrical analogies affirms their place not just in the history of engineering, but in its evolving toolkit for solving complex transport phenomena.

Nomenclature

Symbols

A	Surface area: $L_x L_z$ or $\Delta x \Delta z$ (m^2)
C	Concentration (mol/m^3)
C	Capacitance (F)
D	Diffusivity (m^2/s)
I	Current (A)
L	Dimension (m)
N	Number of layers or discrete volumes

p	Pressure (kPa)
P	Permeability (m^2/s)
Q	Electrical charge (C)
R	Resistance (Ω)
R	Ideal gas constant (8.314 J/mol-K)
S	Solubility
t	Time (s)
U	Center voltage of a unit cell (V)
V	Interface voltage of a unit cell (V)
x	x-coordinate
y	y-coordinate (permeation direction)
z	z-coordinate

Greek symbols

Δ	Space or time increment
ϕ	Filler volume fraction
θ	Time lag (s)
Q	Electrical charge (C)

Subscripts/Superscripts

C	Capacitance

d	Downstream
F	Filler
i	Index of x-axis [1 to N_x]
j	Index of y-axis [1 to N_y]
k	Index of z-axis [1 to N_z]
p	Polymer
t	time
0	Upstream
x	x-coordinate
y	y-coordinate (permeation direction)
z	z-coordinate

References

[1] Welty, James R, Charles E Wicks, and Robert E Wilson. Fundamentals of Momentum, Heat, and Mass Transfer. 3rd Ed. New York; Wiley, 1984.

[2] Wilk J. Heat/mass transfer analogy in the case of convective fluid flow through minichannels. Int. J. Thermal Sciences, 156 (2020), 106467. https://doi.org/10.1016/j.ijthermalsci.2020.106467.

[3] Geankoplis, C.J. Transport Processes and Separation Process Principles . 4th Ed. Upper Saddle River, NJ: Prentice Hall PTR, 2003.

[4] Krantz, W. B, and D. T Wasan. Heat, Mass, and Momentum Transfer Analogies for the Fully Developed Turbulent Flow of Power Law Fluids in Circular Tubes. AIChE, no. 6 (1971): 1360–67. https://doi.org/10.1002/aic.690170616.

[5] Han, S, and R.J Goldstein. “The Heat/Mass Transfer Analogy for a Simulated Turbine Endwall.” International Journal of Heat and Mass Transfer 51, no. 11 (2008): 3227–3244. https://doi.org/10.1016/j.ijheatmasstransfer.2008.01.011.

[6] Kanaś, Paulina, Andrzej Jedlikowski, and Sergey Anisimov. The Influence of Geometrical Parameters on Heat and Mass Transfer Processes in Rotary Heat Exchangers. SN Applied Sciences 1, no. 6 (2019). https://doi.org/10.1007/s42452-019-0540-2.

[7] Ko, Sang-Hyuk & Moon, Deok-Won & Chung, Bum-Jin. (2006). Applications of electroplating method for heat transfer studies using analogy concept. Nuclear Engineering and Technology. 38, 3, 251-258.

[8] Shadid, J. N., and Eckert, E. R. G. The Mass Transfer Analogy to Heat Transfer in Fluids with Temperature-Dependent Properties. ASME. J. Turbomach. January 1991; 113(1): 27–33. https://doi.org/10.1115/1.2927734.

[9] Sakae Y., and D. Kunii. Studies on Heat Transfer near Wall Surface in Packed Beds. AIChE J. 6, no. 1 (1960): 97–104. https://doi.org/10.1002/aic.690060119.

[10] Kim H. and Yeo M. Thermal bridge modeling and a dynamic analysis method using the analogy of a steady-state thermal bridge analysis and system identification process for building energy simulation: Methodology and validation. Energies, 13 (2020), 4422. doi:10.3390/en13174422.

[11] Zueco, J., O.A. Beg, H.S. Takhar, and G. Nath. “Network Simulation of Laminar Convective Heat and Mass Transfer over a Vertical Slender Cylinder with Uniform Surface Heat and Mass Flux.” Journal of Applied Fluid Mechanics 4, no. 2 (2011): 13–23. https://doi.org/10.36884/jafm.4.02.11912.

[12] Aït-Idir W., S. Touhami, M. Daoudi, J. Dillet, J. Mainka and O. Lottin, Oxygen Transport Impedance in a Polymer Electrolyte Membrane Fuel Cell Equivalent Electrical Circuit. 2021 International Workshop on Impedance Spectroscopy (IWIS), Chemnitz, Germany, 2021, pp. 36-39, doi: 10.1109/IWIS54661.2021.9711832.

[13] Ebneyamini A., H. Azimi, F.H. Tezel, J. Thibault. Mixed-matrix membranes applications: Development of a resistance-based model. J. Memb. Sci. 2017a, 543, 351–360. DOI: 10.1016/j.memsci.2017.08.065.

[14] Ebneyamini A., H. Azimi, F.H. Tezel, J. Thibault. Modelling of mixed-matrix membranes: Validation of the resistance-based model. J. Memb. Sci. 2017b, 543, 361–369. DOI: 10.1016/j.memsci.2017.08.064.

[15] Wu H, Zamanian M, Kruczek B, Thibault J. Gas Permeation Model of Mixed-Matrix Membranes with Embedded Impermeable Cuboid Nanoparticles. Membranes, 2020, 10, 422; doi:10.3390/membranes10120422.

[16] Wu H, Kruczek B, Thibault J. A generalized model for the prediction of the permeability of mixed-matrix membranes using impermeable fillers of diverse geometry. Journal of Membrane Science 641 (2022) 119951. https://doi.org/10.1016/j.memsci.2021.119951.

[17] Daynes, H.A. (1920). The Process of Diffusion through a Rubber Membrane. Proc. R. Soc. A Math. Phys. Eng. Sci. 97, 286–307.

[18] Wu H, Thibault J, Kruczek B. The validity of the time-lag method for the characterization of mixed-matrix membranes. Journal of Membrane Science 618 (2021) 118715. https://doi.org/10.1016/j.memsci.2020.118715.

[19] Wu H, Kruczek B, Thibault J. On the limitation of the time-lag method for characterizing mixed-matrix membranes embedding filler particles of different permeability. Journal of Membrane Science 663 (2022) 121074. https://doi.org/10.1016/j.memsci.2022.121074.

[20] De Moura, C.A. and Kubrusly, C.S. (2013). The Courant–Friedrichs–Lewy (CFL) condition: 80 years after its discovery. Birkhäuser. DOI: 10.1007/978-0-8176-8394-8.

[21] Carnahan B., Luther H.A., and Wilkes J.O. Applied numerical methods. John Wiley & Sons, Toronto, 1969.

Chapter 9

Conclusions and Recommendations

9.1 Conclusions

The primary objective of this thesis was to calibrate the new CV system, which enables simultaneous monitoring of pressure decay and pressure rise during a conventional time-lag experiment. This calibration enabled a detailed investigation into how feed pressure, membrane thickness, and the characteristics of the porous plate support influence the experimentally determined fundamental transport coefficients (P, D, and S). Commercial PDMS membranes and nitrogen gas were selected for the experiments. PDMS, a rubbery polymer, exhibits intrinsic transport properties (P, D, and S), particularly when using nitrogen as permeant, which behaves as an ideal gas in the range of feed pressures used in this work. The calibration of the new CV system for the potential effects of feed pressure, membrane thickness and the properties of the porous plate support was necessary to distinguish between experimental artifacts and genuine fundamental trends for the ultimate goal of this research program, which is developing a platform for the complete and reliable characterization of new membrane materials, including glassy polymers and MMMs. The systematic experimental studies were supported by the analytical solution of the governing partial differential equation describing the time-lag experiment. When such a solution was not available, numerical simulations using Finite Difference (FD) and Monte Carlo (MC) methods were employed. In addition, the applicability of the Electrical Network Analogy was also considered and extended to solving transient gas permeation in membranes as an alternative to the FD method.

Chapter 2 begins by validating the functionality of our newly developed CV system, designed to simultaneously monitor pressure rise and pressure decay during time-lag

experiments. This capability was confirmed by observing that the ratio of upstream to downstream time lags closely matched the theoretical value of two. Although the pressure decay could be measured immediately after the initiation of a time-lag experiment by adjusting the pressure in the reference section of the upstream volume, this approach led to an inevitable Joule-Thomson effect resulting from gas expansion at the start of the time-lag experiment. In turn, this compromised the reliability of the early pressure decay data. To overcome this problem, we adopted an alternative strategy: the reference and working volumes of the upstream section of the system were connected at the start of the experiment. The pressure decay results were available after the working and reference volumes were remotely disconnected exactly five seconds after the initiation of the experiment. Although the pressure decay results required some data processing, as described in Chapter 2, excellent repeatability of the experimental results was demonstrated in a series of experiments using the commercial PDMS membrane with nitrogen as the permeating gas.

Having a reliable protocol for simultaneously monitoring pressure decay and pressure rise in our new CV system enabled the exploration in Chapter 3 of alternative methods for determining P, D, and S from time-lag experiments, in addition to the conventional method based on monitoring pressure rise downstream from the membrane. By itself, monitoring of the pressure decay allowed for the evaluation of the upstream time lag, i.e., a method that mimics the conventional method based on the pressure rise. In addition, recognizing that the membrane behaves as a semi-infinite solid immediately after initiation of the experiment, we proposed the so-called two-slope method. The first slope is the initial pressure decay versus the square root of time, and the second slope is the pressure decay as a function of time under steady state permeation. The ratio of the two slopes allows for the independent determination of the diffusivity coefficient. Recognizing that the difference between the gas entering and leaving the membrane represents the time-dependent gas accumulation enabled the direct determination of the steady-state gas accumulation in the membrane. In other words, the simultaneous monitoring of pressure decay and pressure rise enabled, for the first time, the direct determination of solubility from a single-time lag experiment. In all other methods, including those based solely on

pressure decay, the solubility is evaluated indirectly from the ratio of permeability and diffusivity.

One of the specific objectives of this thesis was to evaluate the potential effects of the supporting porous plate properties, such as pore size and porosity, on *P*, *D*, and *S* determined using the conventional time-lag method (Chapter 4). Although the effect of the porosity of the supporting porous plate on the apparent membrane permeability can be easily imagined (*P* decreases with a decrease in the porous plate porosity), the corresponding effects on *D* and *S* are more difficult to envision. Consequently, these effects were investigated by numerically simulating the time-lag experiments in various settings. This allowed for the identification of three key parameters that influence *P*, *D*, and *S* in the conventional time-lag method: the pore size and porosity of the porous plate and the thickness of the tested membrane. Similarly to *P*, *D* decreases with a decrease in the porosity of the porous plate. However, even for very small porous plate porosities, the measured *D* would approach the intrinsic value of the polymer for large ratios of the porous plate pore size to the membrane thickness. Given that in the conventional time-lag method, *S* is the ratio of *P* and *D*, for certain combinations of the properties of the porous plate and membrane thickness, *S* might be greater than the intrinsic value of the polymer. Therefore, Chapter 4 illustrates the danger of artifacts in membrane characterization using the time-lag method arising from the presence of the porous plate support. The latter is not optional because the membrane must be supported during the gas permeation experiments.

Besides the effect of the porous support plate in the system, another potential artifact is the effect of the applied pressure gradient through the membrane. Although plenty of research works have reported that the permeability decreases as the membrane is being compacted, there is no study on the effect of feed pressure on *D* and *S* in dense rubbery membranes. In Chapter 5, to systematically study the effect of the feed pressure and membrane thickness on the *P*, *D*, and *S*, alternative methods introduced in Chapter 3 were applied in a series of time-lag experiments on commercial PDMS membranes with diverse thicknesses and feed pressures. This includes the direct determination of *S* via monitoring gas accumulation in the membrane as a function of time. The results represent that, for a

given membrane thickness, *P*, *D*, and *S* decreased with increasing feed pressure. And such decreases are more significant for the thicker membranes. The results were explained by the decreased free volume between polymer chains when the membrane is compacted.

As introduced in Chapter 3, alternative methods to estimate transport properties of a membrane have been developed when the upstream pressure decay and the downstream pressure rise are simultaneously monitored on the new CV system. Each of the methods yields independent *P*, *D*, and *S* values. Chapters 4 and 5 identified potential deviations requiring calibration with the system, including transducer accuracy, temperature variation, porous plate effects, and pressure compaction effects. Therefore, Chapter 6 implemented a data reconciliation technique to determine the more robust *P*, *D*, and *S* values, which are closest to the intrinsic values of the membrane. Both the reliability of data measurements and the accuracy of each estimation method are taken into consideration. The motivation of this work is to refine the time-lag technique and establish comprehensive protocols for evaluating transport properties in complex membrane systems.

The relative properties of the MMMs embedded with impermeable particles were studied using numerical simulations. Chapter 7 considers the Monte Carlo simulation as a tool for estimating the relative permeability of ideal MMMs over a wide range of polymer and filler parameters. The results are comparable to those obtained by solving Fick's second law of diffusion by the finite difference method and the analytical model. The current MC algorithm uses the relative diffusivity for adjusting the migration of a given molecule in the different phases of the MMM, and the relative solubility to reach the equilibrium at the polymer-solid interface, which can also extend to permeable fillers. The ease of coding and the savings of computational load are apparent advantages compared to other methods.

To simplify the solution of Fick's second law of diffusion for non-porous membranes, Chapter 8 developed an electrical analog model to solve the dynamic gas permeation. By translating diffusion processes into equivalent electrical circuits—where concentration gradients map to voltage differences, diffusive fluxes to currents, and diffusional resistances to electrical resistances—the approach provides an intuitive and

computationally efficient solution method. Unlike the traditional approach, which mostly focuses on the steady-state behaviour, this approach was extended to a dynamic permeation system for direct flux calculations. By validating against analytical solutions and finite difference methods for both homogeneous and complex mixed-matrix membranes, the electrical network framework accurately captures dynamic concentration profiles and fluxes with significantly lower mesh point requirements. The analogy between electrical conduction and molecular diffusion not only provides conceptual clarity but also enables the use of well-established circuit analysis techniques to solve more complex transport phenomena.

9.2 Recommendations

The ultimate objective of this research program is to develop a platform for the complete and reliable characterization of emerging membrane materials, including glassy polymers and MMMs. This thesis marks a significant advancement toward that objective by demonstrating the feasibility of accurately monitoring pressure decay and rise in time-lag experiments, thus enabling the alternative approach to determining key transport parameters. While studying the effect of feed on these properties in commercial rubbery PDMS membranes, additional factors emerged that must be addressed before extending the use of our new CV system for characterizing more complex membrane materials. In particular, we speculate that the effect of feed pressure is coupled with that of the supporting porous plate. To decouple these two effects, the following actions are recommended in future studies.

1. To extend the analysis of the effect of the characteristics of the supporting porous plate on basic transport parameters from the conventional time-lag method (Chapter 4) to the new estimation methods developed in Chapter 3, including the upstream time lag, the two-slope method, and the gas accumulation method.
2. According to the ratio of the pore size of the porous plate support to the thickness of the membranes studied in this thesis, the effect of the porous plate support should not be significant. Theoretically, this effect could be magnified by decreasing the membrane thickness. For this purpose, it is recommended to

fabricate polyphenylene oxide (PPO) membranes of different, but much lower thicknesses than the PDMS membrane used in this work. PPO is a glassy polymer and, theoretically, should be less susceptible to compaction. Moreover, because PPO is less permeable than PDMS, relatively thin PPO membranes should allow observing a clear dynamic behaviour of the upstream pressure decay, thus allowing the application of the new methods (Chapter 3) for determining the basic transport parameters.

3. Apart from varying the thickness of the PPO membrane, it is also recommended to machine in-house porous plates with different, but uniform pore sizes and varying porosities to perform a series of time-lag experiments with both the glassy PPO and the commercial PDMS membranes of varying thicknesses.

While following the above recommendations, in addition to decoupling the effect of the porous plate support from the effect of feed pressure, an extensive dataset for characterizing the glassy PPO membrane will be generated. This extensive dataset can be used in two different ways. First, to uncover the actual gas transport mechanism in glassy polymers. Knowing this, the data reconciliation approach from Chapter 6 can be extended to determine the most realistic transport coefficients and other relevant parameters that affect transport in glassy polymers.

Annex A: Additional Contributions

List of publications

[1] P. Leszczynski, Z. Cao, H. Wu, J. Thibault, and B. Kruczek. Determination of time lag by accurate monitoring of pressure decay in a new generation constant volume system. MethodsX 13 (2024), 102858. https://doi.org/10.1016/j.mex.2024.102858.

[2] Z. Cao, J. Thibault, B. Kruczek, Direct determination of permeability, diffusivity, and solubility of gases in membrane based on simultaneous monitoring of pressure rise and decay in a single time-lag experiment, J Memb Sci 720 (2025). https://doi.org/10.1016/j.memsci.2025.123741.

[3] Z. Cao, B. Kruczek, J. Thibault, Impact of the porous support disc of a gas permeation cell on the estimation of the membrane transport properties, J Memb Sci 721 (2025). https://doi.org/10.1016/j.memsci.2025.123831.

[4] Z. Cao, B. Kruczek, and J. Thibault. "Monte Carlo Simulations for the Estimation of the Effective Permeability of Mixed-Matrix Membranes." Membranes (Basel) 12, no. 11 (2022): 1053. https://doi.org/10.3390/membranes12111053.

[5] Z. Cao, H. Wang, J. Thibault, B. Kruczek, Effect of pressure compaction and effective thickness while evaluating membrane transport properties via the time-lag method, (Submitted to JMS)

List of conferences

[1] Z. Cao, B. Kruczek, and J. Thibault. Data Reconciliation for Accurate Characterization of Membrane Properties in Gas Permeation Cells. 15th European Congress of Chemical Engineering (ECCE), and 3rd Iberoamerican Congress on Chemical Engineering (CIBIQ). 2025, Lisbon.

[2] Z. Cao, P. Leszczynski, H. Wu, J. Thibault, B. Kruczek, New possibilities for membrane characterization arising from monitoring of pressure decay in time-lag experiments, Euromembrane 2024, Prague.

[3] Z. Cao, B. Kruczek, and J. Thibault, Impact of the membrane porous support on the estimation of intrinsic membrane properties, Euromembrane 2024, Prague

[4] Z. Cao, B. Kruczek, and J. Thibault, Evaluating Membrane Properties: An Insight into the Time-Lag Method and Influencing Factors,11th International Conference on Fluid Flow, Heat and Mass Transfer, FFHMT 2024, Toronto.

[5] Z. Cao, P. Leszczynski, H. Wu, J. Thibault, B. Kruczek, Innovative Membranes Characterization by Accurate Monitoring of Pressure Decay on Modified Constant Volume System, Canadian Separation Symposium 2023, Toronto.

[6] Z. Cao, P. Leszczynski, J. Thibault, B. Kruczek, Application of simultaneous monitoring of the upstream pressure decay and downstream pressure rise in the novel constant volume testing system to characterize glassy polymer films, Euromembrane 2022, Naples.

[7] Z. Cao, P. Leszczynski, H. Wu, J. Thibault, and B. Kruczek, Novel time-lag protocol for the characterization of gas separation membranes in a constant volume system, The Canadian Chemical Engineering Conference, CCEC 2022.

[8] Z. Cao, P. Leszczynski, H. Wu, J. Thibault, and B. Kruczek, Overcoming challenges of the time lag measurements based on the upstream pressure decay, The Canadian Chemical Engineering Conference. CCEC 2022.

[9] Z. Cao, H. Wu, B. Kruczek, and J. Thibault, Estimation of Mixed-Matrix Membrane Relative Permeability Using Monte Carlo Simulation, 8th International Conference on Fluid Flow, Heat and Mass Transfer, FFHMT 2021.

[10] H. Wu, Z. Cao, B. Kruczek, and J. Thibault, Generalizability of the Time-Lag Method for Mixed-Matrix Membranes: Does One Method Fit It All?. Heat and Mass Transfer, FFHMT 2021.